DSE - Aphrodite

Revolutionising Solar System Dynamics

H.W.W. Guimarães	4343727	M.K. Makaveev	4373154
S. Khurana	4280652	Z.N. Rabilotta Yañez	4273435
I.M. Konovalov	4195124	I.R. Roza	4380827
N.M. de Korte	4279018	W. Van Gijseghem	4353854
T. van Lith	4359291	W. Van Herck	4382943

Final Report

Design Synthesis Exercise

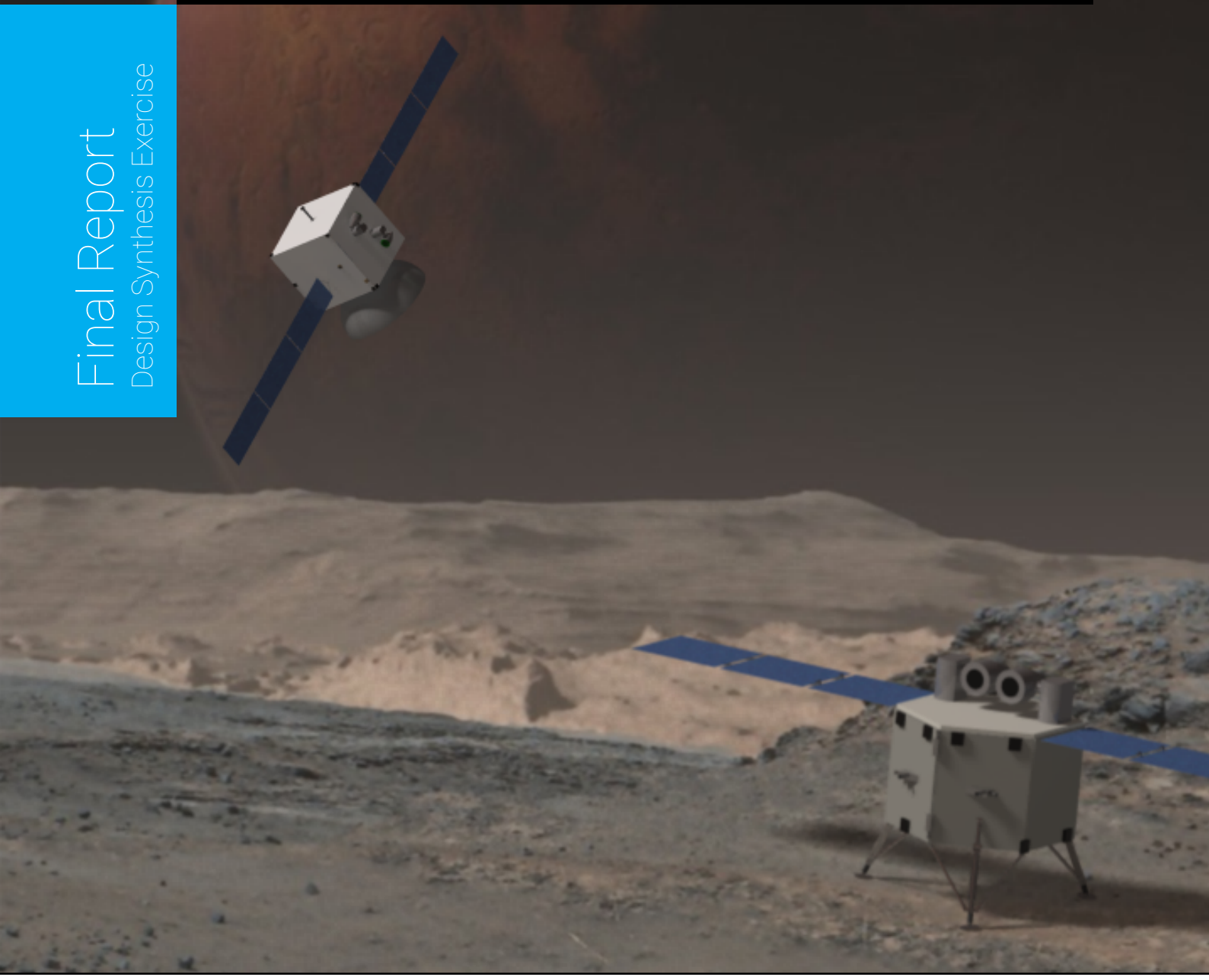

TU Delft Delft University of Technology

Aerospace Engineering

July 4, 2017

[This page is intentionally left blank]

Final Report

Aphrodite:
Revolutionising Solar System Dynamics

by

Group 11

For the Design Synthesis Exercise, at Delft University of Technology.

Student number:	H.W.W. Guimarães	4343727
	S. Khurana	4280652
	I.M. Konovalov	4195124
	N.M de Korte	4279018
	T. van Lith	4359291
	M.K. Makaveev	4373154
	Z.N. Rabilotta Yañez	4273435
	I.R. Roza	4380827
	W.J.L Van Gijseghem	4353854
	W. Van Herck	4382943
Project duration:	April 24, 2017 – July 6, 2017	
Supervisor:	Dr. Ir. D. Dirkx	TU Delft, tutor
	Dr. Ir. J.A. Pascoe	TU Delft, coach
	Dr. Ir. E. Quaeghebeur	TU Delft, coach

TU Delft

[This page is intentionally left blank]

Executive Overview

For centuries, humankind has been trying to characterise the processes governing the solar system by combining Earth and space observations. Using the solar system as a laboratory allows one to test the laws of physics and investigate the physical phenomena emerging from them. Precision laser ranging between planetary bodies will allow advances in the study of fundamental physics and solar system dynamics.

Several leaps have already been taken in the field of interplanetary laser ranging. Starting with passive reflectors on satellites (Satellite Laser Ranging), as elaborated by Seeber [103], and advancing to a lunar passive target (Lunar Laser Ranging) of which details are explained by Dickey et al. [29]. However, these technologies have inherent disadvantages, such as the low signal strength over long distances, which make this technology unfeasible for larger planetary distances. An active laser transponder solves this problem with a two-way laser system. This technology was already demonstrated on the MESSENGER mission at a distance of 0.16 Astronomical units (Smith et al. [108]).

The Aphrodite mission is an innovative mission which has the objective to revolutionise the knowledge of solar system dynamics. The mission aims at providing range measurements within the Martian system and Earth, characterising the geodesy of the Martian moons and the dynamic model of the Martian system more accurately than ever before. This is done by a system of multiple spacecraft consisting of a lander on each of the moons, Phobos and Deimos, in combination with an orbiter in 400 km Mars orbit. Aphrodite exceeds planetary mission standards with high reliability and sustainability at the forefront of the design. It has been designed as part of the Bachelor Design Synthesis Exercise at the faculty of Aerospace Engineering at the Delft University of Technology.

The Aphrodite mission has the following mission statement:

'To accurately measure the distances between Mars, Deimos, Phobos and Earth to increase our understanding of solar system dynamics.'

The goal of Aphrodite is to perform inter- and intra-planetary ranging between Phobos, Deimos, Mars and Earth for a period of eight years. Planetary laser ranging aids the construction of a model to evaluate the formation and evolution of solar system bodies. In addition, the ranging provides invaluable information of relativistic effects and possibilities to test gravitational theories.

The design of Aphrodite revolves around key top-level requirements focused on the reliability of the mission and the accuracy of the ranging systems. During the baseline phase of the project, research was done on the possible ways to reach these requirements. In the Mid-term report, the configuration of the full system was decided upon. Initially basing the design around a lander on each of the bodies, it was found that multiple other options could be selected, involving the use of an orbiter or a lander swarm. A thorough investigation followed and it was found that a system that avoids landing on Mars is more reliable, cost-effective and lighter. Additionally, it became clear that the only feasible method of ranging to the moons is by placement of a lander because maintaining an orbit around the moons requires a high propellant budget as their gravitational pull is too small. The outcome of the midterm phase was the selection of the mission concept which has the highest chance of achieving mission success. This concept is composed of an orbiter around Mars and the landers on Phobos and Deimos.

Along with the configuration selection, design option trees were presented on the main elements of the mission, being communication and ranging, landing, propulsion and launch. A two-way laser ranging system was chosen and a preliminary choice of landing equipment was made. The trajectory of the spacecraft was planned as a high-thrust manoeuvre reaching Mars and then performing the necessary burns to reach the various sites of the Martian system. This was to be done by a monopropellant propulsion system as inspired by the MAVEN mission. The landers and orbiters are to be launched by a single launcher system.

The purpose of the final report is to present the novel Aphrodite mission design, focusing on both the low-cost and the high sustainability.

The Aphrodite mission begins with its launch in 2031 by a reused SpaceX Falcon 9 launch vehicle that places the spacecraft in a 204 day transfer orbit headed to Mars. By executing an hour-long burn, the whole spacecraft bus enters an elliptical orbit around Mars. In this orbit, the spacecraft bus separates into its two landers and orbiter. The landers proceed to target their respective moons, completing their bi-elliptic manoeuvres. The orbiter performs a burn that puts it in a 400 km altitude orbit around Mars. Following the orbital manoeuvres, the landers enter an autonomous landing sequence. Implementing LIDAR and optical cameras for hazard detection allow the landers to find their optimal landing location on the surface, minimising risks of landing on boulders, craters or steep slopes. Furthermore, the landers are equipped with an innovative landing system that is capable of recalculating landing trajectories in case of a preliminary failed landing.

The landers and orbiter are outfitted with an attitude determination and control system responsible for maintaining the landers oriented correctly during the landing phase and with respect to the orbiter, it keeps the lasers pointed correctly in case of actuator failure and performs corrections during burn phases to orient the orbiter into the elliptical transfer orbit. The system is based on four control wheels complemented by twelve 5 N thrusters. Once the crushable honeycomb structured legs have contacted the ground, hold-down thrusters are engaged to keep the lander against the surface as its anchoring system is deployed. Consisting of both footscrews and harpoons, the anchoring system is designed such that it can secure the landers on multiple surface types and toughness. With the landers positions fixed, the orbiter position needs to be determined. This is done by Doppler tracking, laser ranging, accelerometers and ultra-stable oscillators.

The operational phase begins after the two landers have landed and the orbiter entered the circular orbit. The communication system of the landers comprises of an omni-directional antenna and two laser telescopes. The same system is placed in the orbiter with the addition of a high gain antenna, which is needed to perform Doppler tracking and to allow for Very-Long-Baseline Interferometry (VLBI) back on Earth. The ranging system ensures an accuracy of at least 0.5 m between all the bodies. The high gain antenna and laser telescopes have a gimbal to maximise the amount of time they can range and communicate. In order to cope with the high data rates that arise from the ranging, as well as guarantee high reliability, the orbiter is equipped with five command handling units and one redundant memory recorders capable of storing 1 Tb and the landers are equipped with seven command handling units and two memory recorders capable of storing 16 Gb. As the orbiter and landers always meet their communication windows, the orbiter memory units are designed to hold the data acquired by the landers during solar conjunction, when communication with Earth is blocked for 28 days.

Further subsystems include the power, structures, thermal and propulsion systems. The power and thermal subsystems are vital for the operations of the network. The GaAs solar panels and lithium-ion batteries keep the ranging network operational. Structurally, the orbiters and landers have a cylindrical monocoque made of Al5052-H34 that carries the largest loads during launch and operations. Inside are the most temperature sensitive systems and propellants. Other instruments, such as the star trackers and sensors are placed on an outer cubic structure for the orbiter. The outer structure of the landers is hexagonal. The propulsion system is focused on sustainability and reliability, hence it is designed as a pressurised monopropellant system. The propellant used for the mission is LMP-103S, based on ammonium dinitramide, boasts 36% higher performance than hydrazine with lower costs and toxicity risks.

The selection of this propellant is just one of the many design choices that put Aphrodite on the forefront of sustainable space development. Sustainability has been implemented in all trade-offs and design choices, and Aphrodite is proud to be highly compliant with ESA's sustainability indicators, achieving great scores on its design. Other sustainable designs include the choice of a re-usable launcher in Falcon 9 and a detailed production and assembly plan that minimises waste production and makes use of green technologies. Redundancy has been applied in all aspects of the Aphrodite mission in order to successfully accomplish the goal of interplanetary ranging for eight years. Through extensive reliability analysis, Aphrodite achieves its 90% reliability.

The total spacecraft wet mass is 3865 kg of which the orbiter is 3086 kg, the Phobos lander is 395 kg and the Deimos lander is 384 kg. The total mission cost is estimated to be M€931 (FY2017). Using redundant design and thorough risk mitigation, the reliability of the orbiter is 94% and of the landers 91% after their operational lifetime. The complete overview of the lander design and orbiter design are presented in Table 1 and Table 2.

Table 1: Mars orbiter design overview.

Orbiter Design			
General Properties	Mass	Wet mass: 3086 kg	
		Propellant mass: 2375 kg	
		Dry mass: 710 kg	
	Dimensions	2.4 m × 2.4 m × 2.5 m	
	Cost	M€293.8	
	MMOI around x, y and z	3446 kg m^2, 1213 kg m^2 and 3487 kg m^2	
	ΔV	3.344 km/s	
ADCS	Sensors	IRU (SIRU-E)	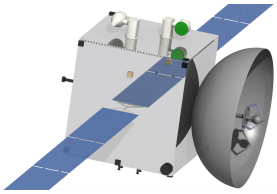
		4 × Accelerometer	
		3 × Star tracker (Terma)	
		12 × Coarse Sun sensor (Bradford Engineering)	
		2 × Fine Sun sensor (Bradford Engineering)	
	Actuators	4 × Control wheel (4 × W45ES)	
		12 × 5 N ADN RCS thrusters	
Propulsion	Monopropellant system (LMP-103S)		
	Main engine: 6 × 220 N HPGP thruster		
	Tanks	6 × LMP-103S tanks, with 2364.17 kg propellant	
		1 × Nitrogen tank, with 10.98 kg pressurant	
Power	Solar Arrays	2 × Retractable solar arrays	
		Solar cells: 30% 3J GaAs	
		Total area: 11.9 m^2	
		270 W (EoL at apoapsis)	
	Battery	Battery cells: 8 in series Lithium-Ion	
		EoL power: 278 W	
		Volume: 4.6 l	
	Bus	28 V regulators	
C&R	2 × steerable laser telescopes		
	1 × S-band omni-directional antenna		
	1 × Steerable Ka-band/X-band high gain antenna		
Thermal	Passive insulation	Aluminium backed Teflon MLI	
	Passive thermal system	2 mm CPL heat pipes	
		5 × TMT panel radiators and SNC louvres	
	Active thermal system	3 × Raytheon CTSU	
		10 × Tayco Solid-State Controller heater	
		2 × Glauber's salt PCM coolers	
C&DH	5 × Compact PCI 6U		
	1 × MPC 826D solid state recorder		
Structures	Hexagonal structure with CFRP and Al-Al panels. Corner beams transferring the load from the hard points. Inner cylinder carries the main loads.		
	Mechanisms	Separation spring system by NEA Electronics: model 9103 and model 9102G	
		Solar panel actuators by MOOG: Type 2 ADA, Heavy Duty IP44	

Table 2: Phobos and Deimos lander design overview.

Lander Design			
General Properties Deimos Lander	Mass	Wet mass: 384 kg	
		Propellant mass: 96 kg	
		Dry mass: 288 kg	
	Dimensions	1.4 m × 1.0 m × 2.5 m	
	Cost	M€186.8	
	MMOI with solar panels deployed around x, y and z	106 kg m^2, 52 kg m^2 and 88 kg m^2 (same for the Phobos lander)	
	MMOI with solar panels retracted around x, y and z	91 kg m^2, 74 kg m^2 and 70 kg m^2 (same for the Phobos lander)	
	ΔV	0.79 km/s	
General Properties Phobos Lander	Mass	Wet mass: 395 kg	
		Propellant mass: 124 kg	
		Dry mass: 272 kg	
	Dimensions	1.4 m × 1.4 m × 1.0 m	
	Cost	M€207.0	
	ΔV	0.99 km/s	
ADCS	Sensors	IRU (SIRU-E)	
		4 × Accelerometer	
		3 × Star tracker (Terma)	
		12 × Coarse Sun sensor (Bradford Engineering)	
		2 × Fine Sun sensor (Bradford Engineering)	
	Actuators	3 × Control wheel (2 x RW1 and 1 × RW2)	
		12 × 5 N ADN RCS thrusters	
Propulsion	Monopropellant system (LMP-103S)		
	Main engine: 4 × 50 N HPGP Thruster		
	Tanks	1 x LMP-103S tank, Phobos with 122.96 kg propellant Deimos with 95.85 kg	
		1 × Nitrogen tank, Phobos with 0.57 kg pressurant/ Deimos with 0.45 kg propellant	
Power	Solar Arrays	2 × retractable solar arrays	
		Solar cells: 30% 3J GaAs	
		Total area: 2.8 m^2	
		261 W (EoL at apoapsis)	
	Battery	Battery cells: 6 in series Lithium-Ion	
		EoL power: 188 W	
		Volume: Phobos 5.01 Deimos 17.81	
	Bus	28 V regulators	
C&R	2 × Steerable laser telescopes		
	1 × S-band Omni-directional Antenna		
Thermal	Passive insulation	Aluminium backed Teflon MLI	
	Passive thermal system	2 mm CPL heat pipes	
		3 × TMT panel radiators and SNC louvres	
	Active thermal system	3 × Raytheon CTSU	
		10 × Tayco Solid-State Controller heater	
		2 × Glauber's salt PCM coolers	
Landing	Landing sensors	Doppler LIDAR (ALHAT Doppler LIDAR)	
		Flash LIDAR (SOLID GoldenEye)	
		2 × Camera (ECAM-C50)	
	Mechanisms	3 × Harpoons	
		3 × Foot screws with actuators	
C&DH	7 × Compact PCI 6U		
	1 × Airbus Solid State Recorder		
Structures	Hexagonal structure with CFRP and Al-Al panels. Corner beams transferring the load from the hard points. Inner cylinder carries the main loads.		
	Mechanisms	Separation spring system by NEA Electronics: model 9103 and model 9102G	
		Solar panel actuators by MOOG: Type 2 ADA, Heavy Duty IP44	

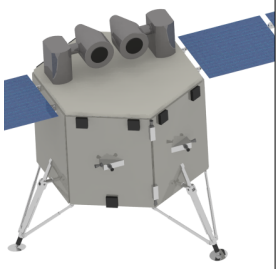

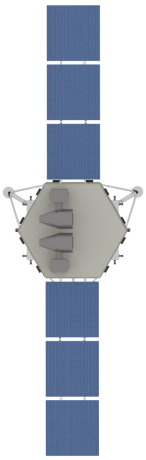

Contents

List of Symbols

Symbol	Definition	Unit
A	Area	m^2
A_D	Frontal Area	m^2
a	Semi-Major Axis	m
a	Acceleration	m/s^2
b	Width of Solar Panel	m
Cm	Centre of Mass	m
Cp_s	Centre of Solar Pressure	m
C_D	Drag Coefficient	-
Cg	Centre of Gravity	-
c	Speed of Light	m/s
d	Width of a Honeycomb Side	m
E	Stiffness	GPa
f	Frequency	Hz
H	Momentum	Nms
h	Height	m
I	Second Moment of Area	m^4
I	Mass Moment of Inertia	kgm^2
I_{sp}	Specific Impulse	s
i	Inclination	°
K	Thermal Conductivity	W/(mK)
k	Spring Constant	N/m
L	Length	m
M	Bending Moment	Nm
m	Mass	kg
N_r	Number of Moon Rotations	-
P	Load	N
q	Distributed Load	N/m
q	Reflectance	-
Q	Design Factor	-
Q	Irradiance	W/m^2
Q	Heat load	W
R	Radius	m
R	Distance to the Sun	m
$R(t)$	Reliability	-
$\mathbf{r}$	Position Vector of Body	m
$\dot{r}$	Velocity	m/s

Symbol	Definition	Unit
ssp	Solar Separation Angle	rad
s	Honeycomb Cell Diameter	m
T	Temperature	K
T	Period	s
T_D	Disturbance Torque	Nm
t	Time	s
t	Skin Thickness	mm
v	Velocity	m/s
V_∞	Escape Velocity	m/s
ΔV	Change in Velocity	m/s
$\dot{v}$	Acceleration	m/s^2
α	Inclination Difference	rad
α	Absorptivity	-
α	Scale Parameter	s
α	Coefficient of Thermal Expansion	1/°C
γ	Reduction Factor	-
γ	Shape Parameter	-
ϵ_c	Across-Track Error	-
ϵ_r	Ranging Error	-
ϵ	Emissivity	-
η	Efficiency	%
θ_a	Pointing Accuracy	rad
θ_g	Z-Axis Deviation	rad
μ	Standard Gravitational Parameter	m^3/s^2
ν	Poisson Ratio	-
ρ	Density	kg/m^3
σ	Normal Stress	MPa
τ	Shear Stress	MPa
τ	Eclipse Paramter	-
Φ	Solar Intensity	W/m^2
ϕ	Geometric Parameter	-
ϕ_i	Solar Incidence Angle	rad
Ψ	Angle Between Two Planetary Bodies	rad
ω	Rotational Velocity	rad/s

List of Abbreviations

Abbreviation	Definition
ADCS	Attitude Determination and Control System
ADN	Ammonium Dinitramide
ASTROD	Astrodynamical Space Test of Relativity using Optical Devices
BELA	BepiColombo Laser Altimeter
BER	Bit Error Rate
BoL	Begin-of-Life
CAP	Closest Approach Point
CCD	Charge-Coupled Device
C&DH	Command and Data Handling
CFRP	Carbon Fibre Reinforced Polymers
CMG	Control Moment Gyroscope
COSPAR	Committee on Space Research
C&R	Communication and Ranging
CPU	Central Processing Unit
CTSU	Cryogenic Thermal Storage Unit
DEM	Dense Elevation Map
DOD	Depth of Discharge
DOT	Design Option Tree
EM	Engineering Model
EME	Earth Mean Equator
EEPROM	Electrically Erasable Programmable Read-Only Memory
EoL	End-of-Life
ESA	European Space Agency
EU	European Union
FBS	Functional Breakdown Structure
FFD	Functional Flow Diagram
FTA	Failure Tree Analysis
FoV	Field of View
GALA	Ganymed Laser Altimeter
GNC	Guidance, Navigation and Control
FPGA	Field-Programmable Gate Array
HAN	Hydroxylammonium Nitrate
HDA	Hazard Detection and Avoidance
HGA	High Gain Antenna
HGR	Hemispherical Resonator Gyro
HPGP	High Performance Green Propellant
GETTEME	Gravity, Einstein's Theory and Exploration of the Martian Moons' Environment
IMU	Inertial Measurement Unit
INC	Inclination
IPS	Instructions per Second
IRU	Inertial Reference Unit
JUICE	Jupiter Icy Moons Explorer
LADEE	Lunar Atmosphere and Dust Environment Explorer
LATOR	Laser Astrometic Test of Relativity
LCA	Life Cycle Analysis
LCI	Life Cycle Inventory
LGA	Low Gain Antenna
LIDAR	Light Detection and Ranging
LIO	Linux Input/Output
LLCD	Lunar Laser Communication Demonstration
LRO	Lunar Reconnaissance Orbiter
MLI	Multi Layer Insulation
MMOI	Mass Moment of Inertia
MOI	Mars Orbit Insertion
MME	Mars Mean Equator
MRO	Mars Reconnaissance Orbiter
MS	Margin of Safety
MTBF	Mean Time Between Failures
NGO	Non-Governmental Organisation
NASA	National Aeronautics and Space Administration
NTSP	Non-tracking Scientific Payload
PCEC	Project Cost Estimation Capabilities
PCM	Phase-Change Materials
PLR	Phobos Laser Ranging
PMD	Propellant Management Devices
PR	Public Relations
QM	Quality Model
QM	Qualification Model
QPSK	Quadrature Phase Shift Keying
RCS	Reaction Control System
RF	Radio Frequency
RMSE	Root-Mean-Square Error
RWA	Reaction Wheel Actuator
SA	Solar Array
SDL	Separation, Descent and Landing
SLOC	Source Lines of Code
SNR	Signal to Noise Ratio
SOI	Sphere of Influence
SRAM	Static Random-Access Memory
SRP	Solar Radiation Pressure
STM	Structural and Thermal Model
SuROM	Start-up Read-Only Memory
TOI	Transfer Orbit Insertion
TRN	Terrain Relative Navigation
TV	Thermal Vacuum Test
TWTA	Traveling-Wave Tube Amplifier
WBS	Work Breakdown Structure
WDE	Wheel Drive Electronics
WFD	Work Flow Diagram
TV	Thermal Vacuum
VLBI	Very-Long-Baseline Interferometry
VSA	Vibrational, Shock and Acoustic Test

1 Introduction

For centuries, humankind has been trying to characterise the processes governing the solar system by combining Earth and space observations. Using the solar system as a laboratory allows one to test the laws of physics and investigate the physical phenomena emerging from them. Precision laser ranging between planetary bodies will allow advances in the study of fundamental physics and solar system dynamics. Several leaps have already been taken in the field of interplanetary laser ranging. Starting with passive reflectors on satellites (Satellite Laser Ranging), as elaborated by Seeber [103], and advancing to a lunar passive target (Lunar Laser Ranging) of which details are explained by Dickey et al. [29]. However, these technologies have inherent disadvantages, such as the low signal strength over long distances, which make this technology unfeasible for larger planetary distances. An active laser transponder solves this problem with a two-way laser system. This technology was already demonstrated on the MESSENGER mission at a distance of 0.16 Astronomical units (Smith et al. [108]).

This project aims to develop an interplanetary ranging system which is used to improve the determination of the dynamics of the Martian system. A ranging system will be deployed on Phobos and Deimos and around Mars which will perform inter-system (Earth to Martian system) and intra-system (inside the Martian system) ranging. This report is preceded by three other reports. Firstly, the Project Plan (Khurana et al. [58]) was presented, where the general outline of this project was described. This was followed by the Baseline Report (Khurana et al. [57]), which described the requirement analysis together with a design concept generation. Finally, there was the Mid-term Report (Roza et al. [96]). The Mid-term presents the chosen design option with two moon landers and one orbiter, together with the final concepts for communication and ranging, propulsion, guidance, navigation and control and moon landing. This report builds on these three previous reports.

The purpose of this report is to present the final design of the Aphrodite mission by means of a mission overview, subsystem design and an integration procedure.

The structure of the report is as follows: firstly, Chapter 2 provides a mission description, evaluating the mission goals and analysing its market value. Secondly, Chapter 3 presents an overview of the final design of the Aphrodite mission. Thirdly, the presentation of the nine different subsystem designs starts with Chapter 4, which explains the communication and ranging subsystem. The trajectory to Mars and to its moons, and the orbit determination of the orbiter itself is presented in Chapter 5. This is followed by a description of the structural design of the orbiter and landers in Chapter 6. Furthermore, Chapter 7 explains what the landing approach is and the sensors and actuators used during landing. The propulsion subsystem is presented in Chapter 8, followed by Chapter 9 which deals with the attitude determination and control subsystem. The command and data handling subsystem is discussed in Chapter 10. Chapter 11 elaborates on the power subsystem, followed by Chapter 12, which treats the final subsystem; the thermal control system. After the subsystems have been presented, the integration of all subsystems is presented in Chapter 13. Then, the mass, power, cost, and ΔV budgets are given in Chapter 14. This is followed by a description of the operational timeline from launch to the end-of-life-procedure in Chapter 15. The global risk assessment and a reliability analysis is presented in Chapter 16. Afterwards, the development of the Aphrodite mission after this project and its additional characteristics are discussed in Chapter 17. At the end, the report is concluded and recommendations are given in Chapter 18.

[This page is intentionally left blank]

2
Mission Description

This chapter aims to put the Aphrodite mission in context. It will first elaborate on the purpose of the mission, which is explained in Section 2.1. Secondly, in Section 2.2, the importance of the mission will be explained; it will go deeper in the necessity of the mission and the parties who profit from it.

2.1. Mission Overview

The Aphrodite mission is developed to fulfil a need and objective:

Mission Need Statement: To accurately measure the distances between Mars, Deimos, Phobos and Earth to increase our understanding of solar system dynamics.

Project Objective Statement: The design of a ranging system to be deployed at the bodies in the Martian system and at Earth with an operational lifetime of more than eight years, with the main scientific goal of improving the dynamical characterisation of the solar system to an accuracy of less than 0.5 metres, accomplished by ten students in ten weeks.

In this report, the mission design is presented in order to fulfil both of them. To fulfil this goal, the mission consists of two landers targeting the Martian moons and one orbiter, which will enter a low Martian orbit. The mission starts on the 26th of February 2031 with the launch of the system using the Falcon 9. On the 23rd of September 2031 the operational phase of the mission will start. The orbiter and the landers will perform 25 hours of laser ranging to Earth each month. Additional to the Earth ranging, intra-system ranging is performed for four hours each month between each body. All this ranging data will be measured with an accuracy of at least 0.5 metres. The mission is able to carry a secondary payload. After eight years the mission ends, which does not mean the orbiter will shut down. The spacecraft is designed to have a high reliability. Therefore, it is possible to continue the range measurements or use the orbiter as a communication relay. The maximum project cost should be less than one billion euros.

2.2. Market Analysis

This section deals with the market analysis for the Aphrodite project. This analysis is to identify potential parties that would be interested in this project and its data. The first step in the market research is to identify the market opportunities for the Aphrodite Project. The next step is to identify the stakeholder of the mission based on the market opportunities. Finally, the markets for both the scientific data, which is obtained during ranging, and for the 10 kg secondary payload with a power consumption of 10 W are described. The outcome of the market analysis should provide the project team with a better idea of how this mission can contribute to the scientific community and what equipment would be best suited as a secondary payload in order to do so.

2.2.1. Market Opportunities

The spike of interest in Mars opens up a number of opportunities for the Aphrodite mission. The opportunities the ranging data provides for the academic community are going to be explored to justify the importance of obtaining that data and thus of the Aphrodite mission. Furthermore, analysing the market opportunities is key to determine the most suitable choice of instruments to install as the secondary payload.

Ranging Data

The science mission, provided by Aphrodite, will focus on the measurement of (inter)planetary distances with the use of laser ranging supplemented by Radio Frequency (RF) tracking. Once the distance between the bodies is obtained, their velocities with respect to each other can be retrieved. With these velocities, the gravitational fields of the bodies can be calculated. The gravity field parameters of the bodies, Love numbers, librations and other non-geodetic observable are used to calculate the mass and composition of each member of the Martian

system. As a result, the development and origins of the solar system as well as the theory of general relativity can be understood better, as explained by Kopeikin et al. [59]. Therefore, the ranging data obtained by the Aphrodite mission will be of great value for both planetary scientists and fundamental physicists, thus making them one of the main stakeholders of the project.

The theory of relativity has been a subject of research for almost a century now. General relativity involves the effect of massive bodies on the space-time continuum, which plays an important role in the dynamics of the universe. The greater the number of bodies that are tracked, the better. According to Battista et al. [14], using only three bodies is an approximation of a more intricate system, therefore, having a ranging network in the Martian system, that can be monitored from Earth, will help determine the dynamics more precisely. The movement of each body will be tracked by every other one that is a part of the network, thus providing the velocity of the tracked body relative to several others.

Secondary Payload

The secondary payload will allow third parties to use the Aphrodite mission to send instruments to the Martian system that will provide them with data they require. Potential stakeholders that may be interested in the secondary payload include academia, space agencies and private companies (like SpaceX). However, there are restrictions to which this secondary payload should adhere. The total mass should not be more than 10 kg with power consumption of no more than 10 W. The allowed data rate is 10 Mbit per day and the operating temperature range is from 270 K to 320 K. Several suitable candidates for the secondary payload were discussed by Khurana et al. [57]. Those are: a high resolution camera, a seismograph and an auger.

Both the seismograph and the auger can be installed on a lander only, therefore they are not considered feasible as secondary payload for the orbiter. This leaves the high-resolution camera as the best candidate to put as secondary payload on the orbiter. This would allow the orbiter to send pictures back to Earth; an often used PR strategy in space missions in order to keep the public interested and supporting the mission.[1,2] Furthermore, a camera on the orbiter, capable of also capturing ultraviolet wavelengths, could allow to create a weather map for the parts of Mars over which the orbiter passes.[3] This map can help characterise the seasonal and year-to-year variations in the climate of the Red Planet as well as allowing for observations of dust storms.

Besides a high-resolution camera, the landers could also host a seismograph or an auger. The former will provide the opportunity to study the internal structure of Phobos and Deimos of which little to nothing is currently known. In order to do so, a seismometer like the one put on Rosetta's RoLand (description of RoLand is given by Ulamec et al. [125]) can be installed on the Phobos and Deimos landers. The seismometer consists of four identical single-axis accelerometers arranged in a tetrahedral pyramid. Detailed information about this seismometer can be found in Banerdt et al. [10]. Such an instrument would provide valuable information about not only the Martian moons but also about asteroids.[4] Currently, not much is known about the structure and characteristics of this type of celestial bodies, therefore the information obtained by the seismometer will be of great value for the scientific community [10]. An auger, on the other hand, can provide detailed and precise data about the chemical composition of Phobos and Deimos. A similar instrument was installed on Philae with the same objective.[5] Drilling into the bodies to obtain soil samples that will be analysed with the help of a scanner can reveal information that would otherwise stay hidden from the seismometers.

2.2.2. Stakeholder Analysis

Perhaps the most important part of conducting the market analysis is the identification of stakeholders. Once the stakeholders have been established, their ability to influence the project can be analysed together with the impact of the project on these stakeholders.[6] For the Aphrodite project the following stakeholders are identified:

Government: The project would be beneficial for this stakeholder, because it would boost the country's image within the scientific field. The data that will be gathered during the mission's lifetime will be valuable for the scientific research in the country's academia. Finally, the publicity that the mission will get is going to have a positive influence on the image of the country by showing it is willing to invest in scientific undertakings. A government can contribute to the project by providing funding and research facilities or locations to build

[1] `https://www.nasa.gov/mission_pages/newhorizons/images/` [Accessed on: 23 June 2017]
[2] `https://www.nasa.gov/mission_pages/juno/images/index.html` [Accessed on: 23 June 2017]
[3] `https://mars.nasa.gov/mro/mission/instruments/marci/` [Accessed on: 23 June 2017]
[4] `https://phys.org/news/2007-11-views-martian-moons.html` [Accessed on: 23 June 2017]
[5] `http://www.esa.int/Our_Activities/Space_Science/Rosetta/Philae_found` [Accessed on: 23 June 2017]
[6] `http://www.tools4dev.org/resources/stakeholder-analysis-matrix-template/` [Accessed on: 2 June 2017]

mission-crucial infrastructure. It is important to also mention that this stakeholder has the capabilities to block the project by declining to provide funding or by limiting the access to governmental scientific facilities. In order to engage this stakeholder, the benefits the Aphrodite project can bring them should be clearly explained. These include the advances in the scientific field and improved image of the country in front of the rest of the world.

Space Agencies: For the space agencies, such as ESA, NASA and ROSCOSMOS, it is important to realise the goals of the space community while adhering to the governmental policies of the country they serve. They aim at conducting space missions within certain budget and time constraints. This stakeholder helps the project by providing the funding (ESA) and the launch site (NASA). They can also contribute with the enormous amount of experience they have in the field of astronautics and give feedback regarding the project. Since some space will be available in the payload bay of the launcher, it will also be possible for the space agencies (ESA and NASA) to integrate smaller satellites to piggyback on the main payload consisting of an orbiter and two landers. This is beneficial for the Aphrodite project, due to the financial aid that piggybacking would provide. This stakeholder can be engaged by allowing them access to the design and planning of the mission, so they can evaluate it for themselves. To fully incorporate the space agencies in the Aphrodite mission, the space agencies will also be given full access to the data gathered during the mission.

Private Companies and Entrepreneurs: Private companies focus on the financial benefits of a certain project, while entrepreneurs also pursue publicity. Due to the fact that the Aphrodite mission would be the first of its kind to perform simultaneous ranging between several points in space, it would attract attention from the public. In addition, this stakeholder would be interested in the technology behind the Aphrodite project, in order to utilise it for themselves. Last but not least, they also find it of use to help in the development of space technologies because it could give them an edge over their competitors. Also, companies like SpaceX and MarsOne would be interested in the data gathered during the mission because they can use it to better understand the Martian environment. This will immensely help them in their future colonisation efforts. For this stakeholder, it is possible to contribute to the project by paying for installation of their equipment as the secondary payload. This is located in the orbiter and both landers. A financially attractive proposal would appeal to these stakeholders. Piggybacking can also be considered by private companies. This would grant them access to space.

Academia: Academia would be mainly interested in the data gathered during the mission. They would need it to confirm scientific theories or to open up new areas of research. This stakeholder would also be interested in the secondary payload on-board the orbiter and landers because they could use it as a means to collect valuable information needed to validate already existing scientific theories or to discover unknown physical phenomena. The value of the ranging data together with the details of how it is going to be useful for the academic field is discussed in Section 2.2.1. They could contribute by providing expertise with respect to the design and planning of the mission.

2.2.3. Market Analysis

Humanity has been interested in exploring the solar system for decades and recently the interest of the space industry started shifting towards the Red Planet. However, as already stated by Khurana et al. [57], most of the space missions today have Earth orbits as their target. Therefore, few missions are involved on interplanetary exploration and even fewer of these include landers on other celestial bodies. As of this day, there are eight Mars missions that are still active but the amount of proposed missions is much higher.[7] Currently, 16 proposals for missions to the Martian system are in place.[8] In Section 2.2.2 the stakeholders for the Aphrodite project were identified and as it can be seen, the private market for Mars missions is currently emerging with companies like SpaceX, MarsOne and Aerojet Rocketdyne being on the forefront.[9] Some of these companies (SpaceX and MarsOne) have the ambitious goal of colonising the Red Planet. That means that a great amount of knowledge is required about the Martian environment, thus opening up a lot of opportunities in the market of Martian missions. Next to that, scientists that are working on theoretical research related to the properties of the Red Planet or with the dynamics of the celestial bodies would be interested in a mission like Aphrodite. Such a mission would provide them with an opportunity to validate their work. For these reasons it is expected that the market size for missions exploring the Red Planet will increase over the next decade.

In order to obtain better insight into what the market demands are with respect to the ranging data, which is the main mission objective, proposals for similar missions are studied. The outcome of this analysis is an

[7] `https://nssdc.gsfc.nasa.gov/planetary/chronology_mars.html` [Accessed on: 6 June 2017]
[8] `https://www.revolvy.com/main/index.php?s=List%20of%20missions%20to%20Mars` [Accessed on: 6 June 2017]
[9] `http://www.thespacereview.com/article/3080/1` [Accessed on: 2 June 2017]

indication of the potential of the ranging data as well as an illustration of the general market trend for ranging accuracy. The similar missions were already stated in Khurana et al. [57], however they are repeated here for the reader's convenience:

LATOR (*Laser Astrometric Test of Relativity*) was a mission proposed in 2004. The primary goal of the mission was to test the deflection of light in solar gravity. The ranging operations are conducted using optical interferometry. The mission aimed at centimetre level range accuracy (Turyshev et al. [123]).

ASTROD (*Astrodynamical Space Test of Relativity using Optical Devices*) was a mission proposed in 2007. The primary goal of the mission was to map solar system gravity, test relativistic gravity and detect gravitational waves. Ranging operations in this mission are conducted via two-way laser ranging. The mission aimed at a three millimetre range accuracy (Wei-Tou [127]).

PLR (*Phobos Laser Ranging*) was a mission proposed in 2010 to measure the curvature of space around the Sun with high accuracy. The ranging operations are conducted via asynchronous two-way laser ranging between a lander on Phobos and laser ranging stations on Earth. The mission aimed at millimetre level range precision and centimetre level range accuracy (Turyshev et al. [122]).

GETEMME (*Gravity, Einstein's Theory and Exploration of the Martian Moons' Environment*) was a mission proposed in 2011 to conduct ranging operations to Phobos and Deimos. The motivation of the project ranged from researching the origin and composition of the satellites to the time-rate changes of the gravitational constant. The mission uses a combination of laser retro-reflectors on satellites and asynchronous two-way laser ranging between the spacecraft and Earth. The level of accuracy of the ephemeris of the satellites is expected to improve from metre level to centimetre level during the course of the mission and the ranging accuracy of the mission is less than one metre. The mission aims at increasing the ranging precision by using normal point formation (Oberst et al. [80]).

These missions show the trend of increasing interest and a growing market for Mars missions. Furthermore, it can be observed that the general trend of the ranging missions is in the use of optical laser ranging. Most of the proposed missions have accuracy and precision higher than required for the Aphrodite mission. The motivation behind that is to allow for the option of using either radio or optical wave ranging to meet the goals of the mission. An accuracy of 0.5 m would still provide significant information about the origin of Mars and its moons, together with the time-rate change of gravitational constant and the gravity well of the Sun and other celestial bodies.

In conclusion, it can be said that a mission to Mars can offer enough opportunities to be considered attractive to the aforementioned stakeholders.

3
Final Concept

In this chapter, the final concept and the procedure used to design it is presented. Firstly, the design procedure for the system, being the design of all subsystems and their integration, is explained. Then, the functional analysis is shown in Section 3.2, after which the top-level requirements for the Aphrodite mission are given, indicating where in the report it is explained how they are satisfied. Finally, the outcome of the design process for the complete mission is described in Section 3.4.

3.1. Design Procedure

This sections aims to give insight in the design procedure followed in the final stage of the conceptual design phase of the Aphrodite Mission, where all subsystems were designed and integrated. In the Mid-term Report (Roza et al. [96]), a concept was chosen, using two landers on Phobos and Deimos and an orbiter around Mars. A preliminary design was carried out for the subsystems responsible for communication and ranging, landing, propulsion and guidance, navigation and control. The interfaces between the different subsystems, being attitude determination and control, power, thermal control, structures and control and data handling on top of the previously mentioned subsystems were also extensively investigated by Roza et al. [96]. To achieve a conceptual design during the last phase, first a functional analysis was performed. To use the functional analyses in the design of the subsystems, the mission can be divided into different modes. The top-level requirements were analysed again to verify the subsystem requirements flowing from them. Using the functional analysis and the modes, the requirements were analysed for each separate subsystem. Concurrent engineering was performed, taking into account the previously defined interfaces, so that the subsystems were designed while being integrated at the same time.

3.2. Functional Analysis

The first step of the design process in which the subsystems is designed is to perform a functional analysis. In this section, a clear overview of the technical mission functions will be presented. The entire mission will be divided in the major functions in the *Functional Flow Diagram* (FFD), where the order is clearly presented. Furthermore, the *Functional Breakdown Structure* (FBS) will show a more detailed overview of the entire mission.

3.2.1. Functional Flow

The FFD is shown in Figure 3.1 and represents the overall flow of the mission. The dotted lines connect the blocks indicating the main flow.

3.2.2. Functional Breakdown

The FBS, as seen in Figure 3.2, gives a more detailed overview of the functions of the mission.

3.2.3. Division Into Modes

To use the functional analysis in a structured way throughout the design steps, it was decided to divide the mission into different mission modes, based on the different functions that the spacecraft has to perform, described in Figure 3.2. Not all the same subsystems will have to be active during each mode. This division will support the design of the individual systems, in particular, the power subsystem and the ADCS. There are four systems being active all the time: the C&DH, the thermal control, power and the ADCS sensors.

Mode 1: Separation/Orbit Acquisition

In this mode, the spacecraft bus deploys from the launcher or the landers separate from the orbiter and then prepares the spacecraft bus for travel by activating the systems and deployment of the solar panels. During the separation the ADCS, C&DH and thermal control are active on the lander. The communication and propulsion

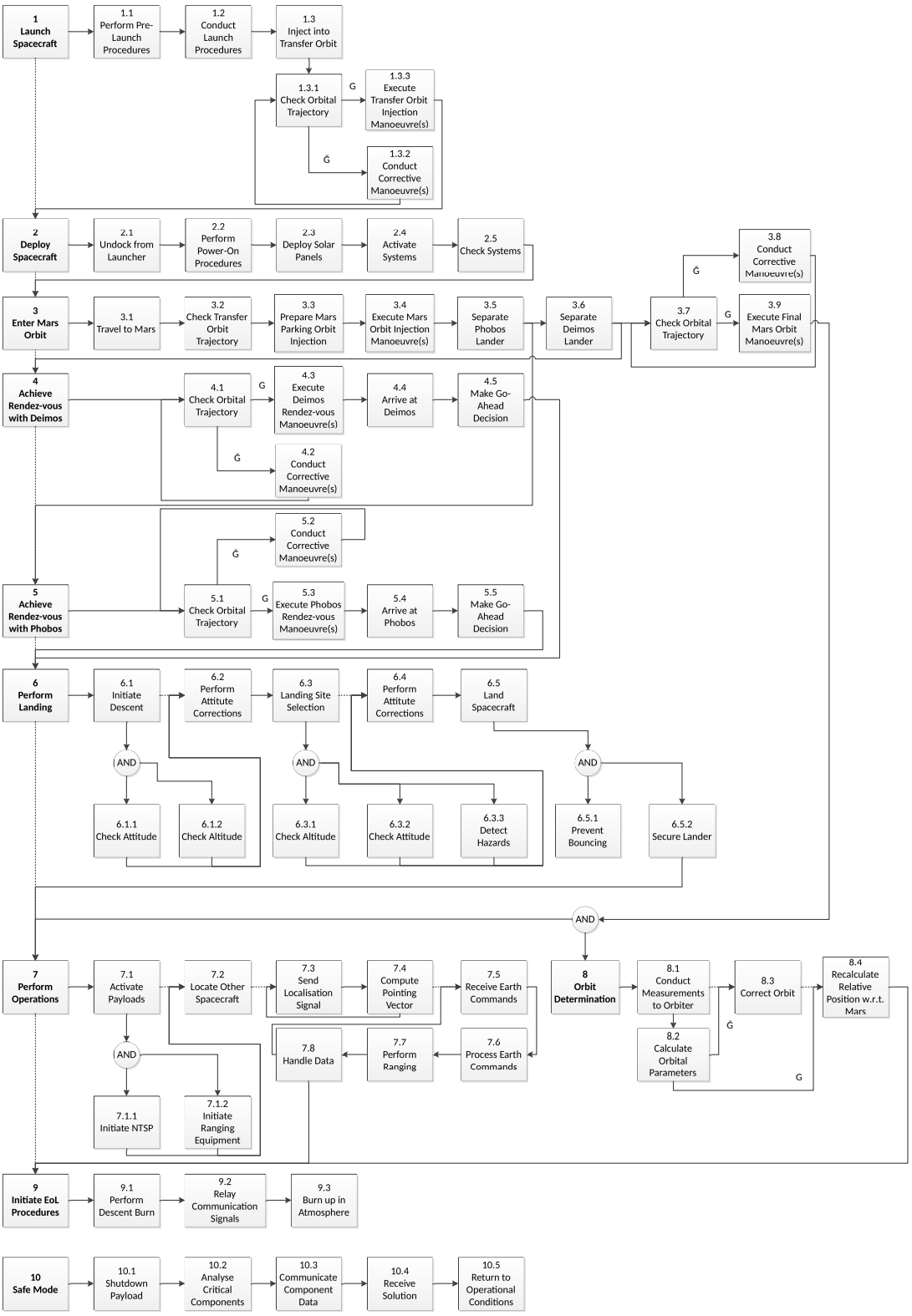

Figure 3.1: The Functional Flow Diagram of the Aphrodite Mission. The G in the FFD means that the result was positive, whereas a $\bar{G}$ means that a result was negative and some extra actions have to be taken. Sometimes, simultaneous functions have to be performed. These are represented with "AND".

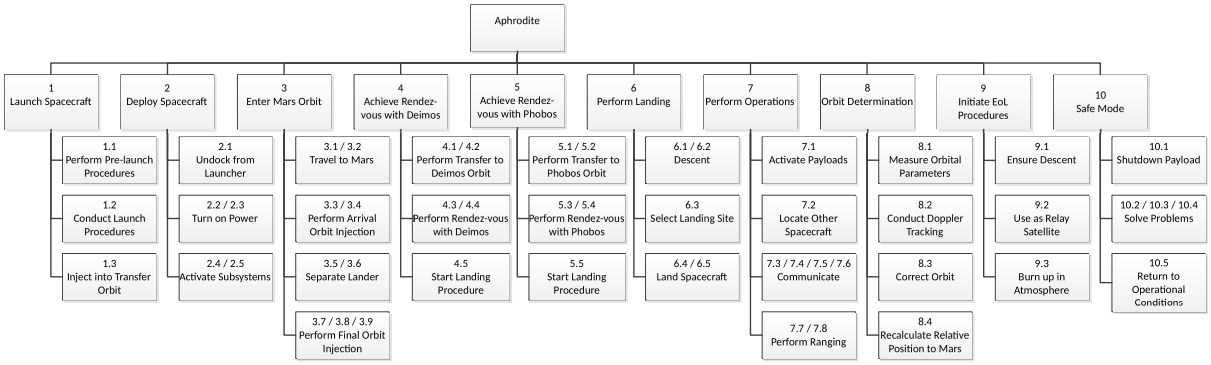

Figure 3.2: The Functional Breakdown Structure of the Aphrodite mission.

system are also active. This mode is called orbit acquisition whenever a component, being the orbiter or the landers, finish their orbit insertion burns and prepare for further travel or landing.

Mode 2: Travel
During the transfer to Mars, the bus will deactivate most subsystems. Occasionally, orbit corrections can be made to ensure the correct arrival at Mars. The orbiter uses the ADCS sensors. The ADCS thrusters also fire to correct the travel orbit. The communication system is used to relay information to Earth. During this travel the solar panels are deployed. This mode is also activated when the separate landers travel to Phobos and Deimos and when the orbiter travels to Mars.

Mode 3: Insertion Burn
The insertion burn mode is activated every time the main propulsion system fires. This is used for the orbital changes. The main engines perform the burn and the ADCS will counteract internal and external disturbances to ensure the right trajectory is followed.

Mode 4a: Operational
During the operational mode, a communication link is made. This mode is activated when communication or ranging is being performed. During operations, almost all subsystems will be active. For the communication, only the laser will be used.

Mode 4b: Eclipse Operational
While the spacecraft are in eclipse, a secondary power source will be used to provide the orbiter and the landers with their required power. At that point only the secondary payload is active.

Mode 5: Slew
The slew mode is activated when the orbiter is turning to reach a different attitude. The power needed for the control system to perform the slew manoeuvre is high. While doing this, the ADCS is fully active, but the power for other subsystems can be decreased.

Mode 6: Safe
When problems are encountered, safe mode is entered. Next to the subsystems that are always active, also the component that ensures communication with Earth is activated, in this case the omni-directional antenna. In this mode, the spacecraft will wait until a solution from the ground base is received.

Mode 7: Landing
The landing mode is activated after the landers have arrived and slowed down at 10 km above the moon surface. The landing loads are expected to have a considerable impact on the solar panels, so they are retracted at the beginning of the landing mode. The entire landing sequence will then be performed using the secondary power source. While landing, the ADCS is active as well as the RCS thrusters. These thrusters are used to control the descent and act as the hold-down thrusters. The sensors for the landing are also active, as they are used to select the landing site.

3.3. Requirement Analysis

To see whether the mission complies with the requirements as specified by Khurana et al. [57], each requirement is analysed in its applicable subsection as described in Section 3.1. For the top-level requirements, they are specified in Table 3.1.

Table 3.1: Stakeholder requirements.

ID	Requirement	Section	Compliance
Reliability			
OPS-SUV-ST-02	**[Driving requirement]** The system shall have a reliability of no less than 90% over its operational lifetime.	16.2	✓
OPS-SUV-ST-01	**[Driving requirement]** The system shall be operational for at least 8 years.	16.2	✓
Ranging to Earth			
OPS-DG-ST-01	**[Key requirement]** The system shall perform ranging measurements to Earth with an accuracy of at least 0.5 m.	4.3	✓
OPS-DG-ST-02	The system shall perform ranging measurements to Earth at an integration time of 60 s.	4.3	✓
OPS-DG-ST-03	The system shall perform ranging measurements to Earth for at least 25 hours per month.	4.4	✓
OPS-DG-ST-04	The system shall perform ranging measurements to Earth on at least 3 separate occasions per month, each separated by at least 1 week.	4.4	✓
OPS-DG-ST-05	**[Key requirement]** The system shall be able to perform VLBI measurements to Earth with an accuracy of less than 1 nrad.	4.3	✓
OPS-DG-ST-06	The system shall be able to perform VLBI measurements monthly.	4.4	✓
OPS-DG-ST-07	The system shall be able to perform VLBI measurements with a tracking duration of at least 2 hours.	4.4	✓
OPS-DG-ST-08	**[Key requirement]** The system shall perform all measurements at the required accuracy for solar separation angles down to at least 2.5 deg.	4.4	✓
Ranging within the Martian system			
OPS-DG-ST-09	The system shall perform intra-system ranging measurements for at least 4 hours per month.	4.4	✓
OPS-DG-ST-10	**[Key requirement]** The system shall perform intra-system ranging measurements with an accuracy of at least 0.5 m.	5.3	✓
Entry, Descent and Landing			
OPS-DEP-ST-13	**[Driving requirement]** The landers shall have a stability better than 0.1 m over the mission duration after landing.	7.7.2	✓
OPS-DEP-ST-14	**[Driving requirement]** A lander system shall be deployed on Deimos and on Phobos.	7	✓
Cost			
CON-CS-ST-01	**[Driving requirement]** The system shall be within the financial budget of 1 billion euro (FY17).	14.4	✓
Sustainability			
CON-LEG-S-01	The system shall comply with COSPAR regulations.	17.2.2	✓
CON-LEG-S-02	The system shall not make use of ITAR-restricted technology.	17.3	✓
Engineering Budgets			
CON-CS-ST-02	The system shall utilise existing ground technology.	16.2	✓
OPS-PAY-ST-01	**[Driving requirement]** The system shall be able to accommodate a 10 kg non-tracking payload.	16.2	✓
FUN-TC-ST-02	The TC shall keep the payload temperature between 270-320 K.	12.2	✓
Others			
CON-TI-ST-01	The system shall be fully operational by the end of 2032.	5.2.13	✓

3.4. Design Overview

In this section, the overall design, which is the outcome of the aforementioned design procedures, will be explained. First, the design of the orbiter is presented in Section 3.4.1. Both the Phobos and Deimos landers are presented in Section 3.4.2, as they are very similar. Lastly, the whole spacecraft is shortly explained in Section 3.4.3.

3.4.1. Orbiter Design

A complete overview of the hardware components of the design of the Mars orbiter is presented in Table 3.2. The orbiter will act as the measurement base for all ranging to Mars. The Mars orbiter is equipped with a laser system, which is used for the ranging, altimetry and communication. The laser is positioned on top of the orbiter for maximum visibility. The laser system is backed-up by a high gain antenna that is able to communicate to Earth and do the VLBI measurements. This large antenna is mounted to the side of the orbiter and will be

used for VLBI to Earth. An omni-directional antenna is added to communicate to Earth during safe mode. The primary structure of the orbiter is cylindrical; it will carry the main loads. Around this main load-carrying structure a secondary structure is added that will act as a thermal and radiation buffer as well as mounting points for the ADCS sensors. The thrusters use ADN monopropellant, which is currently in development. This propellant is chosen for its high sustainability. Multi layer insulation is used to slow the heat transfer. Cryogenic thermal storage units are used to increase the heat capacity of the orbiter. Radiators are used to cool down the systems while in sunlight. The black box secondary payload is also incorporated in the design. A possibility would be a high resolution camera, if it is able to operate in the temperature ranges of the outer shell. Otherwise, the secondary payload can be put in the inner shell, but then it has no field of view to the outside.

3.4.2. Lander Design

The landers conduct the ranging measurements from the moons. The landers are equipped with an omni-directional antenna to communicate with the orbiter during transfer and safe mode. The structure of the lander uses a cylinder as its primary structure, this is surrounded by a hexagonal secondary structure. This secondary structure is used as the thermal and radiation buffer. The hexagonal shape simplifies the mounting of the three landing legs. The landing legs are designed to carry the loads encountered upon landing and incorporate a shock dampening honeycomb structure. The landers carry their own propulsion system to get to the moons after separation. Accelerometers are used to measure the accelerations during the landing sequence. With the aid of these sensors, the exact landing positions are determined. The RCS thrusters are also used during landing and will act as the hold-down thrusters. The secondary payload is easily incorporated in the design. Possibilities are a drill to investigate the surface of the moons or a high resolution camera. When the temperature requirements of the secondary payload are more demanding, it should be put in the inner shell structure.

3.4.3. Bus Design

The landers and the orbiter are joined together in a spacecraft bus. This bus travels from Earth to Mars. During launch and travel, the landers and orbiter are stacked upon each other. The orbiter is the main part of the bus, on which the Deimos lander is connected using a spring actuator system. The frustum-shaped adapter has the radius of the orbiter and is 1 m high. This is to allow for enough clearance between the laser and the thrusters. The Phobos lander is positioned on top of the Deimos lander in an upside-down position with an adapter with radius of the lander and a height of 1 m. This is to avoid damaging the laser system of the Deimos lander with the thrusters of the Phobos lander. The complete spacecraft is shown in Figure 3.3. The mass moments of inertia for the bus with the orbiter's solar panels deployed around the x-, y- and z-axis are respectively 7788 kg m^2, 10360 kg m^2, 4267 kg m^2. Here, the z-axis is aligned with the thrusters of the orbiter, going through both the landers. The y-axis is aligned with the solar panels and the x-axis is placed to complete the right-handed reference system.

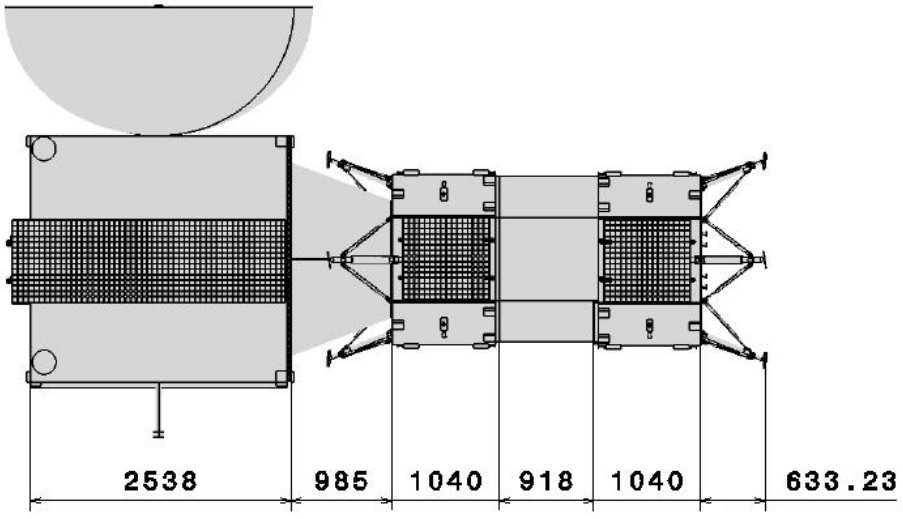

Figure 3.3: A drawing of the spacecraft bus with its dimensions.

Table 3.2: Mars orbiter design overview.

Orbiter Design			
General Properties	Mass	Wet mass: 3086 kg	
		Propellant mass: 2375 kg	
		Dry mass: 710 kg	
	Dimensions	2.4 m × 2.4 m × 2.5 m	
	Cost	M€293.8	
	MMOI around x, y and z	3446 kg m^2, 1213 kg m^2 and 3487 kg m^2	
	ΔV	3.344 km/s	
ADCS	Sensors	IRU (SIRU-E)	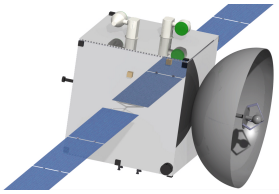
		4 × Accelerometer	
		3 × Star tracker (Terma)	
		12 × Coarse Sun sensor (Bradford Engineering)	
		2 × Fine Sun sensor (Bradford Engineering)	
	Actuators	4 × Control wheel (4 × W45ES)	
		12 × 5 N ADN RCS thrusters	
Propulsion	Monopropellant system (LMP-103S)		
	Main engine: 6 × 220 N HPGP thruster		
	Tanks	6 × LMP-103S tanks, with 2364.17 kg propellant	
		1 × Nitrogen tank, with 10.98 kg pressurant	
Power	Solar Arrays	2 × Retractable solar arrays	
		Solar cells: 30% 3J GaAs	
		Total area: 11.9 m^2	
		270 W (EoL at apoapsis)	
	Battery	Battery cells: 8 in series Lithium-Ion	
		EoL power: 278 W	
		Volume: 4.6 l	
	Bus	28 V regulators	
C&R	2 × steerable laser telescopes		
	1 × S-band omni-directional antenna		
	1 × Steerable Ka-band/X-band high gain antenna		
Thermal	Passive insulation	Aluminium backed Teflon MLI	
	Passive thermal system	2 mm CPL heat pipes	
		5 × TMT panel radiators and SNC louvres	
	Active thermal system	3 × Raytheon CTSU	
		10 × Tayco Solid-State Controller heater	
		2 × Glauber's salt PCM coolers	
C&DH	5 × Compact PCI 6U		
	1 × MPC 826D solid state recorder		
Structures	Hexagonal structure with CFRP and Al-Al panels. Corner beams transferring the load from the hard points. Inner cylinder carries the main loads.		
	Mechanisms	Separation spring system by NEA Electronics: model 9103 and model 9102G	
		Solar panel actuators by MOOG: Type 2 ADA, Heavy Duty IP44	

Table 3.3: Phobos and Deimos lander design overview.

Lander Design			
General Properties Deimos Lander	Mass	Wet mass: 384 kg	
		Propellant mass: 96 kg	
		Dry mass: 288 kg	
	Dimensions	1.4 m × 1.0 m × 2.5 m	
	Cost	M€186.8	
	MMOI with solar panels deployed around x, y and z	106 kg m^2, 52 kg m^2 and 88 kg m^2 (same for the Phobos lander)	
	MMOI with solar panels retracted around x, y and z	91 kg m^2, 74 kg m^2 and 70 kg m^2 (same for the Phobos lander)	
	ΔV	0.79 km/s	
General Properties Phobos Lander	Mass	Wet mass: 395 kg	
		Propellant mass: 124 kg	
		Dry mass: 272 kg	
	Dimensions	1.4 m × 1.4 m × 1.0 m	
	Cost	M€207.0	
	ΔV	0.99 km/s	
ADCS	Sensors	IRU (SIRU-E)	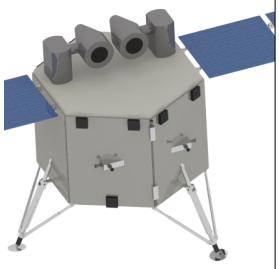
		4 × Accelerometer	
		3 × Star tracker (Terma)	
		12 × Coarse Sun sensor (Bradford Engineering)	
		2 × Fine Sun sensor (Bradford Engineering)	
	Actuators	3 × Control wheel (2 x RW1 and 1 × RW2)	
		12 × 5 N ADN RCS thrusters	
Propulsion	Monopropellant system (LMP-103S)		
	Main engine: 4 × 50 N HPGP Thruster		
	Tanks	1 x LMP-103S tank, Phobos with 122.96 kg propellant Deimos with 95.85 kg	
		1 × Nitrogen tank, Phobos with 0.57 kg pressurant/ Deimos with 0.45 kg propellant	
Power	Solar Arrays	2 × retractable solar arrays	
		Solar cells: 30% 3J GaAs	
		Total area: 2.8 m^2	
		261 W (EoL at apoapsis)	
	Battery	Battery cells: 6 in series Lithium-Ion	
		EoL power: 188 W	
		Volume: Phobos 5.0 l Deimos 17.8 l	
	Bus	28 V regulators	
C&R	2 × Steerable laser telescopes		
	1 × S-band Omni-directional Antenna		
Thermal	Passive insulation	Aluminium backed Teflon MLI	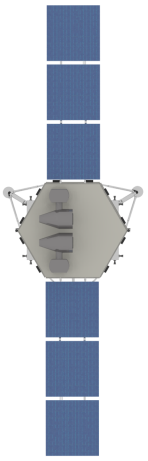
	Passive thermal system	2 mm CPL heat pipes	
		3 × TMT panel radiators and SNC louvres	
	Active thermal system	3 × Raytheon CTSU	
		10 × Tayco Solid-State Controller heater	
		2 × Glauber's salt PCM coolers	
Landing	Landing sensors	Doppler LIDAR (ALHAT Doppler LIDAR)	
		Flash LIDAR (SOLID GoldenEye)	
		2 × Camera (ECAM-C50)	
	Mechanisms	3 × Harpoons	
		3 × Foot screws with actuators	
C&DH	7 × Compact PCI 6U		
	1 × Airbus Solid State Recorder		
Structures	Hexagonal structure with CFRP and Al-Al panels. Corner beams transferring the load from the hard points. Inner cylinder carries the main loads.		
	Mechanisms	Separation spring system by NEA Electronics: model 9103 and model 9102G	
		Solar panel actuators by MOOG: Type 2 ADA, Heavy Duty IP44	

[This page is intentionally left blank]

4
Communication and Ranging

The communication and ranging subsystem is one of the most critical subsystems due to the fact that ranging is the main objective of the Aphrodite mission. The communication and ranging subsystem makes use of novel optical (laser) equipment together with the conventional radio frequency (RF) equipment in order to perform its task. This chapter begins with an overview of the design in Section 4.1 together with a representation of the architecture of both the radio and laser equipment. The design approach follows in Section 4.2. The link, mass and power, and cost budgets are presented in Section 4.2.1, Section 4.2.2 and Section 4.2.3 respectively. After that a functional analysis of the communication and ranging (C&R) subsystem is discussed in Section 4.3. This is followed by an analysis of the possible communication windows, which is described in Section 4.4. The risks of the C&R subsystem are evaluated in Section 4.5 and a sensitivity analysis of the design is performed in Section 4.6.

4.1. Design Overview

This section provides a graphical overview of the C&R links together with the architecture of both radio and laser systems in detail, and serves to provide the reader with the big picture of how the links are established between the orbiter, the landers and Earth.

The C&R subsystem makes use of both optical and radio waves in order to perform ranging and transmit data. The optical equipment is the main system that is used to perform these tasks while the radio equipment serves to provide redundancy, means for very-long-baseline interferometry (VLBI) and to allow for Doppler tracking of the orbiter, which is needed to precisely determine its orbit around Mars. The orbiter is equipped with two laser telescopes, placed on top of the spacecraft, a high-gain antenna (HGA) that is going to be used to communicate with Earth, and an omni-directional antenna. The radio system is used to carry out the communication between the landers and the orbiter because the omni-directional antennae on the landers consume less power than the laser. The high-gain antenna on the orbiter is used to receive and transmit RF signals from and to the landers. This is done because the gain of the HGA is beneficial for closing the link budget between the orbiter and landers. If needed, the laser system could be also used for intra-system communication.

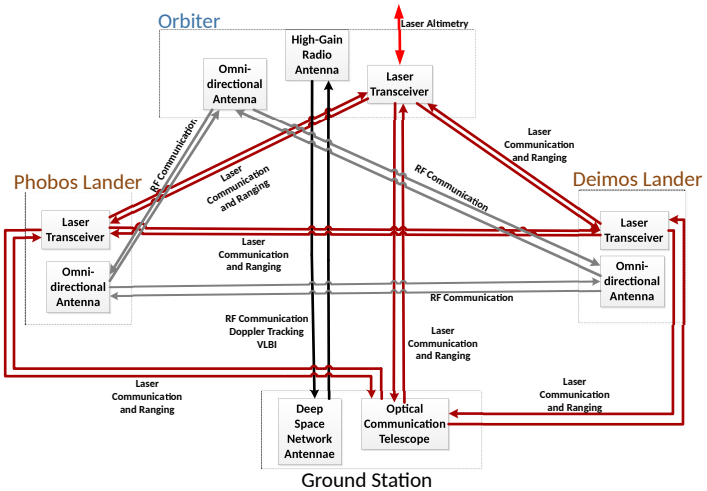

Figure 4.1: Sketch of the communication and ranging channels between the orbiter, landers and ground station. This acts as an overview of all mission units and how they interact together to form a coherent network.

Figure 4.1 represents the C&R network established between the orbiter, the landers and Earth. The presence of two types of C&R equipment will also allow for implementing a calibration method for both of them. Such

a method can be as simple as comparing the obtained ranging data from the optical and RF equipment and looking for large discrepancies. Due to the fact that the laser ranging technique is novel, it is plausible that its accuracy is not near the theoretical value. Having reliable data from the RF ranging to which the laser measurements can be compared, will indicate any major issues with the performance of the optical ranging.

The communication function imposes requirements on the subsystem design in terms of data rate and communication time, which are given in Table 4.8. When communicating to Earth, both the landers and the orbiter use the optical system as the main one. According to the report by Biswas et al. [17], a data rate of 500 kbps can be sustained in the worst case scenario (Mars at its furthest point from Earth, together with bad atmospheric conditions on Earth). If it fails, the landers use the orbiter as a communication hub. They send their gathered data to the orbiter with the use of their omni-directional antennae. Then the orbiter uses its HGA, that is still able to sustain a sufficiently high data rate to Earth, to transmit all of the data, both gathered from the instruments on board the orbiter and received from the landers. The data rate of the HGA ranges between 0.5 Mbps and 4 Mbps, depending on the distance between Earth and Mars and the atmospheric conditions on Earth as explained by Taylor et al. [115]. In case the HGA fails as well, both the landers and the orbiter have to rely on their omni-directional antennae, however they can only sustain very low data rates to the ground station, up to 100 bps depending on atmospheric conditions on Earth as indicated by Jamnejad et al. [55] and Wertz and Larson [128]. Therefore, only vital information about the status of the orbiter and landers together with important commands can be transmitted via this link. Scientific data would not be able to be sent with the use of the omni-directional antennae.

The laser equipment is used to perform ranging. The pointing accuracy and stability requirements imposed on the system are higher than the ones needed for communication as stated by Dirkx [31]. Therefore, the driving requirements for pointing accuracy, pointing knowledge, etc. are the ones derived from ranging and stated in Table 9.3. The C&R subsystem is designed such that it meets those requirements. Next to the laser equipment, the orbiter is also tracked via RF waves, such that its range-rate can be determined by the Doppler shift of the radio signal's carrier frequency as explained by Asmar et al. [7].

Finally, the C&R on the orbiter must be capable of performing altimetry, so its orbit around Mars can be determined precisely, which is required in order to be confident that the ranging data from the orbiter is accurate enough to meet the stakeholder's requirements given in Table 3.1. The altimetry is performed by the laser system. The altimetry functions impose a strict requirement on the pointing knowledge of the orbiter, which can be found in Table 9.3.

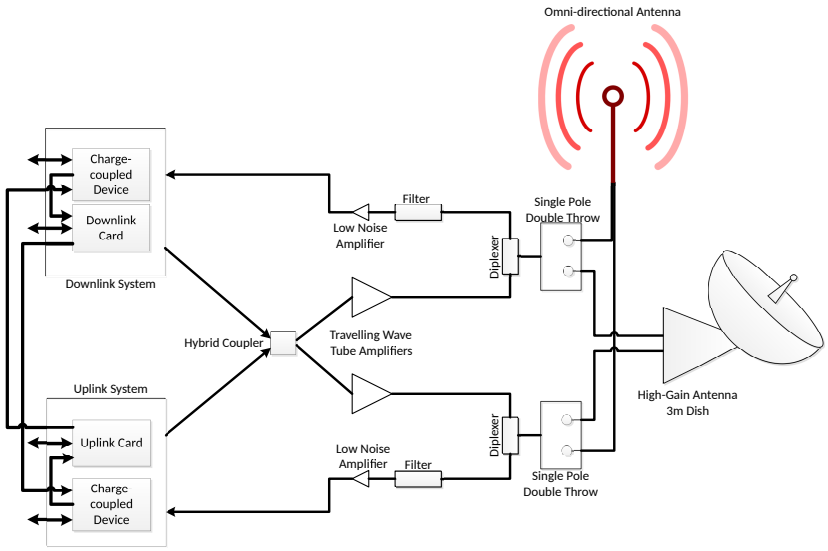

Figure 4.2: Block diagram of the radio system installed on the orbiter.

Figure 4.2 shows the architecture of the radio system of the orbiter. The landers have similar architecture with the difference being the fact that there is no HGA installed on them. Figure 4.3 displays the architecture of the optical system. It is the same for both the orbiter and the landers, as on the landers the altimetry can be used to better determine the orbits of Phobos and Deimos around Mars. The pulses are being transmitted and received by the telescope.

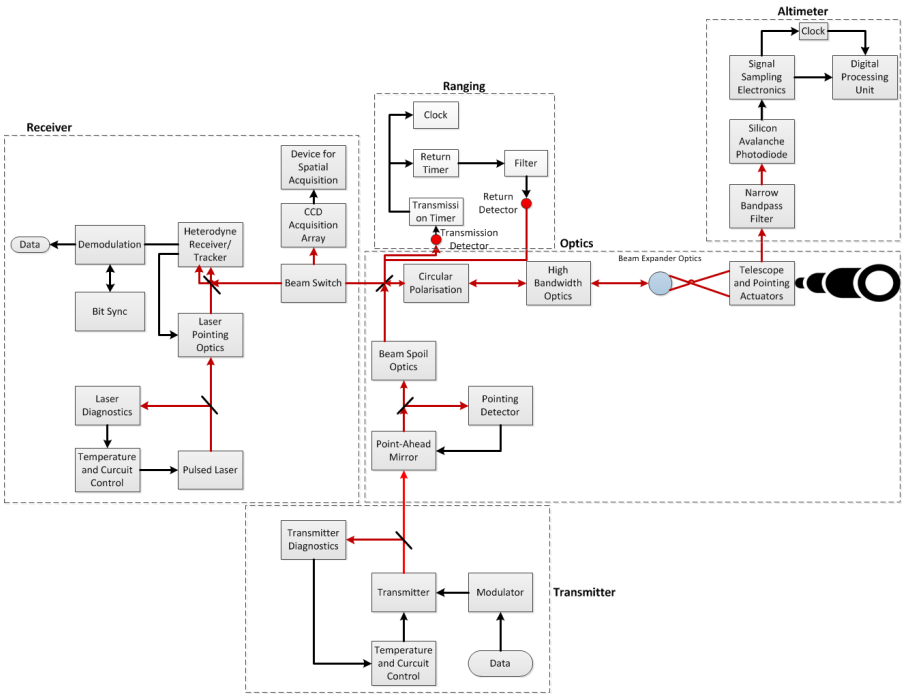

Figure 4.3: Block diagram of the optical (laser) system. non-bold arrows represent laser beams while bold arrows stand for electrical signals. Both the orbiter and the landers have the same laser system architecture.

4.2. Design Approach

The starting point for the design of the communication and ranging system are the top level requirements for accuracy in terms of orbit determination and ranging data. Since ranging is the main objective of the mission the system is designed to meet these requirements. The mass, volume and electrical power consumption of the resulting system become requirements for other subsystems, as elaborated in Chapter 6 and Chapter 11 respectively.

Based on the accuracy needed, a feasible system is picked, either RF or optical. In the case of the Aphrodite mission both are selected. The reason for that lies in the requirement for reliability of 90% of the total spacecraft. Optical communication systems are novel, hence there are a lot of risks associated with them. However, they can provide the necessary accuracy needed for orbit determination of the Aphrodite orbiter. Plus, their behaviour in deep space can be evaluated, as this was not done before, which could provide valuable information for future missions. On the other hand, a RF system is needed not only to meet the reliability requirement but also to allow for Doppler tracking, which is another vital component in determining the orbit of the spacecraft around Mars, and to perform VLBI on Earth. Based on those arguments, installing both RF and optical equipment on the Aphrodite orbiter and landers was considered as the most suitable option.

The systems have to be designed based on the functions they serve as described in Section 4.1. The laser is used for the purposes of communication and ranging/altimetry, meaning that two different modes are needed. The reason is the fact that the pulse frequency of 30 Hz that is needed to conduct ranging and altimetry as explained by Biswas et al. [17], is lower than what is required for communication, namely 388.8 kHz. Therefore, the frequency at which the laser should emit pulses such that it meets the requirements for communication as stated in Table 4.8 must be calculated.

The starting point is to determine the amount of bits that must be send in a single communication window. To find that amount of bits, it is assumed that the data being sent includes the ranging data to all other mission units. In order to calculate the amount of bits gathered in a single ranging session, the values from Table 10.4 are used. For a ranging window of 10 minutes, in total 3.66 Mbits are generated. The time of 10 minutes for communication windows is chosen such that is meets the requirements of Table 4.8 based on the possible communication opportunities analysed in Section 4.4. Assuming that the unit at hand has already ranged to the three other mission units before establishing the communication channel to ground station, the data that must be transmitted in single communication windows becomes 10.98 Mbits. Taking into account commands and other miscellaneous data from Table 10.4, the total number of bits to be transmitted becomes 14.58 Mbits.

The next step is to determine the number of photons that can be detected in a single pulse in order to estimate the needed number of pulses per communication window. According to Dirkx [31], it can be assumed that on average one photon per pulse is being detected. Since 16 photons are required per information bit as given in Table 4.4, meaning that 16 pulses are needed to transmit a single bit of information. Therefore, to transmit all of the gathered of 14.58 Mbits, 233.28 million pulses are needed. Knowing the number of pulses and the duration of the communication windows, the frequency of the emitted pulses is calculated by the following relation:

$$f = \frac{\text{number of pulses}}{\text{time}}\ \text{Hz} = \frac{233280000}{600}\ \text{Hz} = 388.8\ \text{kHz} \tag{4.1}$$

Hence, the optical equipment must be able to provide a pulse frequency of 388.8 kHz, so the gathered data can be transmitted in a single communication window. The length of a single pulse is 200 ps as explained by Biswas et al. [17] and Turyshev et al. [122]. Therefore, 388800 pulses with length of 200 ps can be transmitted in 0.0778 s. That means that the maximum allowed time in-between sequential pulses is 2.37 µs, which is higher than the required time difference such that the pulses can be received separately at the ground station as indicated by Turyshev et al. [122].

The wavelength at which the laser operates is 1064 nm for communication, ranging and for altimetry. This is the same wavelength as the Mars Lunar Communication Demonstration (MLCD) would have used as explained by Biswas et al. [17]. The design of the laser system is inspired by both the Lunar Atmosphere Dust and Environment[1] and the MLCD [17]. However, the optical system of the Aphrodite mission has to also account for the fact that altimetry is performed, therefore modifications are needed to the basic laser system. These modifications of the optical system due to altimetry can be clearly seen in Figure 4.3. The design of this part is explained in details in Section 5.3.

The laser system uses telescopes with a 30 cm aperture, elevated 15 cm above the surface of the orbiter/lander. It has a length of 45 cm which is sufficient to prevent the two telescopes hitting each other when rotating even on the landers. The landers have a diameter of 1.5 m, therefore when both telescopes are rotated to the side, their total length would be 90 cm. Due to the fact that the telescopes are mounted on the opposing ends of the roof of the landers, there is, in the best case, 50 cm of clearance between the two telescopes (clearance of 5 cm on each side to the edge is assumed).

The telescopes have to be precisely pointed, therefore they are actuated and thus free to rotate around two axes just like the LADEE telescopes as stated by Policastri et al. [88]. However, in the case of actuator failure, the spacecraft must be repositioned, such that the lasers can be pointed. Hence, a requirement regarding the slew rate of the spacecraft is imposed, which can be found in Table 9.3.

The design of the orbiter's HGA is derived from the HGA on the Mars Reconnaissance Orbiter (MRO). However, the Aphrodite orbiter supports downlink with frequency of 32.5 GHz instead of 33.8 GHz for the MRO as given by Taylor et al. [115]. Due to that, the focal point for the Aphrodite's HGA had to be recalculated as explained by Cervone [22] and thus the depth of the antenna is different from the HGA of MRO.[2] The resulting dimensions are a diameter of 3 metres and depth of 1.25 metres. The RF system of the orbiter is also comparable to the one used for the JUICE mission which is explained by Parisi et al. [82]. The reason for that is the fact that JUICE also needs to perform tracking with the mean of radio waves and it uses the Deep Space Network to do so, just like the Aphrodite's orbiter. The HGA on the orbiter can be actuated, which allows rotation by about 20° around two axes. The rotation is restricted to only 20° due to its geometry. If the HGA is rotated by more of 20°, it will hit the surface of the orbiter. The reason for making the HGA movable is the fact that the additional mass due to gimbals and drive motors is lower than the additional mass of propellant that would be needed to change the attitude of the spacecraft (even over only 20°) in order to re-point the HGA over the whole mission duration. The omni-directional antennae from the orbiter and the landers are the same. They are 50 cm long with 6 cm diameter and non-moving. Their design is inspired by the Iridium NEXT mission that uses powerful omni-directional antennae.[3] The design of the omni-directional antennae of the Aphrodite mission is elaborated in Section 4.2.2 On the orbiter, the omni-directional antenna is installed on the side opposite of the HGA, while it is positioned on the top of the landers.

[1] `https://www.nasa.gov/mission_pages/ladee/main/index.html` [Accessed on: 30 June 2017]
[2] `http://www.nitehawk.com/rasmit/ras_appl8.pdf` [Accessed on: 30 June 2017]
[3] `https://directory.eoportal.org/web/eoportal/satellite-missions/i/iridium-next` [Accessed on: 25 June 2017]

4.2.1. Link Budget

In this section, the link budget for both the radio and optical systems is presented. The models used in order to calculate the link budgets, together with their assumptions can be found in pages 38 to 41 of Cervone [22] and section 13.3 of Wertz and Larson [128]. The data rates required can be found in Section 4.2. It is made sure that the secondary payload can also send its data to Earth, by incorporating the data rate in the downlink and uplink budget. Therefore the secondary payload can take full advantage of this unique mission. In Table 4.1 and Table 4.2 the values for the data rate have a contingency of 15% applied as well. Both the HGA and the laser system can provide sufficiently higher data rates than what is required as already elaborated in Section 4.1. It is important to note that the pointing error is accounted for in the transmitter gain. The modulation used for the signals is Quadrature Phase Shift Keying (QPSK)

The RF system is able to support one uplink carrier in the K_a-band and two downlink carriers in both X- and K_a-band, similarly to Parisi et al. [82]. The two configurations look like:

(K_a/K_a): K_a-band for the downlink (32.5 GHz) together with K_a-band uplink (34 GHz).

(X/K_a): K_a-band for the downlink (32.5 GHz) together with X-band uplink (7.2 GHz).

For the uplink radio budget only the X-band scenario is going to be budgeted. The reason for that is the fact that lower frequency means higher wavelength and since the main source of loss, namely the space loss, increases with increasing wavelength (Equation 13-26 from Wertz and Larson [128]), that means that the lower frequency signal would require either more power to be fed to the antenna or higher antenna gain in order to close the link budget. Hence, if the link budget is closed for the X-band it is also closed for the K_a-band channel.

Table 4.1: Downlink budget of the radio system of the orbiter.

Parameter	Unit	Value	Source
Downlink Frequency	GHz	32.50	[82], [115]
Wavelength	m	0.00750	Calculated from the frequency, validated from [115]
Distance	m	4E-11	NASA[a]
Pointing Offset Angle	°	0.143	[115]
Antenna Half-power Beamwidth	°	0.175	Calculated from [22]
Transmitter Power	dBW	20.00	[115]
Loss Factor from Transmitter to Antenna	dB	-2.00	[128]
Transmitting Antenna Gain	dB	78.00	Determined such that the link budget is closed
Transmission Path Losses	dB	-7.50	Calculated from [22]
Receiving Antenna Gain	dB	74.66	[107]
Space Loss	dB	-296.50	Calculated from [22]
Antenna Pointing Loss	dB	-8.01	Calculated from [22]
Reception Feeder Loss	dB	-4.50	[128]
Data Rate	kbps	30.00	Section 4.2
System Noise Temperature	dBK	28.82	Calculated from [22]
Received Power	dBW	-143.48	Calculated from parameters in the table and models given in [22]
Received Energy per Bit	dBW	-188.26	Calculated from parameters in the table and models given in [22]
Signal to Noise Ratio (SNR)	dB	11.51	Calculated from parameters in the table and models given in [22]
Margin	dB	9.60	[21]
Excess (SNR after margin is applied)	dB	1.91	-
Link budget closed: Yes			

[a] https://mars.nasa.gov/allaboutmars/nightsky/mars-close-approach/ [Accessed on: 25 June 2017]

Table 4.2: Uplink budget of the radio system of the orbiter.

Parameter	Unit	Value	Source
Uplink Frequency	GHz	7.20	[82], [115]
Wavelength	m	0.0375	Calculated from the frequency, validated from [115]
Distance	m	4E-11	NASA[a]
Pointing Offset Angle	°	0.050	[107]
Antenna Half-power Beamwidth	°	0.036	Calculated from [22]
Transmitter Power	dBW	33.01	[93]
Loss Factor from Transmitter to Antenna	dB	-4.50	[128]
Transmitting Antenna Gain	dB	74.66	Calculated from [107] such that the budget is closed
Transmission Path Losses	dB	-2.04	Calculated from [22]
Receiving Antenna Gain	dB	78.00	Determined in Table 4.1
Space Loss	dB	-296.53	Calculated from [22]
Antenna Pointing Loss	dB	-23.14	Calculated from [22]
Reception Feeder Loss	dB	-2.00	[128]
Data Rate	kbps	30.00	Section 4.2
System Noise Temperature	dBK	27.88	Calculated from [22]
Received Power	dBW	-140.74	Calculated from parameters in the table and models given in [22]
Received Energy per Bit	dBW	-185.51	Calculated from parameters in the table and models given in [22]
Signal to Noise Ratio (SNR)	dB	15.2	Calculated from parameters in the table and models given in [22]
Margin	dB	9.60	[21]
Excess (SNR after margin is applied)	dB	5.60	-
Link budget closed: Yes			

[a] https://mars.nasa.gov/allaboutmars/nightsky/mars-close-approach/ [Accessed on: 25 June 2017]

The communication between the orbiter and the landers is carried out through the omni-directional antennas on the landers. They are able to support S-band carriers, therefore the same frequency is used for both up- and downlink.[4] The configuration is:

(S/S): S-band for the downlink (3.8 GHz) together with S-band uplink (3.8 GHz).

The reason for using the same data rate for the link between the landers and the orbiter as the link between the orbiter and Earth is that it takes into consideration the situation where the landers are using the orbiter as communication hub. In this scenario, the landers must be able to send all of their gathered data (scientific and from instruments) to the orbiter via the omni-directional antennae. By comparing the required value for the data rate with the typical data rate of omni-directional antennae given by Wertz and Larson [128], Taylor et al. [115], it is seen that the omni-directional antennae would be able to meet the required data rate given in

[4] https://directory.eoportal.org/web/eoportal/satellite-missions/content/-/article/envisat [Accessed on: 30 June 2017]

Table 4.3: Link budget of the channel between the orbiter and the landers. It is the same for both up- and downlink.

Parameter	Unit	Value	Source
Uplink or Downlink Frequency	GHz	3.80	[100]
Wavelength	m	0.0750	Calculated from the frequency
Distance	m	23643000.00	NASA [a]
Pointing Offset Angle	°	-	-
Antenna Half-power Beamwidth	°	-	-
Transmitter Power	dBW	10.00	Determined such that the link budget is closed
Loss Factor from Transmitter to Antenna	dB	-2.00	[128]
Transmitting or Receiving Antenna Gain	dB	78.00	Determined in Table 4.1
Transmission Path Losses	dB	-	-
Space Loss	dB	-191.96	Calculated from [22]
Antenna Pointing Loss	dB	-	-
Reception Feeder Loss	dB	-4.50	[128]
Data Rate	kpbs	30.00	Section 4.2, Section 4.3
System Noise Temperature	dBK	21.30	Calculated from [22]
Received Power	dBW	-120.46	Calculated from parameters in the table and models given in [22]
Received Energy per Bit	dBW	-166.37	Calculated from parameters in the table and models given in [22]
Signal to Noise Ratio (SNR)	dB	40.92	Calculated from parameters in the table and models given in [22]
Margin	dB	9.60	[21]
Excess (SNR after margin is applied)	dB	31.32	-
Link budget closed: Yes			

[a] `https://solarsystem.nasa.gov/planets/deimos/facts` [Accessed on: 25 June 2017]

Table 4.3. Typical values for omni-directional data rates vary between 1.37 kbits/s and 4.09 kbits/s over distances similar to those in the Martian system.[5]

In order to reduce the required power of the omni-directional antennae of the landers, the orbiter receives this signal with the HGA, which has a gain of 78 dB. This is beneficial for the landers, because their omni-directional antenna will consume less power (only 10 W), however it is not beneficial for the orbiter, because the HGA consumes more power (279.3 W) than the omni-directional antennae (47.6 W). However, the use of the HGA on the orbiter is not deemed an issue, because it was already accounted for in the power budget. Furthermore, operating only the omni-directional antennae means that they work at power levels that are close to their maximum allowed ones, which imposes a great risk of failure. Of course, if the HGA fails, communication link can still be established with the help of the omni-directional antennae, however at reduced data rate as mentioned in Section 4.1. Since there is little detailed information about a Martian laser system, some parameters of the laser link budget (like transmitter pointing loss and information rate BER) are estimated based on general literature as Wertz and Larson [128]. They are deemed accurate enough for this stage of the mission design as explained by Roza et al. [96]. Laser has different factors that need to be taken into account when estimating noise. An important consideration is the fact that the laser is completely blocked by clouds. For that reason, the laser link has different noise levels than the radio link. The different methods for estimating the noise in the laser link are explained by Biswas et al. [17].

Since the laser is not a continuous link but a series of pulses, the noise and losses shown in Table 4.4 are averaged over all pulses sent during the integration time.

4.2.2. Mass and Power Budgets

In this section, the mass and power budgets of both the laser and radio systems are presented. The contingency applied to the mass of the communication and ranging subsystem components is 2% and the contingency for the power of the components is 15%. These values are taken from Wertz and Larson [128] and Cervone [22].

The mass and power breakdown of the laser system follows the methods outlined by Turyshev et al. [122]. The system treated there shares the same design as the laser system on the LADEE spacecraft as already stated in Section 4.1. The laser system is divided into sub-assemblies with their respective components. On the same row where the sub-assembly is defined (in bold font), its total mass and power are given, followed by a component breakdown of this assembly. The reader should be aware that the breakdown of the laser system into assemblies given in Table 4.5 does not correspond to the assemblies shown in the system architecture in Figure 4.3. The reason for it is that the system architecture serves to provide a functional overview of the system and it is not as detailed as the mass and power budget breakdown. The orbiter and landers have identical laser systems,

[5] `https://directory.eoportal.org/web/eoportal/satellite-missions/content/-/article/envisat` [Accessed on: 30 June 2017]

Table 4.4: Downlink budget of the laser system for both the orbiter and the landers to Earth.

Parameter	Unit	Input	Unit	Output	Source
Laser Power	W	5.00	dBW	6.99	[17]
Aggregate transmitter losses	dB	-1.00	dBW	-1.00	[128]
Transmit aperture gain			dBW	118.94	[17]
Transmit aperture diameter	m	0.30			[17]
Wavelength	nm	1064.00			[122]
EIRP			dBW	124.94	Calculated from [17]
Transmitter pointing loss	dB	-2.00	dB	-2.00	[128]
Space loss			dB	-373.51	Calculated from [17]
Range	m	401E+11			NASA[a]
Channel loss	dB	-4.5	-dB	-4.50	Mars-Earth Terahertz Optical Link[b]
Irradiance at receiver gain			dBW/m^2	-124.62	Calculated from [17]
Receive aperture gain			dB	143.38	Calculated from [17]
Receive aperture diameter	m	5.00			[17]
Aggregate receiver loses	dB	-1.00	dB	-1.00	Assumed the same as for the transmitter
Receiver tracking loss	dB	-0.50	dB	-0.50	Mars-Earth Terahertz Optical Link[b]
Received power			dBW	-113.19	Calculated using [17]
Received photons per information bit	ph/bit	16.11			[17], [122]
Information bit rate	kbps	400.00			[17]
Planck constant	m^2 kg/s	6.63×10^{-34}			NASA[c]
Velocity of light	m/s	3×10^8			NASA[d]
Required ideal power			dBW	-120.08	Calculated from [17]
Required ideal photons per information bit	ph/bit	13.12			Calculated from [17]
Information rate BER		0.000001			[128]
Comm implementation loss	dB	-4.50	dB	-4.50	Mars-Earth Terahertz Optical Link[e]
Coding gain	dB	4.00	dB	4.00	Based on Reed-Soloman 16 over head for 239 transmitted bits
Required Margin	dB	6.00	dB	6.00	[57]
Excess			dB	0.39	-
Link budget closed: Yes					

[a] https://mars.nasa.gov/allaboutmars/nightsky/mars-close-approach/ [Accessed on: 25 June 2017]
[b] telecom.gmu.edu/sites/default/files/publications/TCOM707-Dec-2007-metol.pdf [Accessed on: 25 June 2017]
[c] https://imagine.gsfc.nasa.gov/science/toolbox/emspectrum2.html [Accessed on: 25 June 2017]
[d] https://www.grc.nasa.gov/www/k-12/Numbers/Math/Mathematical_Thinking/how_fast_is_the_speed.htm [Accessed on: 25 June 2017]
[e] telecom.gmu.edu/sites/default/files/publications/TCOM707-Dec-2007-metol.pdf [Accessed on: 25 June 2017]

therefore they have the same mass and power budgets presented in Table 4.5. The masses for the altimetry components are derived from similar space missions, which also require precise altimeters like JUICE and BepiColombo. Detailed information for the altimeters can be found in Section 5.3.

Note that the electrical and thermal components in Table 4.5 are incorporated in the communication and ranging system only and they do not contribute to the mass budgets of the physical electrical power or thermal subsystems of the spacecraft. The reason for that is the fact that most of them come together with the instruments installed in the laser system (like cables or coating).

The breakdown of the radio system into various sub-assemblies and components, which are budgeted in terms of mass and power, follows the breakdown outlined by Taylor et al. [115]. The values presented by Taylor et al. [115] are relevant for the Aphrodite mission radio systems because it is based on the MRO radio system. Two separate budget tables are shown, one for the orbiter and one for the landers, due to the fact that the architecture of the RF system is not the same in the different units.

The mass of the omni-directional antenna structure is calculated by estimating the material volume in the antenna and by assuming that the antenna is made out of aluminium.[6] The dimensions of the omni-directional antenna are given in Section 4.2 from where a volume of 9.25×10^{-4} m^3 follows. Taking 2700 kg/m^3 as average density of aluminium yields a mass of 2.5 kg.[7] This is rather on the low side, since missions like the EnviSat by ESA make use of omni-directional antennae that weigh approximately 8 kg.[8] A possible reason for that may be the usage of different materials with different densities and properties that could also influence the thickness of the antenna.

[6] https://ntrs.nasa.gov/archive/nasa/casi.ntrs.nasa.gov/19870020151.pdf [Accessed on: 25 June 2017]
[7] http://www.coolmagnetman.com/magconda.htm [Accessed on: 25 June 2017]
[8] https://directory.eoportal.org/web/eoportal/satellite-missions/content/-/article/envisat [Accessed on: 30 June 2017]

Table 4.5: Mass and power budgets for the laser equipment. Same for the orbiter and the landers.

Element	Mass [kg]	Power [W]	Reference
Sub-assembly: Optical	**2.46**	**-**	
Primary mirror (×2)	1.33	-	[122]
Secondary mirror (×2)	0.036	-	[122]
Mirror doublets (×2)	0.018	-	[122]
Beam splitters (×2)	0.124	-	[122]
Sun filters (×2)	0.95	-	[122]
Sub-assembly: Ranging	**2.30**	**7.50**	
Digital processing unit	1.30	5.00	[8]
Signal sampling electronics	1.00	2.50	[8]
Sub-assembly: Altimetry	**1.40**	**2.50**	
Detector (×2)	0.60	0.50	[105] Section 5.3
Timer (×2)	0.80	2.00	[101] Section 5.3
Sub-assembly: Electronics	**20.50**	**59.20**	
Power conditioning	3.00	5.25	[122]
Controller	3.00	7.00	[122]
Seed laser	0.50	0.25	[122]
Pump laser	6.00	10.50	[122]
Timing storage	0.50	2.20	[122]
CCD (×2)	2.00	12.00	[122], Figure 4.3
Gilbal drive (×2)	2.00	10.00	[122], Figure 4.3
Point-ahead drive (×2)	0.50	2.00	[122], Figure 4.3
Shutter drive (×2)	0.50	6.00	[122], Figure 4.3
Clock (USO) (×2)	2.00	4.00	[122], Figure 4.3
Thermal coating	0.50	-	[122]
Sub-assembly: Mechanical	**20.29**	**-**	
Telescope gimbal (×2)	9.00	-	[122], Figure 4.3
Point-ahead actuator (×2)	0.13	-	[122], Figure 4.3
Shutter activator (×2)	0.40	-	[122], Figure 4.3
Primary structure (×2)	9.60	-	[122], Figure 4.3
Secondary structure (×2)	1.16	-	[122], Figure 4.3
Sub-assembly: Thermal	**9.64**	**4.00**	
Heat pipe	4.00	1.00	[122]
Insulation (×2)	1.00	-	[122], Figure 4.3
Thermal switches	0.40	-	[122]
Cooler for CCD (×2)	0.60	2.00	[122], Figure 4.3
Thermometers	1.00	-	[122]
Thermal strap	2.40	-	[122]
Fine control heaters	0.040	1.00	[122]
Fine control thermometers	0.20	-	[122]
Total	**58.89**	**73.20**	
Contingency Applied	**60.07**	**87.84**	[57]

Table 4.6: Mass and power budgets for the radio equipment on the orbiter.

Element	Mass [kg]	Power [kilogram]	Reference
Travelling-wave Tube Amplifier	**7.70**	**253.00**	
K_a-band Travelling-wave Tube Amplifier (TWTA) (×2)	1.90	172.00	[115]
K_a-band electronic power converter	1.50	81.00	[115]
Diplexers and brackets	1.50	-	[115]
Waveguide transfer switches	1.50	-	[115]
Other microwave components	1.40	-	[115]
Miscellaneous TWTA hardware	0.20	-	[115]
K_a-band Antennae	**22.70**	-	
HGA prime reflector	19.10	-	[115]
K_a-transponder	0.90	-	NASA[a]
Antenna feed assembly	1.60	-	[115]
Miscellaneous antenna hardware	1.10	-	[115]
HGA gimbals and drive motors	**45.00**	**14.00**	[115]
Waveguides and coax	**8.30**	**-**	[115]
Omni-Directional Antenna	**4.7**	**12.30**	
Antenna structure	2.50	-	Calculated
Antenna feed assembly	1.60	12.00	Scaled from [115]
Miscellaneous antenna hardware	0.70	0.30	Scaled from [115]
Total	**88.70**	**279.30**	
Contingency Applied	**89.80**	**335.16**	[57]

[a] https://icubesat.files.wordpress.com/2012/06/icubesat-org-2012-c-3-2-_presentation_duncan_201206060133.pdf [Accessed on: 29 June 2017]

4.2.3. Cost Budget

A detailed cost breakdown of the communication and ranging system component-wise, like the mass and power budget in Section 4.2.2, is not feasible. The main reason for that is the fact that the papers used to design the Aphrodite mission's communication and ranging systems are several years old, some even more than a decade.

Table 4.7: Mass and power budgets for the radio equipment on the landers.

Element	Mass [kg]	Power [W]	Reference
Travelling-wave Tube Amplifier	**6.9**	**35.3**	
S-band TWTA	0.80	24.00	[115], [a]
S-band electronic power converter	1.50	11.30	[115], [b]
Diplexers and brackets	1.50	-	[115]
Waveguide transfer switches	1.50	-	[115]
Other microwave components	1.40	-	[115]
Miscellaneous TWTA hardware	0.20	-	[115]
Waveguides and coax	**8.30**	-	[115]
Omni-Directional Antenna	**4.80**	**12.30**	
Antenna structure	2.50	-	Calculated
Antenna feed assembly	1.60	12.00	Scaled from [115]
Miscellaneous antenna hardware	0.70	0.30	Scaled from [115]
Total	**20.30**	**47.60**	
Contingency Applied	**20.71**	**57.12**	[57]

[a] http://www.radartutorial.eu/08.transmitters/Traveling%20Wave%20Tube.en.html [Accessed on: 25 June 2017]
[b] http://www.radartutorial.eu/08.transmitters/Traveling%20Wave%20Tube.en.html [Accessed on: 25 June 2017]

The numbers presented there relate to the market situation at the time of writing of the paper and although these numbers can be scaled for the current fiscal year in terms of inflation, it cannot account for the changes in the market.[9] A good example is the change in the demand and supply for certain equipment over time when a new technology is introduced, thus influencing the price of the equipment.

Therefore, it was decided that it is better to make use of a tool that relates cost empirically to the mass of the subsystem. This tool was provided by NASA and it is described in Chapter 14. Table 14.4 contains the cost breakdown of the complete Aphrodite mission. The cost for the communication and ranging subsystems on the orbiter and the landers are M€24.2 for the orbiter and M€25.4 for each of the landers. Thus, totalling at a sum of M€75. These numbers take into account both the radio and optical system.

4.3. Functional Analysis

As already mentioned, the main purpose of the C&R subsystem is to allow for receiving commands from the ground station, sending data to Earth and perform ranging, both to Earth and within the Martian system and to perform altimetry to Mars. Due to the fact that the main objective of the Aphrodite mission is to perform ranging, the requirements for the C&R subsystem stem from the top-level requirements provided by the stakeholders. The latter can be found in Table 3.1. The relevant requirements for the C&R fall under the sections **Ranging to Earth** and **Ranging within the Martian system**. The communication requirements stated in Table 4.8 stem from the rate of scientific data generated described in Chapter 10 and the possible communication windows, analysed in Section 4.4.

Table 4.8: Communication requirements.

ID	Requirement	Section	Compliance
Communication with Earth			
OPS-COM-S-01	The system shall be able to communicate with the ground station at least once per three orbital periods of the system.	4.2	✓
OPS-COM-S-02	The system shall be able to transmit 14.58 MBits of data in 600 seconds.	4.2	✓
OPS-COM-S-03	The system shall be able to communicate with Earth for 60 hours per month.	4.2, 4.2.1	✓
Communication within the Martian system			
OPS-COM-S-04	The system shall be able to transmit 4.86 MBits of data in 600 seconds.	4.2, 4.2.1	✓
OPS-COM-S-05	The system shall be able to communicate between the Martian planetary bodies 120 hours per month.	4.2, 4.4	✓

It was mentioned in Section 4.2 that the capabilities of the Aphrodite's laser equipment are similar to those of the MLCD mission and the LADEE spacecraft. A mission for laser ranging from Phobos is proposed by Turyshev

[9] https://people.duke.edu/~rnau/411infla.htm [Accessed on: 25 June 2017]

et al. [122] that makes use of the same design for the laser equipment. Turyshev et al. [122] claims that with this system a millimetre accuracy can be achieved when ranging from Phobos to Earth. This accuracy is an order of magnitude higher than what is required for the Aphrodite mission. However, the integration time stated by Turyshev et al. [122] is 300 seconds, while the required integration time from requirement *OPS-DG-ST-02* is 60 seconds. Therefore, the Aphrodite's laser equipment will have higher emitting pulse frequency than that described by Turyshev et al. [122]. Due to the fact that the integration time does not influence the accuracy of the measurements, as explained by Dirkx [31], both requirements *OPS-DG-ST-01* and *OPS-DG-ST-02* can be considered met.

The starting point of satisfying requirement *OPS-DG-ST-05* was to develop a methodology for astrometry observations as presented by Park and Folkner [83] and Jones and Folkner [56]. According to them, an accuracy between 2.5 nrad and 5 nrad can be achieved with the latter being the achievable accuracy for a spacecraft in an orbit around Saturn (Cassini). In order to further increase the accuracy of the VLBI, algorithms similar to these described by Duev and Pogrebenko [35] can be implemented such that the accuracy of 1 nrad is met.

4.4. Communication Window Analysis

A detailed analysis is presented by Roza et al. [96], however the most important results are repeated here for the reader's convenience. The communication windows that are analysed in this section include those between the landers, between the landers and the orbiter and to Earth. They are divided as follows:

- Mars and Earth
- Phobos and Earth
- Deimos and Earth
- Phobos and Deimos
- Mars and its moons

In order to perform the analysis, the assumption was made that communication and ranging is possible to every point on Earth. Therefore, a communication window can be established anytime Earth is in the field of view of the orbiter or the landers. This is a valid assumption due to the fact that the Deep Space Network (DSN) is used for the radio-frequency (RF) channel and the International Laser Ranging Service (ILRS) for the optical channel. Both of these networks provide global coverage of Earth.

4.4.1. Mars-Earth

No communication or ranging between Mars and Earth is possible when one of the two following conditions, shown by Equation 4.2 or Equation 4.3, is satisfied.

$$\begin{aligned} \cos(\Psi_{|MaES|}) &< \alpha \\ \|\mathbf{r}_{\mathbf{E,Ma}}\| &> \|\mathbf{r}_{\mathbf{E,S}}\| \end{aligned} \tag{4.2}$$

$$\begin{aligned} \cos(\Psi_{|EMaS|}) &< \alpha \\ \|\mathbf{r}_{\mathbf{Ma,E}}\| &> \|\mathbf{r}_{\mathbf{Ma,S}}\| \end{aligned} \tag{4.3}$$

The first subscript indicates the starting point of the vector while the second subscript indicates its end point. The subscripts stand for: Ma = Mars, E = Earth, S = Sun and α is here set equal to the solar separation angle. A solar separation angle of 2.5° is required from *OPS-DG-ST-08* (Khurana et al. [57]). This angle is measured from the tangent to the surface of the Sun since this is more accurate than the angle from the vector through the centre of the Sun. $\Psi_{|MaES|}$ is the angle between $\mathbf{r}_{\mathbf{E,Ma}}$ and $\mathbf{r}_{\mathbf{E,S}}$. $\Psi_{|EMaS|}$ is the angle between $\mathbf{r}_{\mathbf{Ma,E}}$ and $\mathbf{r}_{\mathbf{Ma,S}}$. The result of the analysis is shown in Figure 4.4. The simulation is validated by comparison to the Mars opposition times by Dirkx [31] shown in Table 4.9.

Table 4.9: Fractions of days per synodic period when ranging and communication is possible between Earth and Mars.

Solar Separation Angle	Simulated	Reference [31]	Error Percentage [%]
1°	0.989	0.98	0.91
2°	0.974	0.97	0.41
5°	0.93	0.91	2.20
10°	0.87	0.83	4.8

As it can be seen, the error between the two fractions is small. The reason why the error increases with increasing solar separation angle (ssp) is the fact that the simulation uses the angle with the tangent of the Sun was used

while Dirkx [31] uses the angle with the vector through the centre of the Sun. That being said, the communication simulation is validated.

OPS-DG-ST-03 states that inter-system ranging shall be performed for at least 25 hours a month and *OPS-DG-ST-04* states that each month inter-system ranging shall be performed on at least three separate occasions with at least a week in-between them. In the Mars opposition period, *OPS-DG-ST-04* cannot be met. As discussed with the stakeholders, this is no problem since no ranging has to be performed during this time. Therefore this is not seen as a violation of *OPS-DG-ST-04* and it is not labelled as a killer requirement.

4.4.2. Earth - Phobos

Communication or ranging to Phobos is not possible when either Phobos is behind Mars or Mars is not visible from Earth. This means if one of the conditions stated by Equation 4.2, Equation 4.3 or Equation 4.4 is fulfilled, no communication or ranging to Phobos is possible.

$$\begin{aligned} \cos(\Psi_{|EMaP|}) &< 0 \\ \|\mathbf{r_{Ma,P}}\| \cdot \sin(\Psi_{|EMaP|}) &< R_{Ma} \end{aligned} \tag{4.4}$$

Equation 4.4 describes the condition when Phobos is in eclipse from Earth. $\Psi_{|EMaP|}$ is the angle between $\mathbf{r_{Ma,E}}$ and $\mathbf{r_{Ma,P}}$ and R_{Ma} is the radius of Mars. The result of the simulation is presented in Figure 4.5. Half the orbital period of Phobos was added since the lander on Phobos is fixed to the Mars facing side of the moon.

The Mars opposition time is not considered as a violation of the requirements since no ranging has to be performed during that period as stated by the stakeholders. In the worst case scenario, where the Solar conjuncture is neglected, no ranging is possible for 4.8 hours within single orbit of Phobos, which orbits Mars 88 times each month. If one ranges the other 2.8 hours, ranging should happen in approximately ten orbital rotations of Phobos.

4.4.3. Earth - Deimos

Using the same rationale as in Section 4.4.2, the time that no communication or ranging is possible between Deimos and Earth is calculated per orbit of Deimos. The result of the analysis is shown in Figure 4.6.

Neglecting the Mars opposition time, in the worst case scenario no channel can be established for 16.5 hours per Deimos orbit. This means if ranging is performed for the other 13.5 hours at three separate occasions during one month, requirement *OPS-DG-ST-09* is easily met. Since Deimos orbits Mars 22 times in one month, plenty of ranging occasions will occur.

4.4.4. Phobos - Deimos

The analysis of the communication window of Phobos-Deimos is similar to the analysis of Earth-Mars with two differences. Equation 4.2 and Equation 4.3 can be used, adapting them to the Phobos Deimos situation and setting α to zero. One extra condition has to be added when Deimos is positioned behind Phobos presented in Equation 4.5. When one of the three conditions is satisfied, no link between the moons is possible.

$$\cos^{-1}\left(\frac{\mathbf{r_{Ma,P}} \cdot \mathbf{r_{Ma,D}}}{\|\mathbf{r_{Ma,P}}\| \cdot \|\mathbf{r_{Ma,D}}\|}\right) < \cos^{-1}\left(\frac{\|\mathbf{r_{Ma,P}}\|}{\|\mathbf{r_{Ma,D}}\|}\right) \tag{4.5}$$

The result of the simulation is presented for one synodic period of Phobos and Deimos in Figure 4.7.

OPS-DG-ST-09 states that intra-system ranging shall be performed for at least 4 hours per month. In one synodic period of 10.25 hours, ranging between Phobos and Deimos is possible for 4.9 hours. This means *OPS-DG-ST-09* can be met after one synodic period.

4.4.5. Mars-moons

This case is easier to analyse considering the orientation of the moons with respect to Mars is fixed. This means communication or ranging to Phobos is possible for 3.8 hours while communication or ranging to Deimos is possible for 15.15 hours.

It is clear that requirement *OPS-DG-ST-09* is easily met between Mars and its moons. Phobos orbits Mars approximately 88 times in one month, which means ranging is possible for 333 hours. Deimos orbits Mars 22 times in one month, which means ranging is possible for 335 hours in one month.

Figure 4.4 to Figure 4.7 show the time that no communication is possible between Mars and Earth (Figure 4.4), between Phobos and Earth (Figure 4.5), between Deimos and Earth (Figure 4.6) and between Phobos and Deimos

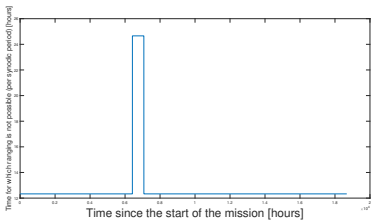

Figure 4.4: Communication windows Mars - Earth.

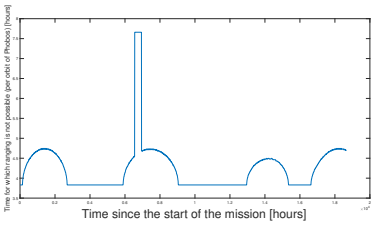

Figure 4.5: Communication windows Phobos - Earth.

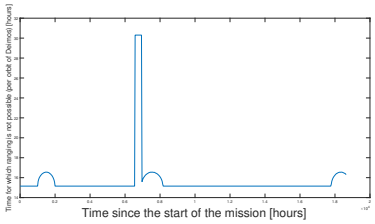

Figure 4.6: Communication windows Deimos - Earth.

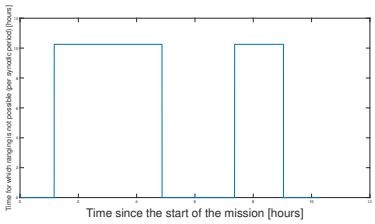

Figure 4.7: Communication windows Phobos - Deimos.

(Figure 4.7). All times are given per single synodic period of the body from which communication or ranging is performed.

4.5. Risk Analysis

This section discusses potential risks related to the C&R subsystem, together with possible mitigation strategies in order to reduce the impact of those risks.

The scale for likelihood and impact goes from 1, corresponding to the lowest probability or impact, to 5, which is the highest probability or impact a risk can have. A score of 5 in terms of impact means that if the risk occurs, it is catastrophic to the functioning of the subsystem as part of the spacecraft.

1. Telescope actuator stuck: If the actuator responsible for the movement of the telescope gets stuck, the telescope would not be able to be re-pointed. Therefore, the impact of this risk materialising would be catastrophic. This issue can be mitigated for the orbiter, by re-pointing the whole spacecraft. However, that is not possible for the landers. It should be noted that by re-positioning the orbiter, the solar panels may be put in shadow, thus impeding their capabilities to recharge the batteries as discussed in Chapter 11. Taking into account these considerations, the impact of the mitigated risk is critical. Due to the fact that the telescope has been implemented on only one space mission before and thus not much information is present, the likelihood of the actuator getting stuck is average. In order to mitigate this risk, molybdenum disulfide dry lubricant is going to be applied to the moving parts. This makes the event of the actuator getting stuck unlikely.

2. Telescope fracture: In case a telescope fracture is present, the optical system would not be able to communicate, range or perform altimetry which would have a critical impact on the mission. Even though a secondary radio system is present on both the orbiter and landers, in case the laser system fails, no ranging would be possible due to the reasons discussed in Section 4.1. Therefore, the risk can be mitigated by the addition of the second telescope, which bring the impact of telescope fracture to moderate levels. In order for a fracture to occur, the telescope has to be hit by an object or to experience high shock loading as explained in Chapter 6. These issues cannot be mitigated, therefore the impact of this risk stays moderate.

3. Mirror misalignment: A misalignment of the mirror may result in focusing the laser beam on a different location than the predicted one. The likelihood of this event is average as similar risks materialised in previous space missions. This would have a critical impact on the Aphrodite mission as it happened with the Hubble telescope.[10] This risk can be mitigated by extensive testing (especially of the scenarios that led to the misalignment of the Hubble telescope's mirrors) and validating procedures, which would bring the likelihood of the risk down to unlikely.

[10] `https://www.newscientist.com/article/mg12717301-000-the-testing-error-that-led-to-hubble-mirror-fiasco/` [Accessed on: 23 June 2017]

4. Omni-directional antenna fracture: The omni-directional antenna is present to provide redundancy for the main optical communication and ranging system. It will also be used during safe mode. A minor fracture in the antenna would not impede its capabilities of transmitting and receiving RF signals, which means it will still be able to fulfil its functions. For these reasons, the impact of this risk is only marginal. The antenna is made of aluminium, therefore fracturing it would be more difficult than the optical telescope and would be possible if the antenna is hit by an object or too high vibrational loads are experienced during launch, which is improbable. That risk can be mitigated by structurally reinforcing the omni-directional antennae, because it is impossible to monitor the very small objects in the Martian system that could potentially hit the antenna and fracture it.

5. HGA fracture: The HGA is required in order to allow for Doppler tracking of the orbiter and to serve to provide redundancy for communication with Earth. If fracture occurs, it is possible that the geometry of the antenna is changed such that it is not able to focus the RF waves in its focal point anymore. That would impede the ranging capabilities of the Aphrodite mission, therefore the impact of this risk is critical. However, this event is improbable to occur, because a high energy collision (being hit by an object with dimensions of at least several centimetres) would be required in order to fracture the antenna and change its geometry. This risk cannot be mitigated due to the same reasons as the ones stated for Risk 4.

6. Radio transmitter or receiver failure: A failure of the transmitter or receiver of the radio system will result in the system being incapable of processing the RF signals. If the transmitter fails, the orbiter would not be able to transmit a signal to Earth, hence Doppler tracking will not be possible and that will be catastrophic for the mission. Transmitters and receivers are components that have been long used for space applications, therefore their technology is mature, however failures have occurred in previous space missions.[11] For these reasons the likelihood for this risk to materialise is average. In order to mitigate it, both the transmitter and receiver units would be modified to serve as transceivers. In that case, those components become redundant. A transceiver is more complex than a transmitter or a receiver, therefore they are more likely to fail, however due to the fact that there are two transceivers in the radio system, the impact of them failing would only be marginal. Although the likelihood of the risk rises, its impact decreases more than the increase in terms of likelihood.

7. Charge-coupled Device (CCD) failure: CCD is needed to copy the light patterns falling on the device to digital form. This allows for the signals received from the C&R system to be conveyed to the rest of the spacecraft. The impact a failure of a CCD would have upon the mission is average. Furthermore, CCD failures are not a regular occurrence, so the likelihood of this risk materialising is considered as unlikely. Mitigation technique for potential CCD failure is placing an alternative path for each transceiver to the neighbouring transceiver's CCD. This would make the impact of this risk negligible.

8. Travelling-wave Tube Amplifier (TWTA) failure: A failure of that component would deem the HGA incapable of delivering the required gain such that the link budget shown in Section 4.2.1 is closed. This would effectively make the High-gain antenna pointless. In that scenario Doppler tracking of the orbiter would not be possible and the use the orbiter's radio system to communicate with Earth would not be possible as well. This will have catastrophic impact on the mission. However, TWTAs have a reliability of around 80% as stated by Weekley and Magnus [126] and therefore it is unlikely that this risk materialises. This risk is mitigated due to the fact that a second TWTA is placed in the radio system. This softens the impact of this risk down to moderate.

Table 4.10: Mitigated risk map of the communication and ranging subsystem.

Almost certain					
Likely		6			
Average					
Unlikely	7	3	2, 8	1	
Improbable		4			5
Likelihood / **Impact**	Negligible	Marginal	Moderate	Critical	Catastrophic

With the risks mitigated, the communication and ranging subsystem is able to meet requirement OPS-SUV-ST-02 for 90% reliability over the mission duration of eight years. A detailed explanation of the reliability for all subsystems, together with total reliability of the whole spacecraft is given in Section 16.2.

[11] `http://www.popsci.com/military-aviation-amp-space/article/2009-03/gallery-top-10-nasa-probe-failures` [Accessed on: 23 June 2017]

In order to provide the reader with a clear overview of the possible causes for failure of the communication and ranging subsystem, two fault tree analyses were developed. One for the RF system and one for the optical system. They can be seen in Figure 4.8 and Figure 4.9 respectively.

A fault tree analysis (FTA) is a graphical tool that serves the purpose of showing the chain of events within a certain system that would lead to its failure. These events are connected by the means of Boolean logic (AND, OR events).[12] The FTA is built top-down meaning that high-level components (or systems) are displayed on top, while the lower-level components (or systems) that make them up are below. Detailed information about this tool can be found in the tecnical report by Goldberg and Everhart [45].

4.6. Sensitivity Analysis

In order to check the robustness of the communication and ranging subsystem design, a sensitivity analysis is performed by varying the uncertainties of the critical parameters that drive the design of the RF and optical systems. The percentage of variation of the uncertainties is based on the contingencies applied to the spacecraft's design as stated by Khurana et al. [57]. Those include the required accuracy of orbit determination, the data rate, the frequency of the links, the system noise temperature and the efficiency of the components that are part of the subsystem.

Accuracy of orbit determination: Currently the requirements for orbit determination accuracy are met with a large margin. Those are 40% for both the orbital altitude accuracy and the radial orbit accuracy and 50% for the along- and across-track accuracy as explained in Section 5.3. In order to do so, altimetry, laser ranging and Doppler tracking are used. Hence, the current system can still be considered feasible even if the stakeholders demand accuracy that is higher by half of its current value, which is unlikely.

Data rate: An uncertainty of 10% in the data rate that can be supplied by the communication and ranging subsystem results in an uncertainty of the signal to noise ratio (SNR) of only 3.2%. Therefore, the link budget can still be closed with the current design of the C&R.

Link frequency: Introducing an uncertainty of 30% in the transmitting or receiving frequency changes the SNR by 9.9%. This change is small enough for the current system to be able to close the link budget with sufficient margin.

System noise: If the noise in the system is actually 10% higher than the assumed value during design, the SNR would decrease by only 3%. This decrease of SNR is insufficient to drop it below the required margin of 9.6 dB as shown in Section 4.2.1, therefore no change of the design is needed.

Efficiency of the C&R equipment: If the efficiency of the C&R subsystem drops by 40% (especially plausible for the optical system as indicated by Trivellin et al. [118]) at the end of the mission, the SNR would be 6.8% lower. Even so, the link budget would be closed, hence no redesign is required.

[12] `http://www.weibull.com/basics/fault-tree/` [Accessed on: 26 June 2017]

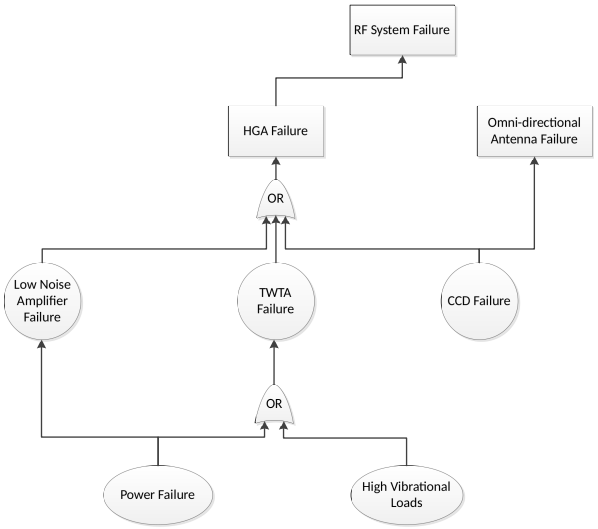

Figure 4.8: Fault tree analysis of the radio system of the orbiter that is part of the C&R subsystem. In case of the landers, no HGA is present.

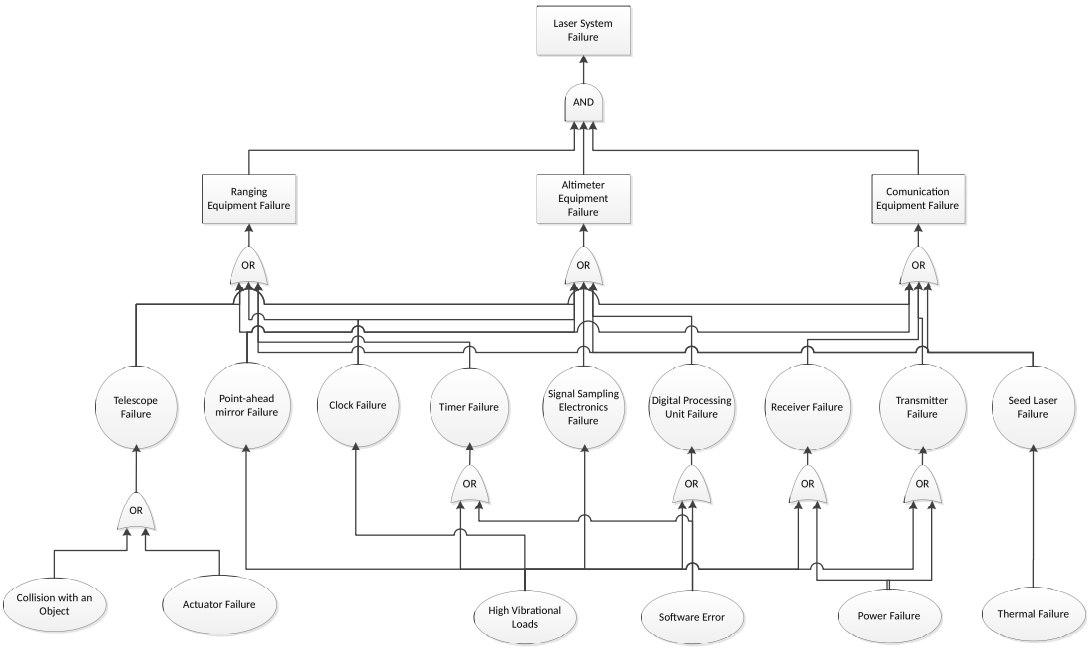

Figure 4.9: Fault tree analysis of the laser system that is part of the C&R subsystem.

[This page is intentionally left blank]

5
Guidance, Navigation and Control

Guidance, navigation and control (GNC) is subdivided into four main elements. The first element treats the functional analyis and the requirement compliance of the GNC system in Section 5.1. In Section 5.2, the trajectories to reach the moons are presented. This includes launch, leaving Earth's Sphere of Influence (SOI), the heliocentric trajectory to the Martian system and the trajectories within the Martian Sphere of Influence, to deploy the landers on the moons and to get the orbiter in the correct orbit around Mars. The third element is the orbit determination of the spacecraft itself. This includes sensors to determine the position of the orbiter, together with along-track and across-track accuracy. This strongly correlates with the ADCS. The difference being that the ADCS focuses on the rotational motion of the spacecraft, while the GNC treats the translational motion of the spacecraft, discussed in Section 5.3. Of course, this system is heavily correlated with the modes mentioned in Section 3.2.3. These will be mentioned throughout the chapter.

5.1. Functional Analysis

The function of the GNC subsystem is to determine and control the translational motion of the spacecraft. In this report, GNC is interrelated with the trajectory analysis. The spacecraft is launched with the Falcon 9 and travels for 204 days to Mars. When the spacecraft reaches Mars, it enters in a bi-elliptic orbit. During the bi-elliptic orbit, the landers separate from the orbiter and manoeuvre into the orbits targeting the moons. The orbiter will manoeuvre into a parking orbit around Mars, where it will orbit for eight years. In this section, it will be shown that the GNC subsystem complies with all the requirement set by Khurana et al. [57]. All the requirements are again listed in Table 5.1, together with whether or not they were complied with and the sections where the requirements are treated.

Table 5.1: GNC requirements.

ID	Requirement	Section	Compliance
OPS-DEP-S-07	The system shall be able to execute all orbit transfer manoeuvres autonomously.	5.2	✓
OPS-DEP-S-08	The system shall be able to execute all required orbit transfer manoeuvres to arrive at the Martian system.	5.2	✓
CON-TI-ST-01	The system shall be fully operational by the end of 2032.	5.2.13	✓
OPS-DEP-S-06	The launch of the spacecraft shall take place between the 18^{th} of February 2031 and the 7^{th} of March 2031.	5.5	✓
OPS-DEP-S-15	The orbit altitude shall be continuously measured with an accuracy of at least 0.5 m.	5.3	✓
OPS-DEP-S-16	The along-track orbiter position shall be determined with an accuracy of at least 5 m.	5.3	✓
OPS-DEP-S-17	The across-track orbiter position shall be determined with an accuracy of at least 2 m.	5.3	✓
OPS-DEP-S-18	The radial orbiter position shall be determined with an accuracy of at least 0.5 m.	5.3	✓
OPS-DEP-S-19	The orbiter shall be able to deliver a ΔV of 3.344 km/s with a margin of 10%.	5.2.13	✓
OPS-DEP-S-20	The Phobos lander shall be able to deliver a ΔV of 0.99 km/s with a margin of 10%.	5.2.13	✓
OPS-DEP-S-21	The Deimos lander shall be able to deliver a ΔV of 0.78 km/s with a margin of 10%	5.2.13	✓

5.2. Trajectory Analysis

The trajectory of the spacecraft is divided in two main optimisation problems: firstly, the trajectory to the Martian system is optimised to minimise ΔV targeting a certain target orbit around Mars; secondly, the trajectory within the Martian system is optimised to deploy the landers on the moons to minimise the total propellant used. Each block of the model is discussed in detail, together with the assumptions and the validation. At the end, the complete trajectory of the spacecraft, from launch to deployment of the landers is presented. Before the model is discussed, a preliminary analysis is presented to determine the input parameters, such as the targeted altitude and inclination around Mars. In Figure 5.1, the flow through the trajectory software is shown.

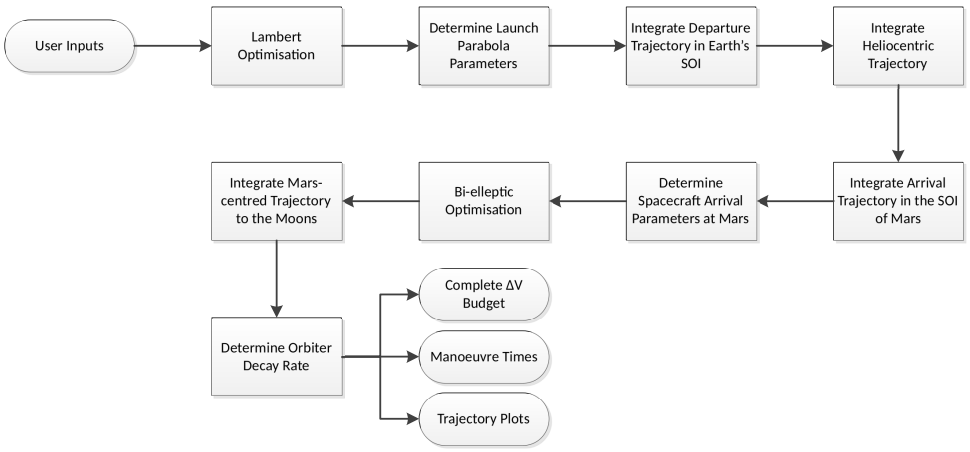

Figure 5.1: Simulation flow diagram of the trajectory software.

5.2.1. Model Assumptions

The two main assumptions used in this model are:

- All high thrust manoeuvres are modelled as impulse burns, which means the mass decrease and the velocity change are instantaneous. The impulsive thrust assumption is generally valid for today's chemical thrusters. The error in the ΔV caused by this assumption is estimated to be lower than 10%, according to Larbi and Stoll [63]. This means burn time is not included in the simulation.
- To calculate the propellant used during the manoeuvres, it is assumed that the Tsiolkovsky Equation holds as explained by Turner [121]. The error, using this assumption, is estimated by Pergola [84] to be less than 1% of the total propellant mass used.

5.2.2. Model Inputs

This model takes the following inputs:

- **Departure date (t_{dep}) and the launch span**: this is the number of days the departure date is allowed to vary. It is known that the spacecraft has to be operational by 2032. Since the transfer to Mars takes around one year, the departure date is set to 1 Jan 2031, with a departure span of 180 days.
- **Estimated arrival date (t_{dep}) and arrival span**: this is the number of days which the arrival date is allowed to vary. From the departure date, the arrival date is set to 1 Jan 2032, with an arrival span of 180 days.
- **Target orbit specifications**: the height of the orbit above the Martian surface and targeted inclination of the orbit. Targeting a very high orbit around Mars requires a lot of ΔV to enter the orbit. However targeting a low orbit around Mars needs more ΔV to reach the moons. This preliminary trade-off is explained in Section 5.2.3 and in this section, the targeted inclination is also determined.
- **Planetary constants**: this includes the gravitation constants of all planets, the gravity model of Mars and Earth, the position of all planetary bodies and the radius of Earth and Mars. The gravitational constants and radii are found in the NASA Fact Sheets.[1] The gravity model of Earth is based on the EGM2008 model.[2] Up to 30 coefficients are used for an accurate model of Earth's gravity field. The gravity model of Mars is

[1] `https://nssdc.gsfc.nasa.gov/planetary/factsheet/` [Accessed on: 1 June 2017]
[2] `http://earth-info.nga.mil/GandG/wgs84/gravitymod/egm2008/` [Accessed on: 2 June 2017]

Table 5.2: Comparison of the different trajectories to the moons.

Target	400 km (INC = Deimos)	5981.8 km (INC = Phobos)	20630 km (INC = Deimos)
ΔV delivered by orbiter [km/s]	2.82	4.00	5.47
ΔV Phobos lander Hohmann [km/s]	1.16	0	0
ΔV Deimos lander Hohmann [km/s]	1.68	0.75	0
ΔV Phobos lander bi-elliptic [km/s]	2.31	0	NA
ΔV Deimos lander bi-elliptic [km/s]	2.10	0.76	NA
Total mass Hohmann [kg]	2624.57	6129.37	5486.83
Total mass bi-elliptic [kg]	1630.32	2637.67	NA

based on the Goddard Mars model 2B.[3] Again 30 coefficients are used in order to get a detailed simulation of the motion of the spacecraft in Mars's Sphere of Influence. The positions of all planetary bodies are obtained for the planetary and lunar ephemeris *DE 421*. The lunar orbit is known to submetre accuracy. The orbits of Venus, Earth and Mars are known to subkilometre accuracy. Mecury's orbit is determined to an accuracy of several kilometres using radar ranging. The orbits of Jupiter and Saturn are determined to accuracies of tens of kilometres. The orbits of Uranus, Neptune and Pluto are not that well determined.[4] The *DE 421* files are implemented in MATLAB by David Eagle.[5] The position of Phobos and Deimos is determined using the MAR085 model, with an approximate error of 50 km.[6] To read this ephemeris file, the *jplephem* package in Python was used.[7]

- **Mass and frontal area of orbiter**: these inputs are needed for the drag and solar radiation pressure calculations. These inputs are obtained after several iterations and set to 705.1 kg and 20.3 m^2.

5.2.3. Model Preliminary Analysis

Before the core of the simulation can be discussed, an initial trade-off has to be performed to determine the target orbit around Mars and the orbits inside the Martian system. There are two methods to perform a high thrust trajectory inside the Martian system: the Hohmann transfer (two impulse burn) or the bi-elliptic transfer (three impulse burn). Three different orbits can be targeted: the Deimos orbit with the inclination of Deimos, the Phobos orbit with the inclination of Phobos or a low Martian orbit with the inclination of either Deimos or Phobos. For the low Martian orbit, it makes no difference with respect to the ΔV whether the inclination of Deimos or Phobos is targeted due to the conservation of energy principle. For this mission, it was chosen to target Deimos' inclination. The low Martian orbit altitude is set to 400 km altitude. The reason for this altitude is that 400 km is the lowest altitude where no ΔV is needed for orbit keeping during eight years and the lowest altitude is targeted because it provides the highest accuracy for the altimeter measurements. 400 km is also the altitude of the Mars Reconnaissance Orbiter.[8] For this trade-off, a simple Hohmann transfer or a simple bi-elliptic transfer is used to estimate the ΔV needed in each scenario. From these ΔV, the propellant used by the orbiter and the two landers is determined. These calculations are not accurate and provide a rough estimate to compare the options. Note that a bi-elliptic transfer can only be used to get from a lower altitude to a higher altitude orbit. Therefore when targeting Deimos orbit, only Hohmann can be used. For this estimation, the preliminary dry mass of the landers and the orbiter from Roza et al. [96] are used, together with an assumed specific impulse (Isp) of 250 s. The results are presented in Table 5.2.

When targeting the Deimos orbit, the orbiter brings the landers to the moons and then transfers to the orbit around Mars. When targeting the low Martian orbit, the orbiter performs the MOI burn, while the landers continue independently. This means each lander needs to be equipped with a propulsion system. Even considering the added weight of these propulsion systems, it is clear that targeting the low Martian orbit and using bi-elliptic transfer orbits to the moons is the most advantageous trajectory when considering propellant mass, saving at least one tonne of propellant compared to the other options. Therefore, the target orbit is selected to be at an altitude of 400 km with an inclination of 1.79°. However, for the orbit determination of the orbiter with the altimeter and the Doppler data, an inclined orbit is needed. This is discussed in detail in

[3] `https://bowie.gsfc.nasa.gov/697/MARS/GMM2B.html` [Accessed on: 2 June 2017]
[4] `http://www.cv.nrao.edu/~rfisher/Ephemerides/ephem_descr.html` [Accessed on: 29 May 2017]
[5] `https://nl.mathworks.com/matlabcentral/fileexchange/39203-a-matlab-implementation-of-the-jpl-ephemeris` [Accessed on: 29 May 2017]
[6] `https://naif.jpl.nasa.gov/pub/naif/generic_kernels/spk/satellites/a_old_versions/mar085.cmt` [Accessed on: 2 June 2017]
[7] `https://pypi.python.org/pypi/jplephem` [Accessed on: 3 June 2017]
[8] `https://spaceflightnow.com/mars/mro/status.html` [Accessed on: 5 June 2017]

Section 5.3. In order to be able to accurately determine the orbital parameters of the orbiter, an inclination of 15° is needed. Therefore, when the landers are deployed, the satellite will continue on the highly elliptical orbit and perform an inclination change of 13.3° at the apoapsis, where this inclination change is the most efficient.

5.2.4. Lambert Optimisation

The simulation starts by varying the departure time (t_{dep}). For each t_{dep}, it loops through all arrival times (t_{arr}) in the arrival span. For each combination of t_{dep} and t_{arr}, it solves the Lambert Problem.[9] To solve the Lambert problem, Gooding's solution is used, as elaborated by Gooding [46]. This is an extremely robust solver with linear running time. From the Lambert Problem, the velocity of the spacecraft with respect to the Sun is determined $\mathbf{c_{sc/Sun,1}}$ and $\mathbf{c_{sc/Sun,2}}$, at departure from the Earth's SOI and arrival at Mars's SOI respectively. The ΔV needed to escape the Earth's SOI is then calculated with Equation 5.1.

$$\Delta V_1 = \sqrt{\left|\mathbf{r_{sc/Sun,1}} - \mathbf{r_{Earth/Sun}}\right|^2 - 2\frac{\mu_{Earth}}{r_{SOI,Earth}} + 2\frac{\mu_{Earth}}{R_{Earth}+h_{Earth}}} \tag{5.1}$$

In Equation 5.1, $\mathbf{r_{Earth/Sun}}$ is the heliocentric position of Earth at t_{dep}, μ_{Earth} is the gravitational constant of Earth, R_{Earth} is the radius of Earth, h_{Earth} is the apoapsis height of the launch hyperbola and $r_{SOI,Earth}$ is the radius of the Earth's SOI.

Since the inclination of the Deimos orbit is targeted at the arrival at Mars, one has to include the ΔV needed to perform the inclination change from the arrival trajectory inclination to the Deimos' inclination. This results in Equation 5.4, for which Equation 5.2 and Equation 5.3 are used.

$$V_1 = \sqrt{\frac{2\mu_{Mars}}{R_{Mars}+h_{Mars}} + \frac{\left|\mathbf{r_{sc/Sun,2}} - \mathbf{r_{Mars/Sun}}\right|^2}{\mu_{Mars}}} \tag{5.2}$$

$$V_2 = \sqrt{\frac{\mu_{Mars}}{R_{Mars}+h_{Mars}}} \tag{5.3}$$

$$\Delta V_2 = \sqrt{V_1^2 + V_2^2 - 2V_1V_2\cos\left(i_{traj} - i_{Deimos}\right)} \tag{5.4}$$

In Equations 5.2 to 5.4, $\mathbf{r_{Mars/Sun}}$ is the heliocentric position of Mars at t_{arr}, μ_{Mars} is the gravitational constant of Mars, R_{Mars} is the radius of Mars, h_{Mars} is the targeted orbit altitude above the Martian surface, i_{Deimos} is the inclination of Deimos, while i_{traj} is the inclination of the arrival trajectory. This is calculated by transforming $\mathbf{r_{sc/Sun,2}} - \mathbf{r_{Mars/Sun}}$ from the heliocentric EME2000 reference frame to the MME2000 reference frame. This is called $V_{\infty,MME}$. The inclination is then found by applying Equation 5.5.

$$i_{traj} = tan^{-1}\left(\frac{V_{\infty,MME_z}}{V_{\infty,MME_y}}\right) \tag{5.5}$$

The rotation from the EME2000 to the MME2000 reference frame is time dependent. More information about the transformation matrix is given by Conte [24]. Minimising $\Delta V_1 + \Delta V_2$ results in the optimal launch and arrival date.

This module is validated with data provided by Conte [24]. The module's input is changed and compared to the output of [24] in Table 5.3 The errors are smaller than 1% thus the module is validated.

Table 5.3: Output of the simulation, which is compared to Conte [24].

Parameter	Simulation	David Conte [24]	Error
ΔV_{tot} [km/s]	5.43	5.41	0.36%
Departure date	July 31, 2020	July 31, 2020	0 Day
Arrival date	February 27, 2021	February 27, 2021	0 Day
C_3 at launch [km^2/s^2]	14.90	14.88	0.13%
Arrival i (MME) [°]	6.31	6.32	0.15%

[9] `http://ccar.colorado.edu/imd/2015/documents/LambertHandout.pdf` [Accessed on: 3 June 2017]

5.2.5. Determine Launch Hyperbola Specifications

From the t_{dep} and the velocities found in the Lambert Problem, it is possible to determine the specifications of the launch hyperbola. Since the Falcon 9 is used to launch the spacecraft, Cape Canaveral is chosen as the launch site with a latitude of 28.5°. As specified by SpaceX, the Mars Transfer Injection happens at an altitude of 200 km and an inclination between 28.5° and 35°. For this mission the inclination is set to 30°. Using the method proposed by Brown [19], the location of the periapsis of the launch hyperbola and the velocity of the spacecraft at that periapsis is determined.

The module is validated by using the data provided by David Eagle.[10] David Eagle validated his launch simulator in STK.[11] The error percentages are presented in Table 5.4. It is clear that the errors are very small and therefore negligible.

Table 5.4: Comparison between simulation and David Eagle's results.

Parameters	**Simulation** [km]	**David Eagle** [km]	**Error [%]**
Position hyperbole periapsis	(-6.28,-1.79,-8.16)	(-6.29,-1.79,-8.15)	(0.15,0,0.12)
Velocity hyperbole periapsis	(3.31,-9.57,-5.28)	(3.30,-9.57,-5.28)	(0.30,0,0)

5.2.6. Integration of Departure Trajectory

The Lambert problem only gives the velocities of the spacecraft at departure of Earth's SOI and arrival at Mars's SOI. In order to accurately determine the spacecraft's trajectory, its equations of motion have to be integrated. Three different equations of motion are established: the equations of motion in the Earth's SOI, the heliocentric equations of motion and the equations of motion in the Mars's SOI. In this section, the equations of motion within Earth's SOI are discussed. In these equations of motion, two different effects are accounted for:

- Acceleration due to Earth's gravity field, approximated to 30 coefficients.
- Acceleration due to the Sun and the Moon, which are modelled as point masses.

These accelerations are included using Cowell's Formulation as presented in Equation 5.6. For more information on how to implement the accelerations due to the perturbations, please refer to Turner [120].

$$\begin{bmatrix} \dot{\mathbf{r}} \\ \dot{\mathbf{v}} \end{bmatrix} = \begin{bmatrix} \mathbf{v} \\ \mathbf{a_{gravity}} + \mathbf{a_{Sun}} + \mathbf{a_{moon}} \end{bmatrix} \tag{5.6}$$

Integration is performed by the ODE45 function in MATLAB, with relative and absolute tolerance set to 10^{-10} for the required accuracy (10 digits after the decimal point). This relative and absolute tolerance control the number of correct digits in all solution components. This module can be validated comparing the time and position when the spacecraft exits Earth's SOI from the simulation by the results obtained from GMAT for the MAVEN mission. The MAVEN mission has already been programmed in GMAT.[12] The comparison is presented in Table 5.5. It is clear that the error percentage is very small and therefore the module is validated. The difference in kilometres is due to the fact that in the simulation the Earth's SOI is defined as a sphere while in GMAT it is defined by the gravity field of Earth and is not a perfect sphere. That is why the exit position differs.

Table 5.5: Comparison between the output from the simulation and the output from GMAT.

Parameters	**Simulation**	**GMAT**	**Error [%]**
Time from departure of exit Earth's SOI [days]	2.41	2.39	0.83
Heliocentric position of exit [km]	$10^8 \cdot (-1.39, 0.46, 0.19)$	$10^8 \cdot (-1.40, 0.46, 0.19)$	(0.7,0, 0)

5.2.7. Integration of Heliocentric Trajectory

The equation of motion for a spacecraft outside the SOI of both Mars and Earth includes four different accelerations:

[10] `https://nl.mathworks.com/matlabcentral/fileexchange/39973-a-matlab-script-for-earth-to-mars-mission-design?focused=3865540&tab=function` [Accessed on: 8 June 2017]

[11] `https://www.agi.com/products/engineering-tools` [Accessed on: 16 June 2017]

[12] `http://gmat.sourceforge.net/doc/R2011a/html/MarsB-PlaneTargeting.html` [Accessed on: 10 June 2017]

- Point-mass gravity of the Sun.
- Point-mass gravity of all eight planets and Pluto.
- Point-mass gravity of the Earth's moon.
- Accelerations due to the solar radiation pressure (SRP), when the spacecraft is not in eclipse. The spacecraft is said to be in eclipse when $\tau < 0$ or $\tau > 1$, with τ calculated in Equation 5.7 in McClain and Vallado [73], in which $\mathbf{r_{sat}}$ is the vector from Earth to the satellite and $\mathbf{r_{Earth,Sun}}$ is the vector from Earth to the Sun.

$$\tau = \frac{\mathbf{r_{sat}} \cdot \mathbf{r_{sat}} - \mathbf{r_{Earth,Sun}}}{\left|\mathbf{r_{sat}} - \mathbf{r_{Earth,Sun}}\right|} \tag{5.7}$$

The acceleration due to SRP is calculated with the following equation from McClain and Vallado [73]:

$$\mathbf{a_{radiation}} = -\frac{p_{SR} c_R A_s}{m} \frac{\mathbf{r_{sat,Sun}}}{|\mathbf{r_{sat,Sun}}|} \tag{5.8}$$

p_{SR} is the solar pressure with the nominal value of $4.51 \times 10^{-6}\,\mathrm{N/m^2}$, c_R is the reflectivity assumed to be 2.0 by Wertz and Larson [128] and A_s is the spacecraft's exposed area to the Sun. These perturbations result in the following equations of motion:

$$\begin{bmatrix} \dot{\mathbf{r}} \\ \dot{\mathbf{v}} \end{bmatrix} = \begin{bmatrix} \mathbf{v} \\ \mathbf{a_{Sun}} + \mathbf{a_{planets}} + \mathbf{a_{SRP}} + \mathbf{a_{moon}} \end{bmatrix} \tag{5.9}$$

This module is validated by simulating the orbit of Mars around the Sun with it. Comparing the heliocentric position of Mars about from the *de421* ephemeris data, it is possible to make an error estimate of the module during one Mars orbit. Comparing the position, a root-mean-square error (RMSE) in the x-direction of 1.6857×10^{-8} km, in the y-direction of 8.6978×10^{-9} km and in the z-direction of 9.5481×10^{-9} km is found. These RMSE are very small and they indicate a percentage error of less than 0.01%. This means the heliocentric orbit of Mars is simulated very accurately and the module is validated.

5.2.8. Integration of Arrival Trajectory

Once the spacecraft enters Mars's SOI, the gravity of Mars becomes the dominant force, therefore, Mars cannot be treated as a point mass anymore. These equations of motion are also used to evaluate the long-term behaviour of the orbiter around Mars, so it is important to also include the acceleration due to the drag of the Martian atmosphere and the solar radiation pressure. These perturbations have only long-term effects and thus do not need to be included in the departure trajectory. The accelerations included in the equations of motion are:

- Point-mass gravity of the Sun.
- Point-mass gravity due to Deimos and Phobos.
- Acceleration due to the gravity field of Mars, up to 30 coefficients.
- Acceleration induced by the SRP.
- Acceleration due to the atmospheric drag.

This means the equations of motion can be written in the following equation.

$$\begin{bmatrix} \dot{\mathbf{r}} \\ \dot{\mathbf{v}} \end{bmatrix} = \begin{bmatrix} \mathbf{v} \\ \mathbf{a_{Sun}} + \mathbf{a_{Phobos}} + \mathbf{a_{Deimos}} + \mathbf{a_{gravity}} + \mathbf{a_{drag}} + \mathbf{a_{SRP}} \end{bmatrix} \tag{5.10}$$

The acceleration due to the Martian drag is calculated using Equation 5.11. The atmosphere is modelled by fitting a cubic spline through the density data found in Alexander [2].

$$\mathbf{a_{drag}} = -C_D \frac{1}{2} \rho \frac{A_D}{m} |\mathbf{v}|^2 \frac{\mathbf{v}}{|\mathbf{v}|} \tag{5.11}$$

where C_D is the drag coefficient, assumed to be 2.5 by Wertz and Larson [128], ρ is the atmospheric density, A_D is the frontal area of the spacecraft and m is the mass of the spacecraft. A_D and m are obtained from the other subsystems. Therefore the drag calculations are iterated several times until the final values of A_D and m have been determined. Note that these equations of motion are also used to model the trajectory of the landers and the orbiter in Mars's SOI and not solely to integrate the arrival trajectory.

This module is validated by comparing the long-term behaviour of the orbiter to the long-term behaviour predicted in Krop [61]. Simulating the orbit at an altitude of 525 km at an inclination of 20° for 30 years results in a periapsis height of 295.6 km. With the method proposed in [61], a periapsis height of 298.4 km is found. Comparing $\Delta\omega$, $\Delta\Omega$ and Δi, results in an error of 0.05 %, 1.2% and 0.56%. These error percentages are considered small, certainly over a span of one year. This module is hence also validated.

5.2.9. Determine Spacecraft Arrival Parameters

From the integration of the three equations of motion in Section 5.2.8, one can determine the arrival parameters of the spacecraft at the closest approach point (CAP) at Mars. At this closest approach point, the burns are executed to get the orbiter and the landers in the correct orbits and inclinations. The $\mathbf{r_{CAP}}$ and $\mathbf{v_{CAP}}$ are transformed to orbital elements to check semi-major axes and inclination.[13] This module is easily validated by comparing the targeted arrival parameters to the obtained arrival parameters. An error of less that 0.01% between the two is found. This outcome validates the entire simulation.

5.2.10. Bi-elliptic Optimisation

The decision is made in Section 5.2.3 to use bi-elliptic transfers to the moons. This will require the landers to have their own propulsion system. The travel time is an important factor, as at the arrival in the Phobos orbit the lander must have the same velocity as Phobos. Therefore, the landers have to arrive at the same position as their respective moons. This requirement can be modelled with the following equation.

$$T_a + t_a + t_t = T_m + p_m \cdot N_r \tag{5.12}$$

T_a: The time of arrival at Mars in Julian date.
t_a: The travel time from the Mars arrival orbit insertion to the moon transfer orbit insertion.
t_t: The travel time from the moons transfer orbit insertion to the moon orbit insertion.
T_m: The first time when the moons are at the position where the landers will arrive in the moon orbit in Julian date.
p_m: The time it takes for the moon to complete one orbit.
N_r: The number of rotations the moon makes before arrival.

T_a is known as it is determined by the Mars transfer orbit in Section 5.2.7. T_m is read from the MAR085 ephemeris file. p_m is also a known parameter. The optimisation program for the bi-elliptic transfers iterates through several semi-major axis for the Mars arrival orbit and determines the travel time, t_a. Then the required travel time, t_t, is calculated for several N_r (from 0 to 10 rotations). For these required t_t orbits and ΔV are calculated. From all these options, the option with the lowest total ΔV is presented as the most optimal transfer.

In order to verify the model the values for the orbits are replaced by the values in Table 5.6 from Conte [24]. This resulted in 1.584 km/s, which is 0.6% higher than the 1.575 km/s of Conte [24].

Table 5.6: Verified parameters of the bi-elliptic module.

Parameter	Value
Arrival velocity [km/s]	2.52
Arrival periapse altitude [km]	400
Apoapsis of bi-elliptic transfer [km]	75000
Arrival inclination [°]	6.32

In order to validate the model, the spacecraft's position is integrated over the trajectory. The ΔV changes and the times at which these burns take place are implemented and give the final trajectories. Since the spacecraft arrives at the right time at the moons and the moons are also at the right position to start the landing sequence, the model is said to be valid.

5.2.11. Integration Mars-Centred Trajectory to the Moons

When the optimal sequence of burns is determined by the module explained in Section 5.2.10, the trajectory is integrated using the equations of motion given in Section 5.2.8. This integration is done using the ODE45

[13] `https://downloads.rene-schwarz.com/download/M002-Cartesian_State_Vectors_to_Keplerian_Orbit_Elements.pdf` [Accessed on: 5 June 2017]

function in MATLAB. Since the integration is time based, the position of the moons can also be determined using the ephemeris files. The integration results in an accurate 3D-orbit. This module is already validated in Section 5.2.8.

5.2.12. Long-Lifetime Behaviour Orbiter

The last module of the simulation evaluates the long-term behaviour of the orbiter. This long-term behaviour is dictated by the various perturbations working on the orbiter. Since the ODE45 method is prone to propagating errors over long periods of time, it was opted to not use the equations of motion in Section 5.2.8. The orbiter is modelled using GMAT, an open-source space mission design tool developed by NASA.[14] However, GMAT does not include an atmospheric model of Mars, therefore a separate model is made in MATLAB to simulate the accelerations due to drag on the spacecraft, using the method discussed in Section 5.2.8. GMAT has an interface incorporated to connect it to MATLAB, so MATLAB programs can run in GMAT.

5.2.13. Results

Now that all the modules of the simulation are explained, it is time to present the results of the simulation.

Launch

The mission will be launched from Cape Canaveral at 21:32 UTC on the 26th of February 2031. After a launch sequence of 3 minutes and 42 seconds, the spacecraft reaches a height of 6578.1 km. The launch happens with launch azimuth of 80° and a declination of outgoing asymptote of -66°. At 21:36, the booster stage has delivered a ΔV of 3.97 km/s. At this point, the booster separates from the spacecraft and the travel to Mars starts.

Trajectory in Earth's SOI

The spacecraft leaves Earth's SOI at 06:58 on the 1st March 2031 in separation mode. This trajectory in the Earth's SOI is presented in Figure 5.2. The asterisk is the location where the launcher delivers the spacecraft and the TOI burn is executed. During the trajectory, the spacecraft is in travel mode.

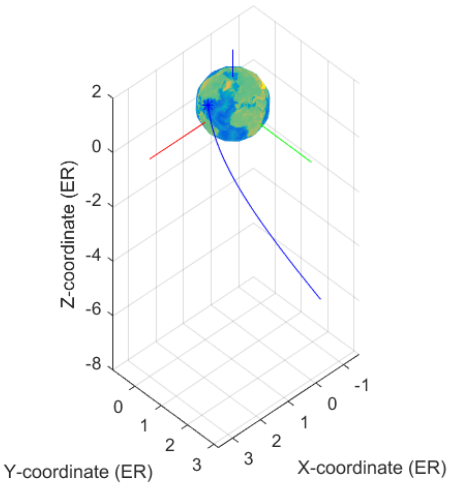

Figure 5.2: Earth-centred trajectory leaving Earth's SOI. The units on the axes is ER, which is Earth radii. The position of the spacecraft is divided by the Earth radius to make the plotting in MATLAB easier.

Interplanetary travel

Now that the spacecraft left Earth's SOI, the interplanetary trajectory starts. The total time of travel is 204 days. This means the spacecraft arrives at the closest Mars approach point at 01:16 on the 19th of September 2031. The heliocentric trajectory of the spacecraft is graphically presented in Figure 5.3.

[14] `https://gmat.gsfc.nasa.gov` [Accessed on: 15 June 2017]

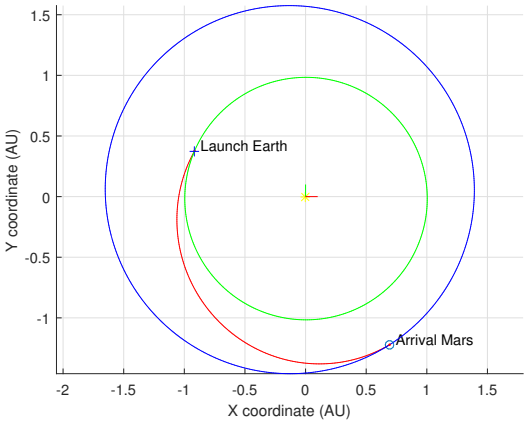

Figure 5.3: Heliocentric trajectory between Earth and Mars.

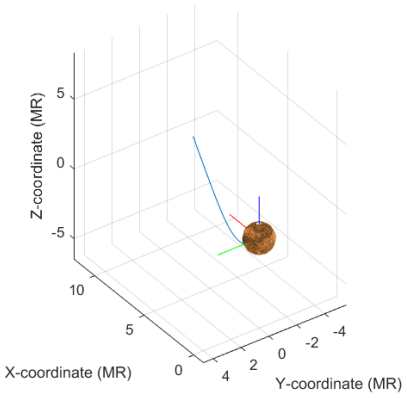

Figure 5.4: Mars centred trajectory to the closest approach point of Mars.

Entrance in Mars's SOI

Since the equations of motion are different when the spacecraft enters Mars's SOI, the integration method changes when the entrance in Mars's SOI is detected in the simulation. The trajectory of the spacecraft within the Mars's SOI to the CAP is shown in Figure 5.4. In Figure 5.4, the unit MR is Mars radii.

At the closest approach point, the Mars Orbit Insertion (MOI) burn is performed. This MOI-burn delivers a ΔV of 1.50 km/s. The spacecraft enters a highly elliptical orbit. During this elliptical orbit, the spacecraft separate right before the second burn. At this point, the spacecraft is in orbit acquisition mode. During the impulse, the spacecraft is in insertion burn mode.

Bi-elliptic orbit

On the 20th of September 2031 at 17:37, both landers perform two separate burns to enter in their respective bi-elliptic orbits, with the Deimos lander giving a ΔV of 0.0021 km/s and the Phobos lander a ΔV of 0.014 km/s. The second burn of the bi-elliptic orbit happens at the periapsis to perform the necessary inclination and eccentricity changes of the orbit. The Deimos lander performs a ΔV manoeuvre of 0.38 km/s on the 21st of September 2031 at 13:25 and the Phobos lander performs a manoeuvre of 0.18 km/s on the 21st of September 2031 at 11:28. The third and last burn in the elliptic orbit is to obtain an orbit 10 km from Phobos and Deimos respectively. The Deimos lander performs the third manoeuvre with a ΔV of 0.236 km/s at the 22nd of September 2031 on 20:29, while the Phobos lander performs a ΔV change of 0.629 km/s on 22nd September 2031 at 08:15. Now the orbiter and landers are in travel mode.

Orbiter trajectory in Mars's SOI

The orbiter does not perform a burn when the landers enter their bi-elliptic orbits. It continues on the elliptical and performs an inclination change manoeuvre at the apoapsis. This is necessary since the orbiter has to target an orbit at an inclination of 15°. This is to enable the orbiter to determine its position using the altimeter as explained in Section 5.3. The ΔV required is 0.0858 km/s. This burns happens on the 21st of September 2031 on 13:48. The last manoeuvre of the orbiter is the Mars Parking Orbit insertion burn, which is a burn of 1.2298 km/s, to get into a parking orbit at 400 km which is performed on the 22nd of September 2031 at 09:59.

All the burns and the dates of the manoeuvres are summarised in Table 5.7. The complete trajectory design in the Martian system is presented in Figure 5.5, including the entry trajectory into the Mars's SOI. For clarity, the orbits of the orbiter, the Deimos lander and the Phobos lander have been presented separately after separation of the landers in Figure 5.7, Figure 5.8 and Figure 5.9, together with the orbit which the complete spacecraft performs in Figure 5.6. When the orbiter starts orbiting around Mars, the orbiter remains in operational mode.

Landing sequence

The landing sequence of the landers is started when the landers are closest to the moons. This distance is set to 10 km. The landing sequence of the Deimos lander is initiated on the 23rd of September 2031 at 02:43, while the landing sequence of the Phobos lander is initiated on the 22nd of September at 08:44. During the landing, the landers are in landing mode. When the landers have landed, they switch on operational mode.

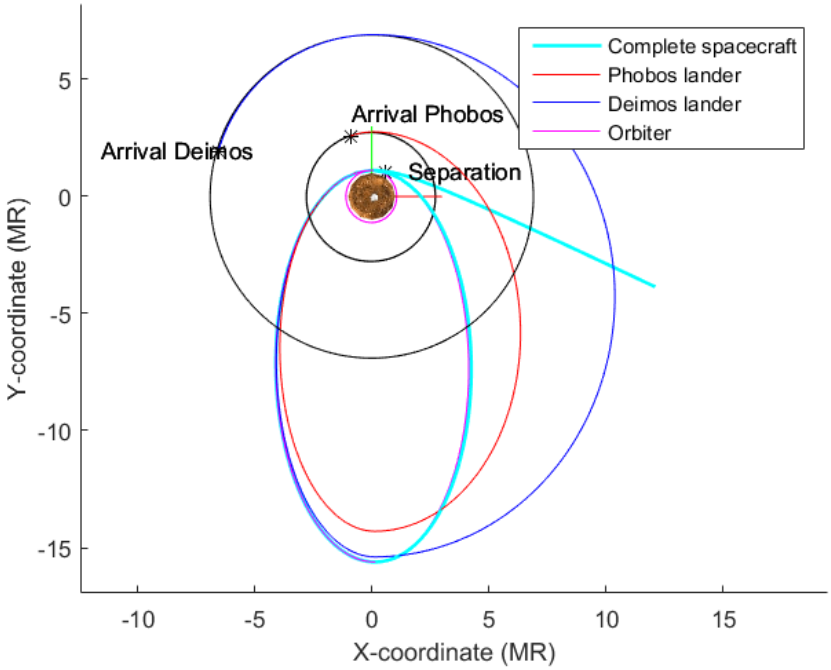

Figure 5.5: Complete trajectory of the spacecraft in the Martian system to target the moons and the parking orbit.

The burn phases in Table 5.7 are used in Chapter 8. Since the booster stage of the Falcon 9 will perform the TOI-burn, this ΔV is not included in the ΔV budget of the spacecraft. In total the orbiter has to perform manoeuvres adding up to a ΔV of 3.29 km/s. The Phobos lander will perform a total ΔV of 0.93 km/s and the Deimos lander needs a ΔV of 0.713 km/s. Note that a 10% margin is incorporated to account for unexpected events. The overview for the Phobos lander, Deimos lander and orbiter are presented in Section 14.3.

Now that the orbiter has arrived in the parking orbit of 400 km, the long-term behaviour of the satellite is investigated. The perturbations due to solar radiation pressure, point-mass gravity of the Sun, Phobos and Deimos and the gravity field of Mars, up to 30 coefficients, alter the orbit of the spacecraft. Note that the atmospheric disturbance was not incorporated in this simulation since GMAT does not incorporate an atmospheric model of Mars. The orbit is simulated for 100 days, to limit the computational time. A pattern is clearly visible. The orbit altitude decays to 370 km and then increases again to 434 km. The altitude of the orbiter is presented in Figure 5.10. The inclination of the orbiter changes with time and this is crucial for the orbiter determination system. As explained in Section 5.3, if the inclination drops below 7.5°, the orbit determination is not accurate enough. From Figure 5.12, it can be seen that the inclination never drops below 8.4° and thus the requirement is complied to.
Since the lowest altitude is 370 km, the acceleration due to the drag is investigated at an altitude of 370 km. The decay of the orbit altitude over eight years due to drag is presented in Figure 5.11. The orbit decays 18 km in eight years. The dense atmosphere of Mars only starts at 200 km. Therefore no propellant is necessary for the orbit keeping during the lifetime of eight years. It is expected that the orbiter will enter the dense Martian atmosphere after 20 years. This analysis is done with the drag equation presented in Section 5.2.8.

5.3. Orbit Determination System

The Orbit determination is needed in order to prove that requirements *OPS-DEP-S-15* to *OPS-DEP-S-18* are met. These requirements flow from the needs of the mission as described in Section 2.2.1. To perform the orbit determination, use is made of Doppler tracking, laser ranging and laser altimetry to Mars.

5.3.1. Altitude Determination

In order to meet requirement *OPS-DEP-S-15* that requires the orbital altitude to be measured with an accuracy of at least 0.5 m, the orbiter must be capable of performing laser altimetry to the Martian surface. The laser

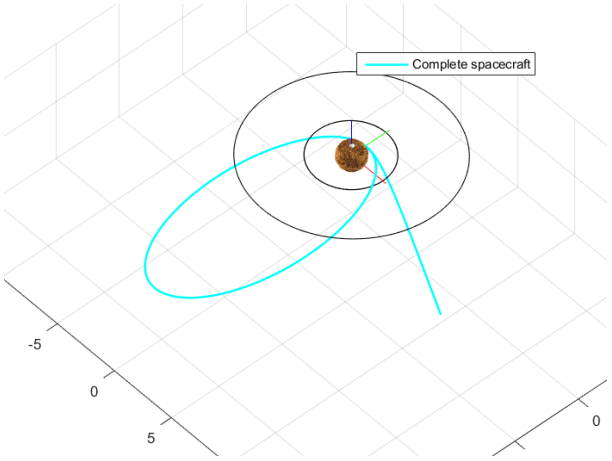

Figure 5.6: Trajectory of the complete spacecraft in the Martian system.

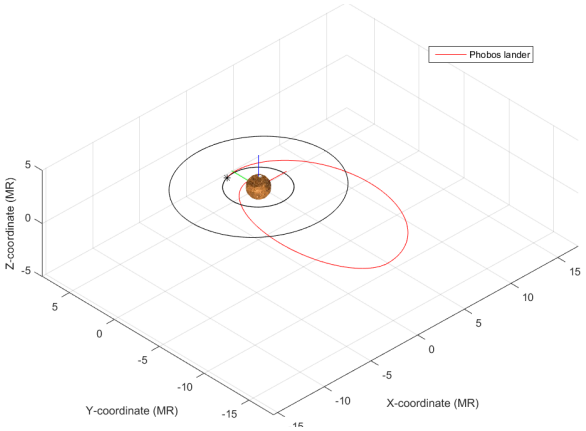

Figure 5.7: Trajectory of the Phobos lander after separation with the orbiter.

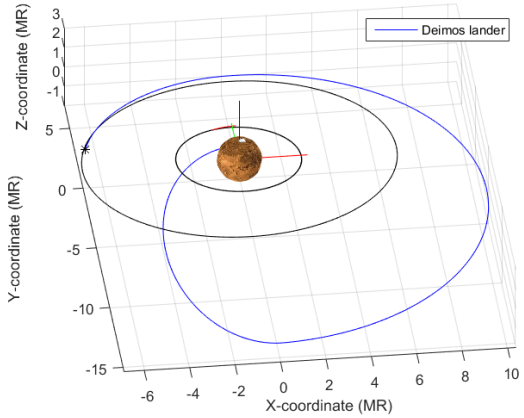

Figure 5.8: Trajectory of the Deimos lander after separation with the orbiter.

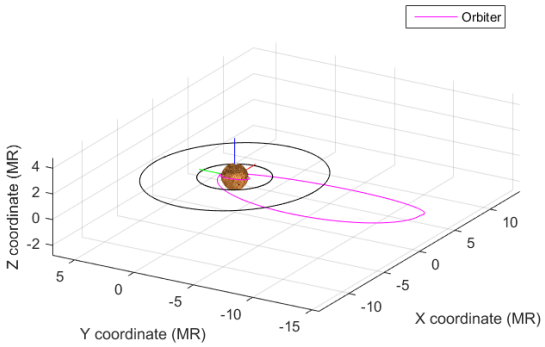

Figure 5.9: Trajectory of the orbiter after deployment of both landers.

equipment that is part of the communication and ranging system, described in Chapter 4, is going to serve as an altimeter as well. This would require slight modifications to the architecture of the current system. To do so, the missions JUICE and BepiColombo by ESA, that have both performed laser altimetry around celestial bodies, were analysed.[15,16]. Based on those, an altimeter was designed and encorporated in the laser system as it can be seen in Figure 4.3.

The BepiColombo Laser Altimeter (BELA) emits laser pulses at a frequency of 10 Hz to perform altimetry.[17] The reflected beam is captured by a 20 cm diameter, F/5 telescope. The wavelength of the altimetry laser is 1064 nm, the same as the one used for communication and ranging, therefore no modifications are needed there. The time resolution BELA is able to provide is 2 ns which translates to an accuracy range of 30 cm, limited by the system. This range value refers to the scenario of having optimal data return which is possible up to an altitude of 1000 km above the surface of the object to which altimetry is performed. The altitude of the Aphrodite orbiter is 400 km, which places it in the optimum data return area.

The JUICE Mission makes use of The Ganymede Laser Altimeter (GALA). According to Lingenauber et al. [69], its telescope is a 25 cm diameter, F/1. The pulse frequency is 30 Hz and its time resolution is 1 ns. That value transfers to 15 cm accuracy with an optimum data return up to altitudes of 1300 km, which is higher than the Aphrodite orbiter's altitude above Mars. The wavelength of the laser emitted to perform altimetry from the GALA instrument is again 1064 nm.

[15] `http://sci.esa.int/juice/` [Acessed on: 21 June 2017]
[16] `http://sci.esa.int/bepicolombo/` [Acessed on: 21 June 2017]
[17] `http://pig.space.unibe.ch/pig/science/projects/bela-and-laser-altimetry.html` [Accessed on: 21 June 2017]

Table 5.7: The final delta-V budget for every burn.

Manoeuvre	Δ**V** [km/s]	**Time**
TOI-Burn	3.970	21:36:21 26/02/2031
Burn Phase 1: MOI-Burn	1.501	01:16:19 19/09/2031
Burn Phase 2: Deimos 1st Insertion Burn	0.00216	17:37:53 20/09/2031
Burn Phase 2: Phobos 1st Insertion Burn	0.0140	17:37:53 20/09/2031
Burn Phase 3: Deimos 2nd Insertion Burn	0.379	13:25:14 21/09/2031
Burn Phase 3: Phobos 2nd Insertion Burn	0.177	11:28:54 21/09/2031
Burn Phase 4: Deimos 3rd Insertion Burn	0.236	20:29:12 22/09/2031
Burn Phase 4: Phobos 3rd Insertion Burn	0.630	08:15:46 22/09/2031
Orbiter Inclination Change Burn	0.0858	13:48:40 21/09/2031
Mars Parking Orbit Insertion Burn	1.230	10:02:20 22/09/2031

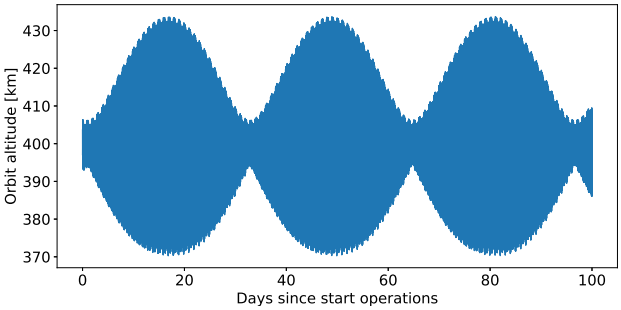

Figure 5.10: Behaviour of the satellite over 100 days.

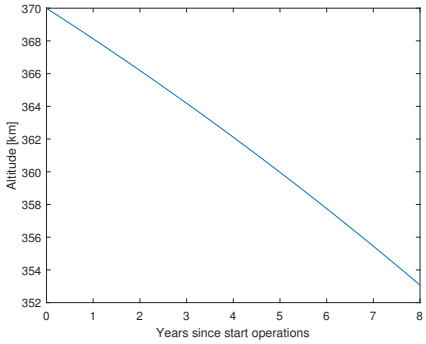

Figure 5.11: Altitude decay due to drag.

It is seen that both BELA and GALA instruments can meet the accuracy requirement of 0.5 m given in requirement *OPS-DEP-S-15*. Therefore, the lighter BELA instrument is chosen as the basis for the modifications to be done on the orbiter's laser system. The difference in albedo for the different missions should also be taken into account. BepiColombo is a mission to Mercury, while the Aphrodite mission targets Mars. Mercury's albedo is 0.12, while that of Mars is 0.25.[18,19] The relation between the albedo and the power required for altimetry is one-to-one as explained by Morris et al. [76], therefore the Mars altimeter would have to be twice as powerful as the BELA.

When performing altimetry, the beam is directed from the telescope to a narrow bandpass interference filter. This filter is needed in order to refocus the light onto a silicon avalanche photodiode which turns it into an electric signal.[20] After that, this signal is sampled via the signal sampling electronics. The clock determines the time of travel of the laser pulse (time between emitting the pulse and receiving it back) and passes the data, together with the signal itself to the digital processing unit. This addition to the laser system of the Aphrodite orbiter is clearly shown in Figure 4.3. With a mean for laser altimetry in place, requirement *OPS-DEP-S-15* is met.

5.3.2. Along-Track Determination

Requirement *OPS-DEP-S-16* imposes an accuracy for the along-track determination of the Aphrodite orbiter that can be met by the means of dual Doppler tracking. Since dual frequency ranging is needed, also a Ka-band transponder needs to be installed as part of the radio system (shown in Table 4.6). Other missions that need such accurate along-track orbit determination, like BepiColombo as described by Genova et al. [42], make use of data from precise accelerometers as a supplement to the Doppler tracking. The BepiColombo mission has a requirement for the along-track accuracy of 1 m, which translates to 10^{-8} m/s^2 in terms of acceleration accuracy as discussed by Iafolla et al. [54]. The Italian Spring Accelerometer (ISA), that was designed specially for that

[18] `https://nssdc.gsfc.nasa.gov/planetary/factsheet/mercuryfact.html` [Accessed on: 30 June 2017]
[19] `https://nssdc.gsfc.nasa.gov/planetary/factsheet/marsfact.html` [Accessed on: 30 June 2017]
[20] `https://www.cosmos.esa.int/web/bepicolombo/bela` [Accessed on: 21 June 2017]

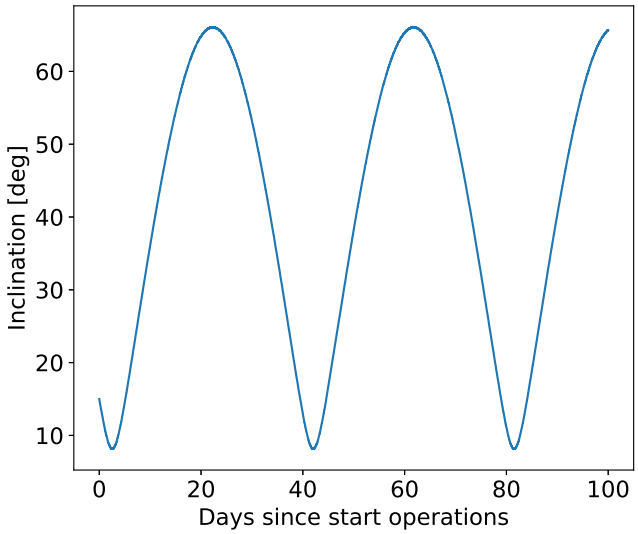

Figure 5.12: Change of inclination over 100 days

mission, is able to determine the accelerations of the Mercury Planetary Orbiter (MPO) to an accuracy of 10^{-9} m/s^2 [54]. The precise accelerometers are installed as part of the ADCS subsystem as stated in Section 9.3 of this report. With the ISA and the USO, BepiColombo is able to meet a requirement for along-track accuracy of 1 m [54]. The accelerometers on the Aphrodite orbiter are able to provide acceleration determination accuracy of 3×10^{-15} m/s^2 (this is explained in detail in Section 9.3), which makes them more accurate than the ISA. The high accuracy accelerometers, together with the USOs and the Doppler tracking capabilities of the Aphrodite orbiter ensure that its along-track position can be determined as accurate as 1 m. This is more exact than the requirement of 2 m imposed on the Aphrodite mission. Therefore, requirement *OPS-DEP-S-16* is met.

5.3.3. Across-Track Determination

Due to the low inclination of Aphrodite orbit, the across-track orbit determination requirement *OPS-DEP-S-17* of 2 m cannot be met using Doppler tracking. Therefore, a novel method of across track orbit determination using laser ranging is devised. The laser ranging component from the Phobos lander to the orbiter is decomposed into a cross-track component. This is achieved by exploiting the difference between the orbital inclination of the orbiter and Phobos. The angle between the line of sight (laser) vector from Phobos lander to orbiter and the along-track radial plane represents the difference between the inclination of the orbits of both satellites. Therefore the accuracy of laser ranging and the ephemeris of Phobos determine the accuracy of the across-track orbit determination. The accuracy of two way laser ranging between the orbiter and the Phobos lander is estimated to be smaller than 1 cm.

The second uncertainty associated with this method is the ephemeris of Phobos. According to Dirkx et al. [32], an accuracy of 2.5 cm for the ephemeris of Phobos can be achieved when only Gaussian noise is considered. However, when considering a systematic error of 5 mm, a 20 times increase in the ephemeris error can be expected (Dirkx et al. [33]). As Aphrodite has no ground station uncertainty, the systematic error is estimated to be 2.5 mm which leads to an error in ephemeris of 25 cm. Additionally, the ranging between the Phobos lander and orbiter will further improve the ephemeris of Phobos. This is estimated to improve the ephemeris to 12.5 cm.A laser ranging error of 1 cm and an across-track accuracy of 1 m is chosen for the calculation. The across-track accuracy can be calculated using Equation 5.13 as a function of the ranging accuracy from Phobos (including ephemeris error).

$$\epsilon_c = \frac{\epsilon_r}{\cos(90 - \alpha)} \tag{5.13}$$

where, ϵ_c represents the across track error in metres, ϵ_r represents the ranging error between orbiter and Phobos lander in metres and α represents the difference in the inclination of the orbits of Phobos and Mars Orbiter in degrees. Therefore, a 7.5° inclination difference between Phobos and the orbiter is necessary to satisfy

OPS-DEP-S-17 requirement. Figure 5.12 displays the orbit inclination change and it can observed that the orbit inclination does not go below 7.5 °.

As a continuous knowledge of orbit is necessary, ranging operations between the Phobos lander and orbiter must be conducted every orbit. Additionally, as will be seen in Table 9.5,extremely accurate accelerometers will keep propagation errors in an orbit to under 1 m, hence ensuring that *OPS-DEP-S-17* will be met.

5.3.4. Radial Orbit Determination

In order to determine the radial orbiter position with the accuracy required from *OPS-DEP-S-18*, both the laser altimeter and the Doppler tracking are going to be used. To meet the accuracy stated in this requirement, an USO is needed to be able to determine the altimetry laser beam travel time with sufficient precision such that the radial orbiter position can be determined with the required accuracy (a second one is added for redundancy). The JUICE Mission used the same configuration to determine their orbital position as stated by Plaut and Barabash [87]. For the Doppler tracking, JUICE uses its HGA that transmits in the Ka-band range with a frequency of 32.5 GHz. Combining the Doppler tracking together with the altimetry data from the GALA instrument, yields an accuracy for the determination of the radial component of the spacecraft in the order of 0.01 to 0.1 m as indicated by Parisi et al. [82].

The Aphrodite HGA transmits in the Ka-band as well with a frequency of 32.5 GHz. The radio system is designed to provide range rate measurements by that are accurate to 0.003 mm/s at 1000 s integration times as indicated by Parisi et al. [82]. This will be possible due to the dual-frequency radio links Ka band as described in Section 5.3.1. The altimeter used on board of JUICE, has only slightly better accuracy than the one installed on the Aphrodite orbiter. Their difference in time resolution is only 1 ns which translates to accuracy range of 15 cm. This difference is small enough to assume that even with the current altimeter's time resolution, the radial component of the Aphrodite orbiter can be determined with an accuracy better than 0.5 m. Therefore, requirement *OPS-DER-S-18* is met.

5.4. Risk Analysis

In order to ensure that the mission performs as desired, a risk analysis of the GNC subsystem is performed. First, the risks are discussed and mitigated and then a risk map of the mitigated risks is shown in Table 5.8.

1. Bug in trajectory software: The trajectory software will be very elaborate and complex, therefore detecting all bugs in the software is hard. Bugs in the trajectory software can be made unlikely, by making two teams of programmers, program the control software independently. This is common practice in the space industry. Extensive testing of the software also minimises the likelihood of bugs in the trajectory code.

2. Incorrect orbital determination: Incorrect orbital determination is already unlikely and can be easily mitigated by ranging more often. Since one erroneous measurement has a low impact on the mission. The spacecraft is equipped with a redundant sensors when one of the sensors fails. A margin of 10% is incorporated in the design for in the case the system does not perform as expected.

3. Failure to execute manoeuvre: Failure to execute manoeuvre can have two roots, either the thruster failed or the software failed. Either way, missing the manoeuvre time can seriously endanger the success of the mission. Therefore both the landers and the orbiter have a margin of 10% on their ΔV budget which allows one to correct for manoeuvre failure. This would allow the orbiter to target an inclination of 25° and the landers would be able to do two apoapsis burns if the first burn misses the moons.

4. Error in the estimation positions of the moons: The position of the moons is at this moment still only known with an accuracy at kilometre level. Therefore the simulation has at least an uncertainty of 10 km with respect to the moons' position. The margin in the ΔV budget and the margin in the propellant used during landing will be able to minimise the impact of this event.

5. Injection error: The risk exists that the Falcon 9 puts the spacecraft at the wrong injection point. However, this is very unlikely since the Falcon 9 is selected because it is a reliable launcher. Although the Falcon 9 has never injected a spacecraft into a Mars transfer, when launching to GEO and LEO, injection errors never occurred.

6. Faster decay rate than expected: The density model of Mars is the biggest uncertainty of the model simulating the long lifetime of the mission. However, it is determined that the orbiter will not enter the atmosphere of Mars with a 90% certainty within 20 years. Therefore, an inaccurate density model does not pose a big threat to the success of the mission. As an extra mitigation, a margin is included in the ΔV budget. The propellant masses are sized for 1.1 of all ΔV burns.

6. Launcher Delay: Launcher delays are very likely when the weather forecast predicts unsuitable weather for a launch. Launch delays are common in the space industry. To mitigate the risk, a launch window of around 20 days is presented in Section 5.5.

Table 5.8: Mitigated risk map of the GNC subsystem.

Almost certain	1	4			
Likely		6			
Average					
Unlikely			2		
Improbable			3		5
Likelihood / **Impact**	Negligible	Marginal	Moderate	Critical	Catastrophic

5.5. Sensitivity Analysis

It is already explained that the two largest sources of error are expected to be the locations of the moons and the density model of the Martian atmosphere. Therefore the sensitivity analysis is focused on these two aspects.

When scaling the density model by a factor three, the altitude of the satellite only decreases with 50 km over eight years. When the model is scaled with ten, the orbiter crashes on Mars after four years. The uncertainty of the density model is ±30% Alexander [2]. This means the drag module is robust within the uncertainty limits. The uncertainty of the position of the moons in the ephemeris files is around 50 km. With the current margins in the ΔV budget, Phobos can still be reached if the position is approximately 1200 km from the predicted location, while Deimos can still be reached if the position is approximately 1100 km from the ephemeris data. It is thus clear that enough margin is incorporated to account for these uncertainties.

The last important sensitivity analysis is performed on the launch date. Several sources of delay are possible such as technical delay, atmospheric conditions,... Therefore a proper launch window has to be established. This launch window is established by changing the departure date and finding the optimal arrival date. It is found using the simulation described above that a launch later than the 7^{th} of March would not allow the spacecraft to carry enough propellant to reach a Martian parking orbit. A launch before the 18^{th} of February would not allow the Falcon 9 to carry enough propellant to perform the TOI burn. Therefore the launch window is between the 18^{th} of February and the 7^{th} of March, with an optimal launch date at 26^{th} of February. It is found that the burns that have to be performed by the orbiter and the landers are not the limiting factor of the launch window, it is the Falcon 9. Using the maximum mass that can be carried by the Falcon 9 to MTI (4020 kg), one can determine the maximum propellant mass the Falcon 9 can carry. Using this propellant mass and the Aphrodite wet mass, the maximum ΔV of the Falcon 9 to MTI is calculated. This ΔV limits the launch window.

[This page is intentionally left blank]

6
Structure

The structure of the spacecraft is a crucial part of the spacecraft, as in many cases a single structural failure of the spacecraft leads to total mission failure. First, the overall spacecraft design is presented in Section 6.1, including all the values for the mass. Afterwards this will be elucidated by the functional analysis and the design approach, which are shown in Sections 6.2 and 6.3 respectively. Then the design of several ancillary structural mechanisms is elaborated on in Section 6.4. Furthermore, in Section 6.5 the risks are analysed. Finally, Section 6.6 expands on the sensitivity analysis of the structural subsystem.

6.1. Design Overview

The overall design of the bus consists of the three spacecraft stacked upon each other with the orbiter at the bottom, followed by the Deimos lander and the Phobos lander. A clear overview of the entire bus is shown in Figure 3.3. In this configuration, the spacecraft are positioned such that the heaviest component is at the bottom and therefore the bending moment is minimised. The Phobos lander is positioned upside down to prevent the thruster from damaging the laser of the Deimos lander both after separation. The orbiter is connected to the landers by means of a sandwich panel on which a frustum-shaped adapter is mounted that in turn is attached to the primary structure. The connection between the two landers consists of a cylindrical shaped adapter attached to the sandwich panels placed on top of them. The sandwich panels consist of an aluminium honeycomb structure with carbon fibre reinforced polymers (CFRP) face sheets. The bus is shielded against micrometeorites and space debris by means of whipple shields with aluminium and Nextel–Kevlar bumper layers.

A brief overview of the overall structure is provided in Table 6.1. The total length of the bus is 6.5 m, of which the orbiter measures 2.5 m, the two adapters measure 2 m and the two landers equally fill the remaining 2 m. The primary structure consists of a cylindrical monocoque structure that carries the maximum loads endured during its operational life with a sandwich panel on top. In the case of the orbiter, the cylinder is enclosed by four skin panels in order to attach all the instruments and to protect them against radiation. This turns the orbiter into a rectangular box. The outer dimensions of the orbiter are 2.4 m by 2.4 m and both landers have an outer dimension of 1.4 m by 1.4 m. However, the shape of the landers is hexagonal, as a polygonic shape is more beneficial when it comes to stability during landing (Barraclough et al. [11]). The central cylinder of the orbiter has a diameter of 1.9 m and a thickness of 1.7 mm, while the landers contain a cylinder with a diameter of 0.9 m and a thickness of 0.8 mm. The two frustum-shaped adapters measure 1 m in length. The one between the orbiter and the Deimos lander slowly tapers in thickness to prevent stress concentrations from occurring at the point where the thickness suddenly changes and to save structural mass. The adapter in between the two landers just continues on their cylindrical structure. Both the primary and secondary structure consist of aluminium 5052-H34, resulting in a total structural mass of 132 kg of the orbiter. The Phobos and Deimos landers have a total structural weight of 11.6 kg each. The secondary payload is considered in the design of the structure by providing space to attach the payload to the outer shell (for cameras) or to place the payload in the outer or inner shell.

Looking into the inside of the bus, each spacecraft is divided into sections of instruments that need to operate at the same temperature ranges. In Chapter 12, these ranges are explained in further detail. As will be explained in Chapter 8, there are six spherical fuel tanks positioned in two circular configurations of three with a pressurant tank in between the two layers. Keeping them as low as possible decreases the height of the centre of gravity and therefore the bending moment the bus experiences due to lateral, vibrational launch loads.

6.2. Functional Analysis

The structural subsystem of the spacecraft serves four main purposes. First, it should be able to cope with all loads that are endured during operations. Secondly, it should provide mounting possibilities for all the

Table 6.1: An overview of the main parameters in the structural subsystem.

Spacecraft	**Dimensions** [m]	**Inner Diameter** [m]	**Skin Thickness** [mm]	**Total Structural Mass** [kg]
Orbiter	2.4 × 2.4 × 2.5	1.9	1.7	132
Lander	1.4 × 1.4 × 1	0.9	0.8	11.6

instruments. Thirdly, the structure should protect the instruments against radiation encountered in outer space. Finally, it should make sure the instruments and payload survive the thermal environment the spacecraft is in. These functions translate to requirements, listed in Table 6.2.

All requirements are clarified in this chapter. Nonetheless, requirements *FUN-STC-SS-06* and *FUN-STC-SS-08* are covered in Chapter 13, because the inner design of the spacecraft could only be made after the overall structure had been determined.

Table 6.2: Structural system requirements.

ID	**Requirement**	**Section**	**Compliance**
FUN-STC-SS-01	The structural subsystem shall have a maximum mass of 140 kg for the orbiter and 32 kg for each lander.	6.1	✓
FUN-STC-SS-02	The structural subsystem shall have a maximum cost of M€109 for the orbiter and M€54 for each lander (FY17).	6.1	✓
FUN-STC-SS-03	The structural subsystem shall not have any single point of failure.	6.1	✓
FUN-STC-SS-04	The structural subsystem shall be able to withstand all loads during the operational time.	6.1	✓
FUN-STC-SS-05	The structural subsystem shall provide space to allocate the payload.	6.1	✓
FUN-STC-SS-06	The structural subsystem shall be compatible with all interfaces of all other subsystems in the spacecraft.	13.1	✓
FUN-STC-SS-07	The structural subsystem shall prevent the spread of debris during impact.	6.4	✓
FUN-STC-SS-08	The structural subsystem shall enable accessibility to the other subsystems during assembly.	13.1	✓
FUN-STC-SS-09	The structural subsystem shall provide radiation shielding up to a radiation dose of 2 kRad per year.	12.4	✓

6.3. Design Approach

In this section, the design approach for the primary structure of the spacecraft is given and it shows how the sandwich panels are designed, how the material is selected, how the spacecraft is shielded against micrometeorites and space debris and how the landing legs are designed.

6.3.1. Load Carrying Structure

The preliminary design starts with the assumption that the primary spacecraft bus structure would be a cylinder that runs through all three elements which are separated by decoupling mechanisms and adapters. Then the load paths are determined and an initial length and diameter are estimated in order to start the iterative process. The diameter is driven by the composition of the fuel tanks in the orbiter.

The first step in the design process is to size for rigidity in order to resist the frequencies that are induced by the launch vehicle. SpaceX's Falcon 9 was chosen to deliver Aphrodite into space. According to the launch catalogue of SpaceX [109], their rocket has a natural frequency of 25 Hz in the axial direction and 10 Hz in the lateral direction. The following equations, retrieved from Wertz and Larson [128], allow to size for a certain thickness from the cross-sectional area and the moment of inertia respectively. The cross-sectional area of the structure is described by A, the spacecraft mass is denoted by m and its length by L. The other geometrical parameter is I, which represents the moment of inertia. The E in the equations is the Young's modulus of the material.

$$f_{ax} = 0.250\sqrt{\frac{AE}{mL}} \quad (6.1) \qquad f_{lat} = 0.560\sqrt{\frac{EI}{mL^3}} \quad (6.2)$$

Afterwards it is checked whether the material will yield under the launch loads. The lateral load causes the bus to be loaded in bending as well. Therefore, the equivalent force P_{eq} acting on the structure was approximated by Equation 6.3. Because the peak bending stress can occur at any point that is the furthest from the neutral axis of the cylinder, it must be sized for the equal load that would cause this peak stress in the structure. In this equation, P resembles the axial load, M is the bending moment and R is the radius of the cylinder. On top of that, a safety factor of 1.25 has been applied (Wertz and Larson [128]), resulting in the limit load needed to be withstood. Using the next equations from Wertz and Larson [128], the required thickness can be determined.

$$P_{eq} = P + \frac{2M}{R} \quad (6.3) \qquad \sigma_{yield} = \frac{P_{eq}}{A} \quad (6.4)$$

The final failure mode that needs to be investigated is buckling. The critical buckling stress of a cylinder is calculated with Equation 6.7, in which γ (Equation 6.6) represents the so-called reduction factor, that in turn is dependent on the geometric parameter ϕ, as described by Equation 6.5 from Wertz and Larson [128].

$$\phi = \frac{1}{16}\sqrt{\frac{R}{t}} \quad (6.5) \qquad \gamma = 1.0 - 0.901(1.0 - e^{-\phi}) \quad (6.6) \qquad \sigma_{cr} = 0.6\gamma\frac{Et}{R} \quad (6.7)$$

After having validated the model using the values provided by Wertz and Larson [128], the different required thicknesses that are needed to withstand each failure mode could be compared. It turned out that the cylindrical buckling stress was the dominating load case, as can be seen in Table 6.3. Therefore it has been endeavoured to optimise the structure with respect to buckling.

Table 6.3: Table showing the required skin thicknesses for each failure mode.

Failure Mode	**Required Thickness** [mm]
Axial Frequency	0.22
Lateral Frequency	0.10
Tensile Strength	0.72
Compressive Strength	1.7

When the overall structure had been determined and the most adequate material was chosen, thermal stresses were analysed. Using Equation 6.8 from Wertz and Larson [128] and the maximum temperature difference that will occur in the spacecraft, as explained in Chapter 12, it can be checked if the material can be subjected to the thermal stresses without failing, which turned out to be the case.

$$\sigma_{thermal} = E\alpha\Delta T \quad (6.8)$$

6.3.2. Sandwich Panels

For the transfer of loads between the three main elements of the bus, sandwich panels are used. They have been widely used in other space applications and they are well-known for their high strength over weight ratio, which is of vital importance when it comes to spacecraft (European Space Agency [36]). Consisting of two layers with a honeycomb structure in between they are especially effective in carrying a distributed load.

Studying the methods described by Harte et al. [48], it is valid to assume that the face sheets only carry the bending load, while the honeycomb core takes care of the shear loads. Using the equations below and the data about CFRPs from European Space Agency [36] an appropriate sandwich panel design can be presented. Equation 6.9 represents the bending stress in the face sheets, which is given by dividing the bending moment, M, by the product of the core thickness, d, and the face sheet thickness, t. Using the material properties of GY-70 and aluminium 2024, a core thickness of 20 mm and a face thickness of 2 mm were found to be able to withstand the maximum bending moments and shear loads [36].

$$\sigma_f = \frac{M}{td} \tag{6.9}$$

$$\tau_c = \frac{P}{d} \tag{6.10}$$

6.3.3. Material Selection

In Table 6.4, the several materials that have been considered for use on the spacecraft are outlined. All of these have been used on previous space missions and have been shown to be able to with the environment of outer space.

Table 6.4: Table showing the different properties of often used spacecraft materials, retrieved from the book by Wertz and Larson [128] and the Department of Defense of the USA [27].

Material	$\sigma_{\textbf{ultimate}}$ [MPa]	$\sigma_{\textbf{yield}}$ [MPa]	**E-Modulus** [GPa]	**Density** [kg/m^3]	**Stiffness Ratio** $\frac{\sqrt[3]{E}}{\rho}$	**Thermal Expansion** [1/°C]
AL7075-T6	517	450	69	2800	1.46	22.1×10^{-6}
AL6061-T6	290	240	68	2710	1.51	22.9×10^{-6}
TI-6AI-4V	900	855	110	4430	1.08	8.8×10^{-6}
AL5052-H34	234	172	70	2685	1.53	22.1×10^{-6}

To pick the most suitable material, several aspects have to be taken into account. Mass will directly translate to cost, so the material should be lightweight. On the other hand, it is desirable to have the stiffness and strength as high as possible. Therefore the stiffness over weight ratio is a parameter of high importance when it comes to material choice, as buckling is the major failure mode. The coefficient of thermal expansion is not addressed, for it has been shown that it is not a critical failure mode. Looking at the materials in Table 6.4, it was decided to choose AL-5052-H34 for the load carrying structure of Aphrodite. The stiffness ratios of the three types of aluminium does not vary a lot, although it does have the highest ratio. Another benefit is the density of the material, which is the lowest of all.

6.3.4. Hypervelocity Impact

Space debris and micrometeorites are an uncertainty to design for. These objects in space are unpredictable and the amount of damage they can inflict to the spacecraft depends on their mass, their velocity and the angle under which they impact. Thus, the spacecraft should be shielded against these space particles in order minimise the damage done to the system. According to Christiansen [23], passive protection against hypervelocity impact can be achieved through whipple shields with aluminium and Nextel–Kevlar bumper layers. This should shield the spacecraft up to projectiles of 1.3 g with a velocity of 6 to 7 km/s. Combining the areal densities of the shielding materials the total mass sums up to 6.8 kg for the orbiter and 2.4 kg for each of the landers. This is incorporated in the thermal control subsystem, as will be explained in Chapter 12.

6.3.5. Landing Legs

The landing legs have the function to absorb most of the kinetic energy during landing while keeping the landers stable during touch-down and operations. Therefore three main elements of the landing legs are investigated: shock absorption, static loading and stability. At the end the overall deflection of the landing leg under the loads is presented.

Overall Structure

The overall structure of one landing leg is presented in Figure 6.1. It was chosen to use the same layout of the landing legs as is now being implemented in the ESA Phootprint mission Barraclough et al. [11]. The landing gear consists of a primary strut and two supporting secondary struts. Three landing legs are placed on the hexagonal structure. The loads are limited by an aluminium honeycomb shock absorber incorporated in the primary struts. The foot is attached to the primary strut with a spherical bearing. Similar landing legs were already analysed by Destefanis et al. [28] for a lunar landing with a detailed finite element analysis.

Shock Absorption

The kinetic energy during touch-down is absorbed with a chrushable honeycomb structure. This method is frequently used in planetary landers, like the Apollo mission (Sheehan [104]) and the Philae mission (Witte et al. [131]). The crushable honeycomb can be sized with the method proposed by HEXCEL [50]. This method sizes the length of the absorber using the maximum load the lander is designed for. The area of the honeycomb is determined using the conservation of energy. The maximum design load of the spacecraft is 8.5g at launch.

Figure 6.1: Design of one landing leg.

Table 6.5: Validation truss simulation

Truss	**Simulation** [m]	**CATIA** [m]	**Error Percentage** [%]
Displacement Truss 1 in x	0.0256	0.0245	4.49
Displacement Truss 2 in x	0.00125	0.00131	3.8

More details on the equations used to determine the dimensions of the honeycomb can be found in the article by HEXCEL [50]. It is assumed that 70% of the honeycomb is crushed during landing and that there is a 0.635 cm precrush. The velocity at touch-down is determined in Chapter 7 and is 0.15 m/s. All equations used are presented by HEXCEL [50]. The landing legs are sized such that one leg can carry all the loads during touch-down which is the worst case scenario.

For the Phobos lander, the following crushable honeycomb specifications are calculated: the stroke length s, is 1.3 cm, which results in a total length of the honeycomb of 8.3 cm. With these dimensions, the optimal honeycomb is CRIII Aluminium HexWeb 3/8-5052-5.4, with a crush pressure of 2500 kPa (HEXCEL [50]). With this crush pressure, the required surface of the honeycomb is calculated to be 7.69×10^{-4} m^2. For the Deimos lander, a stroke length of 1.3 cm is also found. This is because the landers are sized for the same maximum load. The total honeycomb length is also 8.3 cm. Using the same honeycomb material as with the Phobos lander (CRIII Aluminum HexWeb 3/8-5052-5.4), a surface area of 7.99×10^{-4} m^2 is necessary. Since the kinetic energy is equal to the work performed by the honeycomb, the force acting on the strut is calculated with Equation 6.11 by HEXCEL [50]:

$$F = \frac{1}{2} m \frac{V^2}{s} \tag{6.11}$$

The volume of one shock absorber is 6.3625×10^{-6} m^3 for the Phobos lander and 6.6084×10^{-6} m^3 for the Deimos lander, weighing 3.2×10^{-4} kg and 3.3×10^{-4} kg respectively per landing leg.

Static Load Analysis

The load acting on the landing legs is 2195.5 N for Deimos and 2113.8 N for Phobos from Equation 6.11. This difference is very small. For sustainability, it is advantageous to keep the two landers as similar as possible, decreasing the waste and cost and increasing the production efficiency. Therefore both landers are sized to withstand 2524.8 N, incorporating a safety margin of 15%.

The three struts are modelled as two force members and using a simulation in MATLAB, the forces in the struts are calculated. The simulation is built using the methods explained by Krenk and Høgsberg [60]. The simulation is validated using a simple two-member problem and simulating it in the Truss FEA workbench of CATIA. The error percentages are listed in Table 6.5. The difference is caused by not being able to model the material properties accurately in MATLAB.

It is found that the primary strut is loaded in compression with 9956.4 N and the auxiliary struts are loaded in tension with 4622.8 N. Using these reaction forces, the dimensions of the struts are determined, by finding the optimal solution to the non-linear system of equations in Equation 6.12. This system of equations sets that the struts should fail in yielding and buckling at the same time under the applied load.

$$F_{ext} = \pi \sigma_{yield} \left(r^2 - (r-t)^2\right) \qquad F_{ext} = \frac{E\pi^3}{KL^2}\left(\frac{r^4 - (r-t)^4}{64}\right) \tag{6.12}$$

The variables r and t are respectively the radius and thickness of the strut, σ_{yield} is the yielding stress of the aluminium used, 450 MPa. E is the Young's modulus of the material, 69 GPa. L is the length of the strut, which is 0.54 m for the primary strut. Note that the auxiliary struts do not have to be evaluated for buckling, since they are in tension, thus only the yielding stress is investigated. Using the non-linear solver in Python, the r of the primary strut is determined to be 1.8 cm and t is 6.5 mm. Since the secondary struts are only in tension, the dimensions are very small. It is determined that an r of 1 cm and t of 2 mm would suffice to carry the tension load. Assuming a density of 2800 kg/m^3 for aluminium 7075-T6, the mass of one landing leg can be estimated. The primary strut weighs 0.91 kg and the secondary strut weighs 0.234 kg. This means the total mass of one landing leg is 1.4 kg.

Stability

The stability of the lander during touch-down is hard to evaluate in this conceptual stage of the design. Two basic requirements to guarantee stability during landing can be formulated. First it is known that the radius of the inscribed circle from the three landing legs must be larger than the height of the centre of gravity as explained by Gross [47]. The height of the centre of gravity is estimated from CATIA to be 1.05 m. The radius of the inscribed circle is 1.252 m. The landing system is thus stable. Another main stability criterion, is that the spacecraft does not tilt during touchdown. The driving condition is the event when the lander lands on one leg on a slope, with a certain horizontal and vertical velocity. The maximum ratio of horizontal and vertical velocity in micro-gravity is cited by Rebuffat [92] to be 0.18. From this ratio, the minimum radius of the landing legs is calculated with Equation 6.13 from Rebuffat [92].

$$\frac{V_x}{V_y} < \frac{1 - \tan\left(\alpha_{slope}\right)\frac{h\sqrt{2}}{r}}{\tan\left(\alpha_{slope}\right) + \frac{h\sqrt{2}}{r}} \tag{6.13}$$

in which h is the height of the centre of gravity, r is the radius of the landing legs and α_{slope} is the allowable slope angle of 25°, as determined in Section 7.4. From Equation 6.13, the radius of the landing legs of the Phobos and Deimos lander is determined to be 0.8 m. This is less than the 1.25 m, which means the lander will be stable during touch-down on one leg.

Deformations of the Landing Legs

Using the parameters determined in the previous sections, it is possible to determine the deflections of the landing legs under loading condition during touch-down. The deflections are calculated with the aforementioned MATLAB simulation. The deflections of the landing strut are shown in Figure 6.2. The black struts are the original situation, while the pink struts are the deflected situation. The deflection is 3.3 cm in the negative y-direction, 2.3 cm in the positive z-direction and 0 in the x-direction, which is well within the limits for deformations of aluminium. Note that the deflection of the struts in Figure 6.2 is scaled by a factor of ten, to make the deflection more visible in the figure. In reality, the deflection are ten times smaller. The strain in the primary strut under a loading of 9956.4 N is found to be 2 3954e − 4.

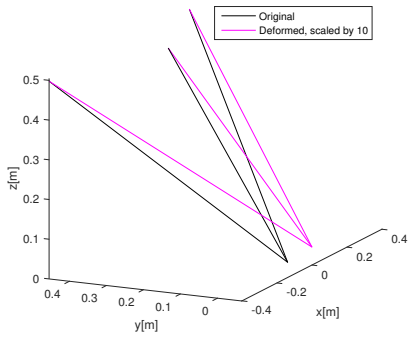

Figure 6.2: Deflections of the landing leg.

The loads from the landing legs are carried by internal struts to the central cylinder of the landers where they are introduced in the structure. This is because the skin panels alone are not capable of carrying the induced loads from the landing legs.

6.4. Mechanisms

This section explains the mechanisms and actuators that are chosen to successfully deploy the solar panels and to have a successful separation.

6.4.1. Solar Array Deployment Mechanism

To prevent the solar panels from being loaded in extreme bending induced by the Falcon 9, they are retracted during launch. This introduces a mechanism that is capable of deploying the solar panels when it is travelling along its interplanetary path. The actuators developed by *MOOG* seem to be suitable for the Aphrodite orbiter.[1] The Type 2 Solar Array Drive Assembly (SADA) will be used on the orbiter. It has a flight heritage that goes back to the 1980s and is capable of handling large solar arrays.. The panels of the orbiter are six times larger than the ones of the landers and therefore its panels will require a strong actuator. Their sizing is extensively described in Chapter 11.

The landers will make use of another actuator. The reason to not use the same actuators as the orbiter has, is because the landers require retractable solar arrays. The solar array mechanism described by Ralph and Chung [90] is a design which is capable of retracting and redeploying the solar panels. The batteries are not capable of providing enough power from the moment of separation until touch-down on the moons, so the panels have to be deployed during this phase. Before the landing phase is initiated, the arrays have to be retracted again, for this will minimise the shock loading the panels will take upon landing.

6.4.2. Separation Mechanism

In order to make the journey to the moons, as described in Chapter 5, the two landers need to be separated from the bus shortly after it has been inserted into a bi-elliptic orbit around Mars. This demands a well-functioning and accurate mechanism to be incorporated in the Aphrodite spacecraft. According to Mitchell [75], the following aspects need to be taken into account to come up with a successful design:

- Adequate clearance between the separating bodies.
- Shock transmission to the payload or structure of the continuing body.
- Damage to or contamination of the continuing body by debris resulting from the operation of the separation mechanism.
- The ability of the mechanism to withstand the natural and induced environments encountered during service.

The mechanism should be designed such that it can cut off the structure after which separation will occur. Two different techniques have been considered: pyrotechnic actuators and regular springs. Pyrotechnic devices make use of explosions, while springs work by unloading them at the time of separation.

Both have shown to be effective in past missions. Nonetheless, it is preferred to not use pyrotechnic mechanisms. They are extremely risky, because the amount of loose parts that is released after separation is uncontrollable, hence there is a chance of them impacting the spacecraft.

The separation will therefore be carried out by an actuator designed by NEA Electronics [78]. Their model 9103 is capable of withstanding loads up to 52 kN, making it a perfect separator to install between the orbiter and the Deimos lander, because the loads acting on the separator are at maximum 43 kN. For this load, the safety factor of 1.25 mentioned in Section 6.3.1 has been used. Between the two landers themselves model 9102G provides the best solution. This actuator can endure loads up to 26.7 kN, but this separator only needs to endure 22 kN, including the safety factor of 1.25. These actuators operate like springs. At least four springs will be used on each of the four sides to constrain the movement of the separated spacecraft.

According to Mitchell [75], the springs are an ideal separation-impulse device with a reliability in the range of 99.90% to 99.99% Despite the fact that the springs have to be loaded for quite a bit of time, this should not cause any problems. Having studied the Huygens mission, described by Meltzer [74], that landed on Titan in 2005, it can be concluded that such a system has shown its effectiveness. Another advantage concerns the relative speed between the separated spacecraft.

[1] `http://www.moog.com/products/actuators-servoactuators/space/spacecraft/solar-array-drive-assemblies.html` [Accessed on: 14 June 2017]

In conclusion, a separation mechanism that makes use of springs will be installed on the spacecraft bus. It can be implemented such that there is enough clearance between the separating bodies and a spring system has a lower shock load compared to pyrotechnic actuators (Mitchell [75]). Furthermore, springs minimise the risk of creating loose parts that could impact the spacecraft and the chosen mechanisms have proven to withstand the natural and induced environments encountered during service.

6.5. Risk Analysis

In order to give a clear overview of the possible causes of failure, a fault tree analysis for the structural subsystem has been made, which can be seen in Figure 6.3. Table 6.6 shows the risks the structural subsystem has to cope with after mitigation. The risks can be split in two categories: one that concerns the mechanisms and one regarding the overall structure of the spacecraft.

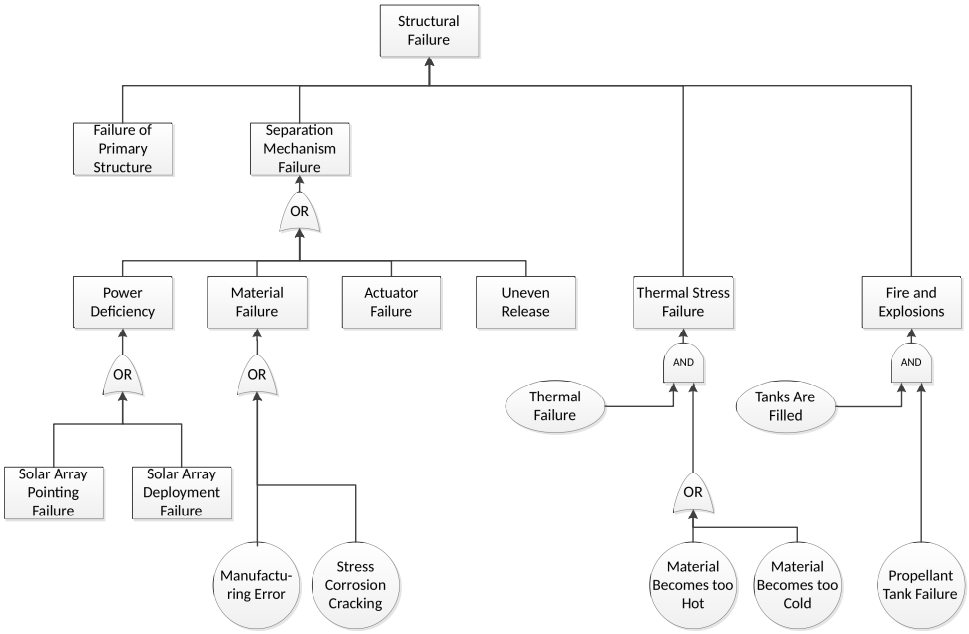

Figure 6.3: A fault tree analysis of the structural subsystem.

1. Space bus separation mechanism failure: The first category contains the solar panel deployment mechanisms and the separation mechanisms. The separation mechanism contains a set of springs to detach the spacecraft from each other. In order to have a successful separation all springs should be released simultaneously and at the right time. In case this does not happen the spacecraft either do not separate or there is a chance of impacting each other due to the misalignment of the spring forces. Unfortunately, no mitigation of this mechanism is possible, because for example redundancy would only lead to an even larger risk. Because the mechanism has a high reliability, while a failure would mean complete mission failure, this is an unlikely, but catastrophic risk.

2. Solar array deployment failure: Another mechanism that has to be analysed is the solar panel deployment system. There is a risk of not being able to deploy the solar arrays resulting in a power deficiency. To mitigate this risk, redundancy of the mechanisms will be incorporated. As the mechanisms have shown a long flight heritage, while a power deficiency would mean mission failure, this is an improbable, but catastrophic risk.

3. Solar array orientation failure: If the arrays do deploy, then there is still the risk of not being able to orient the panels correctly, which is not beneficial for the power supply either. The solution to mitigate this risk will be redundancy of the actuating mechanisms. This failure is also improbable, although it will cause a moderate risk for the mission.

4. Hypervelocity impact: Space debris and micrometeorites form a big uncertainty that has to be taken into account. Aphrodite will be equipped with shielding material that should reduce the damage of the impact. Morover, the chance that it happens is extraordinarily low. Therefore its likelihood is set to improbable and its impact to moderate.

5. Unforeseen stress concentrations: Continuing with the overall structural risks, stress concentrations are a major uncertainty. At each location where multiple structural members join into one, stress concentrations occur. As these are hard to model, a safety factor of 1.25 has been taken into account. According to Wertz and Larson [128] this is a proper factor, due to the possibility of being able to test the spacecraft structure. The chances of unforeseen stress concentrations to occur is improbable, but its impact is critical.

Table 6.6: Mitigated risk map of the structural subsystem.

Almost certain					
Likely					
Average					
Unlikely					1
Improbable			3,4	5	2
Likelihood / **Impact**	Negligible	Marginal	Moderate	Critical	Catastrophic

6.6. Sensitivity Analysis

To check the robustness of the structural subsystem a sensitivity analysis is conducted. In Table 6.7 the results are presented. The table shows the margins of safety, the required skin thickness and the weight of the current design after a weight increase of 10%. It can be seen that it is only required to add 0.02 mm in order to have a positive margin of safety. This is an increase of less than 1.2%.

Table 6.7: Structural sensitivity analysis in case of a final mass increase of 10%.

Spacecraft	**Current Design**			**Including Additional Mass**			
	MS [%]	**Thickness** [mm]	**Mass** [kg]	**MS** [%]	**Thickness** [mm]	**Increase** [%]	**Mass**[kg]
Orbiter	7.3	1.7	132	0.4	1.72	1.18	133.4
Landers	20.3	0.8	11.6	9.4	0.8	0	11.6

If the total mass of the bus would exceed the maximum payload mass the Falcon 9 can deliver to Mars (SpaceX [109]), it has to be checked whether the structure can cope with the accelerations and vibrations caused by a different launcher. It has been agreed upon that the Falcon Heavy will be used in that case. Knowing that heavier launchers usually induce lower accelerations, the structure should be able to handle these loads. As shown in the report by Leadbetter [65], the Saturn V, for example, exerts an axial acceleration on its payload of only 3.5g, which is slightly more than half of the 6g created by the Falcon 9. Besides, Ryan et al. [97] shows that the launch frequencies of the Saturn V are 5.3 Hz, both in axial and lateral direction.

[This page is intentionally left blank]

7
Landing on the Martian Moons

This chapter discusses the landing subsystem of the two landers on Phobos and Deimos. The landing subsystem is responsible for the descent and anchoring of the landers to the Martian moons. Section 7.1 provides an overview of the complete subsystem along with the key budgets. The functions and the requirements of the subsystem are defined in Section 7.2. The design philosophy, motivation and approach is outlined in Section 7.3. Section 7.4 describes the landing site selection procedure for the Martian moons. Section 7.5 and Section 7.6 characterise the descent stage of the lander while incorporating hazard avoidance. The anchoring procedure and mechanisms are characterised in Section 7.7. Section 7.8 and Section 7.9 portray the risk and robustness of the subsystem design. Since two landers are deployed on Phobos and Deimos, *OPS-DEP-ST-27* is satisfied.

7.1. Design Overview

This section provides an overview of the design of the landing subsystem. A landing site is selected in Section 7.4 which maximises probability of smooth and well lit terrain with line of sight to Mars. A descent trajectory is optimised for landing on the chosen landings sites in Section 7.5. LIDAR, doppler LIDAR and optical cameras are chosen for hazard detection during descent in Section 7.6. A harpoon and foot screw system is designed in Section 7.7 to ensure anchoring over a wide range of surface toughness. The hardware and their budgets of the landing sub-system are presented in Table 7.1.

Table 7.1: Landing hardware for the landers.

Hardware component	**Number** [-]	**Total Mass** [kg]	**Power** [W]	**Section**
Camera	4	1	10	7.6
Flash LIDAR	1	6.5	50	7.6
Doppler LIDAR	1	8.1	30	7.6
Harpoon	3	4.5	52.5	7.7
Foot screw assembly	3	6.3	9	7.7
Landing legs	3	4.2	0	6.3.5
Total		**30.6**	**151.5**	

7.2. Functional Analysis

The functions of the landing subsystem are divided into two key modes:

Mode 1: Descent mode

The descent mode comprises the operations undertaken from an altitude of 10 km to the landing site on the surface. This mode is also responsible for active hazard detection and avoidance. This is achieved by using a variety of sensors and ADCS hardware.

Mode 2: Anchoring mode

The anchoring mode ensures that the lander is secured to the surface after descent. This is ensured via the firing and sequential pull back of the harpoons. The design and the subsequent performance of this function is largely dependent on the surface properties of the moons. Additionally, this mode also incorporates foot screws which dig into the surface and ensure long term stability. The requirements for which the landing system is designed are listed in Table 7.2.

7.3. Design Approach

The design philosophy of the landing subsystem is largely driven by reliability and risk minimisation. The first step in the design is the landing site selection for Phobos and Deimos, performed in Section 7.4. The first

Table 7.2: Landing subsystem requirements.

ID	Requirement	Section	Compliance
OPS-DEP-S-10	**[Driving requirement]** The system shall be safely deployed on the planetary body.	7.1	✓
OPS-DEP-S-11	The landing procedure of the system shall be autonomous.	7.5	✓
OPS-DEP-S-12	The system shall land within the target area.	7.5	✓
OPS-DEP-S-13	The system shall be able to measure horizontal velocity with an accuracy of 0.05 m/s.	7.6	✓
OPS-DEP-S-14	The system shall be able to measure vertical velocity with an accuracy of 0.05 m/s.	7.6	✓
OPS-DEP-S-15	The system shall land with a maximum horizontal velocity of 0.05 m/s.	7.6	✓
OPS-DEP-S-16	The system shall land with a maximum vertical velocity of 0.15 m/s.	7.6	✓
OPS-DEP-S-17	The system shall be able to detect and avoid boulders larger than 0.3 m.	7.6	✓
OPS-DEP-S-18	The system shall be able to detect and avoid craters larger than 0.5 m.	7.6	✓
OPS-DEP-S-19	The system shall be able to detect slopes with an accuracy of 5°.	7.6	✓
OPS-DEP-S-20	The system shall be able to detect terrain roughness with an accuracy of 0.1 m.	7.6	✓
OPS-DEP-S-21	The system shall be able to measure altitude with an accuracy of 0.25 m.	7.6	✓
OPS-DEP-S-22	The system shall be able to measure its orientation with respect to the surface with an accuracy of 1°.	7.6	✓
OPS-DEP-S-23	The system shall be able to identify a safe site of at least 10 m × 10 m.	7.6	✓
OPS-DEP-S-24	The system shall have a reliability greater than 97%.	16.2	✓
OPS-DEP-S-25	The system shall be able to provide a hold-down thrust of at least 10 N.	7.7	✓
OPS-DEP-ST-26	**[Driving requirement]** The system shall have a stability better than 0.1 m over the mission duration after landing.	7.7	✓
OPS-DEP-ST-27	**[Driving requirement]** A lander system shall be deployed on Deimos and on Phobos.	7.1	✓
OPS-DEP-ST-28	The anchoring system shall be able to perform at surface toughness ranging from 100 kPA to 10 MPa.	7.7	✓
OPS-DEP-S-29	The landing site shall be at least 1 km wide and 1 km long.	7.4	✓

step is identification of constraints that need to be taken into account. These are power, line of sight to Mars and surface properties. Using previously mapped data and simulations of the defined constraints, an optimal landing site is chosen. These landing site considerations have also been used in Section 6.3.5.

For the descent stage (Section 7.5), constraints for landing are identified that the hazard detection and avoidance system (Section 7.6) needs to satisfy. After identification and quantification of these constraints, an optimisation simulation is run to predict the required thrust and burn time for landing.

For the anchoring stage of the design, the physical properties of the surface are characterised. Using this data, harpoons and foot screws are designed to ensure surface penetration and anchoring stability for a range of surface toughness. This is described in Section 7.7.

7.4. Landing Site Selection

The landing site selection of the moons is based on three major parameters. The first parameter is energy. Due to the eccentricity of the Martian orbit, the solar radiation intensity varies by up to 46% between seasons as seen in Figure 7.1. The radiation intensity is lowest during Northern Summer and highest during Northern Winter. As the subsystems have to be designed for the worst case scenario, it is preferable to have a landing site with the least variance in radiation intensity along the year.

The second parameter is line of sight from the lander to Mars, Earth and the second lander. As the moons are tidally locked, there is a side that always faces Mars.[1] Therefore, apart from high (>60°) latitudes, Mars is visible from a significant part of the moons, as observed in Figure 7.2a and Figure 7.2b. The view from one Martian moon to the other Martian moon and Earth can only be blocked when Mars is in the way. As the orbital period of the three bodies varies significantly and given the relatively large communication windows analysed in Section 4.4, the line of sight blocked by Mars and the Sun should not be a limiting factor.

The third parameter that influences the landing site is surface properties. The surface properties may include craters, ejecta and boulders. It is necessary to select a smooth landing site for a reliable landing.

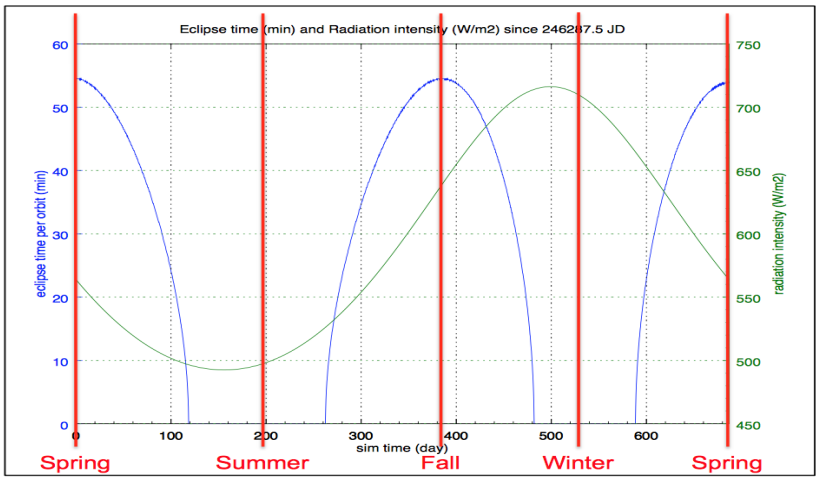

Figure 7.1: Radiation intensity on Phobos across all seasons. The seasons are defined from the perspective of the northern hemisphere (Li et al. [67]).

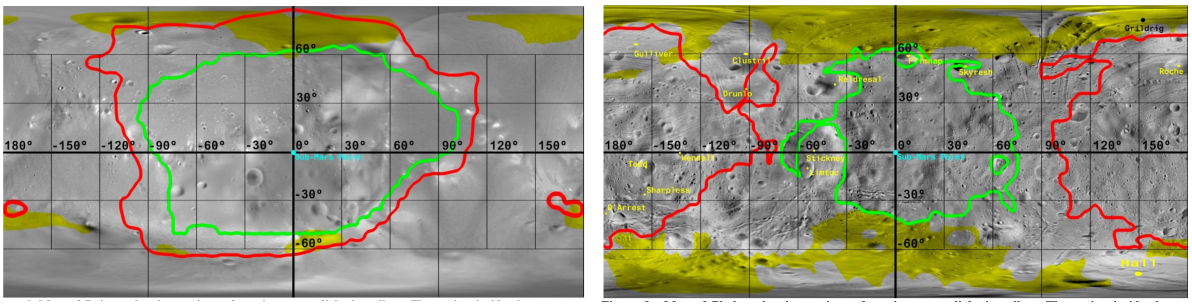

(a) Visibility of Mars from Phobos' surface.

(b) Visibility of Mars from Deimos' surface.

Figure 7.2: Visibility of Mars. The green boundary represents the areas with a complete view to Mars and the red boundary represents the areas with a partial view to Mars (Hopkins and Pratt [52]).

7.4.1. Phobos Landing Site

In the report by Li et al. [67], it is determined that 15° to 20° latitude has the most consistent amount of energy. This is done by making a state model of Sun, Mars, Phobos and Earth and measuring the sunlight duration and solar intensity for eleven different landing sites. The energy data from the report is not directly used because of the difference in assumptions about solar panel efficiency and solar panel pointing capacity [67]. From Figure 7.2a, it is determined that Mars is visible from −30° to 60° longitude. A detailed database of the location and sizes of all the observed craters of Phobos is used to model all craters in and around the region of interest as seen in Figure 7.3.[2] Craters as small as 5 m have been mapped using the Mars Global Surveyer as elaborated by Kuzmin et al. [62].

[1] `https://www.nasa.gov/mission_pages/MRO/news/mro-20080409.html` [Accessed on: 23 June 2017]
[2] `http://cartsrv.mexlab.ru/geoportal/` [Accessed on: 25 June 2017]

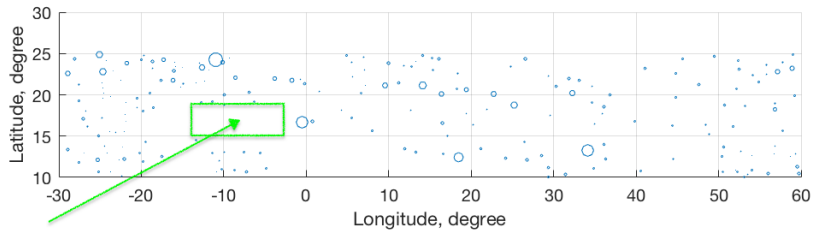

Figure 7.3: Crater map of Phobos's surface. The circles represent the craters. The green box represents the landing zone.

Therefore, in order to land on a smooth surface, a landing site sufficiently far away from craters is chosen as seen in Figure 7.3. Additionally, boulders are usually located on the rims of craters as expressed by Kuzmin et al. [62]. Therefore avoiding craters is the best indication of avoiding boulders as a detailed map of the location of boulders is not yet available. Figure 7.4 also confirms that the current landing zone avoids the Stickney ejecta blanket. Lastly, the slope of the surface is taken into account. Figure 7.5 shows the landing site and mapped surface slope of Phobos's surface. This slope map is made using dynamic height model made for irregular small bodies. As the gravitational parameters of Phobos are quite uncertain, the validity of this model is limited. Given that this model was used for landing site analysis in Phobos-Grunt, it is deemed as a good starting point [62]. It is determined that the lander should be capable of landing at slopes up to 25° from Figure 7.5.

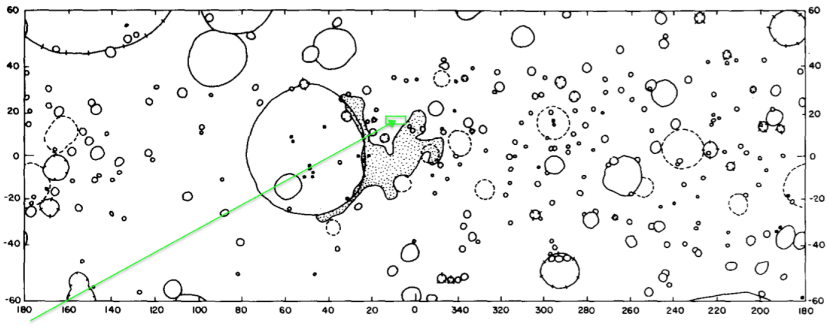

Figure 7.4: The dotted region represents Stickney ejecta blanket on Phobos's surface. The green box represents the landing zone (Thomas [117]).

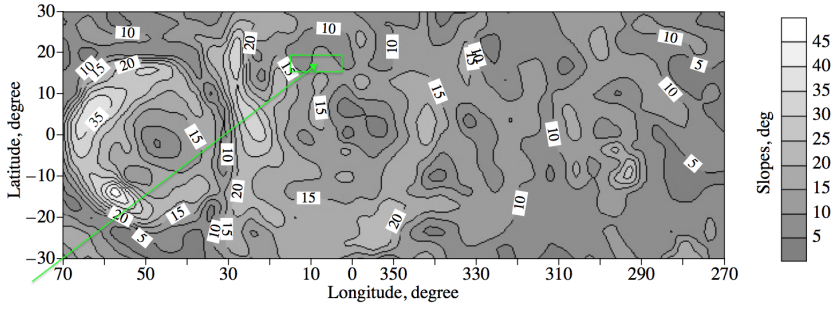

Figure 7.5: Surface slope on Phobos' surface. The green box represents the landing zone (Thomas [117]).

A landing site at −8.5° longitude and 17° latitude is chosen, as can be seen in Figure 7.3. The landing zone extends from −14° to −3° longitude and from 15° to 19° latitude which results in a landing area of approximately 2 km wide to 1.6 km long.

7.4.2. Deimos Landing Site

Unlike Phobos, direct information about Deimos is not widely available. As the inclination difference between Phobos and Deimos is not high, it is assumed that the 15° to 20° latitude on Deimos has the most consistent

power as well.

As a detailed directory of Deimos is not publicly available, the crater map from Thomas [117] is used to determine a lading site. As observed in Figure 7.2b, the entire Martian surface is visible from −90° to 90° latitude. Moreover, no data regarding slopes for Deimos is available, therefore the hazard avoidance system will actively identify the slopes in the landing zone and choose a site with a slope of less than 25°. A higher margin for propellant is taken for the descent on Deimos due to limited information.

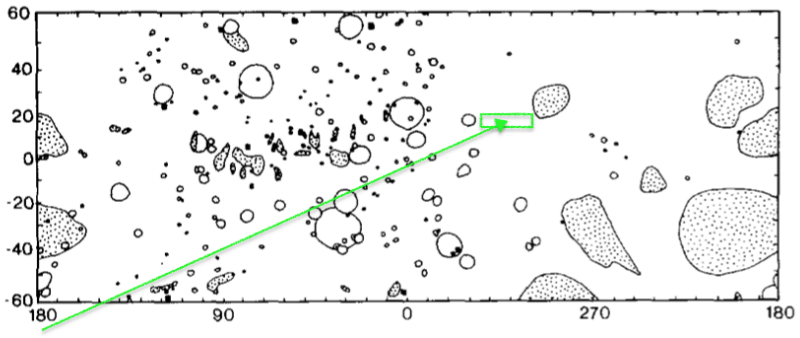

Figure 7.6: Crater map of Deimos' surface. The green box represents the landing zone.(Thomas [117])

A landing site at location 46.5° longitude and 17.5° latitude is chosen as seen in Figure 7.6. Deimos seems to be relatively smooth as compared to Phobos. The landing zone extends from 33° to 60° longitude and from 15° to 20° latitude. This results in a landing zone of approximately 2.9 km wide to 1 km long.[3] As a final consideration, there are no craters in the higher or lower latitudes for the selected longitudes. Therefore those sites may be used as contingent landing sites.

7.5. Descent Trajectory

As described in Section 5.2.13, it takes 39 and 51 hours for the Phobos and Deimos landers respectively to reach 10 km above the surface of the Martian moons. The landing sequence for the landers begins at 10 km above the surface of the moons. Given the long duration of this transfer, it is necessary to deploy the solar panels. However the solar panels are retracted at the beginning of the landing sequence as described in Section 6.4.1 to prevent any damage to the panels upon landing.

An important part of the landing sequence is the plotting of a landing trajectory. A preliminary landing trajectory has been determined, optimised for minimal acceleration. Due to the use of hazard detection this trajectory may still change, especially near the end of the trajectory, since the determined landing site might not be feasible for landing at all.

In order to determine the optimal trajectory, in terms of fuel consumption and thus weight, use is made of a paper by Pingyuan et al. [86] to construct an algorithm. A few assumptions are made while creating this algorithm. The main assumption is the fact that the gravity gradient is assumed to be zero throughout the complete trajectory. Since the gravity of both Phobos and Deimos is very low (<0.006 m/s^2), this assumption is valid for landing on the moons. No other disturbances have been modelled, since these are unpredictable for the moons and their effect is small on the relatively short time span of the landing sequence. The algorithm incorporates a numerical integration of the equations of motion, using the Runge-Kutta method and models the targeting of the landing site as a convex optimisation problem.

In this problem, the sum of all accelerations is minimised, while the end position is set to the landing site and the end velocity is set to zero at touch-down. Linear constraints have been added to the convex problem in order to limit the velocity during the final ten seconds before touch-down. In order to ensure a soft landing, the trajectory has been constrained to have a final velocity of under 0.15 m/s. This will ensure a successful soft landing with minimal chances of bouncing off the surface. The convex problem is solved using SDPT3 algorithm implemented in CVX, Matlab software for Disciplined Convex Programming.[4] The obtained trajectory is only an indication, used to estimate the required fuel mass. The actual trajectory will slightly vary due to unmodeled disturbances and can still greatly vary due to required hazard avoidance which should happen fully autonomously.

[3] `https://solarsystem.nasa.gov/planets/deimos/facts` [Accessed on: 2 July 2017]
[4] `http://cvxr.com/cvx/` [Accessed on: 5 June 2017]

The resulting optimal landing trajectory for Deimos is shown in Figure 7.7. Note that in this trajectory, the origin is the targeted landing spot. The graphs of the accelerations and velocities in x-, y- and z-direction are shown in Figure 7.9. The most fuel-efficient trajectory consists of a long burn at the beginning of the descent trajectory and another long burn at the end of the trajectory. This is a result that can be expected when no gravity and no other disturbances are present in the model. The acceleration in the z-direction includes some impulse burns at the end of the trajectory to comply to the velocity constraints. The total Deimos landing trajectory takes approximately 3000 seconds and uses a total of 2.87 kg of propellant. The optimal trajectory for Phobos is similar. The acceleration and velocity profiles are shown in Figure 7.10 and the trajectory is shown in Figure 7.8. The trajectory is different due to the different initial conditions. The total landing sequence takes approximately 8000 seconds with a total propellant mass used of 7.23 kg.

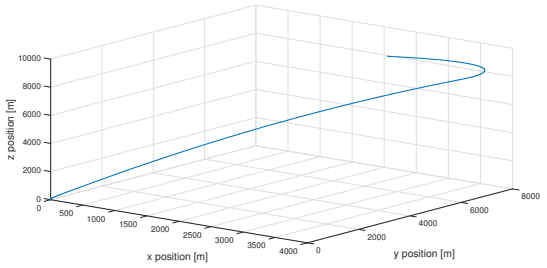

Figure 7.7: The landing trajectory to Deimos.

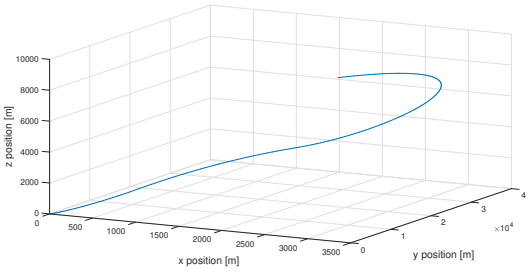

Figure 7.8: The landing trajectory to Phobos.

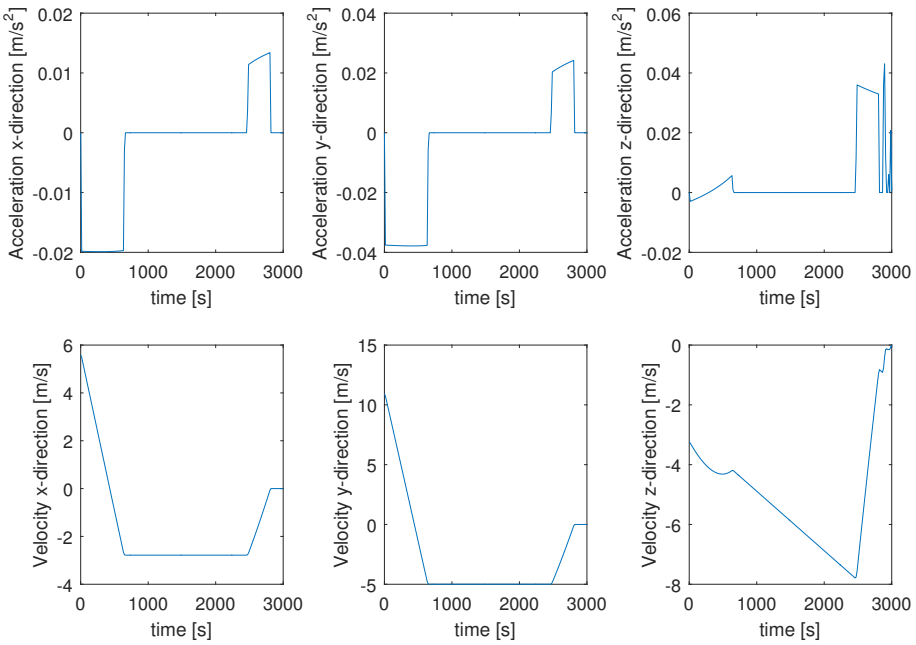

Figure 7.9: Acceleration profiles and velocity profiles for landing on Deimos.

Landing on a micro-gravity body is risky and it is probable that even with all the redundancies in place, the lander bounces. If the lander does bounce, it has to be able to return to the original landing site or select a new site autonomously. For this, a contingency is put in place to ensure a second safe landing. As described by Pingyuan et al. [86], the lander will make use of an intelligent landing strategy, to be deployed when bouncing of the spacecraft is detected. This intelligent strategy includes a burn immediately after bouncing, in order to ensure a controlled ascent above the surface, rather than uncontrolled bouncing and tumbling. This control algorithm adapts the burn strategy to the current state measurements in order to optimise the trajectory for risk and fuel. Secondly, some time after the lander has bounced, a second landing sequence will be initiated,

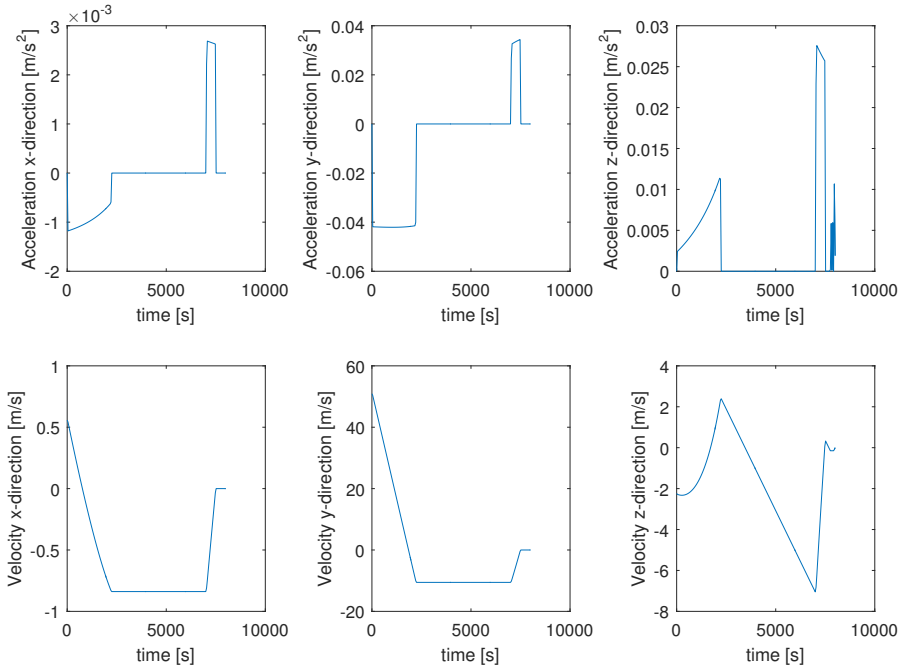

Figure 7.10: Acceleration profiles and velocity profiles for landing on Phobos.

Table 7.3: Verification landing simulation.

Initial velocity [m/s]	**Simulation transfer distance** [m]	**Expected transfer distance** [m]	**Error percentage [%]**
1.52	104	100	3.8
1.56	300	280	6.7

either towards the same nominal landing site, or towards a secondary landing site. The additional propellant mass needed for the first burn and the consecutive second landing manoeuvre on both Phobos and Deimos is estimated to be the same as the mass for the original landing sequence. This doubles the fuel mass and it might be over-designed, but since the surfaces of both bodies are still unexplored, this is deemed necessary in order for the lander to complete a successful second landing trajectory.

This module is verified by changing the inputs and seeing if the output corresponds to the expected result. From Pingyuan et al. [86], it is found that the transfer distance varies almost linearly with the initial velocity. Comparing the simulation output to the expected linear output in Table 7.3, the program is verified. The module is validated by replicating the landing trajectory presented by Pingyuan et al. [86] for asteroid 1620 Geographos. The results of the simulation are compared with the results in [86] in Table 7.4.

7.6. Hazard Detection and Avoidance

Hazard detection and avoidance (HDA) can be classified as the most crucial phase during landing. During this phase the landing site is evaluated to determine the possibility for safe landing. Since Phobos and Deimos have been barely mapped, as explained in Section 7.4, the HDA system will fulfil a crucial role in the active selection of a landing site to ensure successful mission operations for the required mission lifetime.

There are several desired outputs which the HDA system needs to provide. First of all it needs to give

Table 7.4: Validation of the landing simulation.

Parameters	**Simulation**	**Source**	**Error percentages [%]**
Fuel mass used [kg]	1.49	1.45	2.7
Transfer time [s]	300	290	3.3
Maximum velocity peak [m/s]	(0.22,0.89,0.13)	(0.21,0.89,0.12)	(4.5,0,7.7)

information about the hazards at the landing site. These include slope (terrain-relative), roughness, boulder and crater distribution and size and height or elevation. From these features the system should be able to create a dense elevation map (DEM). Secondly, the system needs to provide the navigation system with information about the altitude/position and velocity of the spacecraft so that the spacecraft can perform terrain relative navigation. Finally, it should provide a terrain relative attitude to ensure a correct attitude at landing.

In terms of availability of HDA systems, the most important choice is active versus passive HDA. Both have the capability of performing hazard detection during landing. Active sensors however, are (in some cases) more accurate, at the cost of being more expensive. In order to ensure a robust hazard detection system the choice is made to equip the spacecraft with both active and passive means of hazard detection.

Passive sensors are (nearly) always cameras, while active sensors can be LIDAR or radar. Cameras come in many different forms and sizes but all function in the same way. LIDAR and radar however can be split up into two types: ranging type, which provides distances and sizes, and Doppler type, which provides velocity and orientation.

For ranging LIDAR (and radar) an additional choice has to be made. The choice is between the use of scanning LIDAR or flash LIDAR. Scanning LIDAR uses a beam that travels over a 2D array pixel per pixel and afterwards puts together these measurements. Flash LIDAR uses a beam with the width of the entire 2D array and uses a single pulse to map the entire area. Some advantages of flash LIDAR are speed (entire scene mapped at once), low risk (no moving parts) and lower mass (no actuators). Considering these advantages, the choice is made to only look at flash LIDAR for ranging type LIDAR.

Table 7.5 shows the required accuracies on the different parameters which the HDA system needs to meet. In addition, Table 7.6 shows four different hazard detection systems which have been under consideration, one passive (camera) and three active (flash LIDAR, Doppler LIDAR, radar), and compares these systems in terms of their ability to meet the requirements. Radar Doppler has been included in radar to simplify the overview.

Table 7.5: Performance characteristics for the HDA system.

Feature	Requirement	Accuracy	Reason / Requirement Origin
Slope	< 25°	5°	Landing site selection
Roughness	< 0.15 m	0.10 m	Lander ground clearance
Boulder size	< ⌀ 0.3 m	0.30 m	Lander ground clearance
Crater size	< ⌀ 0.5 m	0.30 m	Landing leg design
	< 0.15 m depth	0.10 m	Landing leg design
Altitude	< 0.25 m	0.25 m	Landing leg design
Attitude	< 2° relative to gravity	1°	Soft landing
Velocity	0.15 m/s vertical	0.05 m/s	Soft landing
	0 m/s horizontal	0.05 m/s	Soft landing
Safe site	> 10x10m	1 × 1 m	Field of View (FOV) at 200m

Table 7.6: Evaluation of camera, LIDAR and radar HDA systems in terms of requirements.

	Camera		Flash LIDAR		Doppler LIDAR		Radar	
	Ability	Accuracy	Ability	Accuracy	Ability	Accuracy	Ability	Accuracy
Slope	✓*	✓	✓	✓	X	-	✓	✓
Roughness	✓*	✓	✓	✓	X	-	✓	X
Boulder size	✓	✓	✓	✓	X	-	✓	✓
Crater size	✓	✓	✓	✓	X	-	✓	✓
Altitude	✓*	(✓)	✓	✓	✓	✓	✓	X
Attitude	✓*	(✓)	X	-	✓	✓	X	-
Velocity	✓*	(✓)	X	-	✓	✓	✓	X
DEM	✓*	-	✓	-	X	-	✓	-

Accuracy is assessed at an altitude of 700-1000m.
* - only with additional data processing using an algorithm.
The brackets indicate that at least one or two of these parameters should be known to compute the other.
Sources: Camera [51, 132], LIDAR [4], Radar [41, 89].

Based on this performance evaluation, the choice is made to equip the lander with a combination of two cameras, a flash LIDAR and a Doppler LIDAR. From Table 7.6, it becomes clear that this combination provides a fully redundant system for all requirements. The use of multiple sensors also increases robustness and reliability of the HDA system.

The strong feature of the camera is its high resolution (compared to LIDAR and radar), which makes it very precise when determining locations and size of boulders and craters. However, regions with higher slopes might be undetectable because of limited lighting conditions. This is also the main disadvantage of using a camera, it

can only operate in combination with an external source of light. It was checked that the landing will take place in the light, thus a camera can be used.

The strength of the (flash) LIDAR is in its high resolution, which becomes important at low altitudes (<1000 m). At these altitudes the smaller hazards, which include small rocks and craters must be detected with high precision. The main benefit of adding the LIDAR sensor to the camera is the fact that, contrary to the camera, the LIDAR can operate in any lighting condition. Additionally, using the Doppler LIDAR provides high accuracy on velocity and attitude (Amzajerdian et al. [5]).

It was decided to drop radar since this is uncommon for planetary landings and also from Table 7.6, it can be seen that using a camera and both types of LIDAR already creates a fully redundant system. Next to that the radar also has a rather coarse resolution, making it unsuitable for detection of small hazards except at low altitudes. For these reasons, radar was not used in the HDA system.

The final equipment chosen to provide the HDA system on the lander is summarised in Table 7.7. All HDA equipment should be mounted on the bottom of the spacecraft, where it has an unobstructed view to the ground. The chosen HDA systems meet the requirements which were set in Table 7.5

Table 7.7: Specifications of the selected hazard detection systems to be used on the Aphrodite mission

	Camera (x2) ECAM-C50 [91]	**Flash LIDAR (x1) SOLID GoldenEye**[a]	**Doppler LIDAR (x1) ALHAT Doppler LIDAR** [5]
Mass [kg]	0.256	6.5	8.1
Dimensions [cm × cm × cm]	7.8 × 5.8 × 4.4	14.5 × 21.6 × 14	28 × 22 × 20
Power [W]	2.5	<50	30
Position Error [m]	-	0.1	0.3
Velocity Error [m/s]	-	-	0.002
FoV [°]	25	3	1-5
Number of Pixels [-]	2650 × 1944	128 × 128	128 × 128
Max altitude [m]	-	3000	1400

[a] `http://www.advancedscientificconcepts.com/products/portable.html` [Accessed on: 6 June 2017]

The choice of camera and LIDAR equipment as presented in Table 7.7 leads to some useful conclusions. Using the field of view (FOV) of the equipment and the amount of pixels, a quick calculation, using simple geometry, can be performed to check the altitudes at which hazard detection will be useful.

In Table 7.5, the requirements for crater size (0.5 m) and boulder size (0.3 m) were defined, and combining these with field of view and pixel size, an altitude at which the camera and LIDAR are able to detect these features, can be defined. This is at an altitude of 1795 m for the camera and 731 m for the LIDAR. This means that this equipment will become useful from these altitudes downward. At these altitudes the camera still has a complete view of 795 m × 585 m and the LIDAR has a complete view of 38 m × 38 m.

Especially the fact that the camera will already be able to identify boulders of the size set by landing requirements at nearly 2 km will allow enough time to take evasive action, should the landing site be deemed unfeasible by the HDA system. Some further research is, however, required into the course of this evasive action and thus it will not be treated further.

7.7. Anchoring

The anchoring mechanisms will ensure that the lander is secured to ground upon contact and does not bounce off. It also ensures the stability of the lander over the operational duration of eight years.

7.7.1. Surface Composition and Properties

While the exact surface properties of Phobos and Deimos remain a mystery, Kuzmin et al. [62] suggest that the entire surface of Phobos is covered with at least 2 m thick layer of regolith. It is assumed that Phobos and Deimos have similar surface properties. The estimated density of the regolith is between 1 to 2 g/cm^3 [62]. There is significant cohesion between the regolith due to high internal friction angle in the regolith. Cohesion inside the regolith leads to higher surface toughness and higher resistance in pulling out the anchors. Unfortunately, no data with respect to the surface toughness of Phobos is available. As the top layer of the surface is filled with regolith, the surface toughness is expected to be in the order of hundreds of kPa. However, according to Biele et al. [16], it was observed in the landing of Philae that the surface toughness varied by multiple orders of magnitude from soft damping surface 80 kPa to 4 MPa. Therefore, given the uncertainty of the surface properties of the moons, the anchoring mechanisms should be capable of performing on a wide range of surface

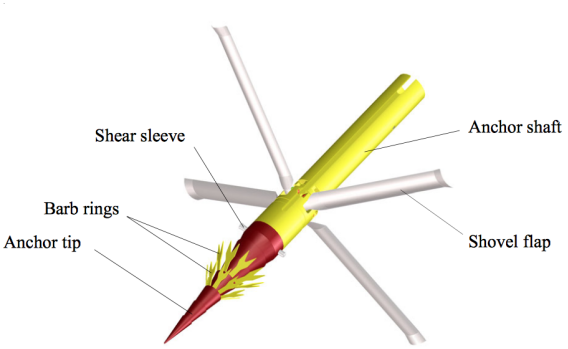

Figure 7.11: Philae harpoon with deployed shovel flaps (Thiel et al. [116]).

toughnesses.

7.7.2. Harpoons

In order to secure the lander to the surface, harpoons are designed. The design of the harpoon is taken from Philae on which certain mission specific modifications are made. The harpoon of Philae was designed to perform at a target material toughness in the range of 300 kPa to 5 MPa as mentioned by Thiel et al. [116], which is similar to the order of magnitude of surface toughness expected at Phobos and Deimos.

The Philae harpoon system consists of a copper beryllium projectile, a gas generator, a cable magazine and a rewind system (Thiel et al. [116]). The base design for the harpoon is exactly the same as the design for Philae. The projectile as seen in Figure 7.11 also includes stainless steel barb rings. These rings provide extra surface traction when tension is applied on the cable connected to the projectile. It can be observed in Figure 7.11 that the cone is discretised into multiple sections. This is done to ensure traction in the case of partial penetration.

Additionally, the projectile includes wide shovel flaps. The function of these shovel flaps is to prevent the harpoon from penetrating the surface deeper than intended. The harpoon system also incorporates a cable brake to slow down the projectile in the event of a soft surface. All moving components inside the harpoon system are coated with molybdenum disulfide to prevent excessive friction [116].

The pyrotechnic gas generator pushes out the projectile at 90 m/s. After the projectile has penetrated into the surface, the the rewind motors pull the cable attached to the projectile in force of small increments. The cable is 1.5 m long so that the projectile does not drag the lander. The maximum tension on the cable is identified by ensuring that the cable tension does not pull out the projectile. Once the maximum tension, up to 30 N, is achieved, the cable is locked using a clutch mechanism. The maximum tension achievable from a penetrated projectile is refereed as the pull back force. This clutch can be released and the cable tension can be increased or decreased on command.

The key differences are the shape and size of the projectile, the gas generator and the type of cable used. The mass of the entire system is, however, kept constant and any differences are considered to be within the margin. Therefore the mass of each harpoon system, inclusive of its lander interface and control electronics, is estimated to be 1.5 kg. The differences and their rationale are described below in their respective order.

In order to ensure redundancy, three harpoons are designed for each lander. A single harpoon should be enough to hold down the lander. The pull back force is proportional to the surface toughness, projectile diameter and penetration depth. Therefore low diameter projectiles will have less pull back force in scenarios with low surface toughness. In order to increase the effective range of operation of materials, the diameter of the harpoons is varied. The mass of 0.1 kg and the ejection velocity of 90 m/s is kept constant.

The cone angle changes according to the change in diameter as seen in Table 7.8. Liu et al. [70] suggest that for angles lower than 45° conical shape provides the least resistance to penetration. Changing the diameter varies the pressure on the tip and hence varies the displacement length of the projectile. The final configuration of the three projectiles is mentioned in the Table 7.8.

The resistance force from the surface for the three configurations is calculated using Equation 7.1, which is retrieved from report by Steltzner and Nasif [112].

Table 7.8: Properties of the harpoon configurations.

Configuration	**Mass of Projectile** [kg]	**Diameter** [cm]	**Length** [cm]	**Cone Angle** [°]	*N* [-]
1	0.1	1.5	12.6	3.4	0.004
2	0.1	2	7.1	8.1	0.020
3	0.1	2.5	4.5	15.4	0.071

$$F = \pi a^2 \left(D + \rho N v^2\right) \tag{7.1}$$

$$\frac{1}{2} m v^2 = F d \tag{7.2}$$

where F is the resistance offered by the surface in N, a is the radius of the projectile in m, D is the surface toughness in Pa, ρ is the density of the surface in kg/m^3, N is a dimensionless property based on the conical angle and v is the velocity of the projectile in m/s. The diameter and N value of the three configurations can be found in Table 7.8. The force varies as the projectile penetrates, but at this stage using a model with constant force provides sufficient information. According to Kuzmin et al. [62], the surface density of Phobos can vary from 1000 to 2400 kg/m^3. In order to calculate the worst case scenario for surface penetration, a surface density of 2400 kg/m^3 is chosen. The velocity used for all configurations is 90 m/s. The value of surface toughness is varied from 100 kPa to 10 MPa. The resultant penetration depth is calculated using the Equation 7.2, in which m is the mass of the harpoon in kg and d is the surface penetration of the harpoon in m.

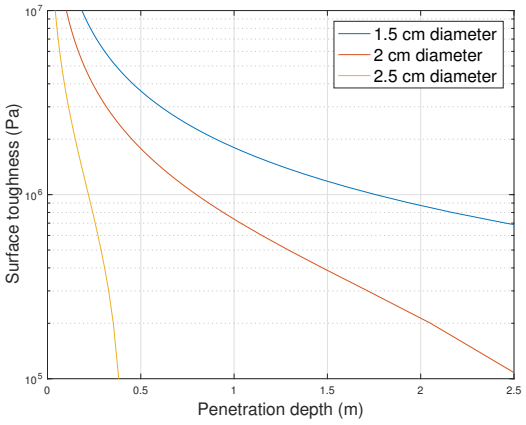

Figure 7.12: Material toughness versus the penetration depth.

Figure 7.12 shows the respective displacement of the three configurations. The harpoons are fired in the order of the configurations as lower cone angle ensures higher penetration. The pull back force of the projectile is represented by the force needed to move a cylinder the diameter of the projectile. Unfortunately, no simple method for the pull back force prediction could be identified. The data from Philae is used to identify the lower bounds of the pull back force of 30 N. According to Kuzmin et al. [62], cohesion of the particles in regolith on Phobos is significant, which increases the pull back force by a significant amount as demonstrated by Liu et al. [70].

The gas generator of the Philae harpoons failed due to the degradation of nitro-cellulose because of contact with partial vacuum and space based radiation.[5] Therefore the 103377-500 Space Standard Initiator from Pacific Scientific is chosen as a gas generator. It has a wide range of operating temperatures from −162 to 145 °C. It can be custom made for the size needs of this mission. Moreover, it is space qualified and has a reliability of 99.99%.[6] As no mass is currently available for the gas generator, it is assumed that the mass is similar to the redundant gas generation system designed for Philae.

In order to achieve high reliability, a steel cable of 0.5 kN was selected on which the maximum pull back forces are only 6% of the ultimate load. Steel cables perform well under low temperatures and do not display significant creep properties at lower loads. Note that if significant displacement of the harpoon is measured by the motor before 30 N, the tensile force is relaxed to 10 N. Upon touchdown, RCS thrusters fire for 5 s in order to

[5] Obtained via email from Dr. Günter Kargl,Space Research Institute, Austrian Academy of Sciences, Graz, Austria

[6] `https://psemc.com/products/pyrotechnic-initiators/103377-500-space-standard-initiator` [Accessed on: 25 June 2017]

prevent the lander from bouncing from the reaction force of the harpoons. The Philae design demonstrated that a reaction force of 5 N was sufficient for the reaction force of similarly sized harpoons. The thrusters can fire up to 10 N, which is considered sufficient to hold down the reaction force of the harpoons on the lander.

7.7.3. Foot Screws

The foot screw assemblies are mounted on the pad of the landing legs. The foot screws are servo actuated. Their operational range of surface toughness is much lower as it is dependent on the torque provided by the actuator, which is 90 N m.[7] Therefore, it can be estimated that they operate at a surface toughness in the order of hundreds of kPa and not MPa. Unfortunately, a complete surface toughness versus penetration depth for the foot screw cannot be performed at this stage. The foot screws are only meant to provide anchoring for long term stability, therefore they will be activated after the harpoons have fired. The foot screws are 5 cm long, 2 cm wide and have a helical shape similar to wood screws. The foot screws are also made of copper beryllium because of its hardness. The mass of each servo is 1.6 kg and the mass of the foot screw and its interface is estimated to be 0.5 kg. Using a combination of harpoons and foot screws, the landers will not move during the operational life, even when subjected to the tidal accelerations on Phobos, which can reach up to a quarter of Phobos's gravitational acceleration. Therefore, it is shown here that the system complies with requirement *OPS-DEP-ST-26*.

7.8. Risk Analysis

This section details the risks that can be expected when landing on the Martian moons. The fault tree analysis is presented in Figure 7.13. This section also classifies the likelihood and impact of the risks on the mission. Mitigation strategies are developed when possible and necessary to accommodate these risks.

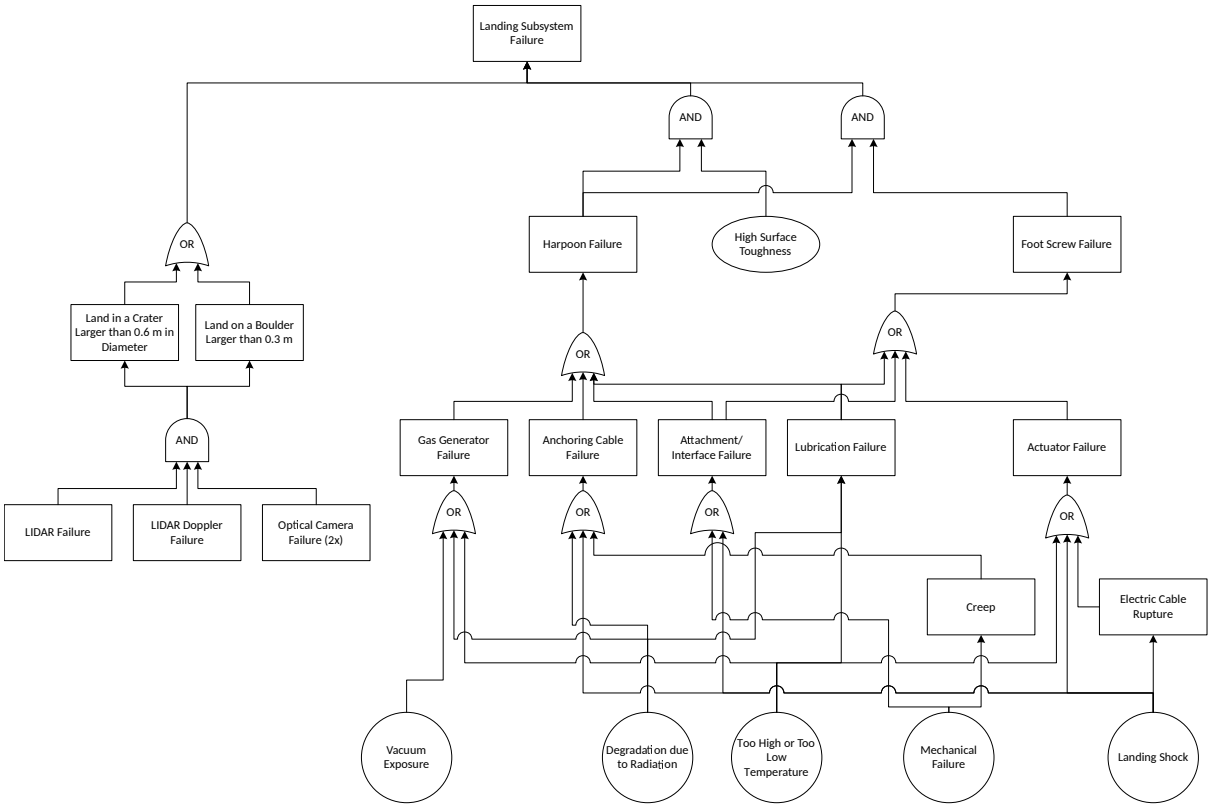

Figure 7.13: Fault tree analysis of the landing subsystem.

1. Craters: According to Basilevsky et al. [13], the depth to diameter ratio of craters on Phobos varies from 0.15 to 0.24 Therefore, in order to meet the crater depth size requirements for the landing legs as described in

[7] `http://www.moog.com/literature/Space_Defense/Spacecraft/Spacecraft_Mechanisms/500-613_Micro3.pdf` [Accessed on: 25 June 2017]

Table 7.5, any crater greater than 0.63 m needs to be avoided. This risk is mitigated using active hazard detection and avoidance. The likelihood of this risk is average and its impact is moderate.

2. Large rocks: As there is no database of rocks on the surface of the moons, there is a fair chance that there will be rocks. According to the requirement mentioned in Table 7.5, the lander needs to avoid any rocks greater than 0.3 m in diameter. This risk is mitigated using active hazard avoidance as well. Hence the likelihood of this risk is low and its impact is critical.

3. The landing site has a high slope: If the landing site is very steep, the landing is more difficult. Also the chances of landing on a single leg increase, which might cause unpredicted horizontal movement of the lander. Considering the selected landing sites, the likelihood of encountering a high slope is average. High slopes may also reduce communication windows. The consequences are moderate. The active hazard detection and avoidance mitigates this as the sensors are capable of measuring slope from large altitudes.

4. The gas generator of harpoons fail to ignite: Failure to ignite the gas generator of the harpoons automatically results in the failure of the function of the harpoons. If the spacecraft is not sufficiently anchored during the mission time, the stability requirement may not be met. The likelihood of this happening is unlikely given the high reliability of the space grade gas generator. The consequence can be either moderate or critical, since the foot screws also provide some anchoring over the mission time and thus function as a backup. The performance of foot screws is strongly dependent on surface toughness.

5. Surface toughness higher than 5 MPa: At least one harpoon is capable of completely penetrating surfaces up to 10 MPa , in almost every scenario. Even at 50 MPa, at least one harpoon will gain partial penetration and as pull back force is proportional to the surface toughness, partial penetration should provide sufficient pull back force. The likelihood of this risk is low, as all studies of regolith of Martian moons suggest much softer surface. The impact of this risk is moderate. Therefore no mitigation strategy is implemented.

6. Surface toughness lower than 100 kPa: If the surface toughness is incredibly low, the pull back resistance offered by the surface will be less. The harpoon with highest diameter will provide the largest resistance. In order to prevent unintentional pull back of harpoons, the pull back force will not be increased if significant displacement of the harpoon is observed. Additionally, foot screws will play a larger role in ensuring lander stability in this scenario as they are effective on surfaces with low surface toughness. The anchoring force needed is dependent on the slope of the surface. The likelihood of this risk is average and its impact is marginal.

7. The surface is highly porous: A highly porous surface provides some risk with respect to anchoring. Since anchoring relies on friction force and a porous surface induces a decrease of this friction force, the chances of the harpoon coming loose from the surface drastically increase. The likelihood of encountering a highly porous surface is high. The consequence is only marginal, since there are still multiple harpoons which provide redundancy if one of them comes loose from the surface.

8. Software failure during descent: During the landing it might happen that the software needed for hazard detection fails. This results in uncontrolled descent and perhaps even crash. By programming multiple versions of the program, the likelihood can be brought back to unlikely, however the impact is still catastrophic for the mission.

9. Sensor malfunction: If any sensor on the spacecraft provides wrong data, or no data at all, this will lead to the actuators not being able to operate anymore. Specifically for the altitude sensors this will have catastrophic consequences, since this will mean the spacecraft will either crash or probably never land. The likelihood has been brought back to improbable by implementing enough redundancy.

10. Thruster malfunction: Thruster failure, or malfunction of a single thruster, might lead to some difficulties in the control of the spacecraft around one axis, this would make landing significantly more difficult. Failure or malfunction of multiple thrusters might even lead to crashing. However, the chances of multiple thrusters failing is highly improbable and therefore the failure of a single thruster will be mapped as having an average likelihood, but only a marginal impact.

11. Angular rates out of set limits: When angular rates get out of the set limits, the hazard detection and avoidance equipment stops functioning properly. This could have some critical consequences for performing a safe landing and thus a successful mission. The likelihood of angular rates getting too high is improbable.

7.9. Sensitivity Analysis

In order to evaluate the robustness of the design of the landing trajectory and the anchoring systems, this section provides a description of the sensitivity analysis. This analysis has been performed by varying the most

Table 7.9: Mitigated risk map of the landing subsystem.

Almost certain					
Likely		7			
Average		6,10	1,3		
Unlikely			5	2,4,11	8
Improbable					9
Likelihood / **Impact**	Negligible	Marginal	Moderate	Critical	Catastrophic

critical factors of the design and seeing how this change affects the design and its feasibility.

Landing trajectory: The landing trajectory can be evaluated in terms of the most important factors for the trajectory algorithm. These are the initial values: initial mass, initial velocity and the final values which constrain the trajectory: final velocity, descent time and the gravitational acceleration. The performance is evaluated in consumed fuel. The results are presented in Table 7.10. There are no severe consequences and even though there is a small percentage increase of the fuel mass for some of the evaluated parameters, the absolute difference is still small, thus it will have a non-significant influence on the design.

Table 7.10: Sensitivity analysis of landing trajectory.

Body	**Parameter**	**Current design** **Fuel mass** [kg]	**Design including 10% margin** **Fuel mass** [kg]	**Increase** [%]
Phobos	Initial velocity	7.23	8.11	12.2
	Initial mass		8.22	13.7
	Descent time		7.07	-2
	Final velocity		7.23	0
	Gravity		7.29	0.1
Deimos	Initial velocity	2.87	3.06	6.6
	Initial mass		3.23	12.5
	Descent time		2.73	-5
	Final velocity		2.87	0
	Gravity		2.90	1.1

Anchoring system : One of the key uncertainties associated with the anchoring system is the surface toughness. However, Figure 7.12 already displays the performance of the harpoons over two orders of magnitude, therefore varying surface toughness will not yield significant results. Another key uncertainty in the harpoons is their mass and ejection velocity. Mass can vary due to difference in material density and ejection velocity can vary due to performance of gas generator and internal friction. Therefore, considering a constant surface toughness of 1 MPa, the velocity and mass of the harpoons are varied by 10% and its impact on surface penetration is observed in Table 7.11. The results are not surprising. The penetration depth is dependent on energy which in turn is linearly dependent on mass and quadratically dependent on velocity. This displays the robustness of the anchoring system and also indicates that increasing the projectile velocity is the easiest way of increasing projectile penetration.

Table 7.11: Penetration depth of harpoons under mass and velocity variations.

Mass [kg]	**Velocity** [m/s]	**Configuration 1** [m]	**Configuration 2** [m]	**Configuration 3** [m]
0.1	90	2.14	0.93	0.24
0.11	90	2.36	1.03	0.27
0.09	90	1.93	0.84	0.22
0.1	99	2.56	1.07	0.26
0.1	81	1.76	0.80	0.22

8
Propulsion

This chapter covers the design of the propulsion subsystem for the orbiter and both landers. The propulsion system is responsible for several tasks, namely: orbit insertion, trajectory and orbit maintenance (RCS), spacecraft attitude control (ADCS) and the active landing system. Firstly, a requirement check is done in Section 8.1. Secondly, Section 8.2 explains the procedure taken in the design of the propulsion system and Section 8.3 discusses the propellant and design challenges for the system. Section 8.4 describes the final implemented design of the propulsion system. Additionally, an alternative propulsion system has been investigated in Section 8.5 as a risk mitigation strategy. Lastly, Section 8.6 presents the mitigated risks involved in the system and Section 8.7 investigates the sensitivity of the design.

8.1. Functional Analysis

In this section the requirements that have been established are evaluated for the current propulsion system. They are shown in Table 8.1.

Table 8.1: Propulsion system requirements.

ID	Requirement	Section	Compliance
FUN-PR-SS-01	The propulsion system shall have a maximum mass of 25 kg for the landers and 170 kg for the landers.	8.4.2	✓
FUN-PR-SS-02	The propulsion system shall have a maximum power usage of 1000 W for the orbiter and 300 W for each lander.	14.2	✓
FUN-PR-SS-03	The propulsion shall have a maximum cost of M€15 for the orbiter and M€4.5 for each lander (FY17).	14.4	✓
FUN-PR-SS-04	**[Driving requirement]** The propulsion system shall be able to deliver a ΔV of 4700 m/s.	8.2	✓
FUN-PR-SS-05	The propulsion system shall comply with the ITAR regulations.	Roza et al. [96]	✓
FUN-PR-SS-06	The propulsion system shall have a minimum reliability of 99% over the complete operational time.	16.2	✓
FUN-PR-SS-07	The propulsion system shall not have any single point of failure.	8.6	✓
FUN-PR-SS-09	The propulsion system shall accommodate 3% of propellant for the ADCS system.	8.2	✓
FUN-PR-SS-10	The propulsion system shall burn for a maximum of 1 hour for the initial Mars orbit insertion burn	8.2	✓

Requirement *FUN-PR-SS-05* has been discussed in the Mid-term Report of this mission (Roza et al. [96]), where it is explained that the propulsion system is only considered if it complies with the ITAR regulations. *FUN-PR-SS-02* and *FUN-PR-SS-03* are in Chapter 14.

8.2. Design Approach

The propulsion system is designed in several stages, with the focus being on the main propulsion system responsible for the orbit insertions. This is because these manoeuvres are the most demanding in terms of thrust and ΔV. This is followed by the sizing of the RCS and ADCS that are combined as one system. The landing system is designed with close attention to the RCS and ADCS systems in order to minimise the overall number and variety of thrusters. Section 8.3.1 explains the reasons governing the choice of propellant and Section 8.3.2 overviews the main concerns involved in the design process. For reference, mainly the MAVEN orbiter of NASA has been used in the orbiter propulsion design (National Aeronautics and Space Administration [77]).[1] A ΔV

[1] `http://spaceflight101.com/maven/spacecraft-information/` [Accessed on: 24 June 2017]

budget is provided in Table 8.2.

Table 8.2: Overview of the burns made by the spacecraft at the various phases as stated in Chapter 5. The X phase represents additional manoeuvres such as ADCS, orbit keeping and landing thrust. The ADCS burns are only made by two of the twelve thrusters at any one time.

Spacecraft	**Burn Phase**	**ΔV** [km/s]	**Thrusters**	**Propellant Mass** [kg]	**Burn Time** [min]
Deimos	2	0.00242	4 × 50N	0.35	0.07
	3	0.417	4 × 50N	56.24	11.72
	4	0.260	4 × 50N	30.57	6.37
	X	0.085	2 × 5N	8.69	13.87
Phobos	2	0.0154	4 × 50N	2.33	0.49
	3	0.194	4 × 50N	28.20	5.88
	4	0.693	4 × 50N	84.35	17.58
	X	0.082	2 × 5N	8.09	11.61
Orbiter	1	1.65	6 × 220N	1795.61	56.71
	2	1.35	6 × 220N	491.14	15.51
	X	0.176	6 × 220N	47.74	1.51
		0.11	2 × 5N	29.68	111.62

8.3. Design Option and Trade-off

The design options for the propulsion system revolve around the choice of propellant. Section 8.3.1 describes the decision to use ADN-based LMP-103S and Section 8.3.2 summarises the major difficulties involved in the design process.

8.3.1. Propellant Choice

As explained by Roza et al. [96], the monopropellant to be used for the mission was AF-M315E, based on hydroxylammonium nitrate (HAN) [96]. This was chosen due to its many sustainability benefits as well as its high specific impulse and density in comparison to the commonly used hydrazine. The HAN propellant could be implemented as a blow-down or regulated system for all the propulsion tasks. However, despite plans to implement the propellant in a wide variety of missions, current development of the thrusters is moving slower than expected and no high-thrust thrusters have been made publicly available. Therefore, in order to avoid the use of hydrazine, another sustainable propellant has been selected to replace AF-M315E.

LMP-103S is a promising propellant based on ammonium dinitramide (ADN) (Whitmore et al. [129]). It exhibits similar properties to HAN, but thruster systems using it have already been proven in the PRISMA mission by the Swedish Space Agency (Dinardi [30]). In addition, there has already been significant progress in upscaling the thrusters from 1 N and 5 N to 220 N (Persson et al. [85]). Furthermore, NASA's investigation into LMP-103S, by Whitmore et al. [129], lays out multiple environmental and cost benefits of this propellant due to its lower toxicity and material compatibility. Table 8.3 provides an overview of the properties of LMP-103S, AF-M315E and hydrazine for clear comparison.

Table 8.3: Properties of Hydrazine, HAN and ADN propellants.

Property	**Hydrazine**	**HAN (AF-M315E)**	**ADN (LMP-103S)**
Density [g/cm^3]	1.00	1.47	1.24
I_{sp} [s]	230	257	252
Impulse Density [gs/cm^3]	230	378	312
Flight tests	Multiple proven flights, MAVEN[a]	GPIM (to be launched)[b]	PRISMA (2010)

[a] `http://spaceflight101.com/maven/spacecraft-information/[Accessedon:24June2017]`
[b] Spores et al. [110]

8.3.2. Design Challenges

There are several design challenges related to the chosen propellant system which led to an additional design based on hydrazine propellant. These challenges are related to the technical limitations of burn time, number of pulses, throughput capability and catalyst heating. Despite this, the alternative propellants based on ADN and HAN are promising because the architecture (piping, tanks and thrusters) that would be required is very similar to that of current hydrazine systems (Tam et al. [114]). Nevertheless, there are important differences between the two systems. The main differences between hydrazine and the alternative thrusters is that for ignition of HAN and ADN, the catalyst must be heated to around 400 °C and the exhaust temperatures can be between 1600 and 2000 °C, which is approximately twice that of hydrazine (Larsson and Wingborg [64]). This means that the thrusters have a high power requirement for the catalysts and also tend to be heavier due to the materials necessary to cope with the heat generation. As a consequence of these design changes, thrusters have to be redesigned for the use of LMP-103S and are currently between a TRL of 4 and 9, with low-thrust thrusters already in use (Persson et al. [85]). As a mitigation to the thrusters not being developed in time for the mission, a back-up concept has been investigated using hydrazine (Section 8.5).

However, ADN and HAN propellants have a wider temperature range in which they remain as liquids (Dinardi [30]), therefore decreasing the total power consumption required for maintaining their state. Another benefit is the high density of these propellants. Focusing specifically on LMP-103S, the commercial version of ADN propellant, it can be seen that it has a 24% higher density than hydrazine, with an additional 12% higher specific impulse which gives a total impulse density of 312 gs/cm^3, which is 36% higher compared to hydrazine. This results in lower propellant mass and smaller tank volumes (and hence lighter tanks), which far outweighs the temperature and power disadvantages. This can be seen by comparing the two propulsion system concepts in Section 8.4 and Section 8.5.

8.4. High Level Concept

This section will cover the high level concept of the propulsion system utilising ADN-based LMP-103S propellant. This concept promotes the use of upcoming technology and aims to prove the usefulness of alternative monopropellants. The thruster selection for the orbiter and landers is given in Section 8.4.1 followed by a detailed description of the architecture in Section 8.4.2.

8.4.1. Thrusters

The thrusters that will be used are developed by the *Swedish National Space Board*, in conjunction with *ECAPS* and *EURENCO Bofors*, and range from 0.5-220 N. Firstly, the main propulsion is discussed for the orbiter and the landers followed by the RCS and ADCS thrusters. Finally, the landing thrusters are discussed. The main propulsion is responsible for the high ΔV burns required to insert the spacecraft into their orbits. The calculations for the ΔV have been explained in Chapter 5. The specifications of the chosen thrusters and propellant masses are provided in Table 8.2.

Main Propulsion: For the orbiter, a system of six HPGP ACE thrusters, producing 220 N each, was selected. This choice gives a total burn time of one hour and ten minutes for the orbit insertion to Mars. As explained in Chapter 5, the manoeuvre would be divided into two steps to lower the mass of propellant required. To calculate the mass of propellant, the Tsiolkovsky Rocket Equation (Equation 8.1) is used as explained in Chapter 5, where g_0 is the gravitational acceleration and M_f represents the mass of the spacecraft after the burn. The I_{sp} is taken from Table 8.3 for the relating propellant. The mass of propellant burned in this stage would be just below 1800 kg, or 76% of the total orbiter propellant.

$$M_{prop} = \left(\exp\left(\frac{\Delta V}{I_{sp} \cdot g_0}\right) - 1\right) \cdot M_f \tag{8.1}$$

Regarding the landers, their orbit insertion burns would be accomplished by four HPGP 50 N thrusters. The main reason for using lower force thrusters is because they are lighter and smaller, but are capable of delivering the required ΔV within an acceptable burn time. The mass of propellant burned for the Phobos and Deimos landers during their orbital manoeuvres is 111 and 83 kg respectively.

RCS/ADCS Propulsion: The RCS and ADCS propulsion systems (referred to solely as RCS from now on) have been designed to utilise the same thrusters, thereby decreasing the total number of thrusters necessary. From the GNC analysis, the ΔV required to be delivered by the RCS systems for the landers during orbit and for the orbiter during operations has been found. Furthermore, the orbiter RCS system has the additional task of orbit keeping for the satellite.

First considering the orbiter, the decision was made to utilise the main thrusters for the orbit keeping burns. This varies between previous NASA missions, where for example, the MAVEN orbiter has six dedicated thrusters for orbit keeping. Following the GNC analysis, it is known that the orbiter maintains a repeating orbit trajectory ranging from 370 km to 420 km, therefore there is no requirement to carry propellant or size thrusters for these manoeuvres, however as a precaution, extra propellant is carried on board for an estimated ΔV of 0.16 km/s.

The number of RCS thrusters are estimated by looking at previous Mars missions and orbiters. It is deduced that a reliable number of thrusters is twelve (based on MAVEN).[2] This would place four thrusters on each axis, with pairs facing opposite directions. This form of redundant design ensures good controllability as well as reliability. In Chapter 9, it is calculated that the thrust to dump momentum is around 1 N to 5 N for an average burn time, therefore it would be acceptable to implement HPGP 5N thrusters for RCS (each thruster has a throtteable range of 1 N to 5 N).

For the landers for Phobos and Deimos, a similar approach is taken for the RCS thrusters. Following the analysis from GNC and ADCS of Chapter 5 and Chapter 9, the total ΔV required for orbit corrections and RCS adds up to approximately 0.3 km/s. This would require a propellant mass of 2 kg to achieve instantaneously and is well within the capabilities of the HPGP 5 N thrusters as selected for the orbiter. For the same reasons of redundancy and controllability, particularly in landing, the landers will have twelve thrusters each.

Landing Propulsion: The landing propulsion system is only implemented on the landers of Phobos and Deimos. This system is purely dependent on the SDL requirements as stated in Chapter 7. According to Ulamec and Biele [124], the Philae lander used cold gas thrusters for its hold down operations, however it had no other thrusters on it. Considering that the landers require hot gas thrusters for the ADCS manoeuvres, use can be made of these same thrusters for holding down the lander. They are placed such that their thrust vectors coincide with the hold-down vector (against the surface of the moon). A force of 10 N is necessary, which is easily attainable with the two ADCS thrusters pointing opposite to the surface.

8.4.2. Architecture

There are many additional components to design and size for the propulsion system, the most important of which are the propellant tanks. The propellant tank is generally a flexible component in terms of design, because it is commonly incorporated as a structural component. Typically it represents the largest mass and therefore drives the sizing of the spacecraft bus. The other components of the propulsion system are the pressurant and its tank and the feed system which includes pipes and valves. The feed system is the lightest component but its many moving parts must be designed for redundancy and high reliability to ensure the correct operation of the thrusters. The propellant tank sizing is explained first, followed by the pressurant and the feed system.

Propellant Tanks: The propellant tanks can be designed in multiple ways, with the main goal of reducing mass. The preliminary design was based on spherical tanks as these are the lightest by volume and are most commonly used (Wertz and Larson [128]). Tam et al. [114] states that LMP-103S can be stored in hydrazine tanks with minor structural modifications, for the increased density of the material, due to its compatibility. Therefore, it was possible to use statistical data of previous missions to estimate the mass. Wertz and Larson [128] present an equation to calculate this conceptual mass based on metallic tanks with *Propellant Management Devices* (PMD) or diaphragms. The two types were compared and PMD tanks are considerably lighter (in the order of 50%) for the range of propellant mass being used for Aphrodite. PMD's are simpler devices that rely on inner geometry for the flow of propellant. These tanks can be equipped with vanes and baffles to limit sloshing during manoeuvres for satisfactory performance (Hu et al. [53]). A system of six equally sized propellant tanks were chosen for the orbiter because it provided the highest total mass decrease when considering the structural gain. The tank masses increase but the structural weight of the whole spacecraft decreased to a greater extent. This also allowed for the best use of volume within the spacecraft. Due to the much lower propellant mass in the landers, they only require one tank for all of the propellant.

Pressurant Design: In order to expel the propellant at the correct pressure, a pressurant must be kept at high pressure in a separate tank. According to Wertz and Larson [128], the most common pressurants are nitrogen and helium gas and a decision was made to select the one that would result in the lowest added mass, which is nitrogen. The mass of necessary pressurant is found by applying Equation 8.2 with certain assumptions. The EoL temperature and pressure were estimated at 293 K and 5 bar, based on the minimum pressure acceptable for the thrusters. The temperature is taken from the book by Wertz and Larson [128] and the begin-of-life (BoL) values as well. The amount of pressurant is small enough to fit in a single tank for both the landers and the orbiter and by using the regression analysis of Wertz and Larson [128], the pressurant tank masses are found.

[2] `http://spaceflight101.com/maven/spacecraft-information/` [Accessed on: 22 June 2017]

Table 8.4: An overview of the mass budget of the propulsion system. The totals are written in bold. An addition of 13% is included in the totals for the tank and thruster masses to account for the feed system.

Spacecraft	Thrusters		Tanks		Propellant	
	Type	Mass [kg]	Type	Mass [kg]	Type	Mass [kg]
Deimos	4× 50N	4× 1.5	1× Metal PMD	6.31	LMP-103S	95.85
	12× 5N	12× 0.4	1× Metal	2.20	Nitrogen	0.45
		12.2		**9.62**		**96.30**
Phobos	4× 50N	4× 1.5	1× Metal PMD	7.58	LMP-103S	122.96
	12× 5N	12× 0.4	1× Metal	2.29	Nitrogen	0.57
		12.2		**11.2**		**123.53**
Orbiter	6× 220N	6× 3.7	6× Metal PMD	17.57	LMP-103S	2364.17
	12× 5N	12× 0.4	1× COPV	7.00	Nitrogen	10.98
		30.5		**127.0**		**2375.2**

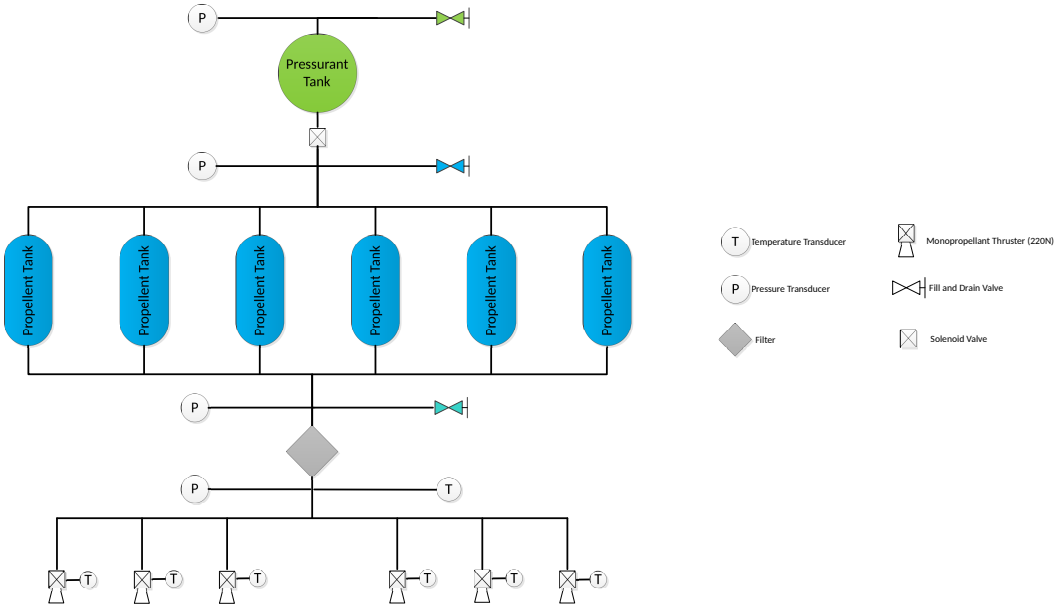

Figure 8.1: Architecture of the main propulsion system for the orbiter. The landers follow a similar structure with four thrusters and one propellant tank.

$$M_{pres} = \frac{P_{EoL} \cdot V_{prop}}{\rho_{EoL} \cdot \left(R_g \cdot T_{EoL} - \left(\frac{P_{EoL}}{\rho_{EoL}}\right)\right)} \tag{8.2}$$

Feed System Design: The design of the feed system does not require specialised components compared to a usual hydrazine spacecraft. Larsson and Wingborg [64] indicates that LMP-103S is compatible with most common materials such as stainless steel and aluminium as well as fluid valves and piping. This s that the architecture does not have to be redesigned with a certain material, so the masses are estimated based on statistical data of previous missions. Wertz and Larson [128] recommend that the feed system is approximated at 13% of the propulsion system dry mass. Figure 8.1 displays the lay-out of the architecture with the necessary devices for the main propulsion.

8.5. Back-up Concept

In this section the hydrazine based propulsion system is summarised. The general architecture of the different hardware components are kept the same because as stated in Tam et al. [114], LMP-103S and hydrazine can utilise the same materials and components. The main differences that can be identified are the following: hydrazine has a lower specific impulse density, there are more space tested hydrazine thrusters and hydrazine is

more complicated to store in a space environment. These three aspects will be explained below:

Impulse: LMP-103S is a considerably higher performance propellant than hydrazine. Its 36% higher specific impulse density means that much less propellant would be required for the spacecraft manoeuvres. The effect of this has been quantified for the Aphrodite mission, and the result is an increase of approximately 50 kg or 46% for the landers and 485 kg or 20% for the orbiter. This has a significant impact on the mission, and would require the improvement of the spacecraft structure as well as the increase in propellant tank sizes. The overall wet mass would be 4320 kg, and would require the selection of a new launcher.

Flight Heritage: Section 8.3 explains the difficulties of choosing a new propellant, with the largest challenge being the development of space tested equipment. Although hydrazine and LMP-103S can employ the use of the same hardware, LMP-103S has only been flight tested on one mission, PRISMA, which used low thrust 1 N thrusters (Dinardi [30]). The MAVEN orbiter on the other hand, has successfully entered Mars orbit on high-thrust (170 N) hydrazine thrusters. As the most common propellant for space, the market for hydrazine thrusters is extensive. Their costs are likely to be cheaper, provided that no testing is necessary. However research by Dinardi [30] shows that hydrazine is a more expensive propellant to handle and dispose of.

Temperature: One of the benefits of LMP-103S over hydrazine is its large surviving temperature range (Dinardi [30]). This means that when not being used, the propellant can be cooled to lower temperature, particularly during a transfer phase or eclipse, drastically reducing power consumption. This would also minimise the risks relating to temperature changes. Section 16.1 describes the possible risks relating to such an effect. Also related to temperature is the high burning temperature of LMP-103S, mentioned in Section 8.3.2, which requires special materials to protect the spacecraft and thrusters. However, this is considered in the thruster development.

8.6. Risk Analysis

The risks of the propulsion system are summarised below. The values in the risk map (Table 8.5) are derived from the systems current technology readiness level and historical data. The risk mitigation strategy for the propulsion system leads to applying a fault tolerant design. This means applying redundancy for the propulsion systems and has been implemented in almost every space mission. The risks shown in Table 8.5 are after mitigation. Risks related to the thrusters are evaluated for one thruster only, however, if many thrusters encounter the same problem, the impact on the system and mission may be larger; for example, if all main thrusters fail, there is no contingency plan that can compensate. Table 8.5 only includes operational risks of the propulsion system but there are risks involving the propellant in the phases before launch. As mentioned earlier, LMP-103S is safer to handle and more environmentally friendly than hydrazine. Risks of toxic spills and biological contamination are significantly smaller when handling LMP-103S. It does not require specialised protective suits and it can be disposed of in a safer and cheaper manner, referred to as a "non-hazardous" procedure (Negri and Grund [79]). A fault tree is presented in Figure 8.2.

1. Valve failure: This risk is easy to prepare for through the implementation of redundant valves placed in series and by making a cross-strapped feed system, which can ensure that the propellant and pressurant have multiple ways of flowing to the tanks and thrusters. Nevertheless, additional valves can add complications to the design and lead to failures.

2. Propellant leak: Propellant leakage is inevitable over such a long mission time and is corrected for by bringing slightly more propellant. This is considered to be within the margins already applied in the design and is therefore ranked as a minimal impact risk.

3. Pressurant leak: Pressurant is less likely to leak than propellant because it flows through less connections. Depending on the amount of pressurant leak, there can be varying impacts. Full loss of pressurant would force the propulsion system to work in blow-down mode, severely reducing thrust capabilities over the mission duration but not causing mission failure.

4. Catalyst bed structural failure: This is one of the most significant risks for the propulsion system. If the catalyst bed becomes damaged during flight it can lead to incomplete decomposition of the propellant and decrease the thrust capabilities significantly. Complete failure of the catalyst would lead to the thruster being inoperable. The mitigation of such a risk can only be done through extensive testing and appropriate shaping of the catalyst bed.

5. Failure to heat catalyst: Similar to risk 4, if the catalyst bed does not heat to the required temperature, LMP-103S cannot decompose and will not produce any thrust. This risk would lead to complete thruster failure but can be mitigated by applying additional heaters.

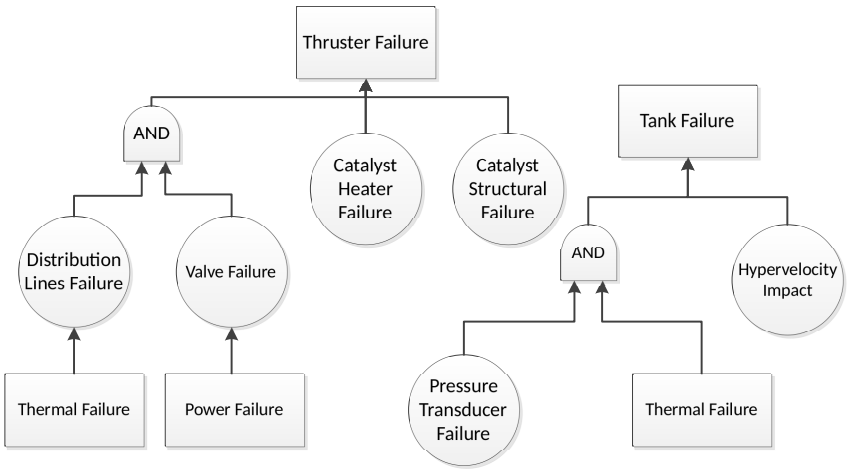

Figure 8.2: Fault tree of the propulsion system.

6. Distribution lines failure: Failure of the distribution lines can be due to many causes such as thermal failure or structural failure caused by increased pressure. However, with sufficient redundancy in the feed system hardware (valves, transducers and heaters), this risk is highly mitigated. Furthermore, the chosen propellant has a very low freezing temperature meaning that a heater failure is not necessarily critical. If the distribution lines do fail, it is clear that the thrusters would be inoperable and leaked propellant or burst piping could cause severe damage to components within the spacecraft.

7. Pressure transducer failure: This failure is harder to detect as a loss or increase in pressure cannot be measured without the transducers. Again, redundant systems can be installed to avoid the over- or under-pressurisation of the propellants. Faults in pressurisation can lead to inconsistent thrust levels in a thruster and may be a cause of distribution line failure.

8. Hypervelocity impact: A hypervelocity impact by other bodies is unpredictable and extremely difficult to mitigate against. Micrometeorites can be stopped by the outer shells of the spacecraft and the materials used in the propulsion system are also capable of withstanding certain impacts, however, a large enough object can puncture the propellant system and lead to complete subsystem failure if it punctures a propellant tank. Depending on the type of impact, propellant may ignite or damage other components of the spacecraft.

9. Thermal control failure: As stated earlier, the propellant is capable of surviving a wide temperature range, and as such this risk is not significant for the propellant. However, the system hardware requires certain temperatures to operate and can fail if temperatures vary too much. Nonetheless, the hardware is certified to work with the large temperature gradients encountered by the propellant and thrusters and is therefore not likely to fail.

10. Technology not ready: This risk is related to the technology readiness level of the LMP-103S propellant and thrusters. In order to mitigate against this, a back-up concept has been researched based on the more common and flight-ready hydrazine technology. The main considerations have been outlined in Section 8.5.

Table 8.5: Mitigated risk map of the propulsion subsystem.

Almost certain	2				
Likely					
Average					
Unlikely		1,9,3		4,10	
Improbable			7	5,6,8	
Likelihood / **Impact**	Negligible	Marginal	Moderate	Critical	Catastrophic

8.7. Sensitivity Analysis

This section will look into the robustness of the propulsion system design by changing the parameters by a certain uncertainty margin. The parameters that will be looked into are ΔV, dry mass, specific impulse and thrust.

ΔV: The ΔV is increased by 10% over the already existing contingency margin of 10%. This increase results in a total wet mass increase of 11% due to the extra propellant and larger tanks needed to accommodate them. The significance of this is that the total spacecraft mass would be above the launcher maximum, and a new launcher would need to be selected, such as the Falcon Heavy, as elaborated upon in Section 13.2.

Dry Mass: Similar to ΔV, an increase in the spacecraft dry mass of 10% accumulates to a total wet mass increase of 10%, which is above the acceptable launch mass.

Specific Impulse: The specific impulse of the thrusters is lowered by 10%, a significant amount, to see the effect on the propulsion system. This leads to a wet mass increase of 14%, because of the extra propellant required to compensate for the I_{sp} reduction.

Thrust: If the thrusters are unable to operate at their highest thrust level, and instead fire at 90% of their capabilities, which could be caused by a valve that does not fully open or by a slight leak in pressurant, the burn times proportionally increase by 10%. This is not preferable but also not critical to the mission as the burns locations can be adjusted to accommodate for extended burn times.

9
Attitude Determination and Control

The attitude determination and control system (ADCS) of the spacecraft is a subsystem that determines and controls the attitude of the spacecraft. It provides the pointing accuracies needed for other subsystems, having full knowledge and control over the angular orientation of the spacecraft in each direction.

The structure of this chapter is as follows: in Section 9.1, an overview is given of the hardware components that are selected for the complete ADCS architecture. Then the approach leading to the design choices made in Section 9.2 is presented. This includes a functional analysis in which the functions of the ADCS are described per mode. With this, the requirements from Roza et al. [96] can be evaluated and extended if needed. Next, the studies that are performed to come up with the final ADCS are explained in Sections 9.3 and 9.4. Their architecture and algorithm is described in Section 9.5. Afterwards, the local risks are identified and assessed in Section 9.6. Finally a sensitivity analysis is shown to prove the robustness of the ADCS design in Section 9.7.

9.1. ADCS Hardware

The final hardware selection for the sensors and the actuators and their mass and power characteristics are shown in Table 9.1 for the orbiter and Table 9.2 for the landers. Note that the budgets for the RCS thrusters are not included in the total ADCS budgets, but in the propulsion system budgets. Also, the total power value given is not the sum of the individual components, but the sum of their average taking into account that multiple components of the same hardware type can be active at the same time.

9.2. Design Approach

The procedure for sizing the hardware starts with a functional analysis per mission mode in Section 9.2. This is done for the spacecraft bus, the orbiter and the separate landers. Then the driving modes are derived and the design for the orbiter and the two landers is presented in Section 9.3 and Section 9.4.

9.2.1. Reference Frames

The reference frame used for the design of the ADCS is a body-fixed reference frame. Note that for the spacecraft bus, the individual landers and the orbiter, the z-axis is assumed to be aligned with the thrusters. The y-axis is aligned with the solar panels and the x-axis is perpendicular to that to create a right-handed reference system. This is visualised in Figure 9.1.

9.2.2. Orbiter Attitude

Before going into further detail, the orbiter orientation is explained. This is crucial for modelling the disturbance environment and for understanding the origin of the requirements. The orbiter can have a vertical or a horizontal

Table 9.1: ADCS hardware components for the orbiter.

Hardware component	**Company**	**Number**	**Total Mass** [kg]	**Average power per unit** [W]	**Peak Power per unit** [W]
Inertial Reference Unit (IRU)	Northrop Grumman	1	7.1	22	43
Accelerometer	-	4	5.5	6	
Star Tracker	Terma	3	3.3	15.2	-
Coarse Sun Sensor	Bradford Engineering BV	12	2.6	0	-
Fine Sun Sensor	Bradford Engineering BV	2	0.8	0.5	-
70 N m s Reaction Wheel Actuator	Moog Bradford	4	32	29	169
Wheel Drive Electronics Box	Moog Bradford	1	2.3	Included in RWA	Included in RWA
5N HPGP RCS Thrusters	-	12	0.4	15	18.75
Total	-	-	53.53	173.7	-

Table 9.2: ADCS hardware components for the landers.

Hardware component	**Company**	**Amount**	**Total mass** [kg]	**Average power per unit** [W]	**Peak power per unit** [W]
Inertial Reference Unit (IRU)	Northrop Grumann	1	7.1	22	43
Accelerometer	-	4	5.5	6	-
Star Tracker	Terma	3	3.3	15.2	-
Coarse Sun Sensor	Bradford Engineering BV	12	2.6	0	-
Fine Sun Sensor	Bradford Engineering BV	2	0.8	0.5	-
4 Nms Reaction Wheel	Moog Bradford Inc.	2	5	5	60
8 Nms Reaction Wheel	Moog Bradford Inc.	1	3.6	5	80
5N ADN RCS Thrusters	-	12	0.4	15	18.75
Total	-	-	28.03	73.7	-

orientation, as can be seen in Figure 9.1. The horizontal orientation is optimal, because having the lasers on top will provide a larger coverage where the spacecraft never blocks the view of the lasers. Because the solar panels have to be pointed at the Sun all the time, having a fixed orientation with respect to the Sun severely reduces the complexity and risk of the solar panels actuators. These actuators otherwise would need to be able to move the solar panels over an angle of 180° around the z-axis continuously, increasing their wear and imposing a continuous momentum change on the spacecraft which can lead to instability. The mass moments of inertia can be found in Chapter 3. It is assumed that they are symmetrical over the x-, y- and z-axis. No attitude requirements are available for the secondary payload.

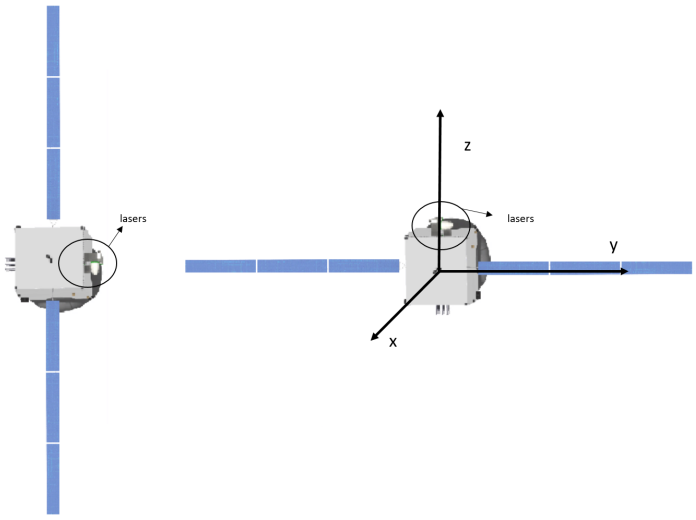

Figure 9.1: On the left, the vertical orbiter orientation can be seen and on the right, the horizontal orbiter configuration. The reference system is also indicated.

9.2.3. Functional Analysis and Requirements

The functions of the ADCS per mission mode are described below. The requirements are displayed in Table 9.3, indicating for which mode they are given. The driving requirements for the ADCS itself were not yet identified, so these are indicated in Table 9.3 as well.

Mode 1: Separation

Mode 1 is relevant for the spacecraft bus after undocking from the launcher. The ADCS shall point the solar panels to the Sun and corrects orientation deviations to prepare the spacecraft for travel. Since the accuracy of the launcher can be a requirement from the Aphrodite mission to SpaceX (SpaceX [109]), this is not a driving factor.

Mode 2: Travel

In travel mode, the actuators from the ADCS are not activated and they are only active when attitude determination is performed. This mode is not a driving factor for the ADCS. If big deviations in attitude are detected, the

spacecraft can go into slew mode to perform trajectory correction manoeuvres as was done during the travel stage of the Mars Reconnaissance Orbiter (MRO). The slew rate needed for that can be low and will not be a driving factor.[1]

Mode 3: Orbit Insertion
During orbit insertion, disturbances can occur due to assembly inaccuracies of the thrusters. Thrusters can be misaligned or their output can be mismatched, causing a torque around the x- and the y-axis. On top of that, a slew needs to be imposed by the ADCS, since the trajectory during the burns is elliptical.

Mode 4: Operational
Only the orbiter uses the ADCS during the operational mode. It has two functions: the first one is to counteract external disturbance torques from the environment and internal disturbance torques such as internal sloshing and movement of other subsystems. The second function is to provide stability and pointing accuracy to the ranging payload. It should be noted that the lasers have their own actuator platform.

Mode 5: Slew
Mode 5 is activated when big attitude deviations are detected. This can be corrected for in slew mode. The requirement comes from the mitigation strategy for laser actuator failure. In this case, the spacecraft has to provide the repointing manoeuvre from one body to the other, imposing a slew rate requirement on the system.

Mode 6: Safe
In safe mode, no actuators are active. The omni-directional antenna is used to wait for a command, but it does not need pointing. Only the sensors are active.

Mode 7: Landing
During landing mode, the landers need to be rotated to prepare for the landing sequence. During the landing sequence itself, the ADCS has to provide the landers with landing stability.

Table 9.3: ADCS requirements.

ID	Requirement	Section	Compliance	Mode
FUN-ACS-SS-01	The ADCS shall have a maximum mass of 135 kg for the orbiter and 30 kg for each lander.	9.1	✓	-
FUN-ACS-SS-02	The ADCS shall have a maximum power usage of 200 W for the orbiter and 100 W for each lander.	9.1	✓	-
FUN-ACS-SS-03	The ADCS shall have a maximum cost of M€58 for the orbiter and M€20 for each lander (FY17).	14.2	✓	-
FUN-ACS-SS-04	The ADCS shall not have any single point of failure.	9.3.1, 9.3 and 9.4	✓	-
FUN-ACS-SS-05	The ADCS shall be able to withstand all loads during the operational time.	6.1	✓	-
FUN-ACS-SS-06	The ADCS of the orbiter shall provide a pointing knowledge better than 300 nrad within 1 standard deviation around all 3 axes.	9.3	✓	4
FUN-ACS-SS-07	The ADCS of the orbiter shall provide a pointing accuracy better than 2.5 mrad within 3 standard deviations around all 3 axes.	9.4.3	✓	4
FUN-ACS-SS-08	The ADCS of the orbiter shall be able to provide a slew rate of minimal 0.5 °/s over the y - or the z-axis.	9.4.3	✓	4, 5
FUN-ACS-SS-09	The ADCS of the orbiter to Phobos shall be able to provide a slew rate of minimal 0.1027 °/s over the x- or the y-axis during the first orbit insertion burn.	9.4.3	✓	3
FUN-ACS-SS-10	The ADCS of the landers shall be able to provide a slew rate of minimal 0.0774 °/s over the x-or the y-axis during their insertion burns.	9.4.4	✓	3
FUN-ACS-SS-11	The ADCS of the landers shall be able to provide a landing stability of 2° over the x-and the y-axes.	9.4.4	✓	7
FUN-ACS-SS-12	The ADCS of the Phobos lander shall be able to turn the spacecraft 180° within 2000 seconds over the x- or the y-axis.	9.4.4	✓	5,7
FUN-ACS-SS-13	The ADCS of the Deimos lander shall be able to turn the spacecraft 180° within 4000 seconds over the x-or the y-axis.	9.4.4	✓	5,7
FUN-ACS-SS-14	The ADCS shall enable full control over the spacecraft during all control operational modes.	9	✓	-
FUN-ACS-SS-15	The ADCS shall have a reliability higher than 99.2% over the complete operational life.	16.2	✓	-

[1] https://mars.nasa.gov/MRO/mission/timeline/mtapproach/approachtcms/ [Accessed:31 June 2017].

For the actuators, the following modes are determined to be driving: for the orbiter operational mode and slew mode; for the landers, the landing mode, as the highest accuracy is needed there. During the orbit insertion of the total spacecraft bus, only the ADCS of the orbiter is activated. Note that the actuators which move solar panels were chosen in Chapter 6. They can rotate the solar panels around the y-axis.

9.3. Sensors

The attitude determination function of the ADCS is undertaken by the sensors. The sensor selection is influenced by the external environment and required pointing knowledge accuracy as observed in Table 9.3. The pointing knowledge accuracy is an essential variable, which is critical for space optical communication systems.

9.3.1. Design Options and Trade-Off

In order to select the sensors, a DOT is created as can be seen in Figure 9.2. The design options are divided in terms of internal and external sensors. In Figure 9.2, sensors in green boxes are chosen and the sensors in red boxes are rejected. Table 9.4 outlines the key characteristics that are considered in the selection of the sensors. While an average indication of key characteristics of sensors is mentioned in the table below, the values can vary significantly over their entire range of availability. A brief description and rationale of the sensors is presented below.

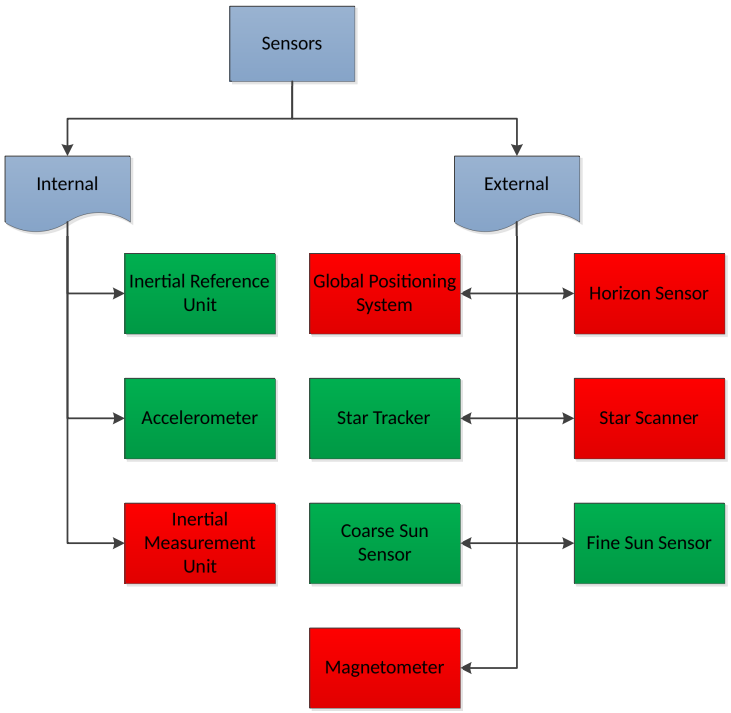

Figure 9.2: Design option tree of attitude determination sensors.

Internal Sensors

Inertial Reference Unit (IRU): An IRU uses a series of gyroscopes to measure the relative position and attitude of the spacecraft with respect to its initial state. IRUs are available with both medium and high accuracy. The high accuracy IRUs were considered due to pointing knowledge accuracy requirement (Starin and Eterno [111]).

Accelerometer: Accelerometers measure the non-gravitational accelerations of the spacecraft in all three axes and integrate over them to determine its position and orientation. Integration errors can build up if external reference is not used at regular intervals. Standard accelerometers have medium accuracy. However, because of the requirements of orbit determination (requirement *OPS-DEP-S-15* until *OPS-DEP-S-18*), highly accurate accelerometers are necessary (Starin and Eterno [111]).

Inertial Measurement Unit (IMU): This is a combination of both an IRU and accelerometers. Thus, it has three

Table 9.4: Trade-off table of sensors.

Sensor	Feasible	Accuracy	Mass
IRU	Yes	High	High
Accelerometer	Yes	High	Medium
IMU	Yes	High	Low
Star Tracker	Yes	High	Medium
Star Scanner	Yes	High	Medium
Coarse Sun Sensor	Yes	Low	Low
Fine Sun Sensor	Yes	Medium	Low
GPS	No	-	-
Horizon Sensor	No	-	-
Magnetometer	No	-	-

gyroscopes and three accelerometers to accurately determine the position and velocity of the spacecraft. It was determined that independent IRUs and accelerometers were a favourable choice because their commercially available options had a higher accuracy comparatively (Starin and Eterno [111]).

External Sensors

Global Positioning System (GPS): GPS is only accurate for Earth-based satellites, where a GPS constellation is available. Therefore, it is impossible to use it on Mars for the Aphrodite mission [111] .

Star Tracker: Star trackers use cameras to obtain a view of the stars and they use existing maps to determine the orientation of the spacecraft in deep space. It is relatively expensive but also essential on interplanetary missions (Starin and Eterno [111]).

Star Scanner: Star scanners are star trackers which are modified to perform the attitude determination using rotation of the spacecraft. They are relatively less accurate. As spin stabilisation is not used during the Aphrodite mission, star scanners are not chosen (Starin and Eterno [111]).

Coarse Sun Sensor: Coarse Sun sensors are lightweight, cheap sensors which are essentially small solar cells. They are used to initially orient the solar panels after deployment and are also essential for orientating the solar panels during safe mode operations. They are not very accurate (Starin and Eterno [111]).

Fine Sun Sensor: Fine Sun sensors are lightweight sensors which are more accurate than coarse Sun sensors. They are used for accurately measuring the two-dimensional position of the Sun, thus allowing the spacecraft to orient the solar panels in the optimal position (Starin and Eterno [111]).

Horizon Sensor: Horizon sensors use the infrared radiation of Earth to determine the attitude of the spacecraft. They are relatively less accurate and are mostly used for Earth-based spacecraft (Starin and Eterno [111]).

Magnetometer: Magnetometers use a the magnetic field of a planet for attitude determination. Mars does not have a (major) magnetosphere of its own, which renders magnetometers useless [111].

Now that the sensor types have been selected, it is deemed to be most efficient to pick off-the-shelf sensors for the spacecraft. The sensors are largely picked based on available data sheets and the key deciding factors are accuracy, lifetime and mass. To avoid any single point of failure, as specified in requirement *FUN-ACS-SS-04*, a redundant set of every sensor is taken. The number of chosen sensors for the orbiter and the lander is mentioned in Tables 9.1 and 9.2. While the orbiter needs the accelerometer for orbit determination, as mentioned in Section 5.3, the lander needs it to perform the landing operations. The IRU chosen is the SIRU-E, beacuse of its high accuracy as specified in Table 9.5. The IRU comprises four hemispherical resonator gyro (HRG) sensors in a tetrahedron orientation. The IRU is internally redundant as there are four HRGs for three axes. Additionally, the IRU has a reliability of 99.7% for a period of 15 years.[2] While one star tracker is sufficient for the pointing knowledge, three star trackers are chosen, because the star trackers have a reliability of 95% for an operational period of 10 years.[3] For reliability purposes, a redundant set of coarse and fine Sun sensors is used.

In order to achieve a pointing knowledge accuracy of 300 nrad for the orbiter, as mentioned in *FUN-ACS-SS-06*, a combination of an IRU, accelerometers, star trackers and ranging data is used. As described in the article

[2] `http://www.northropgrumman.com/Capabilities/SIRU/Documents/Scalable_SIRU_Family.pdf` [Accessed on: 20 June 2017]
[3] Obtained via email from a company representative : Peter Davidson,Systems Engineer, Space Projects (DK), Space

by Lee et al. [66], using relative attitude from internal sensors, attitude from star trackers and ephemeris data from ranging data a pointing knowledge accuracy of 150 nrad can be achieved. The ephemeris data helps in calculating the change in position of the spacecraft. All instruments meet the specified requirements stated by Lee et al. [66] with significant margins.

Table 9.5: Sensors for Attitude Determination.

Sensor	Characterstics	Accuracy	Unit	Interface
IRU [a]	Angle Random Walk	<0.00005	$\text{arcsecHz}^{-1/2}$	As close to centre of gravity as possible.
	Gyro Bias Stability	<0.0005	$^\circ/hr$	
Accelerometers [b]	Sensitivity	3×10^{-15}	m/s^2	As close to centre of gravity as possible.
Star Tracker [c]	Cross-Boresight	1.5	arcsec	External sensor. Should not face the Sun.
	Roll- Boresight	9	arcsec	
Coarse Sun Sensor [d]	Boresight	1.5	$^\circ$	Two sensors on all sides of the spacecraft.
Fine Sun Sensor [e]	Boresight	0.3	$^\circ$	Two Sensors on both solar arrays.

[a] `http://www.northropgrumman.com/Capabilities/SIRU/Documents/Scalable_SIRU_Family.pdf` [Accessed on: 20 June 2017]
[b] `http://iopscience.iop.org/article/10.1088/0264-9381/26/15/153001/pdf`
[c] Obtained via email from a company representative : Peter Davidson,Systems Engineer, Space Projects (DK), Space
[d] `http://bradford-space.com/products/aoce/css` [Accessed on: 20 June 2017]
[e] `http://bradford-space.com/products/aoce/fss/` [Accessed on: 20 June 2017]

9.4. Actuators

For the actuators, first all design options are listed. Afterwards, the disturbances that cause a torque on the spacecraft are detected and, if possible, quantified. Then, the design process and choices are explained for the ADCS of the orbiter and the landers.

9.4.1. Design Options

To discover the different methods of stabilisation and their associated actuators of the spacecraft, a DOT was created, as can be seen in Figure 9.3. The red blocks are options that have been ruled out in the Mid-term Report by Roza et al. [96] or that cannot be used in the Aphrodite mission. The yellow blocks are options that can be used, but will not be considered due to other reasons.

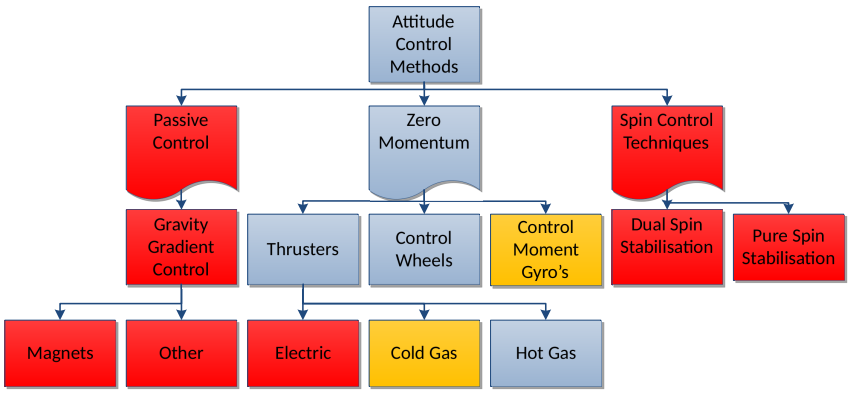

Figure 9.3: Design option tree of attitude determination actuators.

Passive control techniques: Passive control techniques require a strong gravity field and/or a magnetic field and are only applicable to orbiters. However, Mars has no magnetic field, as stated by Acuna et al. [1] and the orbiter has a fixed orientation with respect to the sun instead of to Mars. This orientation is explained in Section 9.2.2. Therefore, passive control is ruled out.

Zero momentum techniques: Zero momentum techniques ensure full control around each axis, which makes it feasible for all mission modes.

Electric RCS thrusters: Electric RCS thrusters were ruled out to decrease complexity of the propulsion system, as described in the report by Roza et al. [96].

Cold gas thrusters: Cold gas thrusters are also not used following the same reasoning as for Electric RCS thrusters.

Hot gas thrusters: Hot gas thrusters, as described in Chapter 8, are taken for auxiliary propulsion (translational motion) and will also be used for attitude corrections (rotational motion), if needed. Their highest advantage is that they can provide high slew rates as mentioned in the book by Wertz and Larson [128].

Momentum exchange devices: Momentum exchange devices are also a good option due to their accuracy performance. Another advantage is that they provide extra gyroscopic stiffness while rotating, which makes the spacecraft less prone to disturbances. Moreover, they can store angular momentum, which then has to be dumped by thrusters. Because the momentum is not directly counteracted, the thrusters have to be fired less often, decreasing the risk of thruster failure. Under momentum exchange devices there are two categories: Control Moment Gyros and control wheels.

Control Moment Gyros (CMG): CMGs show good performance; they can deliver high torque levels, as described by Roser and Sghedoni [94]. However, they are not considered for the Aphrodite mission for two reasons: Firstly, the Aphrodite mission does not need torques higher than 1 N m in its nominal state. The second reason is that CMGs are less reliable because of their high complexity. Because of the reliability requirement for the ADCS over eight years, multiple CMGs have to be taken and in combination with their already high mass, other momentum exchange devices are more suitable for the Aphrodite mission.

Control wheels: Control wheels are momentum exchange devices that will be considered. Note that the definitions of reaction wheels and momentum wheels are often used for the same device. The difference is that momentum wheels have a rotational speed, which increases the gyroscopic stiffness of the spacecraft as described. Reaction wheels are used to impose a torque to counteract disturbances to keep attitude stability, just like momentum wheels. When a reaction wheel has a rotational speed, it acts as a momentum wheel.

Pure spin control: Spin control is letting the spacecraft rotate around its lowest axis, which causes extra gyroscopic stiffness in the other directions. Pure spin control is not an option during landing mode due to hazard detection techniques used. For the orbiter during operational phase, it is not an option, because of the laser pointing: it would impose more risk on the laser system, since it would need a despun platform or a very complex laser actuator system. This is unfavourable, since the performance of the lasers determines mission success for Aphrodite. Combining this with the fact that the solar panels also would need to be repointed at all times, spin stabilisation was crossed out as an option for operational mode. During orbit insertion mode, a slew has to be imposed to follow the correct elliptical trajectory. Combining spin stabilisation with slew would require complex precession control. Turning the spacecraft over the x-or y-axis while it is spinning around its z-axis would also increase the torque required for the slew, resulting in more fuel consumption. In conclusion, pure spin control will not be considered for Aphrodite.

9.4.2. Disturbance Torques:

The disturbance environment causes an external torque on the orbiter that has to be accounted for in order to keep orbital stability and to provide the pointing accuracy to the payload. As the orbiter always keeps the same orientation with respect to the Sun, the external torque will be the biggest around the z-axis. These torques are modelled for the worst-case scenario, where each disturbance torque acts in the same direction. All equations describing the disturbance torques can be taken from the report by Starin and Eterno [111].

Solar Pressure:

Solar radiation pressure (SRP) is exerted on the spacecraft due to sunlight having momentum. If the centre of gravity and the centre of pressure on which this solar radiation acts are misaligned, a torque will be caused. This torque can be described by the equation below:

$$T_s = \frac{\Phi}{cR^2} A_s \left(1+q\right)\left(c_{ps}-c_m\right) cos\left(\phi_i\right) \tag{9.1}$$

In this equation R equals the distance to the Sun in AU. For the orbiter, the difference in distance to the Sun during its orbit around Mars is just 0.003% with respect to the total distance to the Sun as measured from Mars. Therefore, it is assumed that R is constant at a value of 1.5237 AU. Assuming that the solar panels and their orientation are symmetric around the x-and the y-axes, the maximum difference in centre of mass (C_m) and centre of solar pressure (C_{ps}) is 1 m for the orbiter and 0.7 m for the landers. This was an estimate derived from the lay-out of the spacecraft, as described in Section 13.1.1. The average reflectance factor of the spacecraft is given by q, in which zero means it is fully absorbent and one meaning it is fully reflective. Absorbed solar radiation causes momentum, but when the same radiation is reflected, the experienced momentum is twice

as high. The solar intensity at Earth is represented by Φ, which is 1371 W/m^2. The maximum lit surface is A_s, being 20.3 m^2 for the orbiter and 5.70 m^2 for the landers. The solar incidence angle in rad is given by ϕ_i. With the small inclination angle of the orbit and the solar-oriented attitude, an 90° angle is assumed. The speed of light in vacuum is denoted by c.

Atmospheric Drag:
Even though the atmosphere of Mars is a hundred times thinner than that of Earth, there is still atmospheric drag at 400 km altitude (Alexander [2]). The atmospheric drag can be modelled as a single force vector acting on the centre of pressure (C_p). When the C_p and the centre of gravity (C_g) do not coincide, the atmospheric drag creates a torque which needs to be corrected. The atmospheric drag is modelled by Equation 9.2. The atmospheric drag that is imposed when the spacecraft is at more than 400 km altitude is neglected (Starin and Eterno [111]). The drag coefficient is described by C_d and V is the orbital velocity.

$$T_a = \frac{1}{2}\rho C_d A_r V^2 \left(C_{pa} - C_g\right) \tag{9.2}$$

Gravity Gradient:
In orbit around Mars, the C_m may be at an offset from the C_g. The C_m is just a function of mass, whereas the C_g is a function of mass and spacecraft attitude. This offset leads to a torque from the gravitational force acting on the C_m. This torque is the greatest around the z-axis when the x-axis in the solar-fixed reference frame is aligned with the velocity vector. The gravitational constant is denoted by μ and θ_g is the largest possible z-axis deviation in rad, in this case 0.2.

$$T_g = \frac{3\mu}{2R^3}\left[I_z I_y\right] sin\left(2\theta_g\right) \tag{9.3}$$

Internal Disturbances:
The most prominent internal disturbances are: propellant sloshing, rotating machinery such as the laser system, uncertainties in centre of gravity, reaction wheel friction and thruster output mismatch or misalignment as stated in Starin and Eterno [111]. Quantifying these internal disturbances requires exact knowledge of the complete, integrated spacecraft. At this stage, this is not feasible. In Chapter 8, it is explained how propellant sloshing is minimised. Because the thrust levels during operations are low, the thrust misalignment is also not considered to be driving. The external disturbances are therefore expected to be higher than the internal disturbances for operational mode and slew mode. Nonetheless, a momentum margin of 30% will be imposed to take the uncertainties into account.

9.4.3. Attitude Control of the Orbiter

The orbiter is designed to meet all operational requirements. During the operational phase, the orbiter fulfils two main functions: counteracting disturbance torques and providing the laser system with the required stability and pointing accuracy. Note that the orbiter, under normal conditions, does not actively point the lasers itself, because they have actuators implemented in their own system. However, as described in Chapter 4, the spacecraft needs to be able to provide the laser pointing in case an actuator breaks, as a form of mitigation.

Storing Disturbance Momentum
The external disturbance torques, T_D, as explained in Section 9.4.2 result in a momentum that is described by Equation 9.4. To prevent the orbiter from having attitude changes due to this torque, the momentum has to be stored in control wheels. In Table 9.6, the values for external torques around the z-axis are listed, as well as the total momentum per orbit that will be stored in the worst-case scenario where the gravity gradient torque acts in the same direction as the SRP and the drag. There are also external torques around the y-axis, but those are considerably lower. The torque imposed on the orbiter by the disturbance torque will be stored in the control wheel. Not storing this disturbances would lead to a lower power input from the Sun, as there would be deviations from the Sun-oriented attitude, leading to shadowing on the solar panels and a smaller incidence angle.

$$H_{disturbance} = T_D \cdot P_{orbit} \tag{9.4}$$

As can be seen, the biggest disturbance torque is caused by the gravity gradient being two orders of magnitude bigger than the other disturbance torques. The drag is small compared to both other disturbances.

Table 9.6: Sources of external disturbances.

Disturbance source	**Torque** [N m]	**Momentum per orbit** [N m s]
Solar radiation pressure	5.31×10^{-5}	0.23
Drag	4.53×10^{-6}	0.03
Gravity gradient	1.00×10^{-3}	7.38
Total	1.1×10^{-3}	7.65

Meeting pointing accuracy during ranging

To provide the laser ranging system with the required pointing accuracy and orbital stability, the disturbance torques have to be counteracted during the laser ranging. This will be done using a reaction or a momentum wheel, as the other option is to use the RCS thrusters. Using a control wheel, the amount of times the thruster needs to fire reduces, which reduces the risk of thruster failure. The momentum storage needed to keep this accuracy is given by Equation 9.5, taken from the report by Starin and Eterno [111], where θ_a is the pointing accuracy in rad and $P_{pointing}$ is the period over which this value needs to be kept in s.

During ranging, *FUN-ACS-SS-06* specifies a pointing accuracy of 2.5 mrad. Ranging is performed for a maximum of 60 s per orbit for a maximum of one time per twelve orbits. The pointing accuracy needs to be kept over each axis. The momentum storage needed for that can be founf in Table 9.7.

$$H_{stability} = \frac{T_D}{\theta_a} \cdot \frac{P_{pointing}}{4} \tag{9.5}$$

Slew mode as a mitigation strategy

The ADCS is designed in a way that the orbiter can still perform laser ranging if the laser actuator fails. From Chapter 4, it is known that the maximum rotation angle that has to be covered around either the y- or the z-axis is θ_{slew}, being 180° within 360 seconds. In the worst-case scenario, this will happen three times per orbit with ten minutes in between, in which momentum might be dumped. The amount of momentum to be stored in the wheels is described by Equation 9.6. In the worst case, during the slew, the disturbance torque is acting in the opposite way, increasing the control torques that need to be imposed by the control wheels.

$$H_{slew} = \frac{4\theta_{slew} I}{t_{slew}} \tag{9.6}$$

As can be seen in Table 9.7, the momentum needed to be stored in the control wheels is the largest for the slew around the z-axis.

Table 9.7: Required momentum to support payload.

Required torque/momentum storage to	**x**	**y**	**z**
provide pointing stability [N m s]	0.35	0	6.59
impose slew [N m]	0.00	0.12	0.34
provide slew rate[N m s]	0.00	42.34	121.73

Trade-off and results

Commercial products are chosen for the control wheels. To determine the minimum momentum that the reaction wheels need to be able to store, Equation 9.7 is used, where the momentum stability is provided for 60 s. The total momentum needed for the three slew manoeuvres and the momentum caused by disturbances are included. This is then divided by three, because the three worst-case slew manoeuvres allow for momentum dumping in between. The approach to support the orbiter in case of laser actuator failure will be to slew around the y-axis instead of around the z-axis. If that is not possible, thrusters can be used to slew the spacecraft around the z-axis. This means that the driving momentum storage is the one over the y-axis. These actuators will then be implemented over each of the three axes of the orbiter to reduce complexity. This is because reaction wheels need an extra electronics control unit to drive the actuators, so taking the same wheels requires having only one drive control unit and also provides redundancy.

$$H_{min_{wheel}} = \frac{H_{disturbance_{orbit}} + H_{stability} + H_{slew_{total}}}{3} \tag{9.7}$$

Table 9.8: Possible RCS thrusters using ADN monopropellant.

	Thrust range [N]	**Steady state impulse** [s]	**Mass** [kg]	**Average power** [W]
1 N **thruster**	0.25-1	204-235	0.38	8
5 N **thruster**	1-5	243-253	0.40	15

Taking a margin of 30% to account for uncertainties in internal disturbances and using Equation 9.7 the actuators need to provide 55 N m s. A margin of 30% to calculate the required torque to provide the slew rate is taken, leading to a maximum slew torque around the y-axis of 0.16 N m. Reaction wheels from different companies are compared in a trade-off study having the following criteria: momentum storage, maximal torque provided, static and dynamic stability, mass, power and volume. The static and dynamic values are indicators for the internal disturbances that will be generated by three reaction wheels, so a high stability is desired. Finally, reaction wheel W45ES by *Moog Bradford Inc.* was chosen, because of its high momentum storage at a relatively low mass.[4] Its performance parameters are shown in Table 9.10. An additional wheel drive electronics box (WDE) is taken to regulate the control wheels. By choosing these actuators, requirements *FUN-ACS-SS-7* and *FUN-ACS-SS-8* are met.

Reaction Control Thrusters

To dump the momentum from the reaction wheels, thrusters will be used. To have full control over each axis, at least two reaction control thrusters have to be taken per axis. Using multiple thrusters to achieve a higher thrust level is not considered, as this increases the complexity of the propulsion system, resulting in a higher risk of misalignment of thrusters and thruster failure (Starin and Eterno [111]). In the report by Roza et al. [96], it was decided that the RCS thrusters would use the same propellant type as the main propulsion system to reduce complexity. The available ADN monopropellant hot gas thrusters that are currently in development which are described by the paper by Persson et al. [85] and Chapter 8.

Next to momentum dumping, the RCS thrusters also need to be able to perform linear corrections needed for orbit maintenance. There are two thrusters that can function as attitude control thrusters and deliver ΔV for orbit keeping: one with a nominal thrust level of 1 N and one with a nominal thrust level of 5 N. Their characteristics are given in Table 9.8.

Equation 9.8 shows that each of the RCS thrusters would need to dump all the momentum from a saturated control wheel, which in this case would store 70 N m s. The moment arm from the RCS thruster to the centre of gravity is described by L, which is equal to 1.2 m. The thrust level is represented by $F_{thruster}$.

$$t_{burn} = \frac{H_{wheel}}{L \cdot F_{thruster}} \tag{9.8}$$

Assuming that a single thruster over an axis is used and not both, the minimal burn time would either be 33.3 s for the 1 N thruster or 11.7 s for the 5 N thruster. These are both feasible values.

To compare the propellant mass consumption of the two RCS thrusters, Equation 9.9 is used. The 5 N thruster uses 63.2% more propellant compared to the 1 N thruster. They use respectively 14 and 24 g for one slew manoeuvre.

$$m_{propellant} = \frac{F_{thruster} \cdot t_{burn}}{g \cdot I_{sp}} \tag{9.9}$$

Within the ADCS, the thrusters also have to be able to provide the orbiter with its required maximum slew rate in case one of the control wheels fails. This is also done when a slew has to be performed due to unexpected conditions requiring an amount of momentum that the control wheels cannot store. The most critical situation in which this could happen would be when laser actuator failure occurs and it is desired to slew the spacecraft 180° over the z-axis in 360 s. As can be seen in Table 9.7, the momentum needed for that is 121.7 N m s. Equation 9.10 explains how much thrust is needed. The mass moment of inertia over the z-axis is denoted by I. The slew profile of the manoeuvre, that defines for how long the spacecraft is accelerated up to the desired slew rate and then decelerated again, determines α. Combining Equations 9.10 and 9.11, the minimal burn times for slew are determined, being 25.4 s for the 1 N thruster and 5.07 s for the 5 N thruster.

[4] `http://www.moog.com/literature/Space_Defense/Spacecraft/AOCS-GNC/Reaction_Wheel_Unit.pdf` [Accessed on: 16 May 2017]

$$F_{thruster} = \frac{I \cdot \alpha}{L} \tag{9.10}$$

$$\alpha = \frac{\omega}{t_{acceleration}} \tag{9.11}$$

Summarising, the 5 N thruster has an overall better performance, being more efficient and being able to provide the slew rate within a shorter timeframe. On top of that, its mass is only 0.2 kg more than for the 1 N RCS thruster. The only downside is that the power required is almost twice as high. However, as it needs this power for shorter amounts of time, since the required burn times are lower, it does not have a big impact on the trade-off. With this reasoning, the 5 N thruster is chosen. Each axis will have two thrusters to provide for full rotational control. For redundancy, twice the amount is taken as usually is done for missions with a long operational lifetime. The ADCS for the orbiter now does not have a single point of failure, meaning that requirement *FUN-ACS-SS-04* is met. The ΔV taken for ADCS is 160 m/s, which is enough to dump momentum cumulated during counteracting torques and providing the pointing stability for eight years, including a margin of 40 %. This margin can account for control wheel failure and attitude control in the other modes.

Compliance with Orbit Insertion

During orbit insertion, the ADCS has two main functions: imposing a slew over the x- and/or the y-axes to ensure the elliptical trajectory, as given in requirement *FUN-ACS-SS-8* and counteracting the disturbance torque over the x- and/or y-axes caused by the thrust. The slew rates that are required are much lower than the slew rate that the momentum wheels were designed for, so this will not change the design of the actuator system of the orbiter, even when taking into account the larger moment of inertia due to the landers that are still attached at that stage. The mass moment of inertia around the x-axis is below 8000 kg m^2. Using Equation 9.6, it can be determined that the momentum storage needed is 56 N m s, which is well below what the ADCS of the orbiter was designed for. Since thruster misalignment, C_g uncertainties and mismatch of the output of the thrusters cannot be properly quantified now, designing for this will not lead to sensible results. Nonetheless, an approach to counteract the disturbances can be described.

For the resistance of the torque imposed by the main thrusters, the first measure will be to throttle the engine. If there are still deviations detected by the sensors, the RCS thrusters and the control wheels can be used to stabilise the the spacecraft as well. This is a method that was also used by the Mars Global Surveyor and ExoMars. [5,6]

9.4.4. Attitude Control for the Landers

For the landers, orbit acquisition mode and landing mode are determined to be driving. This is because landing on Phobos and Deimos is risky, meaning that it is favourable to have a design that can impose high slew rates to be able to make quick corrections, but also a design that is able to provide a stable landing attitude.

Orbit acquisition mode

The orbit acquisition mode is activated once the landers arrive at their destinations: they have to perform a slew manoeuvre of 180° over the x-or the y-axis to prepare them for their landing sequences. the main thrusters have to be pointed downwards towards the surface. The timespans within which this has to be done are respectively 2000 s and 4000 s for the Phobos and the Deimos lander. Using Equation 9.6 the momentum storage needed for that is determined, using the mass moments of inertia for the landers with retracted solar panels. The values can be found in Table 9.9. Because no research for Aphrodite has been done yet on slewing the landers while having the main propulsion or a set of RCS burners thrusting, it is now assumed that the turn will be done while the landers have slowed down to a low velocity before turning.

Landing mode

During landing mode, the ADCS has to correct for rotational deviations within a timeframe of respectively 8000 s and 2000 s for the Phobos and Deimos lander. Requirement *FUN-ACS-SS-11* specifies a maximum allowable deviation of 2° over the x-and the y-axes, to make sure that the feet of the landers are pointed towards the surface. Philae used a momentum wheel of 5 N m s on the z-axis to ensure this stabilisation. Having a rotating

[5] http://blogs.esa.int/rocketscience/2016/10/17/burn-baby-burn-the-technology-of-the-mars-orbit-insertion-burn/ [Accessed on: 30 July 2017.]

[6] http://www.msss.com/mars/global_surveyor/mgs_msn_plan/section5/section5.html [Accessed on: 30 July 2017]

Table 9.9: Momentum storage needed over the x-axis for the driving modes of the landers.

Disturbance	Phobos	Deimos
t_{slew} [Nm]	2000	4000
θ_{slew} [°]	180	180
T_{slew} [Nm]	3.33×10^{-4}	8.33×10^{-5}
H_{slew} [Nms]	0.666	0.333
$\theta_{a_{landing}}$ [°]	2.00	2.00
$t_{landing}$ [s]	8000	3000
$H_{landing}$ [Nms]	0.589	2.26

wheel over the z-axis, would make the spacecraft less prone to disturbances in the x- and y-direction (Budnik and Morley [20]). The momentum storage required is determined by Equation 9.5. The results can be found in Table 9.9.
Accurately quantifying disturbances other than the SRP and the gravity gradient on Phobos and Deimos is not feasible, because little is known about their surfaces. However, misalignment of the RCS thrusters can occur, causing rotational errors. Besides, the torque that will occur with a misalignment of 1 cm is not higher than 2 Nm, which can be solved by throttling of the RCS thrusters during landing.

Trade-off and results

A reaction wheel that is spun up and therefore acts as a momentum wheel is used on the z-axis. This can also be used to correct disturbances or impose a torque around the z-axis next to providing the gyroscopic stiffness around other axes. The momentum storage required for the aforementioned two modes are shown in Table 9.9. It is the largest over the x-axis, so the values for the x-direction are given.

The values for the two landers are similar: the momentum to be stored is within the range of 0.4 Nms-2.5 Nms. This is a range that can be covered by the same type of reaction wheels.[7,8] Note that, although there are direct requirements related to the z-axis, it does not mean that the lander can turn uncontrollably around the z-axis. The wheel on the z-axis is chosen such that it can also store additional momentum and provide a torque if desired. It needs to have a storable momentum up to at least 5 Nms. This is bigger than for the control wheels around the other axes, simply because it will have more functions during the landing sequence and it will be continuously rotating at higher speeds than the other control wheels.

For the other axes, the torques required for landing are low, so this is not a driving factor for the reaction wheels. The momentum storage will be at least 3 Nms. After performing a trade-off having the same criteria as for the control wheels for the orbiter, the control wheels are shown in Table 9.10. The reason for the big margins is not only the uncertain disturbance torques, but also the fact that no redundant control wheels are taken, because the lifetime of the ADCS of the landers is very low compared to the lifetime of eight years for the orbiters. To perform the landing sequence, as described in Chapter 7, the same linear RCS thrusters as for the orbiter are taken. They can be used when unanticipated fast slew manoeuvres are required. Having the control wheels with the RCS thrusters as a back-up, there is full control over each axis and no single point of failure. This means that requirements *FUN-ACS-SS-04* and *FUN-ACS-SS-14* are satisfied. The propellant needed for landing is included in the propellant budget margin of 100% as described in Chapter 7, because accurately quantifying the disturbances at Phobos and Deimos is not possible. This is the same margin as used for the ESA Phootprint mission in the report by Rebuffat [92].

Compliance with orbit insertion mode

The slew rate required over the x-and the y-axis during orbit insertion mode for the landers, needed to follow an elliptical trajectory, are given by requirement *FUN-ACS-SS-10*, being 0.0774 °/s. Using Equation 9.6 with the mass moments of inertia with deployed solar panels, it was determined that the maximal slew rate over the x- and the y-axis are 0.0094 and 0.0193 Nms, so the control wheels cannot provide the required slew rate. Instead, the thrusters will be used. This is the same orbit insertion strategy as used by the Mars Global Surveyor (MSG).[9]

[7] `http://bluecanyontech.com/reaction-wheels/` [Accessed: 20 May 2017]
[8] `https://www.rockwellcollins.com/Products_and_Services/Defense/Platforms/Space/RSI_12_Momentum_and_Reaction_Wheels.aspx` [Accessed: 20 May 2017]
[9] `http://www.msss.com/mars/global_surveyor/mgs_msn_plan/section5/section5.html` [Accessed on: 16 June 2017]

Table 9.10: Actuators for the control system.

Actuator	N	H[Nms]	T[Nm]	Static Balance [gcm]	Dynamic Balance gcm^2	Mass [kg]	Size[mm]	Pmin [W]	Pmax [W]
W45ES (orbiter)	4 in pyramid	70	0.25	0.5	5	8		30	150
WDE (orbiter)	1	-	-	-	-	2.3		Implied in W45ES	Implied in W45ES
RW1 (lander)	2 (x and y)	4	0.06	n/a	n/a	2.5	17x17x7	3	30
RW8	1 (z)	8	0.11	n/a	n/a	3.6	19x19x7	3	40

Verification and Validation

The code used to quantify the maximum disturbances was verified using the Firesat II example from the report by Starin and Eterno [111]. All the input values for the disturbance torques and the slew and stability are known and given as input to the code. The difference on the individual momentum storage requirements using the inputs from Firesat II were within 3% between the calculated values and the given output values in the source. Also, the actuator setup is compared to previous missions. For example, the Mars Reconnaissance Orbiter (MRO). MRO has four reaction wheels that could store up to 100 N m s, being 10 kg per piece, which can be found in the paper by You et al. [134]. This is a comparable setup when considered that MRO has a higher dry mass compared to the orbiter, which explains the higher momentum storage capacity.

9.5. ADCS Architecture

In Figure 9.4, the architecture diagram of the ADCS is shown. The control laws define when momentum needs to be dumped, which can happen because a desired attitude will add momentum that cannot be provided to the wheels, because the wheel already stored momentum up to a certain amount, or when the wheel is saturated. The RCS thrusters will be activated when a rotational torque needs to be provided which exceeds the maximum torque of the control wheels. Note that Figure 9.4 shows the diagram for the orbiter. The only difference with the diagram for the ADCS architecture of the landers is the wheel drive electronics box, which is not present. This is because the smaller control wheels require less power regulation.

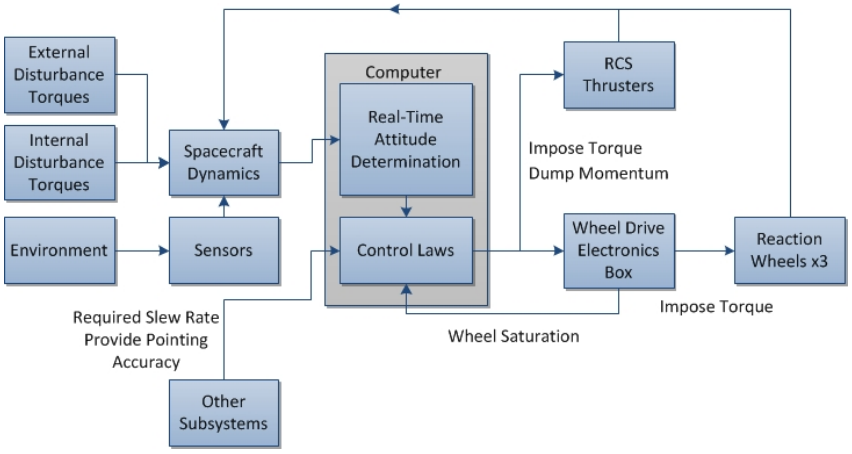

Figure 9.4: Diagram of the ADCS systems.

9.6. Risk Analysis

Good risk management decreases the chance of subsystem failure. A top to bottom risk analysis is performed using a FTA, which can be seen in Figure 9.5. The risks that stem from the ADCS itself are listed below, including their likelihood and impact. The mitigated risks can be found in Table 9.11.

1. Bearing failure: Bearing failure is a restricting factor for the lifetime of the reaction wheels. For the landers, the likelihood of bearing failure occurring is improbable, because of the short lifetime that the reaction wheels have to operate. For the orbiter, the probability of bearing failure is brought back to unlikely, due to implementation of a redundant reaction wheel and choosing commercial, space-qualified reaction wheels. Moreover, a way to limit bearing failure is to perform more frequent moment dumping when unanticipated disturbance torques are experienced, so the average rotational speed decreases.

2. Power shortage: The power needed to impose the required torques and to provide the needed stability is

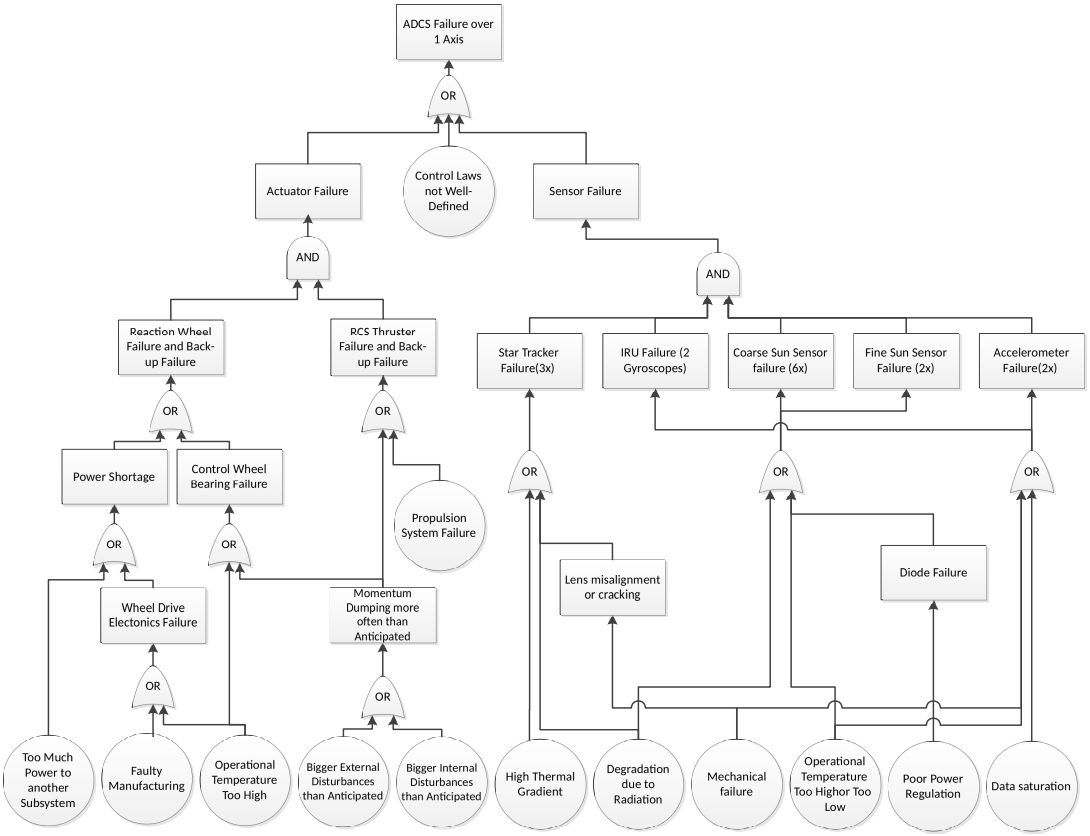

Figure 9.5: Fault Tree Analysis of the ADCS.

dependent on the rotational speed of the wheel. If the power needed is not available, it is possible to perform momentum dumping with the RCS thrusters, which need less power, so the required power for the control wheel decreases. All redundant sensors can be turned off in case of power shortage. The IRU can be turned off when ranging operations are not being conducted.

3. Hardware failure of wheel drive electronics: The WDE can fail due to reasons that are not directly related to power supply. It can have manufacturing issues or cabling failure. Because the WDE does not consist of mechanically moving components, the likelihood of hardware failure is low. Moreover, the WDE chosen is space-qualified.

4. Thruster failure: The impact of thruster failure for the orbiter is mitigated by taking one RCS thruster extra for each of the RCS thrusters. For the landers, the likelihood of RCS thruster failure was already low due to their short operational lifetime.

5. Control law bug: If a control law that is programmed into the spacecraft computer contains a bug, there is a possibility that not all of the functions can be covered. This can be prevented by taking two separately developed codes onto the spacecraft and extensive testing.

6. Lens misalignment or cracking: During landing or other high acceleration operations, the lenses in star trackers can move or crack. The likelihood of this risk is unlikely as the star trackers are rated for high acceleration operations. However, the impact the of this risk is critical.

7. High thermal gradient: As the star trackers are partially inside and partially outside the spacecraft, high thermal gradients may lead to thermal stress and thermo-mechanical fatigue. The likelihood of his risk is average and the impact is moderate. The impact is moderate, as the multi-layer insulation around the spacecraft covers large areas of the star trackers outside the spacecraft.

8. Data saturation: Data saturation in IRU and accelerometers can take place when unexpected large rotations or accelerations are experienced. Data saturation can have catastrophic impact, as was observed in the Schiaparelli failure.[10] The likelihood of the risk can be brought down to improbable by adding safeguards to

[10] `http://exploration.esa.int/science-e/www/object/doc.cfm?fobjectid=59175` [Accessed on: 26 June 2017]

prevent and detect data saturation.

9. Degradation due to radiation: This is a general risk valid for all components of the spacecraft. However, given that star trackers and Sun sensors are partially or completely outside the spacecraft, radiation plays a more significant role. The impact of this risk can range between marginal or critical. Nonetheless, by choosing sensors that are radiation hardened and rated for high radiation doses, the likelihood of this risk can be reduced to unlikely.

10. Diode failure: Overvoltage, overcurrent and extremely high temperatures can lead to diode failure in the Sun sensors. This risk is mitigated by using space grade power regulators and choosing sensors capable of functioning over a large range of temperatures. While the impact of the risk is moderate, its likelihood is improbable.

Table 9.11: Mitigated risk map of the ADCS.

Almost certain					
Likely					
Average		2	7		
Unlikely		4,5	1	6,9	
Improbable		3	10		8
Likelihood / **Impact**	Negligible	Marginal	Moderate	Critical	Catastrophic

9.7. Sensitivity Analysis

To evaluate robustness of the design, the uncertainties on the requirements of the design are evaluated to check if the hardware chosen would change if the requirements change by their uncertainty. This is done for the slew mode for the orbiter, since that is the driving mode that requires momentum up to an order of magnitude greater than for the other mode.

Slew mode for the orbiter.
Varying the mass moment of inertia by 10%, H_{min}, as denoted by Equation 9.7, results in an increased momentum storage from 55 N m s to 61 N m s. The same happens if the slew rate required is increased, following from the linear relation in Equation 9.6. An increase in either slew rate, mass moment of inertia, or momentum storage by unexpected internal disturbances of 70% is needed to make the control wheels not suited for slew over the y-axis. The torque that the reaction wheels can deliver is only 0.25 N m and is only surpassed by a 200% increase of mass moment of inertia, or momentum storage by unexpected internal disturbances. The momentum wheels are therefore designed for a large range of uncertainties. On top of that, failure of more than two wheels can be accounted for by using the RCS thrusters.

Landing mode for the Phobos lander.
For the Deimos lander, the required moments of inertia have a momentum storage margin of almost 200%, meaning that a sensitivity analysis does not add value. The Phobos lander however, has a driving landing mode because of the long time over which the landing stability needs to be provided. Increasing the landing time by 225% will demand momentum wheels that can store than more 5 N m or momentum dumping by the RCS thrusters, which is unfavourable because the stability required would be lost during the momentum dumping. Therefore, doubling the landing times for the Phobos lander should be avoided.

[This page is intentionally left blank]

10
Command and Data Handling

The command and data handling (C&DH) system is the central hub from where all subsystems are controlled. This system is also responsible for the distribution and storage of the generated data. First, Section 10.1 gives a short summary of the subsystem. Section 10.2 shows the requirements with which the C&DH system has to comply. In Section 10.3, the hardware is chosen and the cost of the software is estimated. Finally, the reliability and risks are discussed in Section 10.4.

10.1. Design Overview

The orbiter is equipped with five CompactPCI 6U computers and one 1 Tb Airbus solid state recorder. Both landers are equipped with seven CompactPCI 6U command handling units and one MPC8260 solid state data recorder. An overview of all components is given in Table 10.1. The secondary payload is incorporated in the design by adding the required data rate of the payload to the data rate budget.

Table 10.1: The C&DH budget and parameters.

Element	**Mass** [kg]	**Cost** [M€]	**Power** [W]	**Radiation** [krad]	**Dimensions** [mm]
Command Handling Orbiter	4.245	1	2 × 7.5 W @5 V	100	233 × 160
Command Handling Lander	5.943	1.4	2 × 7.5 W @5 V	100	233 × 160
Data Handling Orbiter	8	0.6	10 W @10 V	40	250 × 250 × 300
Data Handling Lander	2.2	0.2	6.5 W @15 V	25	330 × 165 × 38
Software Cost	-	5.1	-	-	-

10.2. Functional Analysis

In Table 10.2 the compliance of the requirements are shown.

Table 10.2: C&DH Requirements.

ID	**Requirement**	**Section**	**Compliance**
OPS-DG-SS-11	The computer system shall be able to store 2115 Mbits before overwriting.	10.3.2	✓
OPS-DG-SS-12	The computer system shall have a processing power that handles all real time operations of the satellite	10.3.1	✓
OPS-DG-SS-13	The computer system shall have a throughput of 300 KIPS.	10.3.1	✓
OPS-DG-SS-14	The computer system shall have a maximum mass of 20.6 kg for the orbiter and 10.4 kg for each lander.	10.1	✓
OPS-DG-SS-15	The computer system shall have a maximum power usage of 103 W for the orbiter and 69 W for each lander.	10.1	✓
OPS-DG-SS-16	The computer system shall have a maximum cost of M€27 (FY17).	10.1	✓
OPS-DG-SS-17	The computer system shall not have any single point of failure.	10.4	✓
OPS-DG-SS-18	The computer system shall have a minimum reliability of 98% for the orbiter and 99% for the lander during the operational time.	10.4	✓
OPS-DG-SS-19	The computer system shall be verified to withstand a total radiation dose of 10 krad.	10.1	✓

10.3. Design Approach

The hardware consists of two main aspects. The first being the central processing unit, which is chosen based on the required instructions per second (IPS) that have to be processed. The board computer also has to contain enough memory to store the code for all subsystems. The second part, the memory, is needed to store all data until it can be sent to Earth. Besides the hardware, the cost of the software is estimated.

10.3.1. Command Unit

The command unit for the orbiter has to handle approximately 300 KIPS as shown in Table 10.4. This is not much for today's standards and many options exist. The CompactPCI 6U with RAM6000 Board computer is chosen, as it has a high reliability.[1] It is able to compute 2.1 MIPS. The CompactPCI 6U has 64 Mb of RAM which is sufficient to store the 1.1 Mb of code and 0.9 Mb of data required for the operations. The lander will require 240 KIPS and because this is similar to the orbiter the same command unit will be used.

10.3.2. Memory Unit

The generated household data is difficult to estimate and has multiple uncertainties. It is based on the parameter which have to be measured, the precision and the execution frequencies and is presented in Table 10.4. For the landers, all this passively generated data has to be stored for a maximum of three days in addition to two hours of intra system ranging data. For the laser ranging, 30 pulses are sent every second with a precision of 100 bits. The secondary payload generates an additional 10 Mb each day. The total memory size required is calculated with Equation 10.1.

$$8.3 \cdot 3 \cdot 86400 + 30 \cdot 0.1 \cdot 2 \cdot 3600 + 10 \cdot 3 = 2145 Mb \tag{10.1}$$

The MPC8260 Solid State Data Recorder is used, which can store up to 16384 Mb.[2] This storage is capable of storing up to 23 days of data in case of safe mode.

The data storage unit needs to be capable of storing data for 28 days during the solar conjunction. Since communication between the landers and the orbiter is still possible, it is opted to equip the orbiter with a larger storage unit (Airbus Solid State Recorder).[3] This storage unit can store up to 1 Tb and would enable to store all data of the three systems for 450 days.

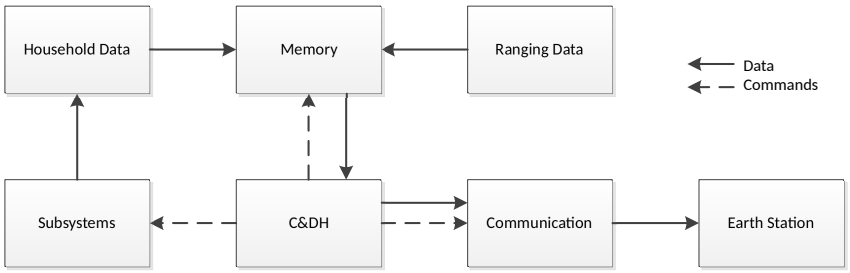

Figure 10.1: The data handling diagram shows how the data flows trough the components.

10.3.3. Software

The development of software for space applications is a very expensive process. The size of software is mostly expressed in source lines of code (SLOC). One SLOC consisting of 200 bits is estimated to cost €500, this includes the coding as well as the testing of the code. The code of the orbiter is 2034.4 Kbits as shown in Table 10.4, which is equivalent to 10.1 thousand SLOC. This would total up to M€5.1 for all the required code. In Figure 10.2, the interactions between the subsystems and the C&DH are shown for which software has to be developed.

[1] `https://www.digchip.com/datasheets/parts/datasheet/568/RAD6000-pdf.php` [Accessed on: 8 June 2017]
[2] `https://www.sst-us.com/SSTL/files/21/2158d012-854d-4fa4-a567-2c0a8b530104.pdf` [Accessed on: 8 June 2017]
[3] `http://datasheets.globalspec.com/ds/667/AirbusGroup/DD01972E-4723-48B8-BCDA-1954C5B895AA` [Accessed on: 8 June 2017]

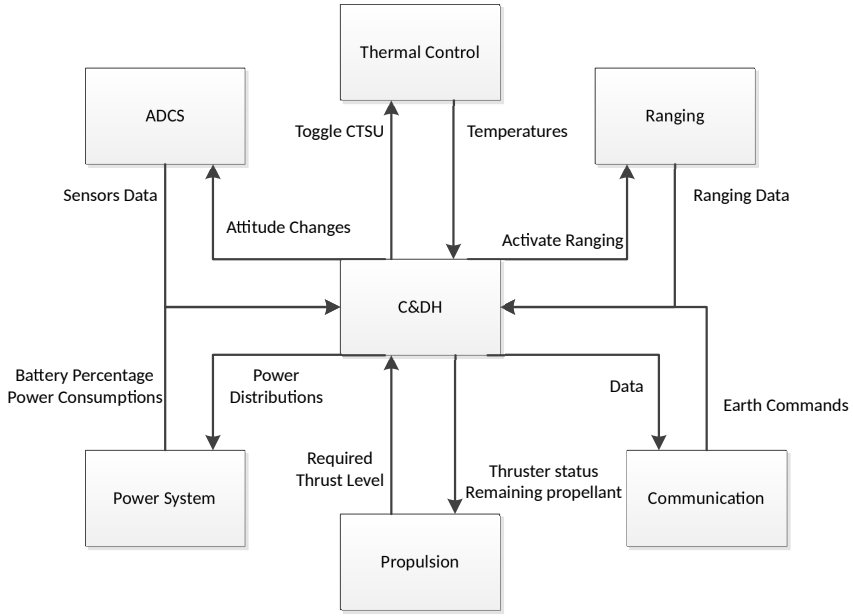

Figure 10.2: The software map shows the interactions between the C&DH and the other subsystems.

10.4. Reliability Analysis

Of all spacecraft systems, the command handling systems are the most prone to failure. The CompactPCI has a mean time between failures (MTBF) of 375000 hours.[4] In order to get a reliability of 98% over eight years, five units are used on the orbiter. This is calculated in Section 16.2. There will always be two active in parallel and in case of failure an extra board computer will be booted. Most spacecraft use redundant CPUs in order to ensure their reliability. Most notably, the Space Shuttle used five APA-101S computers.[5] Due to the high risk introduced by the landing on Phobos and Deimos, two extra units are required, as shown in Section 16.2, to make the reliability of 99% over eight years. Mitigation of these risks requires modifications to be made to the CompactPCI, which may lead to high prices.

10.5. Risk Analysis

The C&DH consists of many small components which all have a chance of failing. To give a clearer overview, a fault tree of the orbiter is shown in Figure 10.3. This fault tree only includes the most likely failures. The risks are based on the layout of the RAD6000 as explained by Martin [72]. Mitigation of these risks require modifications to be made to the CompactPCI, which may lead to high prices. The mitigated risks for one C&DH system can be found in Table 10.3.

1. Clock failure: The C&DH system has three clocks for each unit. Two of these are driving the RAD6000 CPU and one takes care of the other processes. The risk can be mitigated by adding another 50 MHz clock.

2. Software error: The software for all processes is written on all electronically erasable programmable read-only memory (EEPROM) and static random-access memory (SRAM). If both of these are cleared at the same time, no processes can be executed. A solution is to copy the software from another system back to the SRAM.

3. Reboot failure: A reboot occurs when the SRAM gets cleared. The EEPROM will be copied to the SRAM. When the C&DH does not get enough power, the start-up random access memory (SuROM), which performs the start-up cannot be activated. This risk is only possible to be mitigated by not rebooting the C&DH. Not rebooting the C&DH introduces more risks and will therefore not be done.

[4] `https://www.digchip.com/data/568/rad6000_sbsc.pdf` [Accessed on: 8 June 2017]
[5] `http://www.cpushack.com/space-craft-cpu.html` [Accessed on: 8 June 2017]

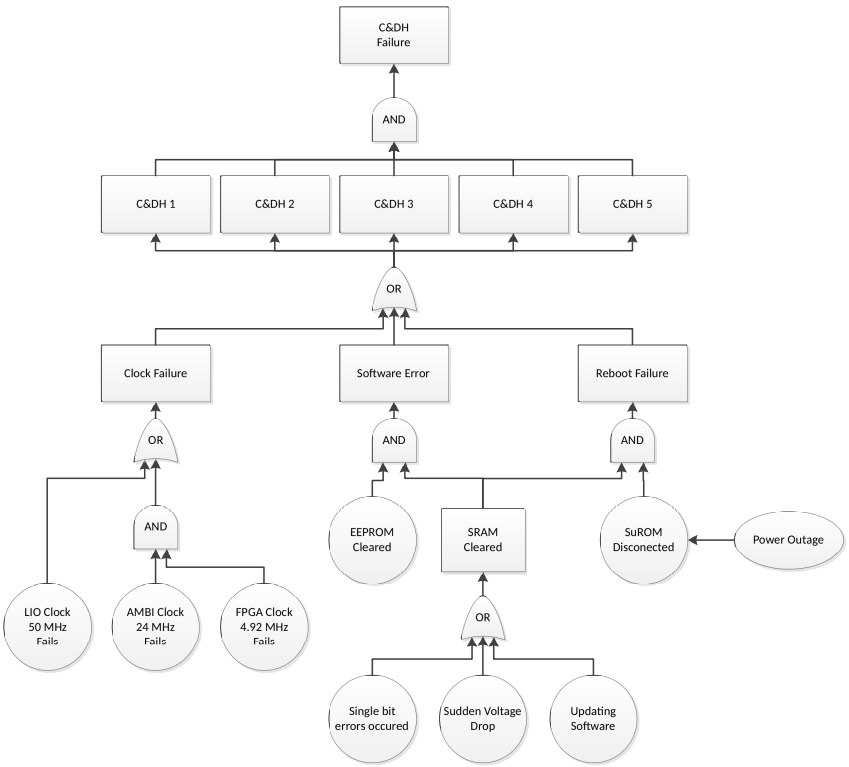

Figure 10.3: The fault tree with the most important risks of the C&DH subsystem.

Table 10.3: Mitigated risk map of the C&DH subsystem.

Almost certain					
Likely		1			
Average			3		
Unlikely			2		
Improbable					
Likelihood / **Impact**	Negligible	Marginal	Moderate	Critical	Catastrophic

Table 10.4: This table shows the required throughput of the processor and the required space for RAM, as well as the data generated by the equipment. This code size and the throughput are taken from Wertz and Larson [128], the data generation is estimated with the execution frequency from Wertz and Larson [128] and the complexity of the system.

Function	Size [Kbits]		Throughput [KIPS]	Data Generation [bps]
	Code	Data		
Ranging				
Laser Transmission	16.0	64.0	7.0	2000
Photon Detection	16.0	40.0	3.0	2000
Communications				
Command Processing	16.0	64.0	7.0	100
Telemetry Processing	16.0	40.0	3.0	2000
Attitude Sensor Processing				
IRU	12.8	8.0	9.0	100
Coarse Sun Sensor (x12)	2.0	0.4	1.0	10
Fine Sun Sensor (x2)	8.0	1.6	2.0	10
Star Tracker (x3)	32.0	240.0	2.0	1
Attitude Determination & Control				
Kinematic Integration	32.0	3.2	15.0	100
Error Determination	16.0	1.6	12.0	1000
Precession Control	52.8	24.0	30.0	100
Thruster Control	9.6	6.4	1.2	20
Reaction Wheel Control	16.0	4.8	5.0	20
Complex Ephemeris	56.0	40.0	4.0	500
Orbit Propagation	208.0	64.0	20.0	1000
Autonomy				
Simple Autonomy	32.0	16.0	1.0	100
Complex Autonomy	240.0	160.0	20.0	1000
Fault Detection				
Monitors	64.0	16.0	15.0	50
Fault Correction	32.0	160.0	5.0	50
Other Functions				
Power Management	19.2	8.0	5.0	10
Thermal Control	12.8	24.0	3.0	100
Operating Software				
Executive	56	32	+30%	0
Run-Time Kernel	128	64	0	0
I/O Device Handler	32	11.2	+5%	0
Build-In Test and Diagnostics	11.2	6.4	0.5	200
Math Utilities	19.2	3.2	0	0
Total Orbiter	**1123.6**	**910.8**	**294.6**	**10371**
Total Lander	**947.6**	**862.8**	**237.6**	**8471**

[This page is intentionally left blank]

11 Power

The purpose of this chapter is to present the power subsystem of the Aphrodite mission. First, a global overview is given in Section 11.1. Secondly, a functional analysis is presented in Section 11.2. Thirdly, the design approach and the design itself are presented in Section 11.3 and Section 11.4, respectively. Afterwards, in Section 11.5 a risk analysis will be presented. Finally, the sensitivity analysis is performed in Section 11.6.

11.1. Design Overview

The power subsystem consists of the solar panels, the batteries and, the power distribution and conversion equipment. It is designed to provide the necessary power to the electronic components in the spacecraft. The solar cells that are used are TJ GaAs and the batteries are lithium-ion (Li-Ion). Furthermore, the solar panels consist of sandwich panels with a carbon fibre reinforced polymer skin and an aluminium core. The budget for the orbiter can be found in Table 11.1 and for the landers in Table 11.2. The cable mass is estimated to be 4.5% and 6.8% of the total power mass for the orbiter and landers, respectively, as stated by Brown [19]. The secondary payload is considered in this design by adding 10 W to the budget for the secondary payload during the operational and eclipse phase.

,

Table 11.1: Budget for the hardware used in the power subsystem of the orbiter.

Component	**Quantity**	**Total mass** [kg]
TJ GaAs Solar Cell	3975	11.83
Battery	8	5.75
Solar Panel	2	72.71
Regulators & Chargers	9	0.1

Table 11.2: Budget for the hardware used in the power subsystem of the landers. Both landers have the same components, except for the number of batteries.

Component	**Quantity**	**Total mass** [kg]
TJ GaAs Solar Cell	940	2.71
Battery Phobos	10	6.48
Battery Deimos	35	19.44
Solar Panel	2	17.19
Regulators & Chargers	10	0.1

11.2. Functional Analysis

The power subsystem is key for the success of the mission, since any power shortage can cause a complete mission failure. Therefore, the power subsystem has to be designed to take into account the consumption of every component in the different modes. Furthermore, the power subsystem has to achieve a reliability of 98.3%. The total power, supplied by the system at the different stages of the mission is presented in Table 11.3. A more detailed overview of the power budget is presented in Table 14.2 of Chapter 14. Additionally the requirements for the power subsystem are presented in Table 11.4.

Next to that, to ensure that the power subsystem is designed adequately, the eclipses and cycles need to be taken into account. These are presented in Table 11.5. Figure 11.1 and Figure 11.2 show the graphs of the eclipses of the Martian moons, as computed in Chapter 5.

Table 11.3: The budget that the power subsystem, including the secondary payload, needs to provide during the different modes.

Unit	**Separation** [W]	**Burn** [W]	**Travel** [W]	**Landing** [W]	**Operations** [W]	**Safe Mode** [W]	**Eclipse Operations** [W]
Phobos Lander	135.2	472.8	269.3	474.3	210.0	152.8	187.9
Deimos Lander	135.2	472.8	257.2	474.3	197.9	152.8	187.9
Orbiter	565.0	1035.7	1050.4	-	845.6	388.0	278.4

Table 11.4: Requirements for the power subsystem.

Requirement ID	**Requirement**	**Section**	**Compliance**
SUB-PW-001	The power subsystem shall be able to provide a power of 1050.4 W for the orbiter.	11.4	✓
SUB-PW-002	The power subsystem shall be able to provide a power of 474.3 W for the Phobos lander.	11.4	✓
SUB-PW-003	The power subsystem shall be able to provide a power of 474.3 W for the Deimos lander.	11.4	✓
SUB-PW-004	The power subsystem shall provide 10 W for the secondary payload.	11.4	✓
SUB-PW-005	The power subsystem shall have a reliability of 98.3% after eight years.	16.2	✓
SUB-PW-006	The power subsystem shall provide the necessary average power for the subsystems during all modes.	11.4	✓
SUB-PW-007	The power subsystem shall control and distribute power to the spacecraft.	11.4	✓
SUB-PW-008	The power subsystem shall have a maximum depth of discharge of 60%.	11.4	✓

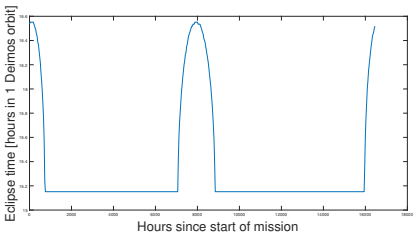

Figure 11.1: Eclipse time of Deimos.

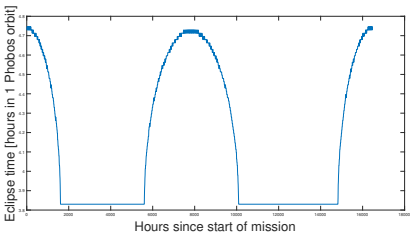

Figure 11.2: Eclipse time of Phobos.

11.3. Design Approach

In this section the approach taken to design the power subsystem is explained. First, the primary source of power is selected and sized from Section 11.4.1 to Section 11.4.3. For this the eclipse times need to be taken into account. The primary power source is heavily influenced by the different modes of the spacecraft and the average power needed. Secondly, the secondary energy source is designed, which serves as main power source during landing and eclipse, this is presented in Section 11.4.4. This is designed with the peak power values. Finally, in Section 11.4.5, a power regulation and control system is presented.

11.4. Subsystem Design

This section deals with presenting the subsystem design. The primary energy source are solar panels and the batteries serve as energy storage during eclipse. The power regulation and control is performed by diodes and regulators.

11.4.1. Solar Cell Selection

The selection of the solar cell is crucial for the design of the solar panels. Every type of solar cell has a different efficiency and reliability. In the space industry, the most commonly used solar cells are multi-junction cells

Table 11.5: Key characteristics that will drive the design of the power subsystem.

Parameter	Orbiter	Phobos Lander	Deimos Lander
Eclipse time [h]	0.77	3.84	15.1
Day time [h]	1.20	3.84	15.1
Eclipse power [W]	300	190	190
Energy output [Wh]	231	732	2869
Cycles [-]	3.6×10^4	9.2×10^3	2.3×10^3

due to their small thickness, lightness and efficiency, as explained by Wertz and Larson [128], Lin et al. [68] and Bett et al. [15]. Multi-junction cells are composed of multiple layers of different materials to absorb as much energy from the light as possible. Therefore, the Aphrodite mission is also equiped with multi-junction cells. The two most efficient solar cells in the space market are InGaP/GaAs/Ge from AzurSPace and InGaP/GaAs/InGaAs/InGaAs from SolAero Technologies Corp.[1,2] In order to choose between them, they were compared in efficiency and TRL in Table 11.6. From Table 11.6, it can be concluded that to fulfil the reliability requirement, the best option is a GaInP/GaAs/Ge composition, because of its high TRL. This cell is bought with an external silicon bypass diode, interconnectors and cover glass, but a blocking diode is added to each cell to prevent the back-flow of the current. A number of cells are placed in a series arrangement to obtain a certain voltage, so the voltage of each cell adds up, after which the groups of cells are placed in parallel. This can be seen in Figure 11.3.

Table 11.6: Relevant information about the choice for the two solar cells on the market with the highest efficiencies.

Composition	Efficiency [%]	TRL
InGaP/GaAs/Ge	30	9
InGaP/GaAs/InGaAs/InGaAs	33	7

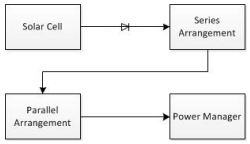

Figure 11.3: Diagram of the connection from the cell to the power manager.

11.4.2. Solar Array Sizing

After choosing the solar cells, the solar array is designed. For this, the values shown in Table 11.3 are used. The solar panels are sized for the maximum power needed, when the panels are deployed, to ensure that the area is large enough for the proper functionality of every component. But, to obtain the total power needed for operations, the solar arrays' power was calculated with Equation 11.1, where P_e is the power needed during eclipse, t_e is the eclipse time, η_e is the photovoltaic efficiency during the eclipse period, P_d is the power required during day time, t_d is the day time and η_d is the efficiency during day time as stated by Wertz and Larson [128]. Photovoltaic efficiencies of 86% and 73% were used for day and eclipse, respectively (Wertz and Larson [128]). These are the efficiencies for the conversion of energy. After the power required from the arrays has been computed, the respective cell efficiency, absorptivity and degradation is added. For the degradation, a value of 1% per year was used (Wertz and Larson [128]).

$$P_{SA} = \frac{\frac{P_e t_e}{\eta_e} + \frac{P_d t_d}{\eta_d}}{t_d} \tag{11.1}$$

[1] http://www.azurspace.com/index.php/en/products/products-space/space-solar-cells [Accessed on: 5 June 2017]
[2] https://solaerotech.com/products/space-solar-cells-coverglass-interconnected-cells-cic/ [Accessed on: 3 June 2017]

Thereafter, the solar irradiance is taken into account. For this, the irradiance at the apohelion of the Mars orbit around the Sun is used, so the irradiation for the orbiter is 493 W/m^2.[3] For Phobos and Deimos the irradiance at their apohelion was also used. The solar irradiance was calculated to be 492.96 W/m^2 and 492.90 W/m^2 for Phobos and Deimos, respectively. Because not all components are active at the same time during operations, the power subsystem was computed for the travel time with the addition of 86% photovoltaic efficiency and the 91% absorptivity of the cells. A contingency margin of 15% for the shadowing, indirect sunlight or unexpected increase in the power needed was applied. According to Brown [19], a minimum contingency of 10% shall always be taken for sizing the power subsystem. With the contingency, the areas for the solar panels were computed, (Table 11.7), with the quantity of cells and the total weight of the cells. To verify this, the power of the Mars Reconnaissance Orbiter has been looked at. The orbiter has 3744 solar cells to generate 1000 W at a 26% efficiency.[4] The orbiter of the Aphrodite mission has been sized for 1050.4 W.

Table 11.7: Number of cells, area and mass of each solar array, computed for the respective power.

Unit	**Power** [W]	**Area** [m^2]	**Number of cells** [-]	**Mass** [kg]
Orbiter	1050.4	11.92	3975	84.64
Phobos lander	269.3	2.81	940	20.0
Deimos lander	269.3	2.81	940	20.0

11.4.3. Solar Panel Structure

The structure of the solar panels is of key importance for the fulfilment of the mission. The solar panels have to be able to withstand the design load in order for the mission to succeed. Although the panels do not have to carry a large quantity of external mass, they can still fail due to the frequencies experienced during launch. In the aerospace industry, the most used material/structure for spacecraft is a honeycomb panel, usually aluminium based, with either aluminium or carbon fibre skin. This is due to the properties of the materials, according to Paik et al. [81] and as already explained in Section 6.3, such as high bending stiffness versus a low weight.

For the stress and frequency analysis, the equations provided in Section 6.3 are used, with the natural frequencies having the highest weight. The panels should also withstand the deployment acceleration of at least 1.775 rad/s^2. In order to compute these, the moment of inertia needs to be obtained, this can be done with Equation 11.2. For the area, Equations 11.3 and 11.4 were used to later obtain a mass estimation for the arrays. Furthermore, the Young's Modulus was calculated with the use of Equation 11.5. All these equations were published by Paik et al. [81]. The height of the core is given by h_c and h is the height of the core plus two times the thickness of the skin. The equivalent density of the core is denoted by ρ_c and t_c the thickness of the honeycomb wall. The width of the panel is described by b, d is the length of a hexagon side and E_c is the equivalent Young's Modulus of the core. The core will be made out of AL7075-T6, whose properties have already been explained in Table 6.4 of Section 6.3. The properties of the high modulus carbon fibre were obtained from Performance Composites.[5]

$$I = \frac{h^3 - h_c^3}{12} b \tag{11.2}$$

$$A = h \cdot b \tag{11.3}$$

$$\rho_c = \frac{8}{3\sqrt{3}} \frac{t_c}{d} \rho_{aluminium} \tag{11.4}$$

$$E_c = \frac{2t_f}{\sqrt{3h_c^2 + 6h_c t_f + 4t_f^2}} E_{aluminium} \tag{11.5}$$

With the previous equations, the following values were found: E_c=118 GPa, $\rho_c = 4.31\,\text{kg/m}^3$, $I = 6.62 \times 10^{-7}\,\text{m}^4$ and $A = 26 \times 10^{-3}\,\text{m}^2$. For the design of the honeycomb, the different dimensions of the structure were continuously switched to obtain the best design that would withstand the stresses and frequencies. Moreover, the deployment would cause a bending stress lower than 0.1 MPa, since the panels only carry their weight for a

[3] http://ccar.colorado.edu/asen5050/projects/projects_2001/benoit/solar_irradiance_on_mars.htm [Accessed on: 9 June 2017]

[4] https://mars.nasa.gov/MRO/mission/spacecraft/parts/electricalpower/ [Accessed on: 15 June 2017]

[5] http://www.performance-composites.com/carbonfibre/mechanicalproperties_2.asp [Accessed on: 18 June 2017]

height of 16 mm. To validate the values obtained, the work of Ferrari [40], Paik et al. [81], Sun et al. [113] were consulted, where, for instance, the h_c values range from 10 mm to 17.5 mm. Paik et al. [81] states that a panel of h_c of 12.5 mm can withstand a stress of 0.3 MPa. Table 11.8 presents the dimensions of the solar arrays, where L is the length of one side of the solar arrays. Furthermore, to ensure the functionality of the solar arrays, an insulation layer will be placed between the solar cells and the carbon fibre to protect the material from the radiation and the electrical conductivity of the cells.

Table 11.8: Dimensions of the solar panel array.

Dimension Element	Value	Unit
t_c, core thickness	1.00	mm
d, with of a honeycomb side	7.00	mm
t_f, face thickness	1.75	mm
b, width of the panel	0.0	m
$L_{orbiter}$, length of the panel	7.95	m
L_{phobos}, length of the panel	1.88	m
L_{deimos}, length of the panel	1.88	m
h_c, height of the honeycomb	16.00	mm

11.4.4. Batteries

During their operational lifetime, the landers and the orbiter will mostly rely on the solar panels for power supply. However, during eclipse, a different power source is needed to support the system. There are different options for secondary power sources, however, usually batteries are used. Fuel cells and flywheels are not an option because of Aphrodite's long lifetime of eight years. Due to the fact that it is cheaper and more reliable to use a system with a high flight heritage, secondary batteries are suggested. They are rechargeable over a large number of cycles. The type of batteries and their size is dependent on the eclipse characteristics and on the total energy they need to provide during eclipse, shown by Equation 11.6. The type of batteries is also dependent of the number of life cycles which is in this case equal to the number of orbits around Mars. The aforementioned characteristics are summarised in Table 11.5. The landing procedure is also powered by the batteries as the solar panels are retracted to decrease structural impact during landing. The landing sequences only cover 8000 s and 3000 s for Phobos and Deimos respectively, yielding an energy requirement that is lower than for eclipse. Therefore, eclipse mode is the driving factor for the batteries.

$$E_{out} = P_{eclipse} \cdot t_{eclipse} \tag{11.6}$$

Having defined these required lifetimes and energy outputs, a choice can be made on the type of secondary batteries used. From Wertz and Larson [128], it is derived that two types of batteries are suitable to this specific mission requirements: lithium-ion (Li-Ion) or nickel-hydrogen (NiH_2). The nickel-cadmium batteries, although space qualified, have lower specific energy densities and do not provide a better lifetime performance.

The following elements of the battery cells are important for the battery choice: the nominal cell voltage, the energy density per kilogram and per litre and the depth of discharge (DOD). A high cell voltage is favourable, since the operational spacecraft bus voltage has to be met by connecting the cells in series. The spacecraft bus voltage is set to be 28 V, as this is the highest voltage required by the instruments as can be seen in Table 11.13. This directly influences the mass and volume of the total batteries. The DOD is the fraction to which the battery is discharged. Discharging the batteries decreases the quality of the battery. This means that the total energy capacity that the battery can store drops over its lifetime. Thus, DOD is a function of the number of cycles. The relationship can be found in Wertz and Larson [128]. Table 11.9, shows the batteries characteristics.
As can be seen, for the landers, Li-Ion batteries have better performance than NiH_2. Therefore, Li-Ion batteries are going to be installed on the landers. The only disadvantage is that the charge and discharge rates of the batteries need to be carefully monitored as this is not controlled by the cells themselves (Dudley [34]). For the orbiter on the other hand, the life cycles are more critical as the DOD significantly decreases, although improvements are continuously being researched as described in Fellner et al. [39]. The other performance parameters still might have a positive effect on the the mass and volume of the final battery, so the mass and amount of cells were calculated for Li-Ion and the NiH_2 batteries.

First, the energy that needs to be stored in the battery is calculated, using the values from Table 11.9. This is done with Equation 11.7, where η is the efficiency.

Table 11.9: Performance parameters of NiH_2 and Li-Ion secondary batteries.

Parameter	**NiH_2**	**Li-Ion**
Energy density [Wh/kg]	75	125
Energy density [Wh/L]	60	250
Cell voltage [V]	1.25	3.5
Efficiency [-]	0.7	0.98
Depth of discharge orbiter [-]	0.6	0.3
Depth of discharge landers [-]	0.6	0.6

Table 11.10: Trade-off study for the batteries of the orbiter.

Battery Type	**Stored energy** [Wh]	**Capacity** [Ah]	**Capacity per cell** [Ah]	**N parallel**	**N series**	**Mass** [kg]	**Volume** [L]
NiH_2	550	37	20	2	23	14	17
Li-Ion	786	53	50	1	8	12	5

$$E_{stored} = \frac{E_{out}}{DOD \cdot \eta} \tag{11.7}$$

Then, the capacity that needs to be stored in the battery is calculated using Equation 11.8.

$$C = \frac{E_{stored}}{V_{bus}} \tag{11.8}$$

Then the quantity of cells in series can be determined as the individual cell voltages have to add up to the bus voltage. The number of cells in parallel can be determined as a function of the maximum capacity that individual cells can store. Finally, it is determined that using Li-Ion batteries will cause mass savings of approximately two kilos but a more significant volume saving of twelve litres. Therefore, Li-Ion batteries will be used. The trade-off study can be found in Table 11.10.

Now a commercial battery can be chosen with the desired properties. The VL51ES Li-Ion battery from Saft [99] is chosen for the landers because of its high specific energy density and is space-qualified. For the orbiter, the VES16 Li-Ion from Saft [99] yielded the best result. The total quantity of batteries needed can be determined using the approach followed for the trade-off study. On top of that, it needs to be taken into account that the battery will not be discharged at its nominal current. This causes a decrease in capacity that can be described by Peukert's law in Equation 11.9, with k being the Peukert's constant. For Li-Ion batteries that is assumed to be 1.03. The nominal discharge current of the batteries is 0.67C, where C is coulomb per second, whereas the actual discharge rate of 0.77C, being slightly higher, so the Peukert's law has to be used. The battery sizes for the orbiter and the two landers can be found in the VL51ES and VES16 battery properties can be found in Table 11.11. A contingency of 15% to the power to be provided was added according to Khurana et al. [57].

$$C_{act} = C \cdot \left(\frac{C}{t_{eclipse} \cdot I_{act}} \right)^{k-1} \tag{11.9}$$

This is feasible, because ExoMars used similar batteries, Li-Ion. These had a similar mass and size with a similar power requirement as the Aphrodite mission (Amos and Brochard [3]).

11.4.5. Power Management and Distribution

The voltage provided by each cell is 2.35 V. The cells are placed in such way that the voltage obtained by them is 23.5 V, so ten cells in parallel. In order to ensure that all the components work properly, regulators have to be used. These regulators are DC-DC converters, and thus they regulate and convert the voltage obtained by the solar arrays into what the components need, so the batteries can be charged and the different components can function. The different voltages can be seen in Table 11.13. Another function these regulators have is controlling the current, so that it also remains constant. For each component different regulators were chosen. Some components will use the same model of regulator, since that model can be adjusted to meet the required voltages and the components have voltages that are not common for regulators, this can be seen in Table 11.14. Figure 11.4 shows how different components in the power subsystem are interconnected.

Table 11.11: Properties of the VL51ES and VES16 batteries.

VES16	**Value**
Cell capacity [Ah]	4.5
Nominal Voltage [V]	3.6
Weight per cell [kg]	0.155
Height [mm] × diameter [mm]	60 × 33
Peukert's constant [-]	1.03
VL51ES	**Value**
Cell capacity [Ah]	51
Nominal Voltage [V]	3.6
Weight per cell [kg]	1.08
Height [mm] × diameter [mm]	222 × 54
Peukert's constant [-]	1.03

Table 11.12: Final battery properties.

Unit	**Battery type**	**N parallel**	**N series**	**Mass** [kg]	**Volume** [L]
Orbiter	VES16 Li-Ion by Saft	14	8	17.36	5.75
Phobos lander	VL51ES Li-Ion by Saft	1	6	6.48	3.05
Deimos lander	VL51ES Li-Ion by Saft	3	6	19.44	9.15

For charging the battery the Stand-Alone Synchronous Switch-Mode Li-Ion Charger BQ24610 will be used.[6] Furthermore, automatic switches will be placed between the regulators and the components to control when they are powered. Moreover, all the components will be connected by means of insulated cabling. The secondary payload has still not been determined, therefore a regulator for it will be chosen once this has been done.

Table 11.13: Voltages of different components needed to find a suitable regulator.

Component	**Voltage** [V]
Batteries (Section 11.4.4)	27.0
Fine Sun Sensor[a]	15.0
Startracker[b]	22.0-34.0
Single Board Space Computer (Section 10.1)	5.0
Solid State Data Recorder (Section 10.1)	15.0-50.0
Laser (Section 4.2.2)	4.5
IMU[c]	15.0
High Gain Antenna (Section 4.2.2)	25.0
Thermal Heaters (Gilmore [43])	27.0

[a] `http://bradford-space.com/products/aoce/fss/` [Accessed: 13 June 2017]
[b] `https://www.terma.com/media/101677/star_tracker_he-5as.pdf` [Accessed: 13 June 2017]
[c] `http://www.northropgrumman.com/Capabilities/LN200sInertial/Documents/ln200s.pdf` [Accessed: 13 June 2017]

11.5. Risk Analysis

In this section the risks that can be encountered by the power subsystem will be analysed. Figure 11.5 shows a fault tree of the risks of the power subsystem. Those are explained in detail together with their mitigation strategy. Finally, Table 11.15 provides a risk map of the mitigated risks. The local risks that threaten the power subsystem are the following:

1. Diode failure: Diodes control the direction of the current while blocking the current in the opposite direction. A failure in a diode could be critical, since it could cause both solar panels and batteries to fail. In order to keep the likelihood of this happening to a minimum, specialised diodes for blocking and for bypass will be used.

2. Connector failure: Every component is connected to another via cabling and ports, yet if one connection fails, the mission fails. This can mean that a crucial component will not receive power. The chances of this

[6] `http://www.ti.com/product/bq24610` [Accessed on: 15 June 2017]

Table 11.14: Spacecraft components with their respective regulators and nominal voltages.

Component	**Regulator**	**Voltage Regulator** [V]
Batteries	Battery Regulator[a] (TPS61081)	27.0
Fine Sun Sensor	Regulator 2[b] (TL431)	15.0
Startracker	Regulator 5 (TL431)	28.0
Single Board Space Computer	Regulator 1[c] (TL4050C50)	5.0
Solid State Data Recorder	Regulator 5 (TL431)	28.0
Laser	Regulator 3 (TL431)	4.5
IMU	Regulator 2 (TL431)	15.0
High Gain Antenna	Regulator 4 (TL431)	25.0
Thermal heaters	Regulator 5 (TL431)	28.0

[a] http://www.ti.com/product/TPS61081 [Accessed on: 16 June 2017]
[b] http://www.ti.com/product/TL431 [Accessed on: 16 June 2017]
[c] http://www.ti.com/product/TL4050C50-Q1 [Accessed on: 16 June 2017]

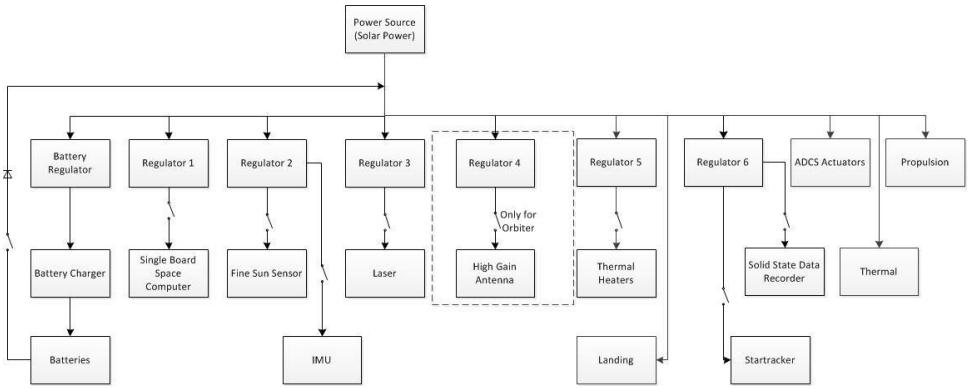

Figure 11.4: Diagram of the power subsystem structure.

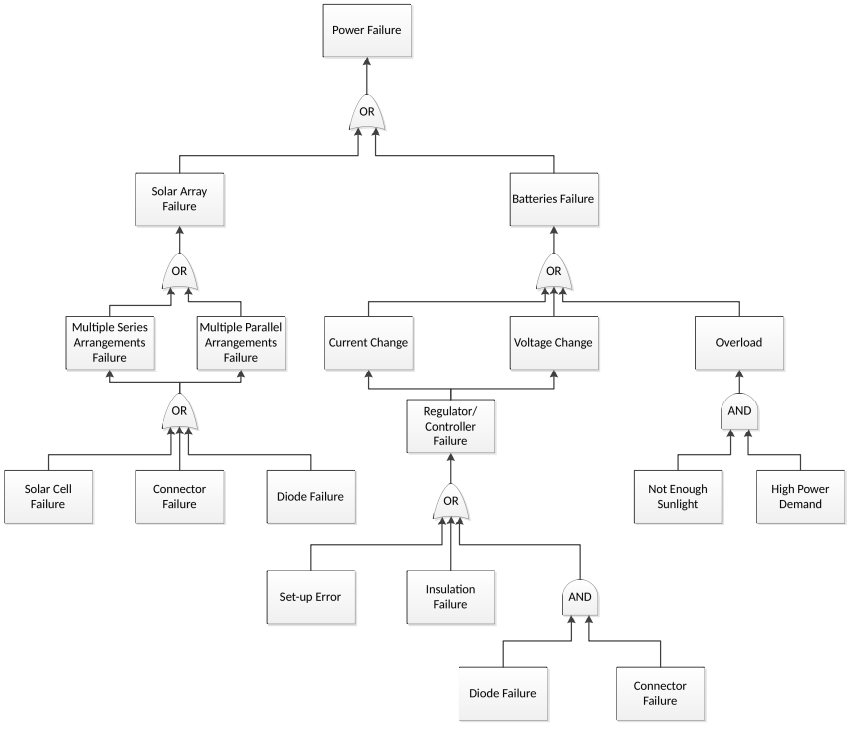

Figure 11.5: Fault tree of the risks of the power subsystem.

Table 11.15: Mitigated risk map of the power subsystem.

Almost certain					
Likely	3				
Average					
Unlikely			6		
Improbable					1, 2, 4, 5, 7
Likelihood / **Impact**	Negligible	Marginal	Moderate	Critical	Catastrophic

happening can be decreased by making sure that every component is properly connected and all equipment has been qualified for the mission.

3. Solar cell failure: If a solar cell fails, the energy produced will not be enough. This risk can be easily mitigated, since there is already a contingency margin in case there is shadowing, thus with this margin a cell failure is negligible.

4. Set-up error: An error in the set-up of the regulators can cause the component, it is connected to, to fail. To minimise this likelihood, enough attention needs to be put in the set-up.

5. Insulation failure of the cables: An insulator can fail due to either deterioration, mechanical stress or heat.[7] Therefore, to minimise this, the cabling will be kept within a temperature range.

6. Poor system performance: This is a risk that can be mitigated by designing for worst case scenario and applying contingencies. There is an unlikely likelihood with a critical impact, because it can affect the performance of the subsystems.

7. Solar array (re)deployment: This is a catastrophic risk, that has a likelihood that can be mitigated to improbable by obtaining the most reliable actuators possible.

11.6. Sensitivity analysis

To evaluate how sensitive each of the decisions and calculations made during the design of the power subsystem are, a sensitivity analysis has been performed. For the honeycomb structure, height was slightly varied to see how the Young's Modulus and moment of inertia would change. For an increase of one millimetre in the height, there is an increase in the mass of the solar panels of 1%.

The time the solar panels are in sunlight can affect the size of the solar arrays and the batteries. An increase in eclipse time means that the solar panel will need to generate more energy, this varies linearly, thus an increase in 30 minutes, taking the orbiter for example, means an area increase of 2 m^2, assuming all components are always active. The 15% contingency can compensate for this, in case all components are active with this extra eclipse time, because this percentage increases the area by 1.9 m^2. Moreover, the batteries also work according to the eclipse times, therefore, those 30 minutes of extra eclipse makes the spacecraft need twice as many batteries. The 15% contingency makes up for 5 minutes of extra eclipse time.

Furthermore, for an increase of 0.25 m^2 in the area of the solar panels, 20 W extra can be produced.

[7] `http://www.reuterhanney.com/news/main-reasons-insulation-failure/` [Accessed on: 21 June 2017]

[This page is intentionally left blank]

12
Thermal Control

From bleak eclipse conditions to the scorching heat experienced in sunlight, the spacecraft is required to keep its instruments operational. In order to provide a stable and functional temperature range, a thermal control system must be implemented. This system, and all its components, is presented in Section 12.1. Subsequently, the requirements set for the thermal control system are checked in Section 12.2. The design approach taken to reach the chosen system is explained in Section 12.3. The component choices are justified in Section 12.4. Finally, Section 12.5 and Section 12.6 will detail analyses on the risk and sensitivity of the system, respectively.

12.1. Design Overview

The thermal control system for both landers and the orbiter comprises of a layer of insulation on both the inner core and outer shell, radiators, louvres, backup phase-change material (PCM) coolers, backup heaters, cryogenic thermal storage units (CTSUs) and heat pipes. These systems are similar in amount and type for both the orbiter and the landers, though the number of radiators differs.

The system is designed such that the inner core is kept between 283 K and 318 K, and the outer shell between 253 K and 313 K, based on the most strict temperature range requirements of the other subsystems, as presented in Table 12.2. In addition, the need for active thermal control systems is designed to be minimal in order to reduce the power consumption. The full list of components of the thermal control system architecture is presented in Table 12.1.

12.2. Functional Analysis

As the thermal control system is very much a support system, requirements flow from the other subsystems. *FUN-TC-SS-01* and *FUN-TC-SS-02* are based on the most strict temperature bounds of all the spacecraft components. As can be seen from Table 12.2, the batteries provided the driving temperature requirement in the inner cylinder for the orbiter and in the outer shell for the landers. The requirement for the temperature region in the outer shell of the orbiter was provided by the ADCS.

FUN-TC-SS-03, *FUN-TC-SS-04* and *FUN-TC-SS-05* were imposed in the report by Khurana et al. [57], and later revised based on the temperature requirements described before. *FUN-TC-SS-06* and *FUN-TC-SS-07* are obvious, yet essential requirements ensuring reliable operations during the mission. *FUN-TC-SS-08* and *FUN-TC-SS-09* concern the working of the subsystem in eclipse and sunlight conditions.

12.3. Design Approach

With the preference to minimise the power consumption in mind, the first step in the design process was to calculate the temperature of the outside faces while in direct sunlight and during eclipse. This was done by use of Equation 12.1.

$$\sigma T^4 = \frac{\alpha}{\epsilon} \frac{A_{projected}}{A_{total}} \cdot Q_{total} \tag{12.1}$$

Heat loads used to determine Q_{total} are presented in Table 12.3. The albedo of Mars was found to be 0.25.[1] $A_{projected}$ is the area affected by the radiation heat, while A_{total} is the total area of all six sides.

$Q_{Mars,radiated}$ was calculated using Boltzmann Law, with the night-time surface temperature of Mars being 150 K.[2] The surface area, being the side of the orbiter that faces Mars, was determined to be 6 m^2:

$$Q = \epsilon \sigma T^4 A \tag{12.2}$$

[1] `https://nssdc.gsfc.nasa.gov/planetary/factsheet/marsfact.html` [Accessed on: 25 June 2017]
[2] `https://mars.nasa.gov/allaboutmars/facts` [Accessed on: 30 June 2017]

Table 12.1: Overview of the complete thermal control system, for both the orbiter and the landers.

Spacecraft	**Component**	**Remark**	**Mass** [kg]	**Power** [W]
Orbiter	**MLI**	5 mil aluminium backed Teflon 5 mm outer shell 2 mm inner cylinder	10	-
	Radiator	5 × 0.3 m^2, TMT panel radiator	3.5	-
	Louvre	5 × SNC, 1 per radiator	3.5	-
	CTSU	3 × Raytheon 301	36	20
	Heat pipes	Capillary Pumped Loops (CPL), 2 mm diameter, across all faces, between components and through radiators	< 1	-
	Backup systems	10 × Tayco Solid-State Controller heater, 2 × Phase-Change Material (PCM) cooler using Glauber's salt	2	20
Total			**55**	**40**
Phobos Lander	**MLI**	5 mil aluminium backed Teflon 2 mm outer shell 1 mm inner cylinder	1	-
	Radiator	3 × 0.3 m^2, TMT panel radiator	3.5	-
	Louvre	3 × SNC, 1 per radiator	3.5	-
	CTSU	3 × Raytheon 301	36	20
	Heat pipes	Capillary Pumped Loops (CPL), 2 mm diameter, across all faces, between components and through radiators	< 1	-
	Backup systems	10 × Tayco Solid-State Controller heater, 2 × Phase-Change Material (PCM) cooler using Glauber's salt	2	20
Total			**46**	**40**
Deimos Lander	**MLI**	5 mil aluminium backed Teflon 2 mm outer shell 1 mm inner cylinder	1	-
	Radiator	3 × 0.3 m^2, TMT panel radiator	3.5	-
	Louvre	3 × SNC, 1 per radiator	3.5	-
	CTSU	3 × Raytheon 301	36	20
	Heat pipes	Capillary Pumped Loops (CPL), 2 mm diameter, across all faces, between components and through radiators	< 1	-
	Backup systems	10 × Tayco Solid-State Controller heater, 2 × Phase-Change Material (PCM) cooler using Glauber's salt	2	20
Total			**46**	**40**

Table 12.2: Lower and upper temperature bounds for the most temperature sensitive components.

Component	**Minimum Temperature** [K]	**Maximum Temperature** [K]
C&DH	253	323
Batteries	283	298
Propellant Tank	283	323
Secondary Payload	270	320

Table 12.3: Heat loads used in the thermal calculations.[1]

Heat Load	**Value** [W/m^2]	**Heat Load**	**Value** [W/m^2]
$Q_{Mars,radiated}$	360	$Q_{total,Sun}$	1110
$Q_{Irradiance}$	600	$Q_{total,eclipse}$	360
$Q_{Reflected}$	150		

Table 12.4: Thermal control system requirements.

ID	Requirement	Section	Compliance
FUN-TC-SS-01	The thermal control system shall maintain all subsystems within their pre-defined operational temperature ranges.	12.1	✓
FUN-TC-ST-02	The thermal control system shall keep the payload temperature between 258 and 323 K in the outer shell and between 283 and 298 K in the inner cylinder.	12.1	✓
FUN-TC-SS-03	The thermal control system shall have a maximum mass of 61.3 kg for the orbiter and 51.3 kg per lander.	12.1	✓
FUN-TC-SS-04	The thermal control system shall have a maximum power usage of 40 W per spacecraft.	14.2	✓
FUN-TC-SS-05	The thermal control system shall have a maximum cost of $32 million for the orbiter and $30 million per lander (FY17).	14.4	✓
FUN-TC-SS-06	The thermal control system shall not have any single point of failure.	12.5	✓
FUN-TC-SS-07	The thermal control system shall be able to withstand all loads during the operational time.	12.5	✓
FUN-TC-SS-08	The thermal control system shall fully rely on the passive components during eclipse.	12.4	✓
FUN-TC-SS-09	The thermal control system shall be able to dissipate 200 W while in sunlight	12.4.2	✓

The internal heat generation by the other subsystems is set at 15 W in the outer shell and 55 W to 75 W in the inner cylinder during eclipse for the landers and the orbiter, respectively, based on the power consumption and efficiency of other subsystems. The power consumption by the other subsystems can be found in Table 14.2. It should be noted that the power consumption of the propulsion subsystem during the burn phase generates heat outside of the spacecraft and is therefore not taken into account in the required heat dissipation. Also, the power usage during the travel and operational phase is predominantly required for charging the batteries. This is assumed to be highly efficient (>80%) and it will thus not generate significant amounts of heat.

With the temperature of the outside faces, the heat transfer through the MLI was calculated using Fourier's law.

$$Q = \frac{KA\Delta T}{s} \tag{12.3}$$

Here, K is the thermal conductivity of the MLI set to 1×10^{-5} W/(m K), A is the area of the side of the orbiter that was analysed, s is the thickness of the MLI and ΔT is the temperature difference based on maximum and minimum conditions presented in Section 12.1.

From Equation 12.1 and Equation 12.3 the heat transfer through each wall was calculated both for sunlight and eclipse conditions. The sum of these heat transfers gives the total heat going in or out of the system during these moments. Together with the knowledge on the total internal heat generation during eclipse, the thicknesses t_1 and t_2 of the inner core and outer box respectively, were calculated. With these thicknesses the spacecraft is kept at its preferred operating temperature, taking into account the internal heat generated by the other subsystems operating during eclipse.

The Python script written to perform these calculations was validated by implementing various $\frac{\alpha}{\epsilon}$ values for different materials and by verifying that the resulting heat loads and required thicknesses were similar to those described by Gilmore [43] and Daryabeigi et al. [25], ranging from 1 mm to 5 mm. The reverse calculation was also verified, where the thickness was assumed and the resulting $\frac{\alpha}{\epsilon}$ value was calculated to be equal to 0.16.

With the required thicknesses found for eclipse, presented in Table 12.5, the required heat dissipation during Sun time was calculated. From this required heat loss, the amount and capacity of the radiator(s) could be designed. This is described in more detail in Section 12.4.2. Then, when the heat rejection capacity of the radiator(s) was found, the diameter of the heat pipes was estimated to accommodate the heat transfer from spacecraft components to the radiator, detailed in Section 12.4.3.

Even though the radiator will be accompanied by a louvre, there will be some minor heat losses through this component during eclipse. This loss will be countered by cryogenic thermal storage units (CTSUs). These were sized for both required storage capacity as well as required heating/cooling capacity. The calculations and final design choice are presented in Section 12.4.4.

The backup heaters and coolers were estimated based on the previously determined values for heat flow in

and out of the system. The number of backup systems was predominantly estimated on required capacity, as well as additional cost and weight upon installation.

12.4. Design Architecture

The components, as presented in Table 12.1, are explained in detail below. The calculations performed are explained with all input values used.

12.4.1. Multi Layer Insulation

As one of the most characteristic design features on spacecraft, the multi layer insulation (MLI) provides a key function in keeping the spacecraft temperature within its operational range. With its large number of design options, ranging from the number and type of layers to the outer surface finish, the MLI can be designed such that the thermal control system predominantly operates on passive systems.

To minimise power consumption during eclipse, the MLI blanket surface finish is required to be fabricated out of 5 mil (0.127 mm) aluminium backed Teflon ($\frac{\alpha}{\epsilon} = 0\,15$, q = 0 85) with the values taken from the book by Gilmore [43] and the paper by Henninger [49, pp. 16].

From previous missions, typical thicknesses are in the order of millimetres. Using the approach detailed in Section 12.3, thicknesses are found to be in this range as presented in Table 12.5.

Table 12.5: Multi layer insulation for the orbiter and landers. Positive net heat load values indicate heat that needs to be radiated out of the system.

Spacecraft	**MLI thickness outer shell & inner core** [mm]	**Net heat load eclipse** [W]	**Net heat load in sunlight** [W]
Orbiter	5 & 1	1	200
Phobos	2 & 1	3	110
Deimos	2 & 1	3	110

With the previously mentioned surface finish, the number and type of layers should be designed such that a thermal conductivity of 1×10^{-5} W/(m K) is achieved, as it is a typical value for the thermal conductivity of multi layer insulation according to Gilmore [43, pp. 163].

It should be noted that the heat generated by the thrusters can exceed 2000 K. As a result, the MLI on the bottom (the nozzle side) should be increased to 40 mm to shield the overall spacecraft and in particular, in the case of the landers, the LIDAR system on the thruster side, against the high temperature of the nozzles, as described by Daryabeigi et al. [25].

Radiation was taken into account in the MLI design when it comes to material degradation. The material properties were found to degrade negligibly over the full span of the mission, according to De Groh et al. [26]. Although the MLI is therefore considered resilient to space radiation, the other subsystems have to be analysed for radiation exposure as well. As one of the instruments most sensitive to radiation, the command and data handling (C&DH) system is certified for 25 kRad of radiation exposure before failure. It is assumed that the MLI shields at least in part for radiation, with a radiation dose of 10 kRad after five years, according to Badhwar [9].

12.4.2. Radiators

Since the MLI is sized to the heat load internally generated during eclipse, cooling is required when in sunlight. This is for one, due to the Sun heating the spacecraft to the point where the internal components would heat up to above their upper temperature limits. Another factor is the operation of more subsystems in sunlight than during eclipse, like the communications and ranging subsystem.

Using the approach described in Section 12.3 with the sunlight external heat loads and the insulation thicknesses described in Table 12.5, the heat loads that will size the radiator were found to be 200 W for the orbiter and 110 W for the landers. The difference between the two systems is explained by the fact that the orbiter has a larger surface area in addition to also having a greater internal heat generation compared to the landers.

Even though a spacecraft would heat up to unfavourable temperatures quickly with more than 100 W of internally generated heat, sizing a radiator for this load is nothing out of the ordinary, as explained by Gilmore [43]. Since it is assumed that the radiator would be operating at the spacecraft internal temperature, which is a maximum of around 313 K, because there are no active heating systems in the radiator, according to [43, pp. 208], the theoretical heat rejection capacity is 600 W/m^2 and would thus only require about 0.3 m^2 of radiator

surface area for the orbiter. However, from the paper by Schick et al. [102] it can be seen that 0.3 m^2 yields 56 W of radiation capacity for a structural panel radiator. To reach the required heat dissipation, presented in Table 12.5, this would then require a total radiator surface of 1.2 m^2 for the orbiter and 0.6 m^2 for the landers. Even though this surface area is larger than typical extendable radiators (Gilmore [43]), it is favourable, since the lack of deployment mechanism makes it more reliable and because a louvre will be required, as explained below, a deployable radiator would not be achievable. Hence, to maximise efficiency, it is chosen to install the radiators in a wall of the spacecraft that faces away from the Sun and which does not have instruments in direct line of sight.

Nonetheless, as the radiator should not be operational during eclipse, a louvre is added. This louvre in turn limits the effective emissivity of the radiator to about 0.75, as stated in the catalogue by Sierra Nevada Corporation [106]. Therefore one additional panel radiator should be installed on the orbiter and both landers. As the louvre decreases the effective emissivity of the radiator, it is also found from [106] that the louvre limits the insulation capacity of the structure by having an emissivity of 0.14 when all blades are closed. This additional heat loss will be accounted for firstly in the design of the cryogenic thermal storage units (CTSUs) and secondly in the addition of backup heaters.

12.4.3. Heat Pipes

The spacecraft main structure can be used to transport and store heat energy, but this is difficult to control, as the structure is primarily designed for mechanical support and not for thermal conductivity. Consequently, to distribute both the external and internally generated heat across all surfaces and to move internal heat away from its source, heat pipes are to be investigated. The heat pipes are designed to be a closed two-way liquid-flow cycle, using an evaporator and a condenser to avoid the need for electrical power, as described by Gilmore [43, pp. 489]. These heat pipes ensure more control over the temperature of different parts of the spacecraft.

As the spacecraft is a collection of heat sources, instead of one homogeneously heated volume, heat pipes must be implemented between subsystem components in order to avoid overheating or freezing. Besides, heat pipes along the spacecraft faces, i.e. the outside faces as well as the inner cylinder, aid in distributing heat from the sunlight face across the rest of the structure. This will minimise the risk of overheating on one side and freezing on the others. As heat conductance through the surface speeds up with increase in temperature difference, keeping the outside faces relatively warm will minimise heat loss to the space environment.

In addition to heat pipes between subsystem components and across all the spacecraft faces, the most important heat pipe connections will be between subsystems and radiators. This will ensure adequate heat removal from components and radiated out of the spacecraft in the case of overheating. As the louvres will be closed during eclipse, heat transfer through the heat pipes towards the radiators is minimised to prevent components from cooling down too much. This part of the design will thus consist of heat pipes running from components to, and through, the radiators.

The last components to require special attention concerning heat pipes are the batteries. This is especially true for the landers. There the batteries are located in the outside shell and are thus subjected to more extreme temperature conditions. Adding heat pipes to the batteries will ensure the required operational temperature bound, as additional heat can be removed or added effectively.

The heat pipes are chosen to be capillary pumped loops (CPL) with a diameter of 2 mm with a capillary size of around 5 µm, described in detail by Gilmore [43, pp. 502]. The chosen diameter is sufficient as heat pipes with a diameter of 20 mm have a heat removal capacity of about 2.5 kW as described by Margaris et al. [71].

CPL is chosen as it offers an extended lifetime in addition to fast and strong diode capabilities [43]. In addition, CPL provides flexibility in the overall layout of the spacecraft as they can tolerate complicated transport paths [43].

12.4.4. Cryogenic Thermal Storage Units (CTSU)

As explained above, the main function of the CTSUs is to counter the heat loss due to the louvre. Assuming a radiator temperature of 200 K in eclipse, an emissivity of 0.14 and total radiator area of 1.5 m^2 (Section 12.4.2), using Equation 12.2 it was found that the total heat loss through the louvres will be 20 W. Combined with the eclipse duration from Table 11.5, the required storage capacity for the CTSUs turned out to be 55 kJ.

According to Gilmore and Donabedian [44, pp. 431], a tank from *Raytheon/Swales* with a storage capacity of 32 kJ would have a volume of 30 L. In order to provide the required total storage capacity, two tanks are required. A third unit is added for redundancy.

In addition to the main function, the CTSUs are also used to keep critical sensors or subsystem components in a stable temperature regime. This would then impose less strict temperature boundaries on the core or outer

shell, depending on where the CTSUs are used.

Cryocoolers have a reliability of 95% over 10 years, according to Gilmore and Donabedian [44] and Ross [95]. In addition, sustainability is accounted for by the working fluid being nitrogen (N_2). However, the storage tank will be made of beryllium, which will require specialised manufacturing to ensure safe working conditions and avoid contamination. After manufacturing however, the material is stable, safe and reliable.[3]

In order to meet the mass and power requirements described in Section 12.2 and to provide subsystems with sufficient heating capacity during eclipse, *Raytheon/Swales* high capacity dual volume CTSUs are chosen. The systems require three units with a storage tank volume of 30 L, made out of S-200F and beryllium, as described by Gilmore and Donabedian [44]. These CTSUs have a thermal storage capacity of 32 kJ each.

12.4.5. Backup Heating and Cooling Elements

As can be observed from Table 12.5, the net heat generation during eclipse is close to zero. Hence, additional heaters are necessary in the case of MLI or CTSU failure and to account for miscalculations or events where the internal heat generation by other subsystems will be low.

The weight penalty of adding these heating and cooling elements will be marginal, according to Gilmore [43]. However, the additional power required by this backup system is not to be underestimated and the additional power budget is accounted for in the total budget.

The additional heaters will be installed on the batteries, the propellant tanks and the C&DH, as these are the most temperature sensitive components. In addition, heaters will also be placed on all remaining subsystem components in the outer shell. The heaters will be Tayco Solid-State Controllers (Gilmore [43, pp. 226]), with control power varying per heater based on the heat generation by the component on which it will be installed.

Besides backup heaters, additional coolers will be installed as well. The backup cooling system will be built from PCM type systems. The PCM systems have a high reliability and thermal conductivity, for a low cost and nontoxic operation [43, pp. 384]. The PCM cooling systems will have sodium sulphate (Glauber's salt) as the operating solid-liquid compound and will be installed in the inner cylinder and the outer shell. Each subsystem component will be wired to one of two closed, pumped PCM loops. The temperature range of the PCM should match that of the component it is installed on [43].

During the landing phase, the PCM components will provide sufficient cooling capacity to the operational components. By using PCM cooling, the radiator can be sized for average load, instead of the peak load occurring during the landing phase (page 380 of Gilmore [43]).

12.4.6. Solar Panels

The solar panels require a separate thermal analysis from the rest of the subsystems, as they comprise a large surface area on the outside of the spacecraft. Solar panels also cannot be fully insulated, as they require solar radiation in order to function. Therefore, solar array thermal control design shall be focused on the back of the arrays, or more specifically the surface finish on the back, in addition to the connectors between the arrays and the main spacecraft body.

Solar panels have a large operational temperature range, typically between −60 °C and 300 °C, as observed from Barrett and Lyle [12, pp. 16]. That is why a variety of different surface coatings are applied to the back of the solar arrays, as it is a simple form of passive thermal control. The resulting maximum and minimum temperatures are calculated for Sun exposure and eclipse conditions, respectively. The temperatures are calculated using Equation 12.1, with the values from Table 12.3 as Q_{total}. The results are presented in Table 12.6.

Table 12.6: Maximum and minimum temperatures of the solar arrays for different surface finishes applied to the back of the panels.

Surface finish	$\frac{\alpha}{\epsilon}$ [43]	**Maximum temperature** [K]	**Minimum temperature** [K]
Chemglaze Z306 (black paint)	1.10	720	432
PCBZ (white paint)	0.18	457	275
Alumised teflon	0.15	437	263

From Barrett and Lyle [12], a maximum temperature of 315 °C (588 K) for the solar arrays was found. Thus, the black paint from Table 12.6 does not meet this required upper temperature bound. White paints or aluminium backed Teflon are feasible design choices, though. The maximum temperatures are close to each other and well within the required margin. Nonetheless, PCBZ (white paint) is chosen as the surface finish on the backside

[3] `https://environmentalchemistry.com/yogi/periodic/Be.html` [Accessed on: 22 June 2017]

of the solar panels, as the minimum temperature is higher than that of the aluminium backed Teflon. This is important since the lower temperature bound is more critical, due to the glass temperature of adhesives [12]. Therefore, keeping a safe margin away from this lower temperature bound is favourable.

Next, the insulation of the connectors between the arrays and the main spacecraft body is analysed. If the connectors are not sufficiently insulated, the main body will lose or gain significant amounts of heat during eclipse and Sun exposure, respectively. Minimising the heat flow in the connectors is done by minimising the thermal conductivity through the addition of aluminium backed Teflon. This should also limit the thermal stresses in the connectors, limiting risk of failure and increasing the operational lifetime.

12.5. Risk Analysis

As can be seen from Figure 12.1, several events or combinations of events can lead to failure of the thermal control system. Hence, mitigation measures will have to be implemented to minimise the risk of total thermal control system failure. The impact and likelihood of the mitigated risks are summarised in Table 12.7.

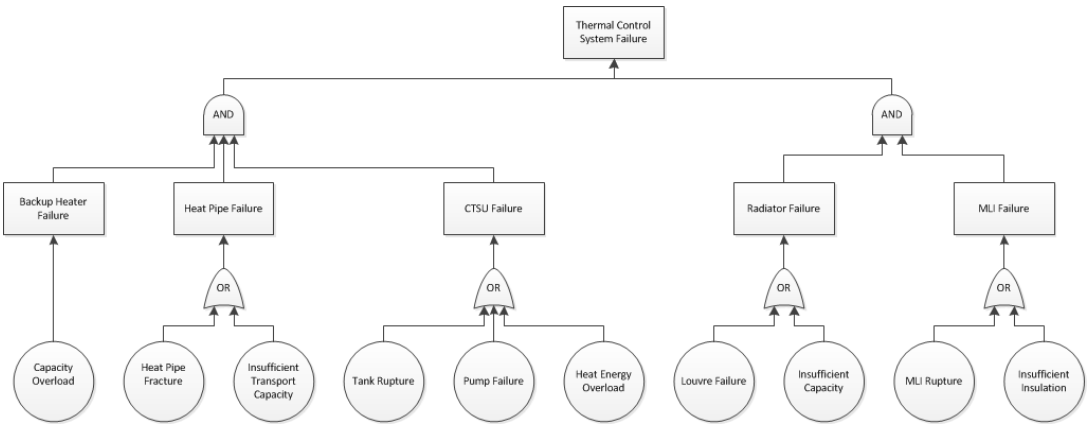

Figure 12.1: Failure tree for the Thermal Control System.

1. MLI rupture: Although the materials used in the MLI are designed for high tensile stresses, rupture could take place due to, for example, hyper velocity impact. The effects are not immediately catastrophic. However, they do have a severe impact on the functioning of the subsystem. The likelihood is very low, especially if a layer of Kevlar or other impact resistant material is implemented to account for hypervelocity collisions.

2. Insufficient insulation: Depending on the degree of insufficiency, the effects are not to be underestimated, but, as the subsystem has several backup components, the impact would only be marginal. The likelihood is average as only a basic heat transfer model was developed. This risk can be mitigated by developing a more complete thermal control model. When this mitigation strategy is applied, the likelihood is set to unlikely, though the impact remains marginal.

3. Louvre failure: In the case of a louvre failure, either too much or too little heat would get lost into the space environment. Louvres typically fail due to wear and degradation. This risk is best mitigated by installing louvres with a high reliability and long operational life. As the louvres described in Section 12.4 are built for a long operational life the risk is considered to be mitigated. Thus the likelihood is unlikely and the impact is negligible.

4. Insufficient radiator capacity: If the spacecraft has to turn to a position where the radiator is in direct sunlight, it would not be capable of providing the necessary heat dissipation. As it is expected that the spacecraft will turn such that the radiators are in direct sunlight several times during the mission, the likelihood is set to likely. Nonetheless, the duration of these direct sunlight events is expected to be short. Therefore, the impact is set to marginal.

5. CTSU heat energy input overload: The maximum heat output of a component should match the maximum cooling capacity of the CTSU installed on that component. If this maximum heat load exceeds the maximum cooling capacity due to, for example, the component being operated for longer than specified, the component will not be sufficiently cooled. However, the CTSU will not be damaged in this scenario and the additional (backup) cooling mechanisms can provide the required cooling capacity. The impact is set to marginal and the likelihood to average.

6. CTSU pump failure: In the case of a failed pump in a CTSU, this entire cooling unit will no longer be operational. Each spacecraft will have redundancy in the CTSU design, but the units are installed on specific components. Even though the CTSUs are designed for high reliability and long operational life, adding a second pump to each unit mitigates this risk. The impact is therefore moderate with an improbable likelihood, as the CTSU is said to have a high reliability according to Gilmore and Donabedian [44].

7. CTSU storage tank rupture: A ruptured or fractured storage tank in the CTSU, caused by damage sustained during launch or degradation, would immediately render the mechanism inoperable, as the operating fluid would boil off. This risk is mitigated by fabricating the storage tanks out of high-strength material. Nonetheless, the tanks are already designed to be constructed out of beryllium that, according to Gilmore and Donabedian [44], is a high-strength material. Therefore the likelihood of storage tank rupture is unlikely. The impact is set to moderate, as the components on which the CTSU is installed are more difficult to keep at a stable temperature.

8. Heat pipe insufficient transport capacity: Insufficient capacity is expected to originate from inaccurate heat values obtained from the simplified model. Mitigation is achieved by developing a more detailed model and by adding additional heat pipes as redundancy. The additional weight penalty is in the order of tens of grams [43]. With sufficient redundancy and detailed calculations, the likelihood is set to be improbable, though the impact would still be critical.

9. Heat pipe fracture: According to Gilmore [43], heat pipes are resistant to extreme temperatures. Although, if fracture were to occur, the entire heat pipe is rendered inoperable as the liquid inside would immediately boil of. However, as mentioned in Section 12.4, heat pipes are resilient and strong [43]. Thus the likelihood is improbable, but the impact is critical as components would not be able to effectively gain or dissipate heat when this risk occurs.

10. Backup system overload: In the case of main thermal control system failure, the spacecraft will rely on the backup systems. If it turns out that these systems are then overloaded, or in other words: lack the required heating or cooling capacity, this would be catastrophic. However, this risk is easily mitigated by sizing the backup system for worst-case scenarios and adding a safety factor. The weight penalty for the proposed backup components is negligible, as is the additional cost [43]. The additional power required is expected to be similar to that of the main thermal control components, therefore the power system does not receive additional requirements from these backup components. After mitigation, the likelihood is set to unlikely. The impact is expected to be moderate.

Table 12.7: Mitigated risk map of the thermal control system.

Almost certain					
Likely		4			
Average		5			
Unlikely	3	2	10	1, 7	
Improbable			6	8, 9	
Likelihood / **Impact**	Negligible	Marginal	Moderate	Critical	Catastrophic

12.6. Sensitivity Analysis

The three CTSUs are incorporated to provide a stable operating temperature to components that require so, with the third unit added for redundancy. If however, during the design phase a third component is found to require a strict temperature range, either the third CTSU has to be installed on this component limiting the redundancy of the whole system, or more care should be taken when designing the rest of the thermal subsystem. The latter is capable of providing a stable temperature with a deviation from the preferred temperature of at most 10 K, according to Gilmore [43].

Another aspect to perform a sensitivity check on is the heat generation during eclipse. The MLI and other thermal control systems are sized for a maximum heat generation of 200 W. During a later design or testing phase it might turn out that this power output differs from these estimated values. However, it was found that the system is robust up to a deviation from the estimated heat output of 10% in both the outer shell and the inner cylinder which could be compensated for by the main thermal control components, and deviations up to 20% when the backup systems are allowed to be operational.

13
Integration

In this chapter, the integration of all the different subsystems is presented. It is very important to consider all interfaces between the subsystems. The integration of the subsystems was continuously taken into account during the design process of the individual subsystems. Firstly, the lay-out of all hardware components in the design of the orbiter and the landers is presented in Section 13.1. Secondly, a sensitivity analysis on the complete system is conducted in Section 13.2. The design parameters will be varied with their measures of uncertainty to determine the influence on the final design. Finally, the natural frequencies of the complete spacecraft during launch are analysed in Section 13.3 to make sure the spacecraft meets the vibrational requirements set by the launcher.

13.1. Layout

This section aims to present the complete layout of the orbiter and the landers. Firstly, the orbiter is presented in Section 13.1.1, which is followed by the landers in Section 13.1.2.

13.1.1. Orbiter

The outside of the orbiter is a rectangular prism, since this was the most convenient interface for the ADCS sensors and communication and ranging subsystems. At each side, the ADCS sensors are attached to determine the attitude of the orbiter. In the front of the orbiter, the HGA is placed. On the top side, two lasers can be found. The omni-directional antenna was placed on the back of the orbiter. The solar panels are quite long with respect to their width to minimise the number of cells that encounter shadowing. On the bottom, the main propulsion thrusters are located. The outer layout of the orbiter can be seen in Figure 13.1. In Figure 13.3, the exploded view is presented in order to view the internal systems of the orbiter.

13.1.2. Landers

For development purposes, both landers have been designed to be structurally equal, this decreases cost and increases sustainability. The outer structure is a hexagonal prism. The landers have three landing legs, this is to provide a better stability in case the landers land on an uneven surface. Furthermore, the laser units are located on the top of the lander to have optimal communication. On two of the sides, the solar panels are located, they are at the top of those sides to minimise the shadowing. The outer layout can be seen in Figure 13.2. Figure 13.4 provides an image of the inner structure inside the hexagonal prism with an exploded view.

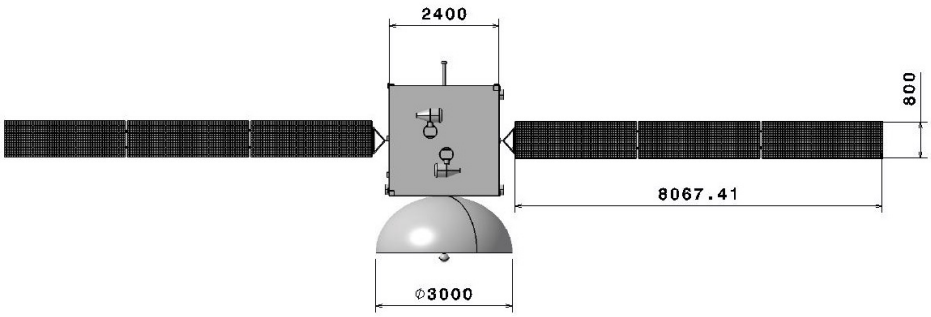

Figure 13.1: Overall layout of the orbiter.

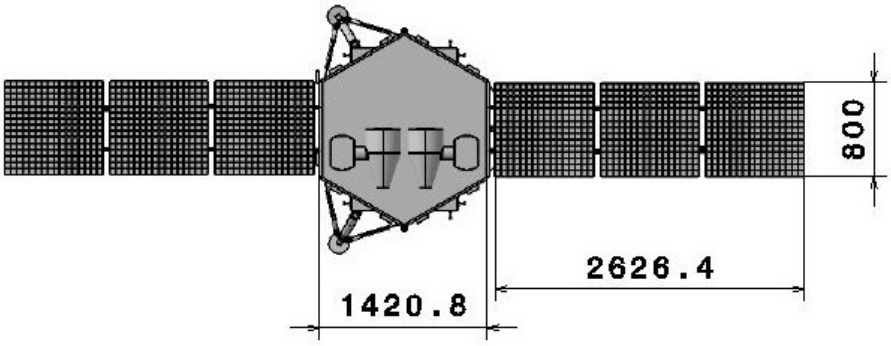

Figure 13.2: Overall layout of the lander.

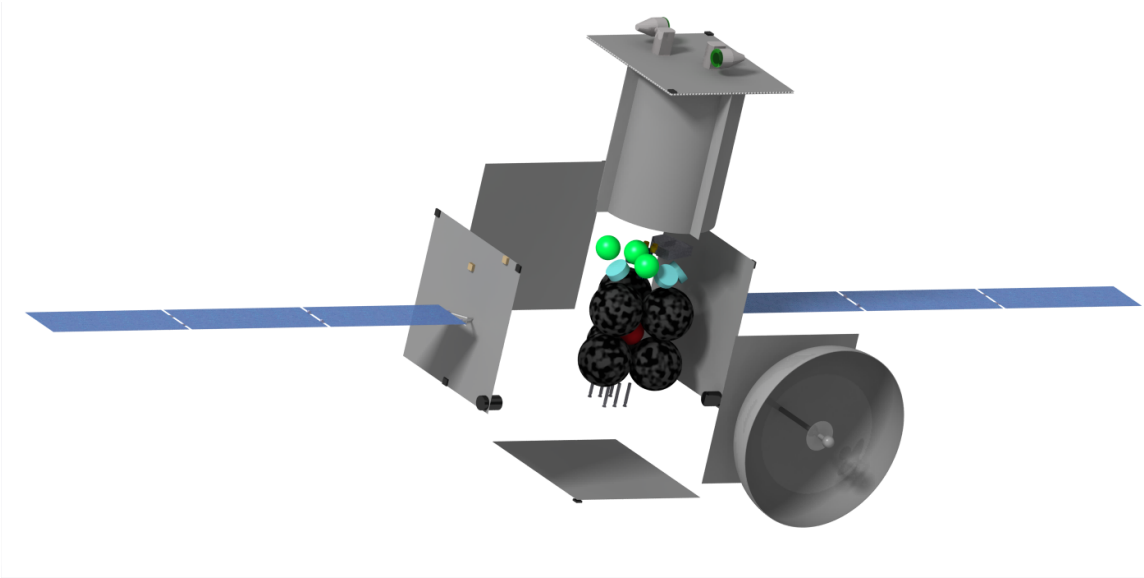

Figure 13.3: Exploded view of the orbiter.

13.2. Sensitivity Analysis

In this section, the effects of changes to the most critical parameters are assessed. The effects on reliability and cost due to a change in mass are discussed. Sensitivity of the complete system is essential for the success of the Aphrodite mission. This is because in the current conceptual phase, uncertainties are still present in the design. The design parameters and inputs have to be varied within these uncertainty margins in order to evaluate the effects of these uncertainties on the design. Sensitivity analyses are already performed on subsystem-level and now the system-level sensitivity analysis is presented.

13.2.1. Increase of Mass

The mass is a critical aspect of every space mission. Therefore, it is investigated what the effect is of a mass increase on the total design. If the total mass of 3865 kg increases with 4% or less, the spacecraft can still be launched by the Falcon 9. If however, the total mass increases by more than 4%, the launcher has to be reconsidered. With the mass being over 4020kg, a more expensive launcher needs to be used. The suggested launcher is the Falcon Heavy which costs M€28 more and thus the total mission cost increases by 3%.[1] In addition to the launcher the spacecraft will also increase in cost. For this, the NASA cost estimation tool is used and it is assumed that the mass ratios of the subsystems, as well as the risk of the components, remain constant. Then the total cost is plotted as a function of the total mass in Figure 13.5. This suggests that the mass cannot increase by more than 10%, to over 4362 kg.

[1] `http://www.spacex.com/about/capabilities` [Accessed on: 22 June 2017]

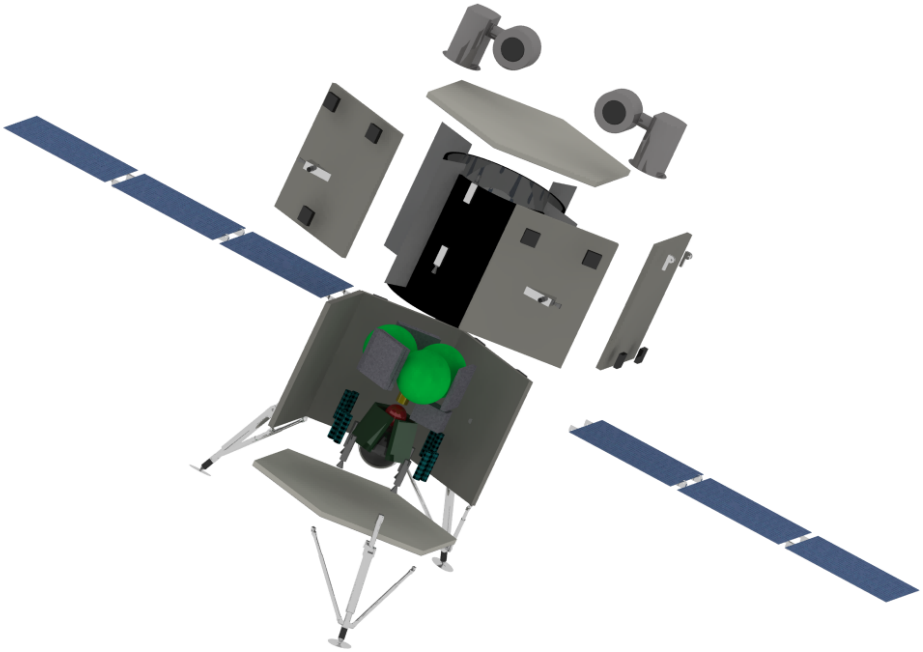

Figure 13.4: Exploded view of the lander.

13.2.2. Increase of Reliability

The reliability is a constraining factor of the design with a very high uncertainty, because reliability of the landing is difficult to estimate. If the reliability ends up slightly below the required 90%, due to the uncertainty of the landing, redundancy has to be added. The power system is the least reliable. This can be increased by using more reliable batteries. This will increase the mass and cost. These changes are difficult to quantify in this stage of the design.

13.2.3. Decrease of Cost Budget

If the cost budget of G€1 is decreased by 7%, the M€68.6 margin is able to handle it. If the cost budget decreases by more than 7%, then some elements of the design have to be reconsidered. The structure and GNC are the most expensive elements. The cost of structures cannot be decreased easily. The GNC for the landers can still be reduced, however this would reduce the reliability of the overall system.

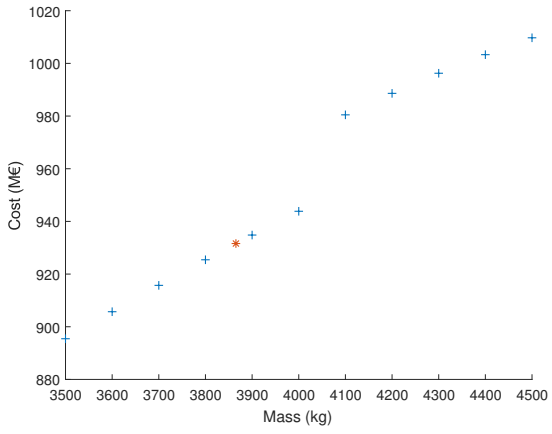

Figure 13.5: The total mission cost is compared to the mass increase.

13.3. Vibrational Analysis

In this section, a preliminary vibrational analysis of the spacecraft during launch is performed. It is checked whether the natural frequency of the spacecraft is larger than the natural frequency at launch of the Falcon 9. A dynamic finite-element analysis of the spacecraft is out of the scope of this report, therefore the orbiter and the two landers are modelled as a three spring-mass system. Each spacecraft is approximated as a beam and a mass on top of that beam. This beam is modelled as a spring with a certain lateral and longitudinal spring constant. The spacecraft consists of three parts: the orbiter, the Deimos lander and the Phobos lander. They are connected to the launcher via a payload adaptor. The spring-mass model of the spacecraft is presented in Figure 13.6. The lateral and longitudinal spring constants are calculated using Equations 13.1 and 13.2, respectively.

$$k_{lat} = \frac{EI}{L^3} \tag{13.1}$$

$$k_{long} = \frac{EA}{L} \tag{13.2}$$

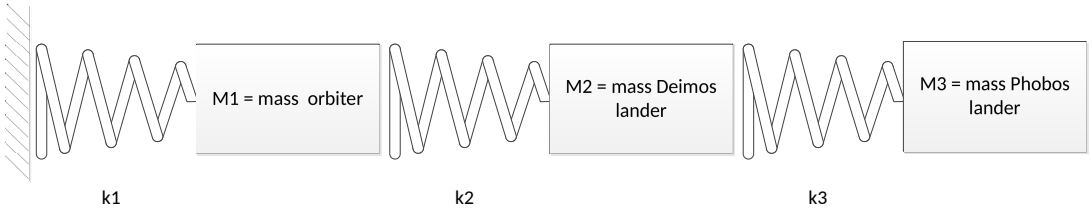

Figure 13.6: Spring mass representation of the spacecraft.

The natural frequency of this multiple degree of freedom spring system can be determined with Equation 13.3, by solving for the natural frequency ω in rad/s. The natural frequency in (f_n) Hz is $\frac{\omega}{2\pi}$.

$$det\left(\begin{bmatrix} k_1+k_2 & -k_2 & 0 \\ -k_2 & k_2+k_3 & -k_3 \\ 0 & -k_3 & k_3 \end{bmatrix} - \omega^2 \begin{bmatrix} m_1 & 0 & 0 \\ 0 & m_2 & 0 \\ 0 & 0 & m_3 \end{bmatrix}\right) = 0 \tag{13.3}$$

The assumption is made that the spacecraft can be modelled as cylinders with a certain radius, height and skin thickness. The dimensions necessary are obtained from the CATIA model which is shown in Section 13.1. From this, three longitudinal natural frequencies and three lateral natural frequencies from the system are determined, listed in Table 13.1.

Table 13.1: Longitudinal and lateral natural frequencies of the system.

Longitudinal frequency	**Value** [Hz]	**Lateral frequency**	**Value** [Hz]
$f_{n_1,long}$	159	$f_{n_1,lat}$	98
$f_{n_2,long}$	35	$f_{n_2,lat}$	15
$f_{n_3,long}$	72	$f_{n_3,lat}$	43

SpaceX dictates that in order for the spacecraft to launch safely with the Falcon 9, $f_{n,long} > 25$ Hz and $f_{n,lat} > 10$ Hz, described by SpaceX [109]. Clearly this is the case here. Therefore the vibrational requirement set by the launcher company is satisfied.

14
Spacecraft Budget

In the previous chapters, all subsystems of the Aphrodite mission have been designed and the integration of all subsystems has been discussed. In this chapter, all budgets of the space mission are presented. First in Section 14.1 the mass budget of the orbiter and the two landers is presented. Secondly, in Section 14.2, the power budget during the different phases is presented. Then in Section 14.3, the ΔV budget for the mission is presented. Finally, the cost budget of the complete mission is presented in Section 14.4.

14.1. Mass Budget

The mass is divided in three parts: the orbiter, the Phobos lander and the Deimos lander. The mass budget of the Phobos lander, Deimos lander and the orbiter can be found in Table 14.1. The contingency values are obtained from Khurana et al. [57]. The dry propulsion mass of the two landers is different because the Phobos lander has to carry more propellant and thus the volume of the tank increases.

The total dry mass of the complete spacecraft is 1270 kg and the total wet launch mass is 3865 kg. This dry mass includes a contingency margin of 71 kg. If the effects of all uncertainties during the design of the subsystem are added, it is judged that the uncertainty margin is withing the limits of the design. Therefore it can be said with confidence that the wet mass of the spacecraft will be smaller than or equal to 3865 kg.

14.2. Power Budget

The power budget is important to determine the size of the solar arrays and the batteries. The power usage of the landers and orbiter depends in which phase the spacecraft is operating. The different operating phases have already been defined in Section 3.2. The complete power budget is presented in Table 14.2. The power usage of the subsystems during the different modes is derived from the respective subsystems and the equipment operating during each mode, explained in Section 3.2.3. The power subsystem is sized using the total power from the most demanding phase. The most demanding phase is the phase with the highest power consumption, not including burn and landing (since these are really short). This is, for the landers, the travel phase and for the orbiter, the operations phase. The power used to actuate the solar arrays is considered negligible for this mission.

14.3. Delta-V Budget

The ΔV budget is a crucial budget for all space missions. Parts of the ΔV budget have already been presented in Chapter 5. In this section, the ΔV budget of the orbiter and the two landers is presented considering the ADCS and EoL ΔV. The complete ΔV budget is presented in Table 14.3. A 10% margin is incorporated in the budget, as described by European Space Research and Technology Centre [38].

14.4. Cost Budget

The last budget that is presented in this report is the cost budget. This cost budget is crucial since it is related to the top-level requirement *CON-CS-ST-01*. The cost of the mission, excluding operations should be less than one billion euros in the financial year of 2017. The cost budget is based on the NASA Project Cost Estimation Capabilities tool.[1] This is a tool, provided by NASA, which uses Cost Estimation Relationships to estimate, based on mass, risk and power, the cost of the subsystems. This estimate is detailed to subsystem level estimates. However due to the limited space, only the higher level costs of the project are presented here. A 10 % contractor fee was included for every system, as is common in the space industry. The launch cost is already known to be 65 million dollars, however the transport of the spacecraft to Cape Canaveral and the integration of the spacecraft

[1] `https://software.nasa.gov/software/MFS-33187-2` [Accessed on: 5 June 2017]

Table 14.1: Mass budget of the landers and the orbiter.

Phobos lander			
Subsystem	**Mass** [kg]	**Contingency** [%]	**Mass w. contingency** [kg]
ADCS	28.0	5	29.4
C&R	74.2	2	80.8
C&DH	8.1	2.5	8.4
Landing	30.6	9.5	33.5
Propulsion	23.4	10	25.7
Structures	12.2	9.5	13.4
Thermal	46.0	11.5	51.3
Power	26.5	8	28.6
Payload	10.0	0	10.0
Propellant	123.5		
Total dry mass with contingency	271.8		
Wet Mass	**395.3**		
Deimos lander			
Subsystem	**Mass** [kg]	**Contingency** [%]	**Mass w. contingency** [kg]
ADCS	28.0	5	29.4
C&R	74.2	2	80.8
C&DH	8.1	2.5	8.4
Landing	30.6	9.5	33.5
Propulsion	21.8	10	24.0
Structures	12.2	9.5	13.4
Thermal	46.0	11.5	51.3
Power	39.4	8	42.6
Payload	10.0	0	10.0
Propellant	96.3		
Total dry mass with contingency	287.5		
Wet Mass	**383.8**		
Orbiter			
Subsystem	**Mass** [kg]	**Contingency** [%]	**Mass w. contingency** [kg]
ADCS	53.5	5	56.2
C&R	146.7	2.5	14.6
C&DH	12.2	0	13.2
Propulsion	157.6	10	173.3
Structures	138.0	9.5	151.1
Thermal	55.0	11.5	61.3
Power	90.4	8	97.6
Payload	10.0	0	10.0
Propellant	2375.1		
Total dry mass with contingency	710.9		
Wet Mass	**3086.0**		

into the launcher also have to be incorporated. The cost of the complete launch sequence is estimated to be 100 million dollars. The complete cost estimation is given in Table 14.4. This cost is calculated using the masses with contingencies. No extra margin is incorporated in the cost budget. The total cost of the mission is M€931. This means the mission complies to the stakeholder requirement. There is still a margin of M€69, to account for unforeseen circumstances, such as extra testing or failure of a crucial part.

Table 14.2: Power budget of the two landers and the orbiter.

Phobos lander							
Subsystem	**Separation** [W]	**Burn** [W]	**Travel** [W]	**Landing** [W]	**Operations** [W]	**Safe mode** [W]	**Eclipse Operations** [W]
ADCS	73.7	73.7	52.6	73.7	43.7	43.7	43.2
C&R	0	47.6	47.6	47.6	77.2	47.6	73.2
C&DH	21.5	21.5	21.5	21.5	21.5	21.5	21.5
Landing	0	0	0	151.5	0	0	0
Propulsion	0	290	90	140	0	0	0
Structures	0	0	0	0	0	0	0
Thermal	40.0	40.0	40.0	40.0	40.0	40.0	40.0
Power	0	0	17.6	0	17.6	0	0
Payload	0	0	0	0	10.0	0	10.0
GNC	0	0	0	0	0	0	0
Total	**135.2**	**472.8**	**269.3**	**474.3**	**210.0**	**152.8**	**187.9**
Deimos lander							
Subsystem	**Separation** [W]	**Burn** [W]	**Travel** [W]	**Landing** [W]	**Operations** [W]	**Safe mode** [W]	**Eclipse Operations** [W]
ADCS	73.7	73.7	52.6	73.7	43.7	43.7	43.2
C&R	0	47.6	47.6	47.6	77.2	47.6	73.2
C&DH	21.5	21.5	21.5	21.5	21.5	21.5	21.5
Landing	0	0	0	151.5	0	0	0
Propulsion	0	290	90	140	0	0	0
Structures	0	0	0	0	0	0	0
Thermal	40.0	40.0	40.0	40.0	40.0	40.0	40.0
Power	0	0	5.5	0	5.5	0	0
Payload	0	0	0	0	10.0	0	10.0
GNC	0	0	0	0	0	0	0
Total	**135.2**	**472.8**	**257.2**	**474.3**	**197.9**	**152.8**	**187.9**
Orbiter							
Subsystem	**Separation** [W]	**Burn** [W]	**Travel** [W]	**Landing** [W]	**Operations** [W]	**Safe mode** [W]	**Eclipse Operations** [W]
ADCS	130.7	130.7	130.7	-	130.7	43.7	130.2
C&R	279.3	0	279.3	-	64.5	279.3	73.2
C&DH	25.0	25.0	25.0	-	25.0	25.0	25.0
Propulsion	90.0	840.0	90.0	-	90.0	0	0
Structures	0	0	0	-	0	0	0
Thermal	40.0	40.0	40.0	-	40.0	40.0	40.0
Power	0	0	485.4	-	485.4	0	0
Payload	0	0	0	-	10	0	10.0
GNC	0	0	0	-	0	0	0
Total	**565.0**	**1035.7**	**1050.4**	**-**	**845.6**	**388.0**	**278.4**

Table 14.3: ΔV budget of the orbiter and the two landers.

Orbiter		**Phobos**		**Deimos**	
Burns	**ΔV** [km/s]	**Burns**	**ΔV** [km/s]	**Burns**	**ΔV** [km/s]
MOI-burn	1.500	1st burn	0.014	1st burn	0.002
Inclination change	0.100	2nd burn	0.177	2nd burn	0.379
Parking orbit insertion	1.230	3rd burn	0.630	3rd burn	0.236
ADCS budget	0.160	Landing	0.080	Landing	0.090
EOL burn	0.050	Margin	0.090	Margin	0.071
Margin	0.304				
Total	**3.344**	**Total**	**0.990**	**Total**	**0.779**

Table 14.4: Cost breakdown of the complete mission

Element	**Cost (M$ FY2017)**
Project Management	*1.8*
Systems Engineering	*57.9*
Safety and Mission Assurance	*8.9*
Payload(s)	*18.6*
Spacecraft	*734.1*
Flight System Project Management	1.0
Flight System Systems Engineering	32.0
Flight System Product Assurance	4.90
Orbiter	**293.8**
Structures & Mechanisms	108.7
Thermal Control	31.5
Electrical Power & Distribution	36.8
GNC	69.0
Propulsion	12.0
Communications	24.2
C&DH	11.7
Phobos Lander	**207.0**
Structures & Mechanisms	49.7
Thermal Control	29.5
Electrical Power & Distribution	34.3
GNC	52.2
Propulsion	4.3
Communications	25.4
C&DH	11.7
Deimos lander	**186.8**
Structures & Mechanisms	52.1
Thermal Control	29.5
Electrical Power & Distribution	35.0
GNC	52.2
Propulsion	4.2
Communications	25.4
C&DH	11.7
Spacecraft Software Development	8.8
Mission Operations System (MOS)	*51.1*
Launch Vehicle/Services	*115.9*
System Integration, Assembly, Test & Check Out	*35.5*
Total Cost (M$ FY2017)	**1046.4**
Total Cost (M€FY2017)	**931.4**

15
Operational Timeline

This chapter presents the operational timeline of the Aphrodite mission. It starts at launch in Section 15.1 and continues through the operational phase in Section 15.2. In this section, the communication with the ground stations is also discussed. At last, the end-of-life strategy is presented in Section 15.3.

15.1. Launch Phase

On the 26th of February 2031 at 21:32:38.6, the Falcon 9 launcher will take off from Cape Canaveral. On-board will be the 3680 kg Aphrodite spacecraft bound for the Martian system. Cape Canaveral is at a latitude of 28.5° North. The Falcon 9 targets the transfer orbit insertion point at 200 km altitude at an inclination of 30°. After the launch sequence of approximately four minutes is finished and the fairings have been deployed, the first stage separates from the booster stage. This first stage will return back to Earth, to land on a drone-ship, which means the first stage can be reused for another mission. This increases the sustainability of the launch drastically. At the top of the launch hyperbola, the booster stage performs the TOI-burn of 3.9 km/s. All the details of the launch are listed in Table 15.1. This information can also be found in Chapter 5.

Table 15.1: Launch hyperbola trajectories.

Element	Value
Launch site latitude	28.5°
Azimuth launch angle	80.2°
Asymptote right ascension	177.21°
Asymptote declination	-66.43°
Earth-centred position of TOI burn (EQ2000)	(5598.4,1314.2,3194.2) km

15.2. Operations Phase

The operations phase includes everything from the spacecraft travelling to Mars until the end of the Aphrodite mission. This encompasses the actual travel of the spacecraft bus to Mars, the Martian orbit insertion, the landers separation from the spacecraft orbiter, the orbit insertions of the landers and their actual landing on the Martian moons, and finally, the carrying out of the scientific mission.

During the travel to Mars, the spacecraft bus is going to be put in travel mode. In order to communicate with the ground station on Earth, only the high-gain antenna (HGA) is going to be used, as the lasers will be in the adapters and the HGA's pointing accuracy is sufficient for communication with Earth. Not using the lasers reduces the power consumption of the spacecraft. In case of complications with the HGA, the omni-directional antenna also could be used, although at a much lower data rate as described in Section 4.1.

Once the spacecraft bus reaches the Martian system, the orbit insertion procedure begins. It will require a ΔV of 1.5 km/s as indicated in Chapter 8. Inducing such high velocity change makes it challenging to keep the spacecraft bus stable. In order to do so, the spacecraft's main engines will be throttled and the RCS thrusters will be fired if that is not sufficient. After that, the two landers separate from the spacecraft bus and enter their own orbits such that they can intersect the Martian moons and land on them.

Once they approach the moons, their detection systems are turned on, thus allowing for precise navigation during descent and landing as explained in Chapter 7. After the landers are separated from the spacecraft bus, the orbiter is put in an orbit around Mars at an altitude of 400 km at an inclination of 15°. When the landers have landed and the orbiter attained its orbit successfully, the laser equipment of the communication and ranging system is switched on, together with any equipment that was turned off during the safe-mode. It effectively

means that the orbiter and the landers are put in operational mode. This marks the beginning of the scientific mission of Aphrodite.

When performing measurements and gathering data, the unit stays in operational mode, however, the orbiter is going to be placed in eclipse-mode every time it is in eclipse in order to save power and extend the life of the batteries by reducing the number of discharge cycles they go through. Due to the fact that the ranging requirements stated in Section 3.3 can easily be met, putting the orbiter in eclipse-mode would not prevent meeting those requirements. Once in operational phase, the secondary payload is switched on.

If there is a problem with a unit, being the orbiter or the landers, it goes into safe-mode until the mission team can determine what the problem is and how it can be solved. For example, if the orbiter gets hit by space debris and the HGA is damaged, it will be put into safe-mode until the damage can be evaluated. During safe-mode, the landers and the orbiter can still communicate with the ground station using the omni-directional antenna.

The ground station used for RF-communication is the Deep Space Network, which is continuously manned and provides global coverage. Nonetheless, timeslots have to be selected in order to not hinder the other missions communicating with the Deep Space Network. The International Laser Ranging System (ILRS) is used to receive and send the laser pulses. The ILRS is also used to monitor the health of the spacecraft and intervenes in the case of calamities.

Near the end of the eight years that are planned for the Aphrodite mission, a potential extension of the mission can be proposed. However, that depends on the condition of the components of the various subsystem on-board the orbiter and also on the landers. The orbiter can be for example used as a communication relay for other Mars orbiters and landers and this increases the sustainability of the mission drastically. Once it is decided that the mission will be terminated, the End-of-Life phase, as described in Section 15.3, will start.

15.3. End-of-Life Phase

To limit space debris and the possible contamination of Mars as much as possible after the primary operations phase, end-of-life procedures must be developed. Several possibilities can be identified. These include providing the spacecraft with a ΔV moving it away from Mars to a heliocentric orbit, or letting the spacecraft burn up in the Martian atmosphere. The ΔV required to move the spacecraft to a heliocentric orbit would require a significant amount of propellant. Therefore this option is deemed unfavourable and focus is moved to having the orbiter enter the Martian atmosphere and burn up. This does, however, impose several requirements on the end-of-life procedure.

The first requirement comes from the strict requirements on avoiding contamination of Mars as stipulated in the Outer Space Treaty.[1] This requirement will be taken into account during the production phase, where the spacecraft will be assembled in a clean room with every part being cleaned individually, similar to the Mars Atmospheric and Volatile EvolutioN (MAVEN) mission.[2] This, along with the long operational time and radiation exposure that will decontaminate the orbiter even further, will ensure that the spacecraft does not contaminate Mars more than regulations stipulate upon burning in the atmosphere.

The second requirement concerns the usability of the spacecraft after its primary operations phase has been completed. Next to continuing the ranging operations to yield more and better data, the spacecraft could also be used as a communications relay for other Mars missions, as it carries a hefty communications package. Obviously, these secondary operations should be carried out as long as possible, but, as these relay operations are not the focus of the mission, it does not receive much budget.

The ΔV required to enter the Martian atmosphere within 20 years after the start of the operations is 50 m/s using the simulation elaborated in Chapter 5. This extra ΔV is included in the budget in Chapter 14. Burning the orbiter in the Martian atmosphere limits the debris orbiting Mars and increases the sustainability of the design.

[1] `https://planetaryprotection.nasa.gov/solarsystem/mars/` [Accessed on: 24 June 2017]
[2] `http://lasp.colorado.edu/home/maven/about/faqs/` [Accessed on: 24 June 2017]

16
Risk and Reliability

In this chapter, the complete system risks are presented as well as the interaction between the risk of the subsystems. Risk management during the Aphrodite mission has the purpose of not only identifying and mitigating risks to prevent mission failure, but to directly relate to requirement *OPS-SUV-ST-02* as well. That requirement states that the mission reliability shall be at least 90% over eight years. The global risks for the Aphrodite mission are described in Section 16.1 and the mission reliability is quantified in Section 16.2.

16.1. Risk Management

Risk management is actively performed throughout all phases of the design. A good risk management strategy makes sure that risks are identified as early as possible, in order to enforce mitigation strategies that will reduce their impact or likelihood to acceptable and specified boundaries. This section explains the risk management approach that was taken throughout the final stage of the project in Section 16.1.1 and then proceeds to the identification and assessment of the global risks in Section 16.1.2.

16.1.1. Risk Management Approach

Risks are divided into two categories: local risks and global risks. Local risks are those that directly have their root cause in the subsystem itself. They are identified and assessed at the end of each subsystem chapter. Global risks are risks that flow from elsewhere and form a risk that impacts multiple mission elements. Global risks can also flow from an aggravation of multiple local risks. They are discussed in this chapter. However, if their impact is directly related to the performance of the subsystem, their local impact and the possible local mitigation strategies are discussed per subsystem as well. The fault tree analyses that can be found in the subsystem chapters clearly show the coherence of local risks and risks directly flowing from other subsystems. Global risks are divided into four categories of risks, described below:

Technical: Technical risks are directly related to performance of a component.

External: External risks are risks that cannot be mitigated within the system, they come from external sources that cannot be influenced.

Schedule: Schedule risks are risks that will lead to delay within the schedule.

Cost: Cost risks are risks that directly influence the cost of the mission.

Once a risk is identified, an appropriate mitigation strategy is proposed, for example to reallocate resources. This can be manpower, facilities, money (cost) or time (schedule).

16.1.2. Global risk assessment

In Table 16.1, the global risks found for the Aphrodite mission are listed together with their mission impact and the mitigation strategy. It should be noted that the first four risks are global risks because they are defined for the subsystems that have the biggest supporting functions for the complete spacecraft. Partial failure of one of these systems does not necessarily mean that the complete spacecraft fails. For example, mitigation for partial power system failure can be to prioritise certain components which are most crucial to the mission at that moment. The components prioritised are the thermal system and the ranging system. The mitigated global risk map are shown in Table 16.2.

16.1.3. Critical mission modes

While risk is critical for all mission modes, two key modes are identified as critical mission modes being Orbit Insertion Mode and Landing Mode. These modes represent short term operations which are critical to the mission. Moreover, these modes also have the highest degree of uncertainties associated with them. The function and occurrence of these modes is defined in Section 3.2. The subsystems that have to ensure successful

Table 16.1: Global risk identification and mitigation.

No	Risk type	Risk	Mission impact	Action
1	Technical	(Partial) Power system failure	Less ranging time, less active attitude sensors, poor orbit determination.	Reallocate power.
2	Technical	(Partial) Attitude control failure	Lower mission life because of continuous propellant usage and decrease of data quality.	Redundancy and differential thrusting.
3	Technical	(Partial) Attitude determination failure	Poor orbit determination, failure to communicate with laser equipment.	Redundancy as described in Chapter 9
4	Technical	(Partial) Active thermal system failure	Battery failure, lower mission life, limited spacecraft performance.	Reallocate power.
5	Technical	Deimos landing failure	Partial mission failure, lower science value.	Active landing control.
6	Technical	Phobos landing failure	Partial mission failure, lower science value, poor orbit determination.	Active landing control.
7	Technical	Orbit insertion failure	Premature end of the mission (can be caused by propulsion failure, GNC failure and ADCS failure).	If possible, select different target which can still be met such as Luna or an asteroid which is close by.
8	Technical	Production errors	Local hardware failure.	Extensive batch testing on components and assembly testing.
9	External	Hypervelocity impact	Solar panels, structural or propulsion system fracture.	Passive protection can be achieved through Whipple shields with aluminium and Nextel–Kevlar bumper layers.
10	External	Launch failure	Premature end of the mission.	Choosing a reliable launcher
11	External	Unexpected environmental conditions	Incorrect models leading to orbit decay, shorter ADCS lifetime and propellant shortage.	Ranging less often to reduce wear or accept lower mission life.
12	Schedule	Launch delay	Mission cannot launch until three years when Mars window opens again.	Ten day launch delay buffer included in design.
13	Schedule	Testing facility not available	Testing has to be delayed or done elsewhere.	Have multiple test facilities.
14	Schedule	Technology development delay	Components not being available at the time needed (most relevant for the propulsion system).	Back-up options proposed in the design.
15	Schedule	Governmental issues	Not being allowed to proceed with the mission.	Select different launcher or launch site. If the launcher is not the issue, wait.
16	Schedule	Transportation issues	Delay in manufacturing.	Logistic planning containing back-up plans.
17	Schedule	Contractor bankruptcy	Other components need to be chosen or designed, causing delay.	Back-up options .
18	Cost	Increase of production cost	Exceeding the mission budget.	Allocate budget or produce elsewhere.
19	Cost	Aphrodite becomes too heavy for Falcon 9.	Not being able to launch.	Allocate budget for Falcon Heavy.

Table 16.2: Mitigated risk map of the Global Risks.

Likelihood / **Impact**	Negligible	Marginal	Moderate	Critical	Catastrophic
Almost certain					
Likely					
Average		13	16,17,8,14		
Unlikely		11,18	2,4,19	1,3,5	7,15,6
Improbable				9,12	10

Orbit Insertion Mode are GNC, propulsion and ADCS, out of which the most uncertainties rest in GNC and ADCS. Any error in timing and duration of the burns can lead to major mission compromising errors. On top of that, there is a fair amount of uncertainty associated with the ephemeris of Phobos and Deimos, which can only be mitigated by the GNC subsystem that could 'search' for the moons. Errors or uncertainties that are related to this therefore have their root cause in the GNC subsystem and they are treated in the sensitivity analysis of the GNC subsystem in Section 5.5. The key risk with ADCS is that it has to deal with disturbance torques that have a great amount of uncertainty rooting in internal disturbances as described in Section 9.4.3. This risk during Orbit Insertion has been mitigated by using thruster throttling and attitude control with the RCS thrusters, however, a fair amount of uncertainty still remains. It is recommended to perform more investigations on the internal disturbances. The key uncertainty associated with landing is the uncertainty in the physical surface properties of Phobos and Deimos. The uncertainty can be divided into the geological and geodesic uncertainties. While geological uncertainties are key in selecting the landing site and the anchoring of the landers, the geodesic uncertainties are critical in the determining the descent trajectory and duration. Given the scarce amount of information available regarding the Martian moons, active hazard detection and avoidance will play a crucial role in landing on the moons. The risks of landing on the moons and their mitigation are described in Chapter 7.

16.2. Reliability Analysis

The reliability of the mission is a crucial element of the design. According to *OPS-SUV-ST-02*, the reliability of all systems should be higher than 90% after eight years, excluding launcher reliability. This is a hard requirement to meet, since such a reliability over a long lifetime is uncommon for space missions. It therefore also deals with the long-term risks of hardware failure due to wear, fatigue and creep.

Reliabilities of certain subsystems are easier to model than others. When using off-the-shelf components, the failure rate is often included in the data of the manufacturer. This is the case for C&DH and ADCS. These subsystems are characterised by constant failure rates and are modelled using a negative exponential reliability distribution. The negative exponential reliability distribution is characterised by the constant failure rate λ. The rest of the subsystems do not have constant failure rates. The reliability of these subsystems is modelled with the Weibull function, which is presented in Equation 16.1.

$$R(t) = e^{-\left(\frac{t}{\alpha}\right)^{\gamma}} \tag{16.1}$$

where α is the scale parameter or characteristic life and γ is the shape parameter. Both parameters for the subsystems are obtained from Bris et al. [18]. In order to incorporate redundant design, the method used in Bris et al. [18] is applied. This method proposes that all redundant systems can be assumed completely independent and connected in parallel. This means that if one component fails, the other component is assumed to take over. Another big assumption in the reliability analysis is that all subsystems are functioning independently from each other. It is assumed that if one subsystem fails, the reliability of the other subsystems does not decrease. In Table 16.3, the constant failure rate for ADCS and C&DH is given, together with the number of redundant systems. In Table 16.4, the scale and shape parameters of the different subsystems are given, obtained from Bris et al. [18] together with the number of redundant systems.

Table 16.3: Constant failure rate for the ADCS and the C&DH subsystem .

Subsystem	**Failure rate** [failures/year]	**Number of redundant systems**
ADCS sensors	0.0006	4
ADCS actuators	0.00018	2
C&DH	0.023	5

Table 16.4: Weibull parameters for the other subsystems.

Subsystem	**Scale parameter** [-]	**Shape parameter** [years]	**Number of redundant systems**
Communication and Ranging	0.39	400982	3
Propulsion	0.33	6206945	6
Power	0.50	169	1
Structures/Mechanism/Thermal	0.35	21308746	0

Of course the reliability of the separate one-time events during operations also has to be included. The events included in the reliability are: separation from booster stage, detachment from orbiter, deployment of the solar panels and landing.

The reliability of the separation from the booster stage is 99 %, (SpaceX [109]). The reliability of separation from the orbiter is estimated to also be 99% (SpaceX [109]). The reliability of the deployment of the solar panels depends on the time until deployment. The solar panels are first deployed 2 days after launch and for the landers they are retracted approximately 215 days after launch and redeployed 216 days after launch and the reliability based on Bris et al. [18] is estimated to be 99.2%. The probability of success of the landing is harder to estimate. There has never been a successful landing on Phobos or Deimos and only three partially successful landings on microgravity bodies: Philae, Hayabusa and Near Schumacher. In order to give an estimate of the probability of success of the landing, a landing is defined as successful when the following system are successful:

- Gas generator fire successfully.
- Actuator which pulls the cables of the harpoons operates as planned and hold-down thrusters fire successfully.
- Optical cameras perform as expected.
- LIDAR works.
- C&DH performs as expected.
- Structure carries the loads for which it is designed.
- Battery and power distribution perform their task.

It is assumed that if one system fails, the landing also fails. The probability that all these systems are still working after 215 days is: 0.97. This probability is calculated, substituting 215 days in the Weibull functions of the corresponding subsystems. In Figure 16.1, the reliability of all the subsystems is plotted together with the total reliability of the landers and the orbiter. The pink dashed line indicates the 95% confidence bound on the reliability. This confidence bound is determined using the method and the variances given by Bris et al. [18]. It is clear from Figure 16.1, that the 90% reliability is achieved within the 95% confidence bound. Note that the probability of success of the discrete events is incorporated in the starting point of the Weibull which is 0.95 for the landers and 0.99 for the orbiter.

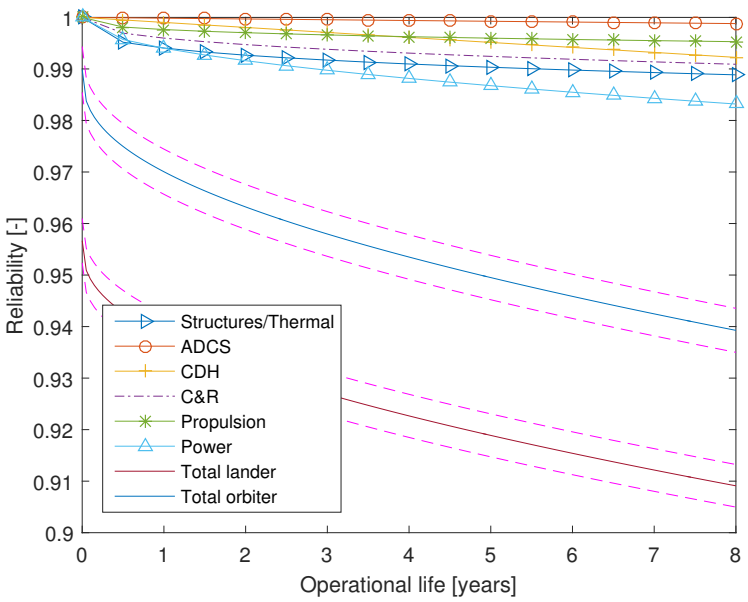

Figure 16.1: Reliability of the lander and the orbiter over the eight years of operational time.

17
Mission Considerations

This chapter discusses the development of the Aphrodite mission and the additional characteristics that are incorporated in the design. Firstly, a complete overview of the mission, after this conceptual design phase up to launch, is given in Section 17.1. The development, manufacturing and testing phase are elaborated in Section 17.2, where all testing methods are presented. The sustainability of the mission is discussed in Section 17.3. In every phase of the design, sustainability of the mission is a major design consideration. Finally, in Sections 17.4 to 17.6, the availability, maintainability and safety of the Aphrodite mission is discussed.

17.1. Logistics

After the preliminary design phase has been completed, multiple other phases have to be conducted in order to reach the final design which can be launched on time to meet the requirements. This section gives an overview of the activities to be performed after the conceptual design stage up to launch. The design and development phase can be split up into four main elements, as described by NASA (Ryschkewitsch [98]):

Design Phase: The design phase includes everything from preliminary design to final design, as well as computer-aided design (CAD). After the conceptual design phase, which is finished with this report, the components and assemblies have to be designed in more detail. The final design phase will result in a detailed design including technical drawings.

The allocated time for this phase is 55 months. This is slightly over the maximum 50 months, stipulated by NASA [98], though this is deemed allowable as the mission concerns complex and novel procedures where no reference missions or software can be used. The complete schedule of the design phase is presented in Figure 17.1 and is based on the schedule presented by Ryschkewitsch [98].

Fabrication Phase: The fabrication phase starts with prototype manufacturing, based on the detailed design. The main prototypes in this phase are the solar arrays, the laser ranging system, the lander leg assembly and the lander foot screws and harpoon. Although the main focus will be on these four elements, the other subsystems must not be forgotten as they also require prototyping and testing. The manufactured prototypes are subjected to vibration, shock and acoustic (VSA) tests and thermal vacuum (TV) tests, fatigue and impact load and penetration capability for the relevant subsystems (see Figure 17.5). If these tests are unsuccessful or the results are unsatisfactory, new prototypes have to be developed and tested until the desired performances are achieved. When the results are sufficient to be able to meet the stakeholder requirements, the project moves to the integration and testing phase.

The time allocated for the fabrication phase is 40 months, which is above the NASA average of 36 months, but well below the maximum (Ryschkewitsch [98]) of 5 years. The complete schedule of the fabrication phase is presented in Figure 17.2.

Integration & Testing Phase: The integration and testing phase starts with the integration of the previously fabricated prototypes into three types of assemblies, a structural and thermal prototype, an engineering prototype and a qualification prototype. This phase is discussed in more detail in Section 17.2. Once the results are satisfactory, a flight model is manufactured. This flight model is subjected to tests mimicking the conditions in space and in the Martian system as closely as possible. The model is also subjected to VSA and TV tests, and tested on software, electronics, flight modes, navigation, pointing and mechanical properties. If these tests result in unsatisfactory data, a new flight model must be manufactured and tested. However, this is very expensive and should be avoided. Once the tests have yielded satisfactory results and the system has received flight qualification, the project will move to the checkout and launch operations phase.

The allocated time for the testing and integration phase is 60 months. This is well above NASA maximum of 45 months which has been chosen deliberately since the reliability requirements are high and thus require extensive testing [98]. Since no mission ever succeeded in landing on the Martian moons, an extra time margin is incorporated in the testing phase. The complete schedule of the integration phase is presented in Figure 17.3.

Launch Operations & Checkout Phase: The launch operations and checkout phase is the final ground phase. This includes all operations from transportation to the launch site up to and including launch, e.g. mounting the spacecraft on the launch vehicle and fuelling.

The allocated time for this is set at seven months. This is lower than NASA average, since it is not an overly complex launch compared to other missions (Ryschkewitsch [98]). The complete schedule of the launch operations and checkout phase is presented in Figure 17.4.

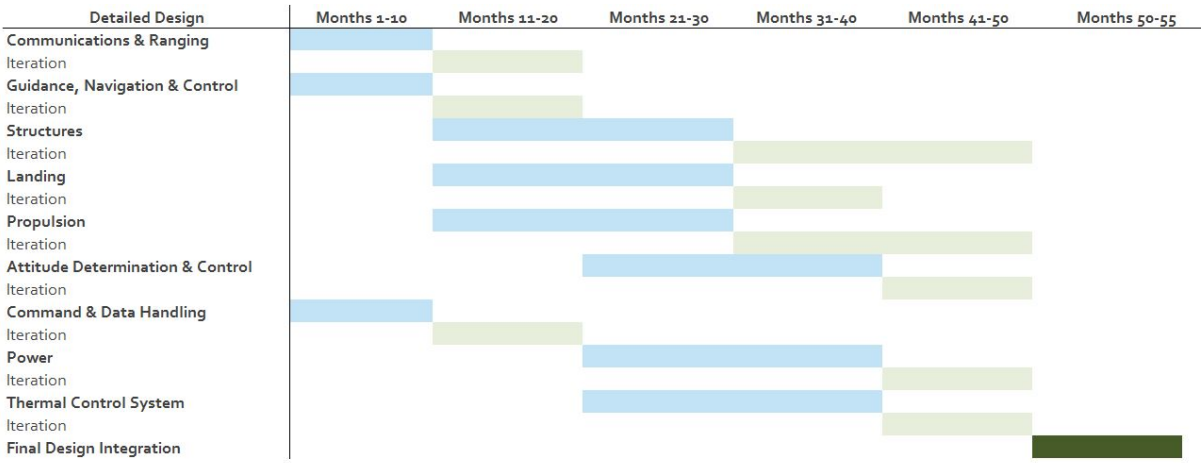

Figure 17.1: A diagram of when the tasks in the design phase are performed.

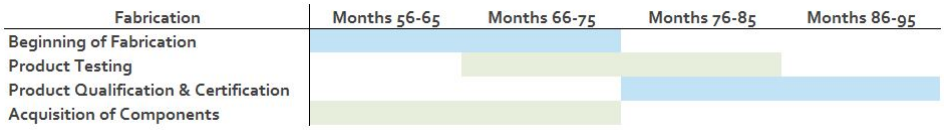

Figure 17.2: A diagram showing when the tasks in the fabrication phase are performed.

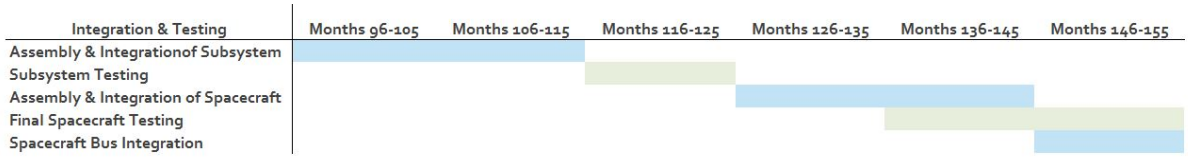

Figure 17.3: A diagram showing when the tasks in the integration testing phase are performed.

17.2. Development, Manufacturing, Assembly and Testing

Manufacturing, assembly and testing is the final phase before the spacecraft is transported to the launch-site for launch. It is of crucial importance that this phase is completed successfully and that the spacecraft is fully space qualified before being launched. The most crucial part is the successful testing of the spacecraft, so that it may survive all the extreme environments it will be subjected to during launch and operational life.

17.2.1. Development

At the beginning of this phase, simple models of the final spacecraft and all relevant sub-assemblies have to be built. These scale-models, which are representations of the actual spacecraft, will then be put to several tests. According to ESA, three different models can be built during this phase.[1] A structural and thermal model (STM),

[1] `http://www.esa.int/Our_Activities/Space_Science/Building_and_testing_spacecraft` [Accessed on: 23 June 2017]

Figure 17.4: A diagram showing when the tasks in the launch operations and checkout phase fabrication phase are performed.

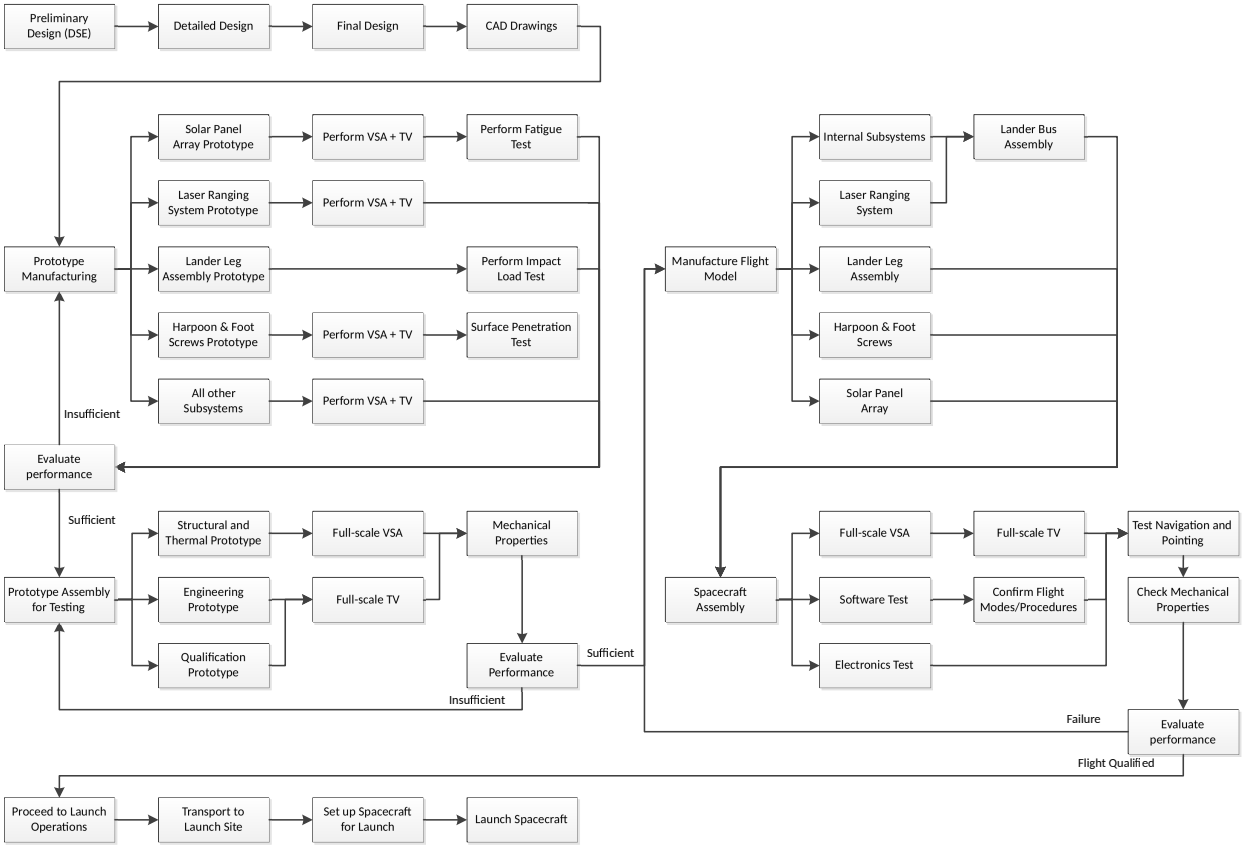

Figure 17.5: Project design & development logic diagram indicating the design, testing and manufacturing phases to be conducted after the preliminary design.

an engineering model (EM) and a qualification model (QM). The tests that will be performed on these models are listed below.

Vibration, Shock and Acoustic Tests: These tests are meant to replicate the conditions during launch, which will impose the structural and mechanical limits on the design. These tests are performed on the STM. During vibration tests, the model is mounted on a vibrating table on which the created conditions are approximately 25% higher than during launch.[1] The shock test is meant to see the impact of shocks (such as during landing) on the spacecraft structure. Finally, for the acoustic test the spacecraft is placed in a special chamber and is subjected to high intensity noise, similar to the noise levels experienced during launch.

Thermal Vacuum Test: The thermal vacuum test is meant to evaluate the performance of the spacecraft in a space-relevant environment. This test is performed on the EM and the QM. The main purpose of this test is to calibrate the thermal systems and to verify the predicted temperatures of the subsystems. This test can also be used to visualise the problems which might arise with the thermal control system, the electronics or any other critical components. For this particular mission this test can be used to evaluate the performance of the laser ranging system in a solar simulator, since this is the most crucial equipment of the mission.

Sub-assembly Qualification and Assessment: Certain sub-assemblies are crucial to the mission and should already be tested at this stage. This includes testing of sub-assemblies in all aforementioned tests. For this particular mission the deployable solar panel arrays, the laser ranging system, the landing leg assembly and the

harpoon and foot screw assemblies should already be tested in this stage, since these are mission specific items that are crucial to the mission.

- **Deployable solar arrays:** The mission uses a deployable solar array, which for the landers should also be retracted again during landing, which is uncommon. This will require extensive testing of the actuator which will retract the panels. This will involve both VSA testing as well as TV testing. The Parker Solar Probe, scheduled for 2018, will have retractable solar panels.[2] A lot of data on the functioning of the solar array mechanism can be gathered from this mission to improve the reliability of the solar array deployment mechanism of the landers. Research has already been done in retractable large solar-panels, together with proposed testing methods, as elaborated by Wolff and Felkel [133]. The solar panel of the orbiter is subject to constantly changing loads over the eight year mission life time. Therefore extensive fatigue tests have to be performed on the solar panel support structure to make sure the structure will not fail during its eight operational years.
- **Laser ranging system:** The entire mission is built around this system, if it fails, the mission fails. The system that will be used is not a completely flight-qualified system and has never been used in the relevant environment. Even though an earlier version of this system has been used in space, it will need extensive testing with at least TV tests, to see how it performs in the relevant environment. Also several elements have been added which up to now have only been proposed in theoretical scientific literature, so VSA tests needs to be performed as well.
- **Landing leg assembly:** The landing leg assembly is a crucial factor for landing on Phobos and Deimos. These moons have never been landed on resulting in a large uncertainty in how the landing site will look. The landing leg assembly will have to be tested for a worst case scenario in case of impact load. Also, the landing leg assembly will need to be mounted on the complete spacecraft model to be able to provide full-scale landing tests which might provide insight in performance when touching down on surfaces with diverse slopes and roughness.
- **Harpoons and foot screw:** The harpoons and foot screws provide the required stability and anchoring force during the mission period and are thus of crucial importance. This will require extensive surface penetration testing of the harpoons and foot screws, including surfaces with varying toughness and porosity while also varying the friction angle.

Balance, Moment of Inertia and Center of Gravity: Using the full-scale prototype, the mechanical properties of the spacecraft are accurately measured. These include weight, moments of inertia, Cg location and degree of unbalance. If these are out of the established boundaries these should be corrected for to ensure the correct performance of the spacecraft during flight and landing. The boundaries are determined by the ADCS system and are treated in Chapter 9.

17.2.2. Manufacturing

When testing of the models is complete, the manufacturing of the complete flight model of the spacecraft commences. When manufacturing the components, sustainability should be taken into account as much as possible. Most of the required parts are off-the-shelf products, which can be put into the spacecraft directly. The main exceptions here are:

- **Laser ranging system:** As previously explained in Chapter 4, most of the components of the laser ranging system have been extensively described in scientific literature and some of them have already been used in space missions. However, some other components have only been theoretically proposed, requiring the production of these for the Aphrodite mission.
- **Bus structures:** Since the structure of the spacecraft bus, both for the landers as well as the orbiter, is always highly mission specific, it will also have to be manufactured for this mission, this includes the manufacturing of the payload adapters.
- **Solar panel support:** The solar panels themselves can be simply off-the-shelf solar panels which can be ordered in the right size. The deployment mechanism however is specific for this mission and will thus need to be specifically manufactured.

One very important remark on the manufacturing of the spacecraft is that all the separately manufactured parts should be fully cleaned, using a clean room, due to the end-of-life solution which includes burning up

[2] `http://graphics.latimes.com/towergraphic-la-sci-solar-probe-plus/` [Accessed on: 16 June 2017]

in the atmosphere of Mars, where there is a small chance of crashing on Mars. The cleaning is required to comply with the Outer Space Treaty, as eplained in Section 15.3. This means that the manufacturing needs to be much stricter and every single part has to be fully cleaned. This will also restrict manufacturing to facilities with a clean room and will make transport significantly more difficult and costly since all parts will have to be transported in bio-containers. Next to these regulations, the manufactured products will comply with the COSPAR regulations as described by Williamson [130].

17.2.3. Assembly

When everything has been manufactured, assembly of the final spacecraft can start. This should take place simultaneously wherever possible and also as many sub-assemblies as possible should be assembled simultaneously at different locations in order to reduce production time. The keyword for this process is lean manufacturing. As little waste as possible should be created at any time during the assembly process, making it as sustainable as possible. Special care has to be take during the assembly of the following systems:

- **Laser ranging system:** If this system is not assembled correctly this can have huge consequences for the operation of the system and thus the successful performance of the mission.
- **Spacecraft bus:** Any joint within the structure of the spacecraft might lead to disastrous events in terms of failure during launch as a consequence of not being able to withstand the vibrational and acoustic loads during launch. This will only be worse because of the creation of stress concentrations at joints.
- **Solar arrays:** For the solar arrays, assembly of the joints is extremely important since the solar arrays should be retracted and redeployed. Misalignment of the joints could hinder this and cause mission failure.

Similar to the manufacturing, assembly needs to take part in a clean room due to end-of-life solution. This will impose the same constraints on the assembly as have already been discussed for manufacturing. Assembling in a clean room is common but the biological decontamination is only performed on planetary landers.

17.2.4. Final Testing

When the assembly of the flight model (FM) of the spacecraft is complete, some final tests should be performed to ensure correct performance. First of all the tests, as described under development, should be repeated with the exception of the destructive tests. In addition to the VSA and TV tests the FM should also be validated again to ensure correct working of the internal electronics. Also, a final software check is performed to ensure that all operating modes and flight procedures are covered. Finally, navigation and pointing are tested. These final checks in terms of space qualifying the spacecraft may take up to two years.[1] At the end of this phase the spacecraft is ready to be transported towards the launch site.

17.3. Sustainability in the Mission

Sustainability is a broad term, often misused for commercial purposes. Therefore, it is important to formally define sustainability to prevent confusion. In this report, the ISO 4001 compliance definition is used, which states: 'Sustainability is creating and maintaining conditions under which humans and nature can exist in productive harmony that permits fulfilling the social, economic and other requirements of present and future generations.[3] In order to prove this design is sustainable, three different impacts of the mission are considered: the social, economic and environmental impacts of the mission. These three elements are investigated in the four main stages of the mission: design, production, testing and operations.

Roza et al. [96] proposed the final mission concept. This mission concept was optimised considering the three components of sustainability. The design is sustainable for society since it fills a scientific gap with the laser ranging data, providing useful information about the Martian system which can be used to prepare human missions to Mars. The environmental impact of the mission is minimised from production to end-of-life. Concerning economic sustainability, the design stays within the budget constraint set by the stakeholders, while stimulating the local economy by maximising the use of instruments which can be produced in the European Union. This is because the main funding for this project will also be provided by EU institutions. A checklist was used to grade the sustainability of the design in Roza et al. [96]. Since the overall design did not change from the one in Roza et al. [96], the checklist is not presented again. For more information about how the sustainability of the design was evaluated, the reader is redirected to Roza et al. [96]. During the detailed design phase, an

[3] `https://www.iso.org/iso-14001-environmental-management.html` [Accessed on: 20 June 2017]

extensive Life-Cycle-Analysis (LCA) of each material, equipment and instrument has to be performed. This LCA involves the following steps: identify the mass of each material, equipment and instrument included in the spacecraft and use this mass to scale the Life Cycle Inventory analysis (LCI) of the respective components. Using these LCI, the sustainability of every production step can be maximised. The LCI databases can be found in the report by the European Space Agency LCA Working Group [37]. An example of the orbiter's solar panel LCI is given in Table 17.1. Similar analyses can be done for the other components of the orbiters and landers.

The solar array of the orbiter consists of the GaAs solar module of 11.83 kg and the solar array structure weighs 72.71 kg. The flow of material in the LCI starts with material input and energy input, goes through the production methods and outputs the products and the waste. In Table 17.1, the LCI for the GaAs solar module and the solar array structure is listed. The database from the European Space Agency LCA Working Group [37] is used to constuct this table.

Table 17.1: Life cycle inventory analysis of the solar array.

GaAS solar module			**Solar array structure**		
Nature	**Quantity**	**Units**	**Nature**	**Quantity**	**Units**
Material Inputs			**Material inputs**		
Ammonia	34.11	kg	Cyanate ester resin	28.72	kg
Arsenic trioxide	8.24	kg	Carbon fibres	42.66	kg
Inorganic chemicals	8.81	kg	**Manufacture Processes**		
Organic chemicals	73.90	kg	Chromic acid anodizing of aluminium alloys	20.52	m^2
Gallium	0.97	kg	Cleaning with solvent	41.11	m^2
Kevlar protector	1.79	kg	Electricity consumption for processes	1308.22	kWh
Hydrogen	34.11	kg	**Transports raw materials**		
Hydrogen chloride	9.67	kg	Truck RM	71.08	tkm
Hydrogen fluoride	6.25	kg	**Waste production**		
Hydgrogen peroxide	24.16	kg	Plastic waster	3.58	kg
Indium	0.044	kg	**Transport of waste**		
Nitrogen	12.51	kg	Truck waste	0.19	tkm
Phosphorus	0.11	kg			
Silver	0.539	kg			
Sodium chloride	0.077	kg			
Sodium hydroxide	7.68	kg			
Organic solvents	14.50	kg			
Sulphuric acid	4.27	kg			
Tap water	284.24	kg			
De-ionised water	937.98	kg			
Others	20.19	kg			
Manufacturing Processes					
Electricity	6237	kWh			
Transport raw materials					
Truck	261.8	tkm			
Waste production					
Disposal solvents	1.45	kg			
Transport of waste					
Truck waste	0.072	kg			

Transportation is measured in tonnekilometres, tkm. This LCI can also be made for the other components and thus the waste during the production can be quantitatively estimated. The production process of the mission has already been explained in Section 17.2. This manufacturing plan puts efficiency and sustainability on the forefront. Sustainable production is defined as production in a manner which is socially beneficial, economically viable and environmentally benign over the whole life cycle.[4] The structure of the satellite is made of aluminium; a lightweight, strong and highly recyclable material. This means that waste material produced during the production can be easily recycled. The assembly of the orbiter and the lander will happen at one dedicated facility, which minimises the transport of material. One more aspect to take into account for sustainability is the system tests. The reliability requirement of the system is high, certainly for a landing on micro-gravity bodies. This high reliability can be partially obtained by extensive testing. This extensive testing comes at the cost of energy usage and waste material. However, this can be compensated by recycling the waste material and obtaining energy necessary for the test from green energy resources such as solar and wind power.

[4] `https://www.journals.elsevier.com/sustainable-production-and-consumption/` [Accessed on: 20 June 2017]

LMP-103S is used as propellant for the mission. LMP-103S is listed as a high performance green propulsion (Anflo and Möllerberg [6]). The emitted gas from the catalyst decomposition of LMP-103S is composed of water, nitrogen dioxide and nitrogen. LMP-103S is considerably more sustainable than all the other mono-propellants on the market today, as explained in Section 8.3.1. The Falcon 9 was selected in Roza et al. [96], taking the sustainability of the launcher into consideration, since a reused booster of the Falcon 9 will be used. This decreases the cost and increases the sustainability of the mission. In order to comply with the ITAR regulations, no use will be made of nuclear sources. One more important aspect about operational sustainability is the EoL strategy. The landers of Phobos and Deimos do not have an end-of-life strategy since they cannot be removed from the moons' surface. Keeping them attached to the surface makes sure they do not become space debris, which can damage the other Mars orbiters. The orbiter will perform an EoL manoeuvre that will ensure the spacecraft burns up in the Martian atmosphere within 20 years as explained in Section 15.3.

17.4. Availability

The availability of the design is strongly inter-related with the reliability. It includes two aspects: first, the aspect that the design is available for launch at the predetermined launch date. Secondly, it refers to the abilities of the system to perform the science measurements according to the stakeholder requirements during the operational lifetime. The launch is in February 2031. It is already shown in Section 17.1, that 14 years is more than enough time to perform the detailed design, the production and elaborate testing. Therefore if the funding is guaranteed, the design is expected to be ready well with in the time limit. In Section 16.2, it is shown that the reliability of the mission after eight years is higher than 90%. Therefore it can be stated that the Aphrodite mission will perform its scientific measurements with a probability higher than 90% after eight years. The availability of the ranging measurements is related to the communication windows. In Chapter 4, the communication windows were analysed and it was shown that abundant opportunity to communicate and range is available.

17.5. Maintainability

Since the orbiter and both landers will be in the Martian system, the system cannot be physically maintained. However, two elements of the mission can be maintained, namely software and the ground stations.

- **Software Maintenance:** the software of both the landers and the orbiter can be updated from the ground station if necessary. However, the data rate of the lasers is not high enough to send the complete updated software in one communication window. Therefore, the software should be sent in parts, which would induce the new risk that the software would not be correctly compiled on the orbiter or landers. It would be more feasible to uplink new error correction algorithms to the spacecraft. These do not take up as much bandwidth and they would significantly improve the performance of the laser ranging measurements. However, software maintenance should only be performed when absolutely necessary, since it could endanger the success of the complete mission.[5]
- **Ground Station Maintenance:** the ground station can be of course physically maintained and updated. The most obvious elements which can be updated are error correction algorithms, pointing accuracy of the antennae and lasers or uplink data rates. Ground stations are updated frequently to optimise the communication performances. If the performances of the orbiter or lander drop due to degradation or long exposure to the deep space environment, the uplink power of the ground station can be increased to enable the same uplink data rate.

17.6. Safety

Safety covers both the lack of hazards to people, as well as the equipment itself. The safety of the people is most relevant in this mission during the production phase. The production methods have already been explained in Section 17.2 and the safety of the production method was a major point of attention. Safety to the equipment during the operations is quantified by risks and risk mitigation. Risk mitigation has been already covered thoroughly in this report (Chapter 16) and will not be repeated in this section. It can be concluded from the active risk mitigation and the innovative production methods that the Aphrodite mission is safe for the people and itself.

[5] https://www.geek.com/tech/software-update-causes-286-million-japanese-satellite-to-break-apart-in-orbit-1654675/ [Accessed on: 18 June 2017]

[This page is intentionally left blank]

18
Conclusion and Recommendations

This report presents the Aphrodite mission, a breakthrough mission aimed at revolutionising solar system dynamics research. Aphrodite sends two landers and one orbiter to the Martian system. The two landers have Phobos and Deimos as their destination, while the orbiter will enter a Martian orbit of 400 km altitude.

The orbiter and the two landers will perform inter- and intra-system ranging to measure the distance within the Martian system and to Earth with unprecedented accuracy of 0.5 m. Using such accurate ranging data could provide hints about the origin of the Martian moons and the interior structure and composition of the moons. Measuring the Martian system dynamics enables scientists to test gravitational physics with unprecedented accuracy.

The Aphrodite mission is used to perform high-accuracy tests of the equivalence principle, to search for a possible time-variation in the gravitational constant and to test predictions of various alternative theories of gravity.[1], The mission uses existing technologies to lower the cost, while complying with high reliability and higher accuracy requirements. Using advanced risk mitigation strategies and life cycle assessment, this mission brings sustainability in space to new heights.

The total mission will cost M€931 for sending a total wet mass of 3865 kg towards the Martian system with the Falcon 9. The mission will be launched on 26 February 2031 and it is planned to be operational by the end of September 2031 until 2039.

Using an interplanetary high-thrust trajectory optimised to minimise ΔV, the spacecraft targets a bi-elliptic orbit in the Martian system. Both landers separate from the orbiter in the Martian system to individually perform the last part of their journey to the moons. The orbiter carries propellant for a total ΔV of 3.34 km/s, the Deimos lander can perform a ΔV of 0.78 km/s and the Phobos lander a ΔV of 0.99 km/s.

There has never been a successful landing on Phobos and nobody ever even attempted to land on Deimos. Therefore, hazard avoidance and risk mitigation are a vital part of the landing sequence. The Phobos lander, having a wet mass of 395 kg and the Deimos lander, having a wet mass of 384 kg, are both equipped with the same landing system, including four cameras, flash LIDAR, Doppler LIDAR, three harpoons and three foot screws on each landing strut. The landing site of the Phobos lander is centred around $-11°$ longitude and 17° latitude. The landing site on Deimos extends from 33° to 60° longitude and from 15° to 20° latitude. The descent trajectory for both Phobos and Deimos has been optimised to minimise the propellant use, resulting in propellant masses of 2.87 kg for Deimos and 7.23 kg for Phobos. These propellant masses are doubled to account for a second descent trajectory if the first landing fails.

The communication and ranging system, which performs the main mission activity, uses both optical and radio waves to transmit and receive data. The ranging is performed by laser telescopes. The radio equipment provides an extra level of redundancy and is also used for Doppler tracking of the orbiter. The Phobos lander uses an average power of 210 W during the operational phase. The Deimos lander uses a bit less with 198 W. The orbiter, on the other hand, consumes 846 W.

The reliability of the mission is estimated to be 91% for the landers and 94% for the orbiter after eight years. This high reliability is achieved by integrating several detailed risk mitigation measures in the design. All systems are designed to be redundant and highly to fail. The landing is still the most risky part of the mission, but by using an active intelligent landing control algorithm and highly redundant landing sensors and actuators, the probability of success is brought up to 97%.

While conducting a thorough and active risk mitigation, sustainability of the mission is also a major concern. It is integrated in the complete mission, from the design phase to the End-of-Life phase. Sustainability management was continuously carried out during each design step, optimising for social, environmental and economical impact of the mission. The production process uses a novel life cycle assessment method, estimating the waste for each component in the spacecraft. The mission is launched by the Falcon 9, of which

[1] `http://www.einstein-online.info/spotlights/equivalence_principle` [Accessed on: 30 June 2017]

the first stage is reused, which increases the sustainability of the mission drastically. The components between the orbiter and the two landers are kept as similar as possible, to minimise waste, production time and cost.

18.1. Recommendations

Of course, in ten weeks, not all aspects of the mission could be investigated in detail. Therefore, a meticulous recommendation section follows to discuss what could be done in the future or what could have been better in this report. First, the overall design recommendations are presented. Afterwards, the recommendations per subsystem are listed.

General Design Recommendations

- Due to the preliminary nature of this design, many uncertainties remain. Therefore, detailed research has to be conducted to reduce their uncertainties.
- The integration and interface of the secondary payload should be investigated further.
- The effects on the mission of launching in 2033 should be investigated, as at that time a more efficient launch window opens. This will decrease the required propellant and allows extended design and production time.

ADCS Recommendations

- In this report, the impact of internal disturbances on pointing knowledge and accuracy was not investigated. It is recommended to do this in the detailed design phase.
- The possibility of using the attitude control system as power storage as described by Tsiotras and Shen [119] can be analysed.

Thermal Recommendations

- The heat flow and exchange have now been approximated using an analytical model. This flow should be modelled using differential Fourier equations, which can be integrated over time.
- The radiation environment was hard to model at this stage of the design. Therefore it is recommended to investigate the effect of the space environment on the spacecraft components in more detail.

Structural and Separation System Recommendations

- It is recommended to investigate creep and stress corrosion cracking (SCC) in the separation mechanism springs. No data about the behaviour of the separation mechanism in deep-space environment had been found.
- In this report, the integration of hardware into the structure was not designed. This should be done in a later design phase.
- It should be evaluated if parts, released during separation, can cause damage to the spacecraft and if any mitigation is necessary.

Landing Recommendations

- A Monte Carlo simulation should be made where the key parameters such as gravity, small craters, boulders, slope, elevation, roughness and surface toughness are varied to obtain a probability of successful landings and develop an active landing algorithm accordingly.
- It is recommended to use newer hazard detection instruments with a larger number of pixels, hence allowing detection of small surface features from higher altitudes and in turn making the landing more reliable.
- It should be considered to send a piggyback probe or instrument on any of the future Mars missions before Aphrodite, in order to better map the surface of Deimos.
- It is recommended to investigate the surface penetration of the harpoons using models that incorporate the friction angle of regolith and its viscous behaviour.

GNC Recommendations

- The behaviour of the landers close to the moons should be studied in detail including all perturbations caused by the proximity of the moons.
- A new simulation should be made that incorporates the burn times in the trajectory and integrates over the decrease of mass and the change in position during the burn.
- A shorter travel time for landers to travel to the moons should be investigated. This could create the option for non-retractable solar panels, as battery power can be used.

Bibliography

[1] M.H. Acuna, J.E.P Connerney, P. Wasilewski, R.P. Lin, D. Mitchell, K.A. Anderson, C.W. Carlson, J. McFadden, H. Rème, C. Mazelle, D. Vignes, S.J. Bauer, and P. Cloutier. Magnetic Field of Mars: Summary of Results from the Aerobraking and Mapping Orbits. *Journal of Geophysical Research of Planets*, 106(E10): 23403—-23417, October 2001.

[2] M. Alexander. Mars Transportation Environment Definition Document. Technical report, NASA, Huntsville, Alabama, USA, 2001.

[3] S. Amos and P. Brochard. Battery for Extended Temperature Range ExoMars Rover Mission . In *E3S Web of Conferences*, volume 16, 2017. doi: 10.1051/e3sconf/20171606001.

[4] F. Amzajerdian, D. Pierrottet, L. Petway, G. Hines, and V. Roback. Lidar Systems for Precision Navigation and Safe Landing on Planetary Bodies. In *Proc. SPIE*, volume 8192, page 202, 2011.

[5] F. Amzajerdian, D. Pierrottet, G. Hines, L. Petway, and B. Barnes. Fiber-based Doppler LIDAR for Vector Velocity and Altitude Measurements . In *Frontier in Optics and Laser Science*, San Jose, California, USA, October 2015.

[6] K. Anflo and R. Möllerberg. Flight Demonstration of New Thruster and Green Propellant Technology on the PRISMA Satellite. *Acta Astronautica*, 65(9):1238–1249, 2009.

[7] S.W. Asmar, J.W. Armstrong, L. Iess, and P. Tortora. Spacecraft Doppler Tracking: Noise Budget and Accuracy Achievable in Precision Radio Science Observations. *Radio Science*, 40, 2005. doi: 10.1029/2004RS003101.

[8] S. Badessi, D. Castrovillari, and B. Collini-Nocker. ENVISAT RA2/MWR Product Handbook. Technical report, European Space Agency, Paris, France, February 2007.

[9] G.D. Badhwar. Martian Radiation Environment Experiment (MARIE). *Space Science Reviews*, 110(1): 31–142, 2004. ISSN 1572-9672. doi: 10.1023/B:SPAC.0000021009.68228.a8.

[10] W. B. Banerdt, T. Pike, R. Martin, and P. Lognonne. A Seismic Investigation of the Interior of a Comet. *Lunar and Planetary Science*, 27:59, March 1996.

[11] S. Barraclough, A. Ratcliffe, R. Buchwald, H. Scheer, M. Chapuy, M. Garland, and D. Rebuffat. Phootprint: A European Phobos Sample Return Mission. In *11th International Planetary Probe Workshop*, volume 1795 of *LPI Contributions*, page 8030, June 2014.

[12] M.J. Barrett and R.G. Lyle. *Spacecraft Solar Cell Arrays*. page 16. NASA JPL, Pasadena, California, USA, May 1971.

[13] A.T. Basilevsky, C.A. Lorenz, T.V. Shingareva, J.W. Head, K.R. Ramsley, and A.E. Zubarev. The Surface Geology and Geomorphology of Phobos. *Planetary and Space Science*, 102:95–118, November 2014. ISSN 0032-0633. doi: 10.1016/j.pss.2014.04.013.

[14] E. Battista, S. Dell'Agnello, G. Esposito, L. Di Fiore, J. Simo, and A. Grado. Solar System Dynamics in General Relativity. *International Journal of Modern Physics D*, 25(14), 2016.

[15] A.W. Bett, S.P. Philipps, S. Essig, S. Heckelmann, R. Kellenbenz, V. Klinger, M. Niemeyer, D. Lackner, and F. Dimroth. Overview About Technology Perspectives for High Efficiency Solar Cells for Space and Terrestrial Applications . In *28th European Photovoltaic Solar Energy Conference and Exhibition*, Heidenhofstraße 2, 79110 Freiburg, Germany, September 2013.

[16] J. Biele, S. Ulamec, M. Maibaum, R. Roll, L. Witte, E. Jurado, P. Muñoz, W. Arnold, and C.S Auster, H.and Casas. The Landing(s) of Philae and Inferences about Comet Surface Mechanical Properties. *Science*, 349(6247):16, July 2015.

[17] A. Biswas, D. Boroson, and B. Edwards. Mars Laser Communication Demonstration: What it Would Have Been. *Proc. SPIE*, 6105(18):610502–12, 2006. doi: 10.1117/12.669551.

[18] R. Bris, C.G. Soares, and S. Martorell. *Reliability, Risk, and Safety, Three Volume Set: Theory and Applications*. EBL-Schweitzer. CRC Press, London, United Kingdom, 2009. ISBN 9780203859759.

[19] C.D. Brown. *Elements of Spacecraft Design*. AAIA Education Series. American Institute of Aeronautics and Astronautics, Castle Rock, Colorado, USA, 1st edition, 2002.

[20] F. Budnik and T. Morley. Rosetta Navigation at its Mars Swing-by. In *Proceedings of the 20th International Symposium on Space Flight Dynamics*, March 2007.

[21] C. Capela. Protocol of Communications for VORSAT Satellite. Master's thesis, Universidade do Porto, Faculdade de Engenharia, Porto , Portugal, September 2012.

[22] A. Cervone. Aerospace Design and Systems Engineering Elements: Spacecraft Telecommunications. University Lecture Notes at Delft University of Technology, September 2015.

[23] E. Christiansen. Design and Performance Equations for Advanced Meteoroid and Debris Shields. *International Journal of Impact Engineering*, 14(1-4):145–156, 1993.

[24] D. Conte. Determination of Optimal Earth-Mars Trajectories to Target the Moons of Mars. Master's thesis, Pennsylvania State University, Old Main, Pennsylvania, USA, May 2014.

[25] K. Daryabeigi, S. Miller, and G. Cunnington. Heat Transfer in High-temperature Multilayer Insulation. In *Thermal Protection Systems and Hot Structures*, volume 631, 2006.

[26] K.K. De Groh, B.A. Perry, J.S. Mohammed, and B. Banks. Analyses of Hubble Space Telescope Aluminized-Teflon Multilayer Insulation Blankets Retrieved After 19 Years of Space Exposure. Technical report, National Aeronautics and Space Administration, Cleveland, Ohio, USA, 2015.

[27] Department of Defense of the USA. *5H: Metallic Materials and Elements for Aerospace Vehicle Structures*, volume 1. pages 3–371, 3–220. US Department of Defense, Atlantic City, New Jersey, USA, 2nd edition, January 2003.

[28] S. Destefanis, R. Buchwald, P. Pellegrino, and S. Schroder. Landing System Development- Design and Test Prediction of a Lander Leg Using Nonlinear Analysis. In *13th European Conference on Spacecraft Structures, Materials & Environmental Testing*, volume 727 of *ESA Special Publication*, page 11, June 2014.

[29] J. Dickey, P. Bender, J. Faller, X. Newhall, R. Ricklefs, J. Ries, P. Shelus, C. Veillet, A. Whipple, and J. Wiant. Lunar Laser Ranging: A Continuing Legacy of the Apollo Program. *Science*, 265(5171):482–490, July 1994. doi: 10.1126/science.265.5171.482.

[30] A. Dinardi. High Performance Green Propulsion (HPGP): A Flight-Proven Capability and Cost Game-Changer for Small and Secondary Satellites. In *26th AIAA/USU Small Satellite Conference*, North Logan, Utah, USA, August 2012.

[31] D. Dirkx. *Interplanetary Laser Ranging. Analysis for Implementation in Planetary Science Missions*. PhD thesis, Delft University of Technology, Delft, the Netherlands, October 2015.

[32] D. Dirkx, L.L.A. Vermeersen, R. Noomen, and P.N.A.M. Visser. Phobos Laser Ranging: Numerical Geodesy Experiments for Martian System Science. *Planetary and Space Science*, 99:84–102, 2014.

[33] D. Dirkx, R. Noomen, P.N.A.M. Visser, S. Bauer, and L.L.A. Vermeersen. Comparative Analysis of One-and Two-Way Planetary Laser Ranging Concepts. *Planetary and Space Science*, 117:159–176, 2015.

[34] G.J. Dudley. Lithium-Ion Batteries for Space. In *Proceedings of the Fifth European Space Power Conference (ESPC)*, September 1998.

[35] D.A. Duev and S.V. Pogrebenko. Spacecraft VLBI and Doppler Tracking: Algorithms and Implementation. *Astronomy and Astrophysics*, 593, May 2012. doi: 10.1051/0004-6361/201628869.

[36] European Space Agency. *Structural Materials Handbook*, volume 1. page 26. ESA Publications Division ESTEC, Noordwijk, the Netherlands, 1st edition, February 1994.

[37] European Space Agency LCA Working Group. *Space System Life Cycle Assessment (LCA) guidelines*. ESTEC, Noordwijk, The Netherlands, October 2016.

[38] European Space Research and Technology Centre. *Margin Philosophy for Science Assessment Studies*. ESA, Keplerlaan 1, 2201 AZ Noordwijk, The Netherlands, 1 edition, June 2012.

[39] J.P. Fellner, G.J. Loeber, S.P. Vukson, and C.A. Riepenhoff. Lithium-Ion Testing for Spacecraft Applications. *Journal of Power Sources*, 119-121:23–24, June 2003.

[40] M. Ferrari. Structurally Optimized and Additively Manufactured Inserts for Sandwich Panels of Spacecraft Structures. Technical report, Swiss Federal Institute of Technology Zurich, Zurich, Switzerland , December 2015.

[41] A. Foessel-Bunting and W. Whittaker. MMW-Scanning Radar for Descent Guidance and Landing Safeguard. In *Proceedings 6th International Symposium on Artificial Intelligence, Robotics and Automation in Space*, Pittsburgh, PA, 2001.

[42] A. Genova, M. Marabucci, and L. Iess. A Batch-Sequental Filter for the BepiColombo Radio Science Experiment. *Journal of Aerospace Engineering, Science and Applications*, 4:17–30, October 2012. doi: 10.7446/jaesa.0404.02.

[43] D.G. Gilmore. *Spacecraft Thermal Control Handbook. Vol. 1.: Fundamental Technologies*, volume 1. The Aerospace Press, 2350 E. El Segundo Boulevard, El Segundo, California, USA, 2002.

[44] D.G. Gilmore and M. Donabedian. *Spacecraft Thermal Control Handbook. Vol. 2.: Cryogenics*, volume 2. The Aerospace Press, 2350 E. El Segundo Boulevard, El Segundo, California, USA, 2003.

[45] B.E. Goldberg and K. Everhart. System Engineering "Toolbox" for Design-Oriented Engineers. Technical report, Marshall Space Flight Cente, December 1994.

[46] R.H. Gooding. A Procedure for the Solution of Lambert's Orbital Boundary-value Problem. *Celestial Mechanics and Dynamical Astronomy*, 48(2):145–165, June 1990. doi: 10.1007/BF00049511.

[47] T. Gross. Conceptual Design of a Mars Transportation System. Technical report, University of Minnesota, Minneapolis, Minnesota, USA, 1992.

[48] A.M. Harte, N.A. Fleck, and M.F Ashby. Sandwich Panel Design Using Aluminum Alloy Foam. *Advanced Engineering Materials*, 2(4):219–222, April 2000.

[49] J.H. Henninger. Solar Absorptance and Thermal Emittance of Some Common Spacecraft Thermal-Control Coatings. Technical report, DTIC Document, Greenbelt, Maryland, USA, 1984.

[50] HEXCEL. HexWeb Honeycomb Energy Absorption Systems. Technical report, HEXCEL, March 2005.

[51] D. Honegger, P. Greisen, L. Meier, P. Tanskanen, and M. Pollefeys. Real-time Velocity Estimation Based on Optical Flow and Disparity Matching. In *Intelligent Robots and Systems (IROS), 2012 IEEE/RSJ International Conference on*, pages 5177–5182, Vilamoura-Algarve, Portugal, 2012. IEEE.

[52] J.B. Hopkins and W.D. Pratt. Comparison of Deimos and Phobos as Destinations for Human Exploration, and Identification of Preferred Landing Sites. In *AIAA Space 2011 Conference & Exposition, Long Beach*, pages 27–29, Long Beach, California, USA, September 2011.

[53] Q. Hu, Y. Li, J.T. Liu, and J.Q. Liang. Research on Liquid Sloshing Performance in Vane Type Tank under Microgravity. In *IOP Conference Series: Materials Science and Engineering*, pages 12–16, Beijing, China, 2016. IOP Publishing.

[54] V. Iafolla, E. Fiorenza, C. Lefevre, S. Nozzoli, R. Peron, A. Reale, and F. Santoli. The ISA Accelerometer for BepiColombo Mission. *Societa Astronomica Italiana*, 16:22, January 2011.

[55] V. Jamnejad, J. Huang, H. Endler, and F. Manshadi. Small Omni-directional Antenna Development for Mars Sample Return Mission. *Aerospace Conference, IEEE Proceedings*, 150, March 2001.

[56] D.L. Jones and W.M. Folkner. Astrometry of Cassini with the VLBA to Improve the Saturn Ephemeris. *The Astronomical Journal*, 149, January 2015. doi: 10.1088/0004-6256/149/1/28.

[57] S. Khurana, H.W.W. Guimarães, I.M. Konovalov, N.M. de Korte, T. van Lith, M.K. Makaveev, Z.N. Rabilotta, W. Van Gijseghem, W. Van Herck, and I.R. Roza. DSE Baseline Report Group 11. Technical report, Delft University of Technology, Delft, the Netherlands, May 2017.

[58] S. Khurana, I.R. Roza, I.M. Konovalov, N.M. de Korte, T. van Lith, M.K. Makaveev, Z.N. Rabilotta, W. Van Gijseghem, W. Van Herck, and H.W.W. Guimarães. DSE Project Plan Group 11. Technical report, Delft University of Technology, Delft, the Netherlands, May 2017.

[59] S.M. Kopeikin, E. Pavlis, and D. Pavlis. Prospects in the Orbital and Rotational Dynamics of the Moon with the Advent of Sub-centimeter Lunar Laser Ranging. *Advances in Space Research*, 42:1378–1390, October 2008. doi: 10.1016/j.asr.2008.02.014.

[60] S. Krenk and J. Høgsberg. *Statics and Mechanics of Structures*. SpringerLink : Bücher. Springer Netherlands, Houten, the Netherlands, 2013. ISBN 9789400761131.

[61] M. Krop. Long Lifetime Orbits about Mars. In *3rd and 4th Aerospace Sciences Meeting*, page 35, Amsterdam, the Netherlands, 1966.

[62] R.O. Kuzmin, T.V. Shingareva, and E.V. Zabalueva. An Engineering Model for the Phobos Surface. *Solar System Research*, 37(4):266–281, July 2003. ISSN 1608-3423. doi: 10.1023/A:1025074114117.

[63] M.K.B. Larbi and E. Stoll. Spacecraft Formation Control using Analytical Integration of Gauss' Variational Equations. In *6th International Conference on Astrodynamics Tools and Techniques, ICATT*, Braunschweig, Germany, 2016.

[64] A. Larsson and N. Wingborg. *Green Propellants Based on Ammonium Dinitramide (ADN)*. InTech, Rijeka, Croatia, 1st edition, 2011.

[65] S.A. Leadbetter. Application of Analysis and Models to Structural Dynamic Problems Related to the Apollo-Saturn V Launch Vehicle. Technical report, Langley Research Center, Hampton, Virginia, USA, June 1970.

[66] S. Lee, G. Ortiz, and J. Alexander. Star Tracker-Based Acquisition, Tracking, and Pointing Technology for Deep-Space Optical Communications. *Interplanetary Network Progress Report*, 42(161):42–161, 2005.

[67] Z.Q. Li, G. de Carufel, E.Z. Crues, and P. Bielski. Lighting Condition Analysis for Mars' Moon Phobos. In *37th IEEE Aerospace Conference*, Big Sky, Montana, USA, March 2016.

[68] G.J. Lin, J. Bi, M. Song, J. Liu, W. Xiong, and M. Huang. III-V Multi-Junction Solar Cells. *Optoelectronics - Advanced Materials and Devices*, 1(1), January 2013. doi: 10.5772/50965.

[69] K. Lingenauber, H. Hussmann, H. Michaelis, J. Oberst, M. Kobayashi, N. Namiki, N. Thomas, K. Seiferlin, and L.M. Lara. The Ganymede Laser Altimeter (GALA) on ESA's JUICE Mission: Overview of the Instrument Design. In *GALA*, number 1. DLR, November 2014.

[70] H. Liu, Z. Zhao, and J. Zhao. Preliminary Anchoring Technology for Landing on the Asteroid. In *Robotics and Biomimetics (ROBIO), 2013 IEEE International Conference on*, pages 2392–2396, Shenzhen, China, December 2013. IEEE.

[71] D.P. Margaris, Z.G. Diamantis, D.I. Photeinos, and D.T. Tsahalis. Performance of Heat Pipes as Capillary Pumps: Modelling and Comparison with Experimental Results. *International Journal of Low-Carbon Technologies*, 2(2):149–161, 2007.

[72] Lockheed Martin. Software User's Guide for the RAD6000 Processor. Technical report, Lockheed Martin, Manassas, Virginia, USA, January 2004.

[73] W.D. McClain and D.A. Vallado. *Fundamentals of Astrodynamics and Applications*. Space Technology Library. Springer Netherlands, 2001. ISBN 9780792369035.

[74] M. Meltzer. *The Cassini-Huygens Visit to Saturn: An Historic Mission to the Ringed Planet*, volume 1. pages 111–114. Springer International Publishing, Oakland, California, USA, 1st edition, January 2015.

[75] D.H. Mitchell. Flight Separation Mechanisms. Technical report, Delft University of Technology, Delft, the Netherlands, October 1970.

[76] R. Morris, U. Von Toussaint, and P. Cheeseman. High Resolution Surface Geometry and Albedo by Combining Laser Altimetry and Visible Images. Technical report, Ames Research Center, Annapolis, MD, United States, January 2001.

[77] National Aeronautics and Space Administration. MAVEN Press Kit. Technical report, NASA, November 2013.

[78] NEA Electronics. Spacecraft Mechanisms Product Catalogue. Technical report, NEA Electronics® Inc., Moorpark, California, USA, April 2014.

[79] M. Negri and L. Grund. Replacement of Hydrazine: Overview and First Results of the H2020 Project Rheform. In *6th European Conference for Aeronautics and Space Sciences (EUCASS)*, Krakow, Poland, 2015.

[80] J. Oberst, V. Lainey, C. Le Poncin-Lafitte, V. Dehant, P. Rosenblatt, S. Ulamec, J. Biele, J. Spurmann, R. Kahle, V. Klein, et al. GETEMME—A Mission to Explore the Martian Satellites and the Fundamentals of Solar System Physics. *Experimental Astronomy*, 34(2):243–271, 2012. doi: 10.1007/s10686-012-9307-0.

[81] J.K. Paik, A.K. Thayamballi, and G.S. Kim. The Strength Characteristics of Aluminium Honeycomb Sandwich Panels. *Thin-Walled Structures*, 35:205–231, November 1999. doi: 10.1016/S0263-8231(99)00026-9.

[82] M. Parisi, S. Finocchiaro, and L. Iess. Multi-Arc and Batch-Sequental Filters for the Orbit Determination of ESA's JUICE Mission. *Planetary and Space Science*, November 2014.

[83] R.S. Park and W.M. Folkner. Very Long Baseline Array Astrometric Observations of Mars Orbiters. *The Astronomical Journal*, 150, October 2015.

[84] P. Pergola. Semianalytic Approach for Optimal Configuration of Electric Propulsion Spacecraft. *IEEE Transactions on Plasma Science*, 43(1):305–320, January 2015. ISSN 0093-3813. doi: 10.1109/TPS.2014.2350078.

[85] M. Persson, K. Anflo, A. Dinardi, and J. Bahu. A Family of Thrusters for ADN-based Monopropellant LMP-103S. In *48th AIAA/ASME/SAE/ASEE Joint Propulsion Conference & Exhibit*, page 3815, Atlanta, Georgia, USA, 2012.

[86] C. Pingyuan, L. Yanjie, Y. Zhengshi, Z. Shengying, and S. Wei. Intelligent Landing Strategy for the Small Bodies: from Passive Bounce to Active Trajectory Control. *Acta Astronautica*, 137(1):232–242, 2017. ISSN 0094-5765. doi: https://doi.org/10.1016/j.actaastro.2017.04.033.

[87] J.J. Plaut and S. Barabash. Jupiter Icy Moons Explorer (JUICE): Science Objectives, Mission and Instruments. In *45th Lunar and Planetary Science Conference*, Berlin, Germany, March 2014.

[88] L. Policastri, J. Carrico Jr., C. Nickel, A. Kam, R. Lebois, and R. Sherman. Orbit Determination and Acquisition for the LADEE and LCD Mission Operations. In *Proceedings of the 25th AAS/AIAA Space Flight Mechanics Meeting*, pages 11–15, Williamsburg, Virginia, USA, 2015.

[89] B.D. Pollard and G. Sadowy. Next Generation Millimeter-wave Radar for Safe Planetary Landing. In *Aerospace Conference, 2005 IEEE*, pages 1213–1219. IEEE, 2005.

[90] E.L. Ralph and Michael A. Chung. Retractable Planar Space Photovoltaic Array. In *21st IEEE Photovoltaic Specialists Conference*, volume 2, pages 1369–1373, Kissimimee, Florida, USA, May 1990.

[91] M.A. Ravine. ECAM Imaging System. Technical report, Malin Space Science Systems, San Diego, California, USA, May 2013.

[92] D. Rebuffat. CDF Study Report, Phobos Sample Return, Phobos Moon of Mars Sample Return Mission. Technical report, ESA, Noordwijk, the Netherlands, 2014.

[93] D.H. Rogstad, A. Mileant, and T.T. Pham. *Antenna Arraying Techniques in the Deep Space Network*, volume 6. John Wiley & Sons, Pasadena, California, USA, 1st edition, 2005.

[94] X. Roser and M. Sghedoni. Control Moment Gyroscopes (CMG's) and their Application in Future Scientific Missions. In *Spacecraft Guidance, Navigation and Control Systems, Proceedings of the 3rd ESA International Conference*, ESTEC, Noordwijk, the Netherlands, November 1996.

[95] R.G. Ross, Jr. Cryocoolers 13. In *Proceedings of the 13th International Cryocooler Conference*, page 20, Pasadena, California, USA, 2005. Springer. ISBN 0-387-23901-4. doi: 10.1007/0-387-27533-9.

[96] I.R. Roza, S. Khurana, I.M. Konovalov, N.M. de Korte, T. van Lith, M.K. Makaveev, Z.N. Rabilotta, W. Van Gijseghem, W. Van Herck, and H.W.W. Guimarães. DSE Mid-term Report Group 11. Technical report, Delft University of Technology, Delft, the Netherlands, May 2017.

[97] R.S. Ryan, J.G. Papadopoulos, L.A. Kiefling, R. Odum, W. Jarvinen, and J. Kennoy. A Study of Saturn AS-502 Coupling Longitudinal Structural Vibration and Lateral Bending Response During Boost. *Journal of Spacecraft and Rockets*, 7(2):113–118, March 1970. doi: 10.2514/3.29884.

[98] M. Ryschkewitsch. *NASA Space Flight Program and Project Management Handbook*. pages 189–219. National Aeronautics and Space Administration Headquarters, Washington, D.C., USA, 1st edition, 2014.

[99] Saft. *Saft batteries... powering outer space for 50 years*. 12, rue Sadi Carnot, 93170 Bagnolet, France, 2017.

[100] V. Sambasiva Rao, M.C. Basava Raj, and L. Nicholas. S-Band Omnidirectional Antenna System for Nano/Micro Student Satellites. *Microwave Journal*, 158:58–64, September 2015.

[101] Scan Automation Technology. Multi-range Analog Timers. URL `http://www.scanelectech.com.tw/pdf/timer_e/T36A.pdf`, Tainan, Taiwan, March 2012.

[102] S. Schick, B. Rusch, and J.C. Batty. Isothermal Structural Panels for Spacecraft Thermal Management. In *25th AIAA/USU Small Satellite Conference*, North Logan, Utah, USA, 2011.

[103] G. Seeber. *Satellite Geodesy*. Walter de Gruyter, Berlin, Germany, 2nd edition, 2003. ISBN 9783110175493.

[104] T. Sheehan. Apollo Program Summary Report. Technical report, National Aeronautics and Space Administration; Lyndon Johnson Space Center, Houston, Texas, USA, April 1975.

[105] S. Shrinivasan, P.M. Norris, J.P. Landers, and J.P. Ferrance. A Low-cost, Low-power Consumption, Miniature Laser-induced Fluorescence System for DNA Detection on a Microfluidic Device. *Clinics Laboratory Medicine*, 1:173–181, March 2007. doi: 10.1016/j.cll.2006.12.010.

[106] Sierra Nevada Corporation. Sierra Nevada Corporation's Space Systems: Space Technologies Product Catalog, 2015.

[107] S. Slobin and C. Chang. 70-m Subnet Telecommunications Interfaces. Technical report, Deep Space Network, La Cañada Flintridge, California, USA, September 2013.

[108] D.E. Smith, M.T. Zuber, X. Sun, G.A. Neumann, J.F. Cavanaugh, J.F. McGarry, and T.W. Zagwodzki. Two-way Laser Link over Interplanetary Distance. *Science*, 311(5757):53–53, January 2006. doi: 10.1126/science.1120091.

[109] SpaceX. Falcon 9 Launch Vehicle: Payload User's Guide. Hawthorne, California, October 2015.

[110] R. Spores, R. Masse, S. Kimbrel, and C. McLean. GPIM AF-M315E Propulsion System. In *50th AIAA Joint Propulsion Conference & Exhibit*, Cleveland, Ohio, USA, July 2013.

[111] S. Starin and J. Eterno. Attitude Determination and Control Systems. Technical report, NASA, San Antonio, Texas, USA, June 2011.

[112] A.D. Steltzner and A.K. Nasif. Anchoring Technology for In Situ Exploration of Small Bodies. In *2000 IEEE Aerospace Conference. Proceedings (Cat. No.00TH8484)*, volume 7, pages 507–518, Big Sky, Montana, USA, March 2000. doi: 10.1109/AERO.2000.879319.

[113] K. Sun, M. Zhu, and Q. Liu. Membrane Material-Based Rigid Solar Array Design and Thermal Simulation for Stratospheric Airships. *Advances in Materials Science and Engineering*, 1(1), August 2014. doi: 10.1155/2014/192707.

[114] W. Tam, M. Bhatia, H. Ali, B. Wise, H. Gutierrez, D. Kirk, D. Jaekle, M. Persson, and K. Anflo. Bringing a PMD Propellant Tank Assembly to the Marketplace: A Model of US-Europe-Industry-Academia Collaboration. In *Space Propulsion Conference*, volume 10, pages 20–30, Cologne, Germany, 2014.

[115] J. Taylor, D. Lee, and S. Shambayati. Mars Reconnaissance Orbiter Telecommunications. Technical report, JPL, September 2006.

[116] M. Thiel, J. Stöcker, C. Rohe, N. I Kömle, G. Kargl, O. Hillenmaier, and P. Lell. The ROSETTA Lander Anchoring System. In *10th European Space Mechanisms and Tribology Symposium*, volume 524, pages 239–246, San Sebastián, Spain, September 2003.

[117] P. Thomas. Surface Features of Phobos and Deimos. *Icarus*, 40(2):223–243, November 1979. ISSN 0019-1035. doi: 10.1016/0019-1035(79)90069-1.

[118] N. Trivellin, M. Meneghini, C. De Santi, S. Vaccari, G. Meneghesso, and E. Zanoni. Degradation of InGaN lasers: Role of Non-radiative Recombination and Injection Efficiency. *Microelectronics Reliability*, 51:1747–1751, November 2011. doi: 10.1016/j.microrel.2011.07.038.

[119] P. Tsiotras and H. Shen. Satellite Attitude Control and Power Tracking with Energy/Momentum Wheels. *Journal of Guidance, Control, and Dynamics*, 24(1):23–24, February 2001.

[120] A.J. Turner. *An Open-source, Extensible Spacecraft Simulation and Modeling Environment Framework*. PhD thesis, Virginia Polytechnic Institute and State University, Blacksburg, Virginia, USA, 2003.

[121] M.J.L. Turner. *Rocket and Spacecraft Propulsion: Principles, Practice and New Developments*. Springer Praxis Books. Springer Berlin Heidelberg, 2008. ISBN 9783540692034.

[122] S. Turyshev, W. Farr, and W. Folkner. Advancing Tests of Relativistic Gravity via Laser Ranging to Phobos. *Experimental Astronomy*, 28(2-3), September 2010. doi: 10.1007/s10686-010-9199-9.

[123] S.G. Turyshev, M. Shao, and K. Nordtvedt. The Laser Astrometric Test of Relativity Mission. *Classical and Quantum Gravity*, 21(12):2773, 2004. doi: 10.1088/0264-9381/21/12/001.

[124] S. Ulamec and J. Biele. From the Rosetta Lander Philae to an Asteroid Hopper: Lander Concepts for Small Bodies Missions. In *7th International Planetary Probe Workshop*, volume 7, Barcelona, Spain, 2010.

[125] S. Ulamec, B. Feuerbacher, K. Wittmann, H. Rosenbauer, G. Haerendel, and F. Lura. Technical Challenge, Scientific Thrill: A Long Term Lander on an Active Comet. *Abstracts of the Lunar and Planetary Science Conference*, 26:1431, March 1995.

[126] J.M. Weekley and B.J. Magnus. TWTA Versus SSPA: A Comparison of On-Orbit Reliability Data. *IEEE Transactions on Electron Devices*, 52(5):650–652, 2005. doi: 10.1109/IVELEC.2004.1316306.

[127] N. Wei-Tou. ASTROD (Astrodynamical Space Test of Relativity using Optical Devices) and ASTROD I. *Nuclear Physics B-Proceedings Supplements*, 166:153–158, 2007.

[128] J.R. Wertz and W. Larson. *Space Mission Analysis and Design*. Space Technology Library. Springer Netherlands, Hawthorne, CA, USA, 3rd edition, 1999. ISBN 9780792359012.

[129] S.A. Whitmore, D.P. Merkley, M.I Judson, and S.D. Eilers. Development and Testing of a Green Monopropellant Ignition System. In *49th AIAA/ASME/SAE/ASEE Joint Propulsion Conference*, page 3967, San Jose, California, USA, July 2013.

[130] M. Williamson. Protection of the Space Environment: The First Small Steps. In *34th COSPAR Scientific Assembly*, volume 34 of *COSPAR Meeting*, Kirby Thorne, United Kingdom, 2002.

[131] L. Witte, S. Schroeder, H. Kempe, T. van Zoest, R. Roll, S. Ulamec, J. Biele, and J. Block. Experimental Investigations of the Comet Lander Philae Touchdown Dynamics. *Journal of Spacecraft and Rockets*, 51: 1885–1894, November 2014. doi: 10.2514/1.A32906.

[132] S. Woicke and E. Mooij. Passive Hazard Detection for Planetary Landing. In *AIAA Guidance, Navigation and Control Conference*, San Diego, California, USA, January 2016.

[133] G. Wolff and E. Felkel. Large Retractable Solar Cell Array. Technical Report 1, Hughes Aircraft Company, Cameron Station Alexandria, Virginia 22314, USA, July 1969.

[134] T.H. You, A. Graat, D. Highsmith, S. Long, R. Bhat, S. Demcak, N. Higa, and M. Jah. Mars Reconnaissance Orbiter Interplanetary Cruise Navigation. In *Proceedings 20th International Symposium on Space Flight Dynamics*, September 2007.